Searching for High-energy Neutrinos from Supernovae with IceCube and an Optical Follow-up Program

DISSERTATION

zur Erlangung des Doktorgrades (Dr. rer. nat.) der
Mathematisch-Naturwissenschaftlichen Fakultät
der Rheinischen Friedrich-Wilhelms-Universität Bonn

vorgelegt von

Anna Franckowiak

aus Wuppertal

Bonn (August, 2011)

Angefertigt mit Genehmigung der Mathematisch-Naturwissenschaftlichen Fakultät der
Rheinischen Friedrich-Wilhelms-Universität Bonn

1. Gutachter: Prof. Dr. Marek Kowalski
2. Gutachter: Prof. Dr. Jochen Dingfelder

Tag der Promotion: 14.10.2011
Erscheinungsjahr: 2011

Für meinen Opa,
der mir das Einmaleins
(und vieles mehr)
beigebracht hat.

"The chances of a neutrino actually hitting something as it travels through all this howling emptiness are roughly comparable to that of dropping a ball bearing at random from a cruising 747 and hitting, say, an egg sandwich."

The Hitchhiker's Guide to the Galaxy, Douglas Adams

Abstract

In violent astrophysical processes high-energy neutrinos of TeV to PeV energies are expected to be produced along with the highest energy cosmic rays. The acceleration of nuclei to very high energies is assumed to takes place in astrophysical shocks and neutrinos are produced in the interaction of these cosmic rays with ambient baryons or photons. The neutrinos then escape the acceleration region and propagate through space without interaction, while the nuclei are deflected in magnetic fields and no longer carry information about their source position. Unlike gamma-rays, neutrinos are solely produced in hadronic processes and can therefore reveal the sources of charged cosmic rays.
The IceCube neutrino detector, which is located at the geographical South Pole, has been build to detect these high-energy astrophysical neutrinos. The deep clear Antarctic ice is instrumented with light sensors on a grid, thus forming a Cherenkov particle detector, which is capable of detecting charged particles induced by neutrinos above $100\,\mathrm{GeV}$.
Transient neutrino sources such as Gamma-Ray Bursts (GRBs) and Supernovae (SNe) are hypothesized to emit bursts of high-energy neutrinos on a time-scale of $\lesssim 100\,\mathrm{s}$. While GRB neutrinos would be produced in the high relativistic jets driven by the central engine, core-collapse SNe might host soft-relativistic jets which become stalled in the outer layers of the progenitor star and lead to an efficient production of high-energy neutrinos.
This work aims for an increased sensitivity for these neutrinos and for a possible identification of their sources. Towards this goal, a low-threshold optical follow-up program for neutrino multiplets detected with IceCube has been implemented. If a neutrino multiplet – i.e. two or more neutrinos from the same direction within $100\,\mathrm{s}$ – is found by IceCube a trigger is sent to the Robotic Optical Transient Search Experiment (ROTSE). The 4 ROTSE telescopes immediately start an observation program of the corresponding region of the sky in order to detect a possible optical counterpart to the neutrino events.
Complementary to previous transient neutrino searches, which have been performed offline on IceCube data on source regions and time windows provided by gamma-ray satellites, this neutrino search is applied – for the first time – in real time to neutrino data at the South Pole. It is sensitive to transient objects, including those which are gamma-ray dark or not detected by gamma-ray satellites. In addition to a gain in sensitivity, the optical observations may allow the identification of the transient neutrino source, be it a SN, a GRB or any other transient phenomenon producing an optical signal. Hence, it enables to test the hypothesis of soft relativistic jets in SNe and may shed light on the connection between GRBs, SNe and relativistic jets.

The content of this work are the development and implementation of the optical follow-up program as well as the analysis of the data collected in the first year of operation. No statistically significant excess in the rate of neutrino multiplets has been observed and furthermore no coincidence with an optical counterpart was found. However, for the first time stringent limits can be set on current models predicting a high-energy neutrino flux from soft relativistic hadronic jets in core-collapse SNe. It can be concluded that a sub-population of SNe with jets with a typical Lorentz boost factor of 10 and a jet energy of 3×10^{51} erg does not exceed 4.2% at 90% confidence.

Zusammenfassung

In energiereichen astrophysikalischen Prozessen erwartet man die Produktion von Neutrinos mit Energien im TeV bis PeV Bereich Seite an Seite mit der Produktion der hochenergetischen komischen Strahlung. Die Beschleunigung der Kerne zu den gemessenen hohen Energien findet vermutlich in astrophysikalischen Schocks statt. In Wechselwirkungen mit den umgebenden Baryonen und Photonen werden dann Neutrinos produziert. Diese Neutrinos können die Beschleunigungsregion verlassen und propagieren ungehindert durch den Raum, während die Kerne in intergalaktischen Magnetfeldern abgelenkt werden und sich ihre Quellen somit nicht mehr zurück verfolgen lassen. Im Gegensatz zu Photonen werden Neutrinos ausschließlich in hadronischen Prozessen erzeugt und erlauben es so, die Quellen der kosmischen Strahlung zu identifizieren.
Zum Nachweis dieser astrophysikalischen Neutrinos wurde am geographischen Südpol der Neutrinodetektor IceCube gebaut. Das tiefe antarktische Eis wurde dafür mit Lichtsensoren ausgestattet und auf diese Weise in einen Tscherenkov Teilchendetektor verwandelt, welcher geladene Teilchen nachweisen kann, die durch Neutrinos mit Energies oberhalb von $100\,\mathrm{GeV}$ induziert werden.
Theoretische Modelle sagen vorher, dass transiente Neutrinoquellen wie Gammastrahlungsausbrüche (GRBs) und Supernovae (SNe) kurze Ausbrüche – sogenannte "Bursts" – von hochenergetischen Neutrinos auf einer Zeitskala von $\lesssim 100\,\mathrm{s}$ emittieren. Während GRB Neutrinos in hoch relativistischen Jets produziert werden, könnten Kernkollaps-Supernovae (CCSNs) einen schwach relativistischen Jet beherbergen, dem es nicht gelingt, die äußere Hülle des Vorgängersternes zu durchdringen, sondern der darin zum Stillstand kommt und so für effiziente Neutrinoproduktion sorgt.
Ziel diese Arbeit ist die Verbesserung der Sensitivität für die Messung diese Neutrinos und die Identifikation ihrer Quellen. Dafür wurde ein optisches Nachverfolgungsprogramm für Neutrinomultipletts entwickelt, welche mit dem IceCube Neutrinodetektor gemessen werden. Falls ein Neutrinomultiplett – d.h. mindestens zwei Neutrinos aus der gleichen Richtung innerhalb von $100\,\mathrm{s}$ – von IceCube gefunden wird, wird ein Trigger an das Robotic Optical Transient Search Experiment (ROTSE) gesendet. Die vier ROTSE Teleskope starten unmittelbar ein Beobachtungsprogramm für die entsprechende Richtung am Himmel, um ein optisches Gegenstück zu den Neutrinoereignisse detektieren zu können.
Im Gegensatz zu den bisher durchgeführten Suchen nach transienten Neutrinoquellen, welche offline durchgeführt und durch die von Gammastrahlensatelliten bereitgestellte Informationen getriggert werden, wird diese Analyse als bislang erste Analyse in Echtzeit auf Neutrinodaten am Südpol angewendet. Sie ermöglicht die Detektion von transienten Objekten, einschließlich solcher, die keine Gammastrahlen emittieren oder die nicht von Satelliten beobachtet werden können. Zusätzlich zu einer Verbesserung der Sensitivität können die optischen Beobachtungen eine Identifikation der Quelle erlauben, unabhängig davon, ob es sich um eine SN, einen GRB oder eine anderes transientes Phänomen handelt, das ein optisches Signal erzeugt. Folglich kann mit dieser Methode das Modell für schwach relativistische Jets in SNe getestet, sowie Aufschluß über die Verbindung zwischen GRBs, SNe und

relativistischen Jets gegeben werden.
Der Inhalt dieser Arbeit ist die Entwicklung und Durchführung des optischen Nachverfolgungsprogramms sowie die Analyse der Daten, welche während des ersten Jahres des Betriebs aufgenommen wurden. In den Daten wurde weder ein statistisch signifikanter Exzess der Neutrinomultiplettrate noch ein optisches Gegenstück zu einem der Neutrinomultipletts gefunden. Diese Analyse erlaubt daher zum ersten mal ein strenges Limit auf aktuelle Modelle zu setzen, welche einen Fluss hochenergetischer Neutrinos aus schwach relativistischen hadronischen Jets in Kernkollaps-Supernovae vorhersagen. Es kann mit einem Vertrauensintervall von 90% ausgeschlossen werden, dass die Subpopulation von SNe mit Jets mit typischen Lorentz Boost Faktoren von 10 und Jetenergien von 3×10^{51} erg 4.2% überschreitet.

Contents

Chapter 1

Introduction

The neutrino was first postulated by Pauli in 1930 [1] to explain the observed energy spectrum of the β-decay. Initially, the β-decay was believed to be a two-body decay. Under that assumption the measured energy spectrum violated the law of energy conservation. To save this fundamental law of physics, Pauli found his "desperate remedy" - he postulated a third particle participating in the decay. Pauli called the new particle a neutron, but it was later renamed neutrino by Enrico Fermi. He predicted the neutrino to be neutral, to have a small mass and a spin of $1/2$, thus obeying the exclusion principle.
It took another 26 years before the first neutrinos were detected by Frederic Reines and Clyde Cowan [2, 3]. They used the process of inverse β-decay

$$\bar{\nu}_e + p \rightarrow e^+ + n \tag{1.1}$$

to indirectly detect anti-electron-neutrinos $\bar{\nu}_e$ produced in large amounts in the nuclear fission processes in nuclear power plants. The positron and the neutron were detected as a pair of delayed pulses in liquid scintillation counters.
Two additional neutrino flavors, the muon and the tau neutrino (ν_μ and ν_τ) have been discovered later in 1962 [4] and 2000 [5] respectively. Oscillations between the different neutrino flavors discovered in solar neutrino and atmospheric neutrino fluxes indicate that neutrinos have a mass [6]. Current experimental limits on the maximum neutrino mass obtained from combining the upper limit on the electron neutrino mass obtained from β-decay of tritium with the mass square difference measured in neutrino oscillation experiments are $m_\nu < 2\,\text{eV}$ [7].
The era of neutrino astronomy began with the detection of solar neutrinos by Ray Davis at the Homestake experiment [8] in 1968. Fusion reactions in the core of the sun produce a large flux of electron neutrinos. After taking into consideration the effect of neutrino oscillation the solar neutrino measurements confirmed the solar model [9]. Nowadays large scale modern neutrino detectors can "see" the sun in neutrinos (see Fig. 1.1). The first and so far only detection of neutrinos from outside our solar system took place in 1987, when the blue giant Sanduleak $69°202$ in the Large Magellanic Cloud ended its life in a supernova explosion[1] (see Fig. 1.2). This was the closest supernova since 1604 and became the best studied supernova ever, yielding a deep inside into the physics of core-collapse supernovae. The light from the supernova reached Earth on February 23, 1987, approximately 3 h after a burst of neutrinos detected by three different underground neutrino detectors, Kamiokande-II [13], IMB [14] and Baksan [15].
While solar and supernova neutrinos reach energies of several tens of MeV, high-energy

[1] Note that the actual explosion took place 160.000 years before, but the signal had to travel $50\,\text{kPc}$ ($160.000\,\text{Ly}$) before it reached the Earth.

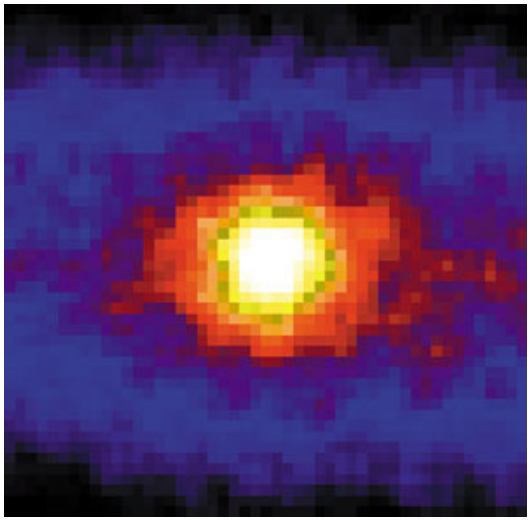

Figure 1.1: The sun in neutrino "light" observed by Super-Kamiokande [10]. The exposure time was 503.8 days and each pixel represents ~1° of the sky [11].

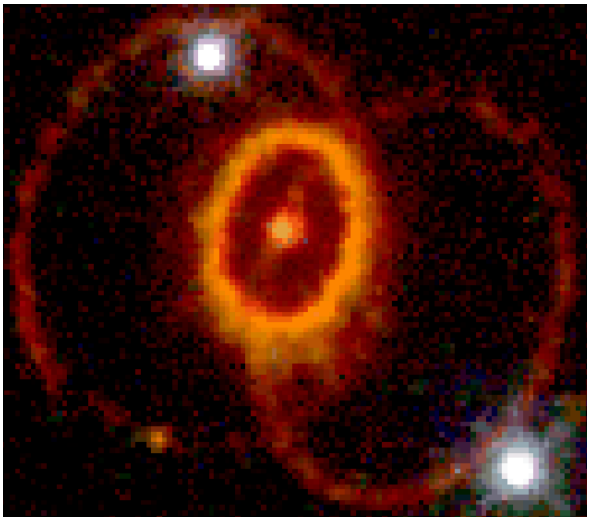

Figure 1.2: SN1987A observed by the Hubble space telescope [12] 20 years after the explosion showing its supernova remnant. The ring structure can be explained by ionization of material, which was ejected by the progenitor star 20000 years before the explosion, by a flash of ultraviolet radiation from the shock wave breakout of the explosion.

neutrinos of TeV to PeV energies are expected to be produced in violent astrophysical processes along with the highest energy cosmic rays. First discovered in a balloon experiment by Victor Hess in 1912 [16], the cosmic radiation is nowadays extensively studied. The cosmic ray spectrum (see Fig. 1.3) covers an energy range of more than 12 orders of magnitudes. It can be described by a sequence of power laws. The first two are separated by a steepening between 10^{15} and 10^{16} eV, which is called the *knee*. It is believed that cosmic rays up to this energy are of galactic origin, most probably accelerated in supernova remnants [17]. The second feature, known as the *ankle*, might be connected to the onset of an extragalactic component [18]. Assuming the cosmic rays with energies above the ankle are protons, an galactic origin can be excluded because the gyroradius of a proton at those energies in the galactic magnetic field exceeds the size of the galaxy. However, recent results of the Pierre Auger Observatory indicate an increasing component of heavy elements [19]. Above a threshold of ~5×10^{19} eV (the Greissen-Zatsepin-Kuzmin (GZK) cutoff) the photo-pion production ($p\gamma \rightarrow n\pi^+$ and $p\gamma \rightarrow p\pi^0$) of protons with the cosmic microwave background becomes dominant resulting in a rapid steepening of the cosmic ray flux [20, 21].

Despite extensive measurement campaigns of comic rays, the sources and mechanisms responsible for the acceleration of the highest energy comic rays are still unknown. Acceleration of protons to very high energies is expected to take place in astrophysical shocks. The charged cosmic rays interact with ambient photons or baryons and produce high-energy astrophysical neutrinos (for reviews see [22, 23, 24, 25]). Neutrinos escape the acceleration region and propagate through space without interaction, while charged particles are deflected in magnetic fields and no longer point back to their source. Unlike gamma-rays, neutrinos are solely produced in hadronic processes and could therefore reveal the sources of the highest energy charged cosmic rays.

Gamma-ray bursts (GRBs) could provide the environment and the required energy to explain the production of the highest energy cosmic-rays [26] and hence are a plausible can-

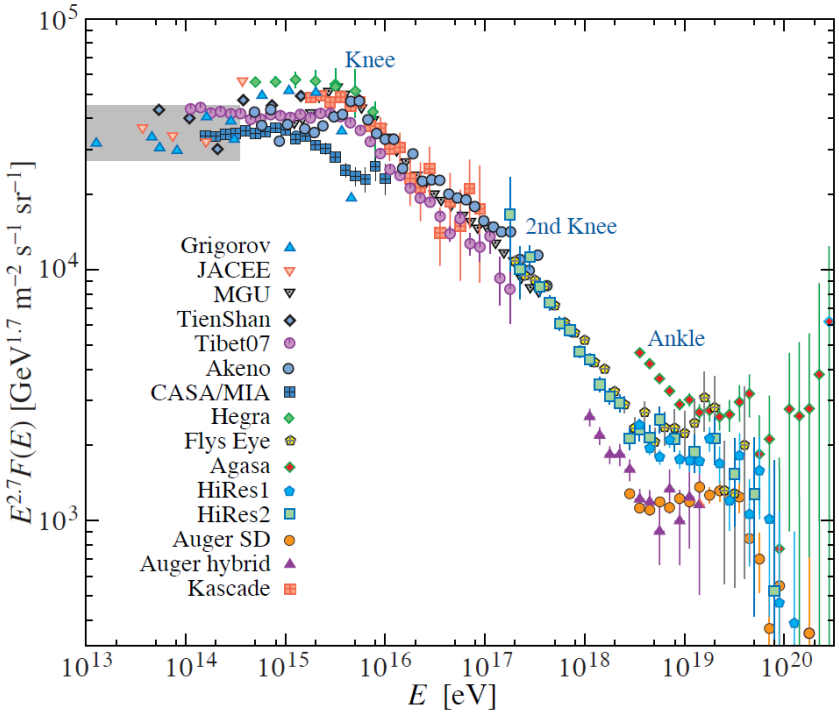

Figure 1.3: Cosmic ray spectrum from air shower measurements. Direct measurements are marked by the shaded area. To better display the features of the steeply falling spectrum it has been multiplied by $E^{2.7}$. [7]

didate. GRBs are short intense flashes of gamma-rays and the brightest known sources in terms of the emitted radiation per solid angle. According to the collapsar model ([27, 28, 29]), long GRBs have their origin in the collapse of a massive, rapidly rotating star into a black hole surrounded by an accretion disk. Relativistic jets form along the stellar axis. Acceleration of charged particles takes place in the jets representing a possible source of high-energy neutrinos.

Recent observations indicate a connection of the two most powerful explosions in terms of released energy: GRBs and core-collapse supernovae (CCSNe), which both have their origin in the collapse of a massive star. This GRB-SN connection gives rise to the idea that GRBs and supernovae (SNe) might have the jet signature in common and a certain fraction of core-collapse SNe might host soft relativistic jets. SN jets are suggested to be equally energetic and more baryon-rich, hence they are only mildly relativistic. Such soft relativistic jets would become stalled in the outer layers of the progenitor star, leading to essentially full absorption of the electromagnetic radiation emitted by the jet and at the same time an efficient production of high-energy neutrinos. This motivates a search for neutrino emission, as neutrinos would be able to escape from within the star.

The IceCube neutrino detector, located at the geographic South Pole, is built to detect such high-energy astrophysical neutrinos. So far GRB neutrino searches have been performed triggered by gamma-ray satellite detections on AMANDA [30] and IceCube [31] data. Time and direction provided by gamma-ray satellites allow an almost background free search. Furthermore, a dedicated search for a neutrino signal in coincidence with the observed X-ray flash of SN 2008D has been conducted by IceCube [32] in order to test the soft jet scenario for CCSNe. Neither the GRB nor the SN neutrino search led to a detection yet, but set upper limits on the neutrino flux.

Early SN detections, as in the case of SN 2008D, are very rare since X-ray telescopes have

a limited field of view. However, neutrino telescopes cover half of the sky at any time. If neutrinos produced in soft relativistic SN jets are detected in real time, they can be used to trigger follow-up observations [33]. This is realized with the optical follow-up program presented here.
In order to implement the optical follow-up program the first online high-energy neutrino event selection has been developed for IceCube. Fast online data processing and accurate reconstruction of the event directions are the key requirements for a successful operation of the program. This is achieved by parallel online data processing at a computer cluster at the South Pole, where filtering and sophisticated reconstructions are applied. A multiplicity trigger selects neutrino burst candidates and the directional information is transferred to the four ROTSE telescopes, which start the follow-up immediately and continue observations for several nights. The obtained optical data is analyzed in order to search for an optical supernova counterpart. Development and implementation of the optical follow-up program as well as the analysis of the data collected in the first year of operation are content of this work.
Complementary to the triggered offline searches, the optical follow-up program is an online search independent of satellite detections. It is sensitive to transient objects, which are either gamma-dark or missed by gamma-ray satellites. In addition to a gain in sensitivity, the optical observations may allow to identify the transient neutrino source, be it a SN, GRB or any other transient phenomenon producing an optical signal. Hence it enables a test of the plausible hypothesis of a soft relativistic SN jet and sheds light on the connection between GRBs, SNe and relativistic jets.
In the following the optical follow-up program is presented starting with Chap. 2, which summarized briefly the physics of gamma-ray bursts and supernova including the expected neutrino emission. The principle of neutrino detection is presented in Chap. 3, followed by a detailed description of the IceCube neutrino detector in Chap. 4. The ROTSE telescopes are introduced in Chap. 6. Chapter 5 outlines the IceCube component of the optical follow-up program while Chap. 7 focuses on the search for the optical counterpart and Chap. 8 deals with the explosion time estimation from the SN light curve. Significance and limit calculations are discussed in Chap. 9, followed by the discussion of systematic errors in Chap. 10. Finally, the results from the first year of data taking are shown in Chap. 11 with a focus on the SN soft jet model. A first limit on the hadronic jet production in CCSNe is presented. Chapter 12 concludes with a summary and outlook to future extensions of the optical follow-up program.

Chapter 2

Transient Neutrino Sources

Bursts of high-energy neutrinos are assumed to be produced in astrophysical processes when protons are accelerated to very high energies in a dense baryonic environment. The most luminous known astrophysical objects are gamma-ray bursts, which release electromagnetic radiation of an energy of typically 3.0×10^{51} erg in less than a minute (this is comparable to the energy emitted by the sun in several billion years or the energy emitted by the galactic center in 100 years.). During this time they are by far the brightest gamma-ray source in the sky. Other candidates for transient neutrino sources are supernovae, which release a similar amount of kinetic energy as GRBs and are believed to have a similar origin. The detection of neutrinos from these sources could reveal the nature of the physical processes responsible for such massive energy outbursts and would carry information from inside the dense objects where no optical signal can escape.
In this chapter the physics of SNe and GRBs is outlined followed by a presentation of the neutrino fluxes expected according to current models.

2.1 Supernovae

Humans have been observing the night sky throughout history. So-called *guest stars* observable for several month up to years appear in many ancient records [34] and are today reconstructed as supernova detections. Chinese records of guest stars range back to 185 AD. Early documented positions of guest stars appeared in documents of Japanese and Chinese observers from 1006, 1054 and 1181. Further well-recorded historical SNe are described by Kepler and Tycho in 1604 and 1572 respectively. Today we know that those guest stars mark the end of the evolution of massive stars. Thanks to accurate position information found in ancient documents some historic SN can be connected to supernova remnants, which are visible today as expanded objects consisting of the ejected material from the explosion. An example is the crab nebular with an extension of $420'' \times 290''$, which was observed as a guest star in 1054.
Nowadays, supernovae are frequently observed and are extensively studied. They are found to be the most energetic events in the entire universe releasing ~10^{53} erg s^{-1} of energy (~10^{51} erg s^{-1} in kinetic energy). They easily outshine entire galaxies and produce most of the heavy elements in nature. However, the complex process of the explosion is not fully understood yet. Several models are used to simulate the physical processes on modern supercomputers, but none is capable of explaining all observations and most fail to explode the star. Open questions are for example the role of neutrinos, rotation and magnetic fields [35]. Large progress has been made in astronomy since the first supernova was detected and improved telescopes allowed the observations of many supernovae outside of our galaxy.

Hence a larger sample of supernova observation can be studied and lead to a classification of supernovae according to their observational features.

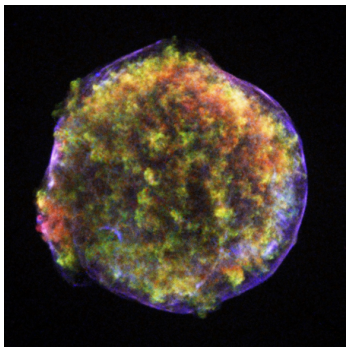

(a) Remnant of the SN observed by Tycho in 1572. Image by the Chandra X-ray observatory [36].

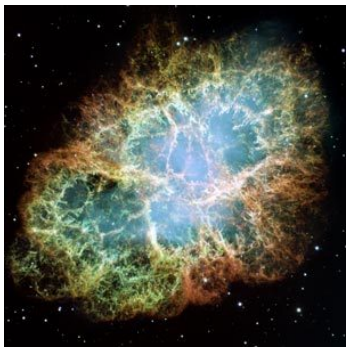

(b) Crab Nebula (supernova remnant associated with historic SN from 1054) observed by the Hubble space telescope [37].

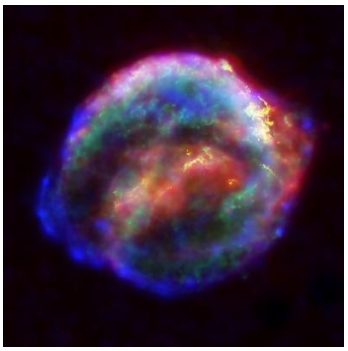

(c) Remnant of Kepler's supernova (1604) observed by Chandra [38]

Figure 2.1: Historic supernovae, today visible as supernova remnants.

2.1.1 Classification

For historical reasons SNe are classified according to the spectral lines from individual elements found in their spectrum. SNe of type II show a hydrogen line in their spectra while the hydrogen line is absent in type Ia spectra. Type I SNe are further classified in Ia, Ib and Ic. Type Ia SNe contain silicon, while type Ib and type Ic SNe do not. Type Ib and Ic differ in the amount of helium. Ib SNe show none or only a weak helium line and Ic SNe a bright line.
Today our knowledge of SNe allows a classification of SNe in two classes: Type Ia and core-collapse SN (CCSN). From a physical point of view SNe type Ia differ from SNe type Ib, Ic and II: Type Ia SNe happen as thermonuclear explosions exclusively in binary systems while SNe type Ib, Ic and II are produced by the core-collapse of a single massive star.
The classification scheme is displayed in Fig. 2.2, while Fig. 2.3 shows spectra at maximum brightness for SNe type Ia, Ibc and II obtained from spectral templates [39]. Type II SNe can

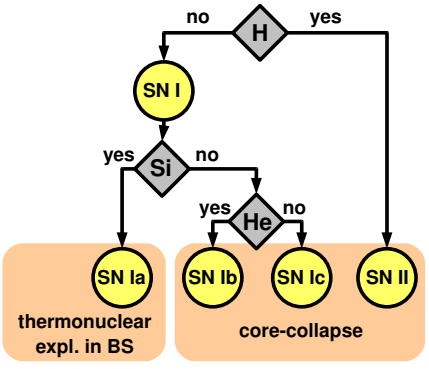

Figure 2.2: Supernova classification scheme.

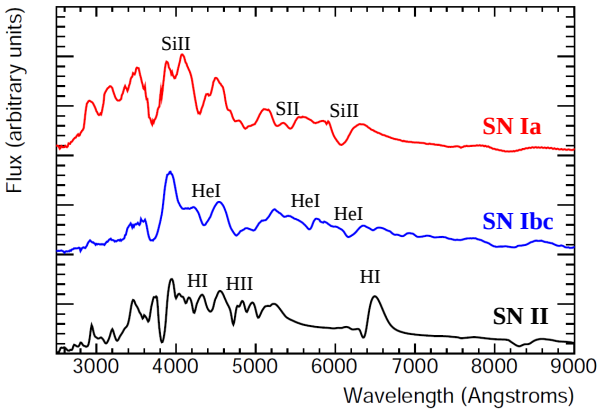

Figure 2.3: Template spectra for SNe type Ia, Ibc and II obtained from spectral templates [39].

be further classified based on the shape of their light curve. SNe of type IIL decline steadily after reaching the maximal brightness, while SNe of type IIP show a plateau in their light curve (see Fig. 2.4). The plateau is believed to be caused by an outer hydrogen envelope, which is expelled by the progenitor star of type IIL SNe. The outer hydrogen layer is ionized by the shock wave of the explosion causing a change in opacity [40].
This work's focus is on core-collapse SNe since those are connected to gamma-ray bursts (see Sec. 2.3) and are expected to produce high-energy neutrinos (see Sec. 2.6).

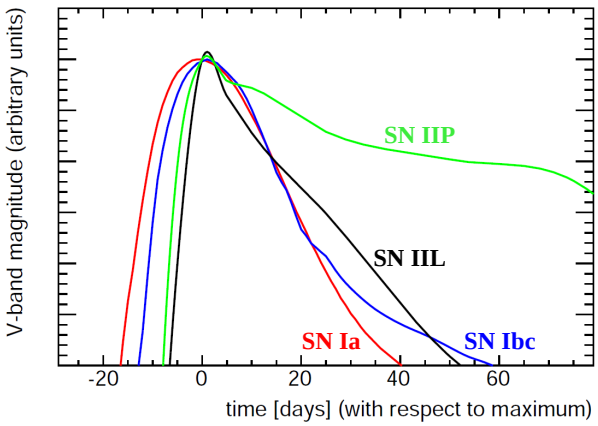

Figure 2.4: Template V-band light curves for SNe type Ia, Ibc, IIL and IIP obtained from light curve templates [39].

2.1.2 Core-collapse Supernovae

Core-collapse SNe mainly occur in active star-forming regions, e.g. in spiral arms of galaxies, where massive stars ($M > m_{\odot}$) are created frequently. Fusion processes take place in the core of the star. The gravitational pressure is supported by radiation pressure powered by the fusion: The star is in pressure equilibrium. At the beginning of the life cycle of a main sequence star hydrogen is burned to helium. Once the fuel of hydrogen is exhausted the radiation pressure decreases and the core of the star contracts. The contraction causes a rise in temperature and eventually increases the temperature enough to start the next step in the fusion chain, fusion of helium to carbon. If the mass of the star exceeds 8-10 $m_{\odot}$ the fusion chain goes on until iron (Fe) is produced in the core. In every step the core temperature increases and accelerates the fusion process of the next step (see table 2.1). With the production of iron the fusion process comes to an end. Iron is the element with the highest nuclear binding energy as illustrated in Fig. 2.5. While heavy elements are produced in the core-region, lighter elements are produced in shells around the core. Iron is the fusion product in the center followed by sulfur (S) on the neighboring shell, followed by silicon (Si), magnesium (Mg), sodium (Na), neon (Ne), oxygen (O), carbon (C), helium (He) and hydrogen (H) in the outer shell. This onion-like structure is displayed in Fig. 2.6. If the star exhausts its fuel the fusion comes to stop. Figure 2.7 (top left) shows the initial phase of the collapse with the core consisting of iron-group nuclei. The radiation pressures disappears and the core collapses. Electron degeneracy pressure cannot support gravity: Neutrons are produced in inverse beta-decay (electron capture) and release a huge number of neutrinos (~10^{58} neutrinos).

$$p + e^{-} \rightarrow n + \nu_e. \tag{2.1}$$

Table 2.1: Burning stages of a star with mass $15\,m_\odot$ (adapted from [35])

Burning Stage	Time Scale	Fuel	Product	Temperature (10^9 K)	Density (gm/cm^3)
Hydrogen	11 My	H	He	0.035	5.8
Helium	2.0 My	He	C, O	0.18	1390
Carbon	2000 y	C	Ne, Mg	0.81	2.8×10^5
Neon	0.7 y	Ne	O, Mg	1.6	1.2×10^7
Oxygen	2.6 y	O, Mg	Si, S, Ar, Ca	1.9	8.8×10^6
Silicon	18 d	Si, S, Ar, Ca	Fe, Ni, Cr, Ti,...	3.3	4.8×10^7
Iron core-collapse	~1 s	Fe, Ni, Cr, Ti,...	Neutron Star	> 7.1	$> 7.3 \times 10^9$

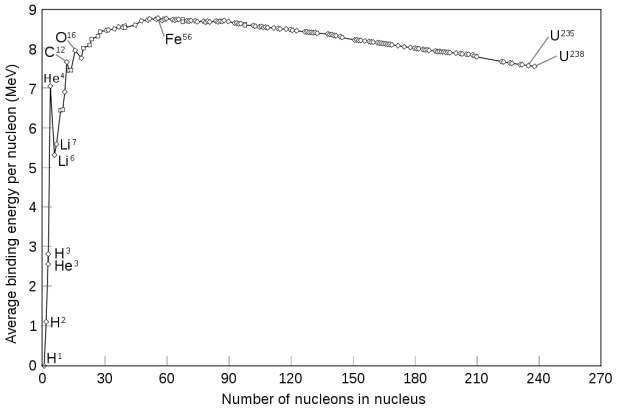

Figure 2.5: Nuclear binding energy as a function of atomic mass (graphic from [41]). Iron is the element with the highest nuclear binding energy. Energy is released by fusion of lighter elements and fission of elements with higher number of nucleons.

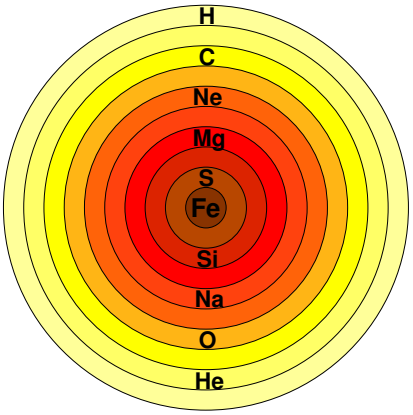

Figure 2.6: Fusion processes inside a massive star: Heavier elements are produced in the core-region of the star and lighter elements are produced in shells around the core. Iron is produced in the center followed by sulfur, silicon, magnesium, sodium, neon, oxygen, carbon, helium, and finally hydrogen in the outer shell.

At the same time the high temperature causes photo-disintegration, i.e. radiation begins to disintegrate the iron nuclei to helium and the helium further to nucleons.

$$^{56}\mathrm{Fe} + \gamma \rightarrow 13\ ^4\mathrm{He} + 4\mathrm{n} \tag{2.2}$$

$$^4\mathrm{He} + \gamma \rightarrow 2\mathrm{p}^+ + 2\mathrm{n} \tag{2.3}$$

The core contracts to nuclear density forming a proto-neutron star. If the density exceeds a density of $\rho_{\mathrm{trap}} \approx 10^{12}\,\mathrm{g/cm}^3$ the neutrino diffusion time becomes larger than the collapse time and the neutrinos are trapped inside the core and thus cannot cool the core further (see Fig. 2.7 upper right). Infalling material bounces back from the dense core (see Fig. 2.7 middle left) and propagates outside as a shock wave, while the outer core continues to collapse (see Fig. 2.7 middle right). The shock wave stalls as it moves into the outer, still collapsing, layers. However, the inner core continues to collapse creating a neutron star radiating away

3×10^{53} erg (10% of its rest mass) and will collapse to a black hole if its mass exceeds $25\,m_{\odot}$. 99.9% of the energy is emitted in neutrinos. The neutrino emission is delayed by the fraction of a second since the trapped neutrinos need to diffuse out of the dense core. The neutrinos deposit some of their energy to the stellar medium in charged current weak interactions

$$\nu_{\mathrm{e}} + n \rightarrow \mathrm{e}^{-} + \mathrm{p} \tag{2.4}$$

$$\overline{\nu}_{\mathrm{e}} + p \rightarrow \mathrm{e}^{+} + \mathrm{n} \tag{2.5}$$

and power an outgoing shock-wave, which ejects the outer layers causing the actual explosion (see Fig. 2.7 bottom left). It is commonly accepted that the explosion can only be explained by the neutrino emission.
Elements heavier than iron might be produced in the shock by rapid neutron capture (r-process) [35] (see Fig. 2.7 bottom right). This might play an important role to explain the abundance of heavy elements in the universe. Once the shock wave breaks out of the star electromagnetic radiation is initially emitted as X-ray or UV flash. Those flashes are short and happen long before the SN light curve reaches its maximum. Hence, they have only been detected for few SNe (for example in the case of SN2006aj [43]). As it expands the supernova becomes visible at optical wavelengths. The photosphere expands increasing the surface area and lowering the density so that trapped radiation can diffuse out more freely resulting in a rise of the light curve [44]. The peak in the light curve occurs when the temperature of the outer layers starts to decrease and the light curve continues in an exponential tail powered by radioactive decay of ^{56}Ni and ^{56}Co

$$^{56}\mathrm{Ni} \rightarrow {}^{56}\mathrm{Co} + \mathrm{e}^{+} + \nu_{\mathrm{e}} + \gamma \tag{2.6}$$

$$^{56}\mathrm{Co} \rightarrow {}^{56}\mathrm{Fe} + \mathrm{e}^{+} + \nu_{\mathrm{e}} + \gamma \tag{2.7}$$

with a half-life of 6 and 77 days respectively. The gamma-rays produced in the radioactive decay down-scatter or thermalize in the ejecta until they emerge as optical or near infrared photons [45].
Despite frequent optical observations, enabled by modern telescope technology, the mechanism of the explosion is not fully understood. Multidimensional simulations are performed to test current models and to obtain a deeper understanding of the complex system of a stellar core-collapse [42, 46]. It is not clear how neutrinos power the explosion and which role is played by rotation and magnetic fields. Neutrino emission could only be detected once in the case of SN1987A. In addition to the neutrinos produced in the stellar collapse, which have energies of 10-20 MeV, CCSN might also be sources of high-energy TeV neutrinos (see Sec. 2.6), which are aimed to be detected in a generic way for the first time in this work. High energy neutrino interactions have larger cross-sections compared to low energy neutrinos. Furthermore less densely instrumented detectors are necessary to detect high energy neutrinos allowing the construction of large detector volumes and hence reaching sensitivity to SNe outside of our galaxy.

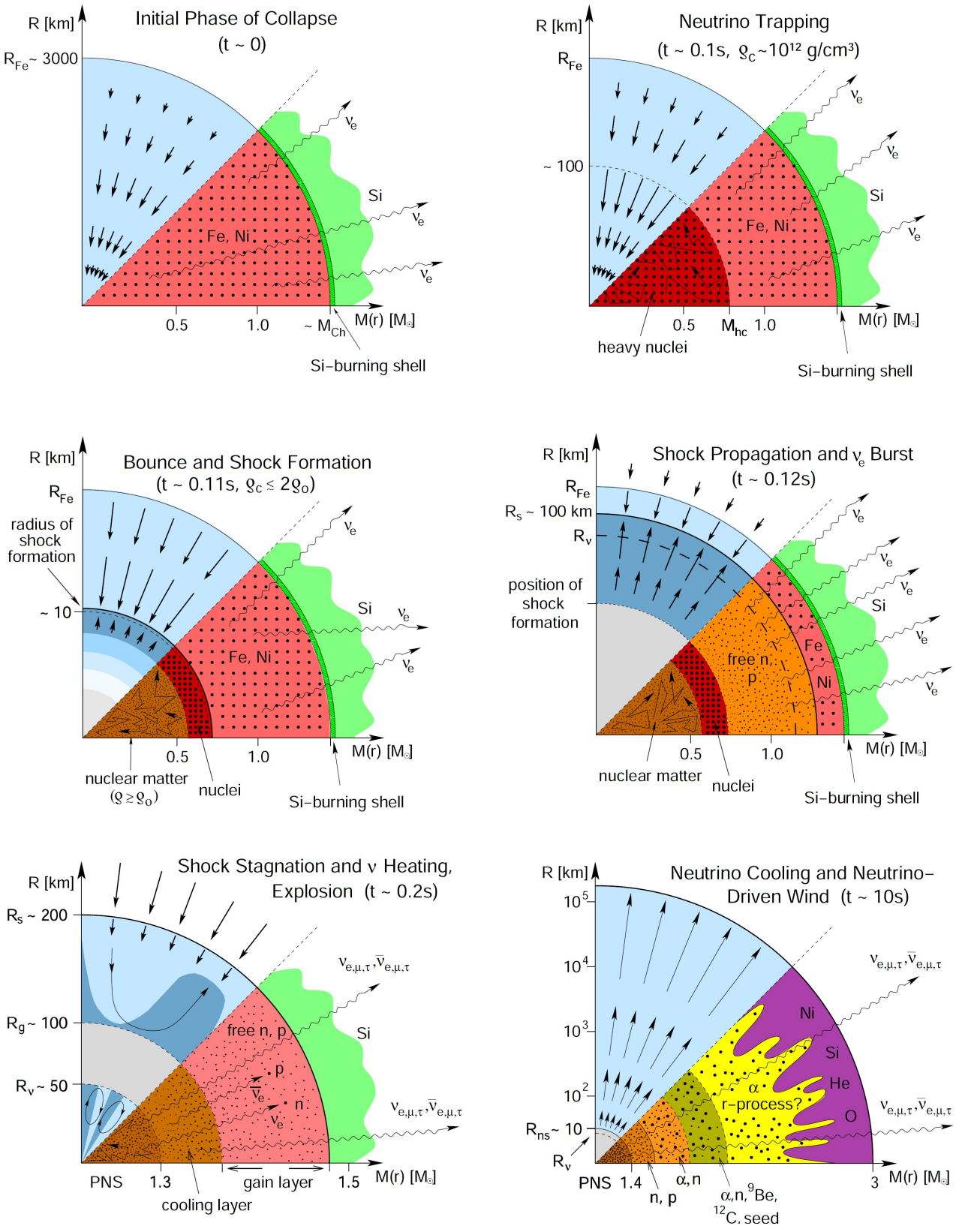

Figure 2.7: Schematic evolution of a CCSN (adopted from [42]). The upper half displays the dynamic conditions with vectors representing velocities while the lower half shows the nuclear composition (see text for explanation).

Core-collapse SN Rates

The rate of core-collapse SN is of special interest of this work, which performs a search for high energy neutrinos emitted by CCSNe, to compute the expected rate of detections. Core-collapse SNe closely follow the star formation rate, since they mark the death of massive stars ($M > 8\,m_\odot$), which have short lifetimes ($0.17(M/(8\,m_\odot))^{-2.5}$ Myr) [47]. The nearby SN rate based on the star formation rate is calculated in [48]. Their calculation results in ~1 core-collapse SN per year within a radius of 10 Mpc. The local star formation rate is obtained from the observation of galaxies in the far-ultraviolet by GALEX [49]. The stellar initial mass function is used to calculate the fraction of stars with masses above $8\,m_\odot$. This continuum limit is compared to results obtained from galaxy catalogs, where the supernova rate is calculated for each cataloged galaxy. The SN rate per galaxy depends on the galaxy's redshift, its morphological type and its optical luminosity. Both results are displayed in Fig. 2.8. Recent measurements imply that the true nearby SN rate is up to a factor of 3 higher compared to the calculations based on star formation rates. This local enhancement might be explained by density fluctuations. However, on larger scales the situation is different, i.e. galaxy density variations average out, and the predicted rate based on star formation is by a factor of two larger than the measured CCSN rate. A large fraction of optically faint SNe (~50%) might be responsible for this discrepancy [47].
The optical follow-up program presented here is mainly sensitive to close-by SNe, because both the neutrino and the optical detection probability is highest for close by SNe. Furthermore, all core-collapses, optically bright, faint or dark, are expected to produce a comparable neutrino flux [47]. Therefore in the following a CCSN rate of 1 per year in a sphere of 10 Mpc radius as obtained for the local universe is assumed. Note that the final result of this work will be presented as a function of the CCSN rate and is hence not directly influenced by the absolute value. However, the absolute CCSN rate does influence the estimation of the expected number of accidentally observed CCSN in coincidence with a neutrino detection, i.e. the number of background supernovae. This uncertainty is included in the systematic error (see Chap. 10).
Compared to the rate of CCSN the rate of gamma-ray bursts presented in the next chapter is small.

2.2 Gamma-Ray Bursts

Besides supernovae, which are the most powerful explosions in the universe releasing a total energy of ~10^{53} erg, gamma-ray bursts presented in this chapter are the brightest objects in the universe a huge amount of electromagnetic radiation within a short period (~10^{51} erg/50 s). Despite their enormous brightness, gamma-ray bursts cannot be observed on Earth, since gamma-rays are absorbed in the atmosphere. This explains why they have not been discovered until the 60's. The first gamma-ray bursts were observed by the Vela satellites. The Vela satellites equipped with gamma and X-ray detectors were launched by the US Air Force in October 1963 with the goal to verify the compliance with the "Treaty Banning Nuclear Weapon Tests in the Atmosphere, Outer Space and Under Water" signed by the United States of America, the United Kingdom of Great Britain and Northern Ireland, and the Union of Soviet Socialist Republics. Occasional occurrence of brief but intense bursts of cosmic gamma-rays was detected by the Vela satellites. The measured flashes of radiation did not have the signature of nuclear weapons and the derived spatial distribution of 39 events detected by the Vela satellites appeared consistent with isotropy. Those were the first observation of Gamma Ray Bursts (GRBs) and first results were published in 1973 [50],

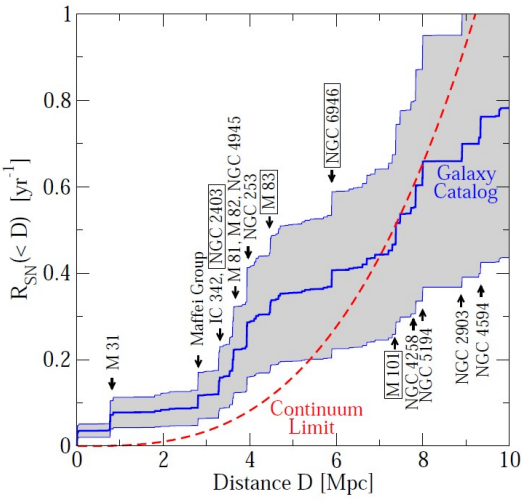

Figure 2.8: Cumulative CCSN rate as a function of distance in the local universe taken from [48]. The blue line is based on SN rates calculated for individual galaxies, while the red line is the continuum limit based on the local star formation rate obtained from GALEX.

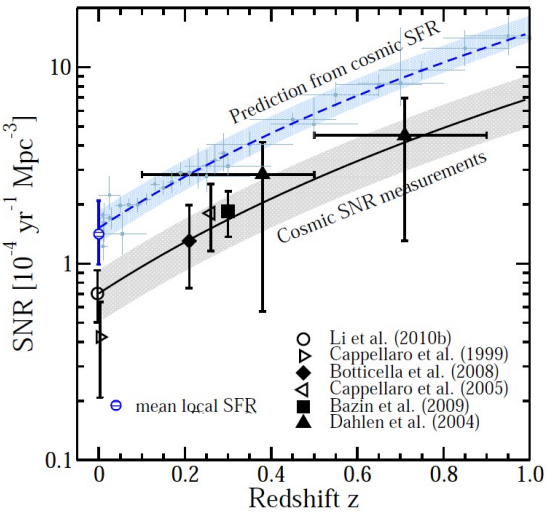

Figure 2.9: Co-moving CCSN rate obtained from star formation rate compared with measurements. The lines indicate fits to the prediction and to the measurements, while uncertainties are displayed as shaded regions (graphic taken from [47]).

starting the modern scientific study of GRBs.
Today gamma-ray bursts are known as electromagnetic signals of short durations in the gamma-ray band (typical energy 0.1-1 MeV) emitted in collimated jets. They are detected roughly once per day from random directions. The average GRB rate integrated over the observable universe is ~7.5 Gpc^{-3} yr^{-1} (for $H_0 \sim 70$ km s^{-1} Mpc^{-1}) [51]. The local GRB rate is small due to the small star formation rate at $z = 0$. It is ~0.025 Myr^{-1} per galaxy (compared to a SN rate of 30 Myr^{-1} per galaxy) or ~0.5 Gpc^{-3} yr^{-1} [52]. Due to their exceptional brightness GRBs are visible to distances encompassing most of the observable universe. During their short duration they are in fact the brightest electromagnetic events in the universe outshining every other source of gamma-rays in the sky. Follow-up X-ray and radio observations by space or ground based telescopes allow an accurate determination of their position, which proves their cosmological distance (up to a redshifts of ~8.1 for the most distant observed GRB 090423 [53]). The angular distribution of GRBs is isotropic as illustrated in Fig. 2.10. The energy released by a single GRB in form of gamma-rays is comparable to the total electromagnetic energy released by a supernovae explosion over many months. A cataclysmic stellar event like the collapse of a massive star (first proposed by Woosely [29]) or the merger of two remnant compact cores (neutron stars or black holes, first proposed by Paczyński [54]) might be responsible for this enormous energy release. Such events are possibly accompanied by non-electromagnetic signals such as cosmic rays [55, 26], neutrinos [56, 57, 58, 59] and gravitational waves [60, 61]. The sources of the highest energy cosmic rays are still unknown. However, gamma-ray bursts could provide the environment and the required energy to explain the production of the highest energy cosmic-rays [26] and hence are a plausible candidate.
Section 2.2.1 describes a selection of observed properties, which lead to the classification of GRBs. Many of those properties are successfully predicted by the Relativistic Fireball Shock Model (Sec. 2.2.3) describing the theoretical scenario of a GRB.

2.2.1 Classification

GRBs are classified in short and long bursts according to the observed bimodal distribution of their duration (see Fig. 2.11) [62]. The burst duration is usually quantified by T_{90}, the time interval over which a burst emits from 5% to 95% of its total number of measured photons. The duration of gamma-ray burst varies over 5 orders of magnitude in the range of 10^{-2}-10^{3} s and shows two populations. Short bursts have a typical duration of 0.2 s and do not last longer than 2 s whereas *long burst* last at least 2 s and have a typical duration of 50 s [63]. Roughly one quarter of the total burst population consists of short bursts while the other three quarters are of long durations.
The two classes of GRBs are believed to have different origins. Most of our current knowledge is based on observations of long bursts while the nature of short bursts to a large extent is still a mystery. The measured light curves are very irregular and individual pulses vary in a wide range. They range from smooth to highly variable curves with many peaks. Some are fast rising with quasi-exponential decay. The curves vary rapidly on time scales less than $\Delta T \sim 10$ ms. Observations show a non-thermal photon spectrum of GRBs. Typically, short bursts have a harder spectrum and a higher peak energy than long bursts, which confirms the assumption that long and short bursts are of different origin [65]. The energy flux peaks at few hundred keV and has a long high energy tail, which in some cases extends up to GeV energies. The prompt spectrum is usually well described by a smoothly joining broken power law, the Band-function, which was constructed empirically [66]:

$$\frac{dN_\gamma(E)}{dE_\gamma} = \begin{cases} A\left(\frac{E_\gamma}{100\,\mathrm{keV}}\right)^{\alpha_\gamma} e^{-\frac{E_\gamma}{E_0}} & \text{for } E_\gamma \leq (\alpha_\gamma - \beta_\gamma)E_0 \\ A\left(\frac{E_\gamma}{100\,\mathrm{keV}}\right)^{\beta_\gamma} e^{\beta_\gamma - \alpha_\gamma} & \text{for } E_\gamma > (\alpha_\gamma - \beta_\gamma)E_0 \end{cases} \tag{2.8}$$

Three independent spectral parameters are involved describing the photon spectrum: the low-energy photon spectral index α_γ, the high-energy photon spectral index β_γ and the break energy $E_\gamma^b = (\alpha_\gamma - \beta_\gamma)E_0$. A is a normalization constant. The Band-function is fitted to the observed photon spectrum. The fitted spectral indices and the break energy, are not universal. For long GRBs the spectral indices usually scatter around average values of $\alpha_\gamma \sim -1$ and $\beta_\gamma \sim -2$, while short bursts usually have harder spectra with $\alpha_\gamma \sim 0$ and $\beta_\gamma \sim -1$. The energy break typically appears at $E_\gamma^b \sim 250$ keV. [24]

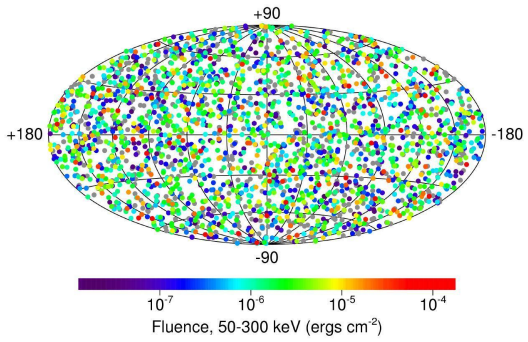

Figure 2.10: The spatial and intensity distribution of all 2704 GRBs from the the burst and transient source experiment (BATSE) catalog shows an isotropic sky coverage. [64]

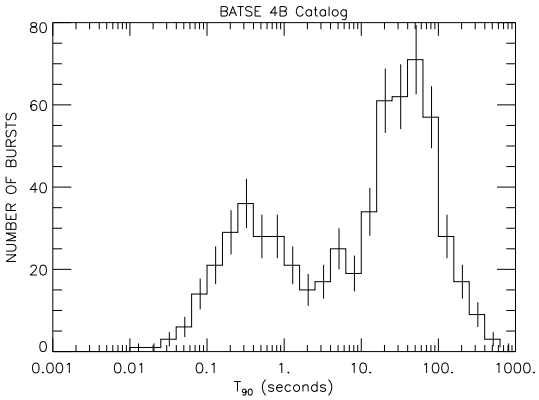

Figure 2.11: Duration distribution of BATSE bursts. The distribution shows a bimodal behavior (from [64]).

The shape of the spectrum can be explained by synchrotron radiation of electrons in internal shock fronts within the jets. The energy break is due to inverse Compton scattering or to synchrotron radiation of electrons at high energies [67]. Theoretical estimations allow the calculation of the neutrino energy spectrum from the observed photon energy spectrum [68] [67] (see Sec. 2.5).

2.2.2 Afterglow Emission

The prompt bursts of GRBs are followed by lower energetic, long-lasting emission in the X-ray, optical, infrared and radio wavelengths: the *afterglow* (see [69] for a review). In some cases the afterglow has been observed several years after the burst. Afterglows are broad band and in each band the light curve generally decays following a power law. The first afterglow was detected in X-rays from GRB970228 by the BeppoSAX satellite in 1997 [70]. The first optical afterglow was discovered two years later by the robotic optical transient search experiment (ROTSE I) from GRB990123 triggered by observations from BATSE [71]. Not all bursts have afterglows detected in all bands. X-ray afterglows are most commonly detected (~95% of all bursts detected by Swift [63]) while optical afterglows are detected in roughly 60% [72]. Example light curves in the optical and X-ray band are shown in Fig. 2.12 and Fig. 2.13. Bursts without observed optical afterglow are referred to as dark bursts. The

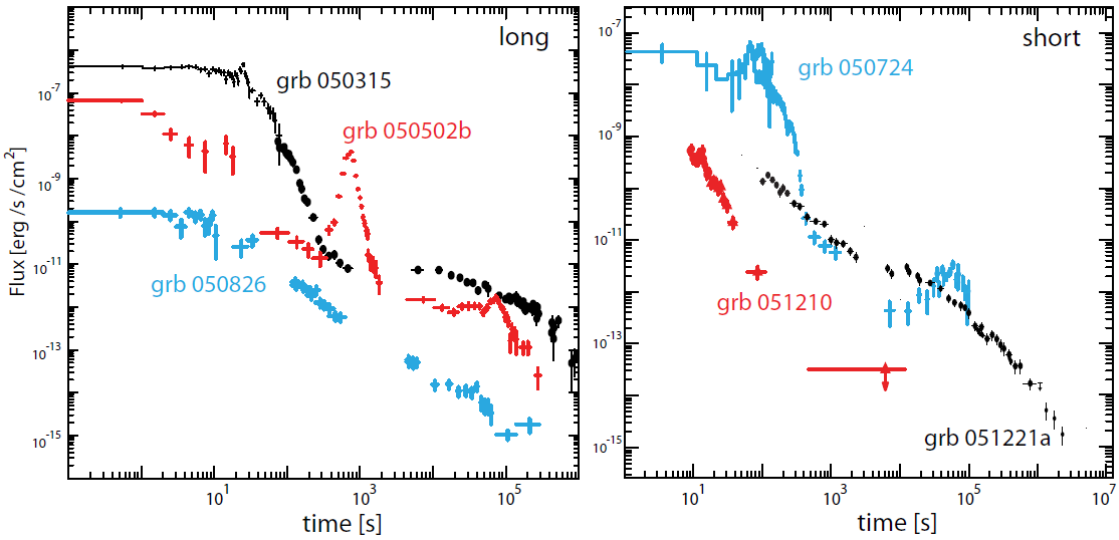

Figure 2.12: X-ray afterglow light curves in the observer frame [63].

lack of an optical afterglow might occur due to dust extinction, high redshift or the intrinsically faint nature of the burst. Accurate position measurements of the afterglow enabled the identification of host galaxies. These are consistent with the association of GRBs with star-forming regions, which gives evidence of GRBs following the star forming rate and indicates that their progenitors might be massive stars, because these have the shortest lifetime. Spectroscopic observation of absorption lines in the spectra of afterglows and emission lines in the spectra of the host galaxy allow the determination of GRB redshifts. The observed redshifts range from 0.0083 [74] to 8.1 [53]. Some GRBs can be associated with supernovae and stellar collapses, because their afterglow light curve shows a supernova signature [75] (see also Sec. 2.3). Breaks in the afterglow light curve indicate that the emission is beamed with beam opening angles of a few degrees (see Sec. 2.2.3) [51] [76]. The afterglow emission was correctly predicted by the relativistic fireball shock model, which made it the most popular model describing the physics of GRBs today.

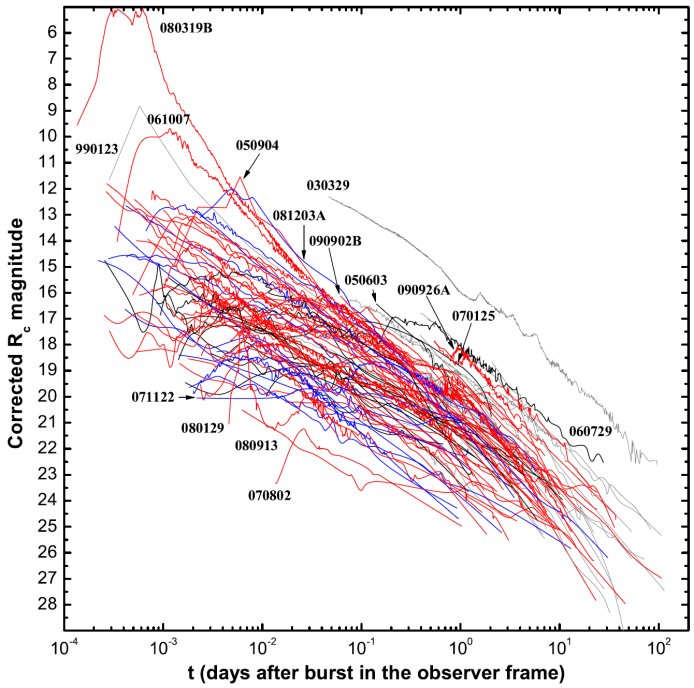

Figure 2.13: Optical afterglow light curves in the observer frame [73].

2.2.3 The Relativistic Fireball Shock Model

The most successful model to explain the various observations of GRBs is the relativistic fireball shock model. According to this model GRB photons are produced by dissipation of kinetic energy of an ultra relativistic wind, a so-called *fireball*. First proposed by Paczyński [54] and further enhanced by Rees and Mészáros [77] the model explains the production process of GRBs, but it does not describe, what kind of inner engine accelerates the relativistic ejecta. The assumption of relativistic movement is necessary to solve the *compactness problem* [78], which arises due to the observed rapid variability of the light curve on the one hand and the observed non-thermal photon spectrum on the other hand. The light curve variations of $\Delta T \lesssim 10\,\text{ms}$ imply a compact object producing the gamma-rays ($R \leq c\Delta T \sim 3000\,\text{km}$). The non-thermal behavior of the photon spectrum requires an optically thin medium where only a few interactions take place. Given the high luminosity $L_\gamma = 10^{51}\,\text{erg}\,\text{s}^{-1}$ implied by cosmological distances results in very high photon densities n_γ. The connection is given by:

$$L_\gamma = 4\pi R^2 c n_\gamma E_\gamma, \tag{2.9}$$

where $E_\gamma \sim 1\,\text{MeV}$ is the characteristic photon energy. The fact that the observed photon energy is above the pair production ($\gamma\gamma \rightarrow e^+e^-$) threshold combined with the very high photon density results in a large optical depth for photons due to electron-positron pair production. The resulting burst would be less luminous and would show a spectrum which differs from the observed non-thermal one. However, introducing relativistic expansion of the source with a Lorentz boost factor $\Gamma \gtrsim 100$ reduces the optical depth and solves the compactness problem [79]. The photon energy in the rest frame is lowered by a factor of Γ and most of the photons will then be below the pair production threshold.
According to the fireball model, the relativistic outflow, the fireball, is accelerated by the inner engine (see Sec. 2.2.3) and dissipates its kinetic energy by collisions of relativistic baryons within the ejecta itself (internal shocks) [80, 81, 56] or with the interstellar medium (external shocks) [82, 83]. This scenario of internal and external shocks is illustrated in Fig. 2.14.

The fireball acceleration is powered by radiation power. Protons couple to electrons in the fireball, which couple to the fireball photons. The shocks generate strong magnetic fields and accelerate electrons and protons by Fermi acceleration. A brief introduction to the acceleration process is given in Sec. 2.4. The inner engine produces an irregular flow of short duration $T \sim 50\,\mathrm{s}$). Spatial fluctuations in the fireball at an early stage are responsible for the creation of a collection of independent sub-shells with slightly different Lorentz factors. Sub-shells might therefore collide with each other. The internal shocks take place at a radius $R \sim 10^{11}$-$10^{12}\,\mathrm{m}$ (comparable to the distance between Sun and Earth of $1\,\mathrm{AU} = 1.5 \times 10^{11}\,\mathrm{m}$) and are responsible for the prompt gamma emission. Electrons and protons are accelerated in the internal shocks, which are expected to be mildly relativistic in the fireball rest frame. Relativistic electrons emit gamma-rays by synchrotron radiation and inverse Compton scattering. The forward inner shocks last as long as the inner engine is active. [84]. The external shocks with the circumburst matter of the ISM take place at a radius $R \sim (10^{12}$-$10^{14})\,\mathrm{m}$. They slow down the ejected particles and are responsible for the long lasting afterglow. At the initial stage of the external shock a short lived reverse shock propagates into the ejecta and produces optical and UV emission. It stops when it runs out of matter as it reaches the inner edge of the flow [82].

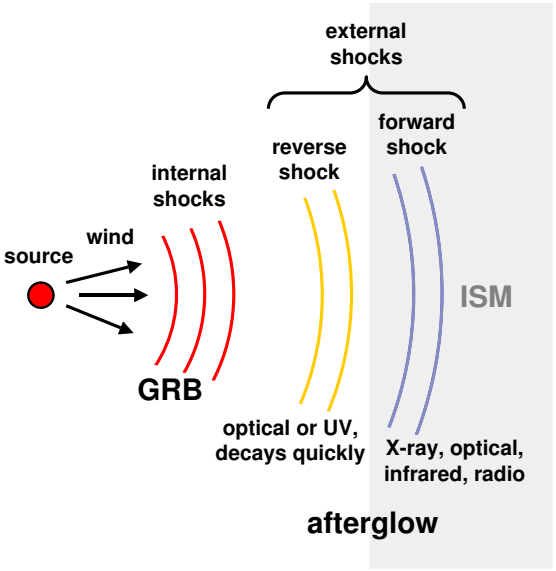

Figure 2.14: The relativistic fireball model: Internal shocks between faster and slower shells are responsible for the GRB itself, the external shocks produce the long duration afterglow emission and a short lived reverse shock creates optical and UV emission (adopted from [85]).

Collimation of Emission

According to the fireball model, the GRB emission is not isotropic but beamed. Calculation of the total energy, assuming an isotropic emission, leads to values up to $10^{54}\,\mathrm{erg}$, which seem unrealistic for any compact source. Significant beaming would reduce the total amount of emitted energy. Due to relativistic effects it is not possible to distinguish a jet from a spherical expanding shell if $\theta > \Gamma^{-1}$, where θ is the jet opening angle. An observer in the direction of the beam only receives information from within the relativistic light cone and does not know, if the emitter is radiating outside the cone or not. As the jet slows down by going through the interstellar medium and Γ decreases, eventually the relativistic beam becomes wider. Radiation and material start to expand sideways when $\theta \sim \Gamma^{-1}$. This effect

results in a break in the light curve as illustrated in Fig. 2.15 and has been observed for many GRB afterglows. Knowing the beam opening angle from the jet break energy, one can infer the total energy released. Comparable values of ~10^{51} erg are found for all bursts. However, the observed energy varies due to variations in the jet opening angle. [86, 87]

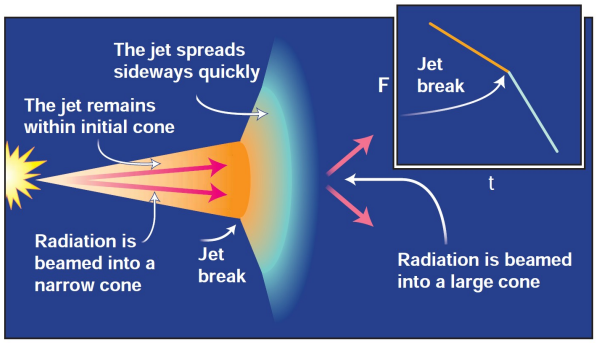

Figure 2.15: A relativistic jet with a Lorentz factor Γ and an opening angle θ is slowed down until its Lorentz factor reaches $\Gamma = \theta^{-1}$. Then it expands sideways, resulting in a jet break in the light curve. A schematic light curve is depicted at the top right (adopted from [87]).

Inner Engine of GRBs

The fireball model requires several conditions for the inner engine:

- It must be able to generate large energies of ~$10^{53}(\Delta\Omega/(4\pi))$ erg, where $\Delta\Omega$ is the solid angle spanned by the jet, and to accelerate $10^{-5} M_{\odot}$ to relativistic velocities.
- It must be able to collimate the emission.
- Fast variations in the light curve (~10 ms) indicate that the inner engine must be a compact object. Average durations of ~50 s exclude an energy release in one single explosion.

Constraints for the inner engine arise from the following observations and reasonings:

- Two classes of bursts might indicate the existence of two different progenitor systems.
- GRBs are rare.
- GRBs are distributed isotropically and seem to follow the star formation rate.
- There is an association with supernovae (see Sec. 2.3).

Many models are ruled out by these requirements. Candidates for the inner engine are collapsars [27, 28, 29] for long bursts and neutron-star neutron-star mergers or neutron-star black-hole mergers [88, 81] for short bursts. Both are capable of releasing a large amount of energy. Beaming of the emission arises naturally in binary merger models, because the flow is emitted preferably along the rotation axis. However, it can also be explained for collapsars, which are massive rotating stars ($M > 25 \cdot M_{\odot}$) forming a black hole after a core collapse. The rest of the star forms a massive accretion disk while falling into the black hole. Rapid accretion of stellar matter into the black hole results in a large energy release and heated gas at the poles expands in a jet-like fireball, which penetrates the shell of the stellar surface [51].
The collapse of a massive star is also believed to be responsible for CCSNe as discussed in Sec. 2.1.2 implying a connection between the two phenomena.

2.3 Connection between SNe and GRBs

Recent observations indicate a connection of long GRBs and core-collapse supernovae. In several cases a GRB or X-ray flash (XRF) has been observed in coincidence with an optical SN light curve implying a common physical origin: a massive stellar explosion (see [75] for a review). Coincidences were observed for SN1998bw and GRB980425 [89], SN2003lw and GRB031203 [90], SN2003dh and GRB030329 [91], SN2006aj and XRF060218 [92], SN2008d and XRF080109 [93] and SN2010bh and GRB100316D [94]. In some cases, spectroscopic observations of bumps observed during the late decline of GRB afterglows have revealed the presence of SN features (e.g. GRB980326 [95] and GRB970228 [96]). Furthermore GRBs and CCSNe were found to release a comparable amount of kinetic energy.
So far, all SNe found to be connected to GRBs were classified as SNe of type Ibc, which represent $\sim 25\%$ of the local CCSN rate [97]. But not all observed Ibc supernovae seem to produce a GRB or XRF. Even after correcting for the fact that GRBs can only be observed if their jet is pointing at the Earth results in a GRB rate of less than 1% of the CCSNe rate [98]. This suggests that GRBs require special conditions such as rapid rotation or high progenitor masses. According to the collapsar model [27, 28, 29], long GRBs have their origin in the collapse of a massive, rapidly rotating star into a black hole surrounded by an accretion disk. Relativistic jets with Lorentz boost factors of 100-1000 form along the stellar axis. The mass of the progenitor and its rotation might be responsible whether a star "dies" in a CCSN or in a GRB. The fact that not all long GRBs have a SN detection associated could be explained by observational biases such as high burst redshifts resulting in faint SNe below the detection threshold of current instruments or bad localization of the bursts not allowing follow-up with powerful but narrow field of view instruments or obscuration of the SN by dust [75].
The GRB-SN connection gives rise to the idea that GRBs and SNe have the jet signature in common. Hence a certain fraction of core-collapse SNe might host soft relativistic jets. The Lorentz boost factor of the jet would be determined by features of the progenitor star, such as its angular rotation. SN jets are suggested to be equally energetic and more baryon-rich, hence they would be only softly relativistic. Such soft relativistic jets could become stalled in the outer layers of the progenitor star, leading to essentially full absorption of the electromagnetic radiation emitted by the jet and at the same time an efficient production of high-energy neutrinos [99, 100]. In this scenario no gamma-rays are emitted, but an optical SNe and a burst of neutrinos produced in the jet could be observed. This motivates a search for neutrino emission, as neutrinos would be the only messenger able to escape from within the star and reveal the existence of the jet. The expected neutrino flux from this model is discussed in Chap. 2.6.
The principle of particle acceleration in astrophysical shocks, which is the basis for proton acceleration and hence also for high-energy neutrino production, is briefly outlined in the next section.

2.4 Fermi Acceleration

The process of particle acceleration in astrophysical shocks is important to explain the phenomena observed in GRBs and SNe. A brief description of the underlying process, first considered by Fermi and hence called Fermi acceleration, is given here based on [101].
One distinguishes between first and second order Fermi acceleration: Acceleration at a shock front is referred to as first order Fermi acceleration, whereas second order Fermi acceleration describes the acceleration by randomly moving, partially ionized gas clouds. Second

order Fermi acceleration was suggested first by Fermi in 1949 [102] while first order Fermi acceleration was proposed in 1978 (see e.g. [103]). Since only shock acceleration is relevant for the work presented here, only first order Fermi acceleration is described in the following. The basic idea is that individual charged particles can gain many times of their initial energy in the transfer of macroscopic energy contained in a moving magnetized plasma. This results in a characteristic non-thermal energy distribution.

2.4.1 First Order Fermi Acceleration

A plane shock front moves with the velocity $-\vec{V}_{\text{shock}}$. Shocked gas flows away from the shock with the velocity $\vec{V}_{\text{rel}}$ relative to the shock front and $|\vec{V}_{\text{rel}}| < |\vec{V}_{\text{shock}}|$. Gas behind the shock moves with $\vec{V}_{\text{down}} = -\vec{V}_{\text{shock}} + \vec{V}_{\text{rel}}$. A sketch can be found in Fig. 2.16.

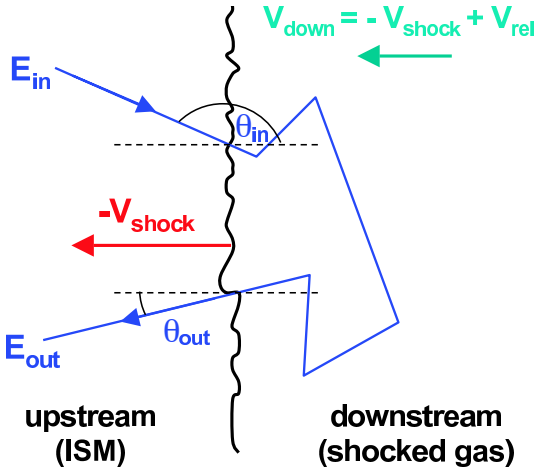

Figure 2.16: First order Fermi acceleration: A relativistic particle from the interstellar medium (ISM) encounters a shock front that moves with velocity $-V_{\text{shock}}$. Shocked gas flows away from the shock with the velocity $\vec{V}_{\text{rel}}$ relative to the shock front and $|\vec{V}_{\text{rel}}| < |\vec{V}_{\text{shock}}|$. Gas behind the shock moves with $\vec{V}_{\text{down}} = -\vec{V}_{\text{shock}} + \vec{V}_{\text{rel}}$. The particle enters the cloud with an energy E_{in} and an angle θ_{in} relative to the shock front and leaves it with an energy E_{out} in the cloud's rest frame and an angle θ_{out} relative to the velocity of the cloud.

A relativistic charged particle encounters the shocked gas, also referred to as *downstream* region, from the unshocked gas region (*upstream* region). The particle carries an energy E_{in} and enters the shocked gas region with an angle θ_{in} relative to the velocity of the shock front as illustrated in Fig. 2.16.
In the rest frame of the moving shock the particle has a total energy

$$E'_{\text{in}} = \gamma E_{\text{in}}(1 - \beta\cos(\theta_{\text{in}})), \tag{2.10}$$

with $\beta = V/c$, where c is the speed of light, and $\gamma = (1-\beta^2)^{-1/2}$. Within the shocked gas region the particle scatters elastically deflected by the magnetic fields, without collisional energy loss. The particle escapes from the shocked gas region with an angle θ'_{out} and an energy $E'_{\text{out}} = E'_{\text{in}}$ in the shock's rest frame. Transformation to the laboratory frame yields

$$E_{\text{out}} = \gamma E'_{\text{out}}(1 + \beta\cos(\theta'_{\text{out}})). \tag{2.11}$$

The relative change in energy is given by

$$\epsilon = \frac{E_{\text{out}} - E_{\text{in}}}{E_{\text{in}}} = \frac{1 - \beta\cos(\theta_{\text{in}}) + \beta\cos(\theta'_{\text{out}}) - \beta^2\cos(\theta_{\text{in}})\cos(\theta'_{\text{out}})}{1-\beta^2} - 1. \tag{2.12}$$

In both, the upstream and downstream gas the particle directions are isotropic. Therefore averaging over all angles yields

$$\langle \cos(\theta'_{\text{out}}) \rangle = -\langle \cos(\theta_{\text{in}}) \rangle = \frac{2}{3}\,, \tag{2.13}$$

where θ'_{out} ranges from -90° to 90° and θ_{in} takes values between 90° and 270°.
Inserting this in equation 2.12 gives an average energy change of

$$\langle \epsilon \rangle = \frac{1 + \frac{4}{3}\beta + \frac{4}{9}\beta^2}{1 - \beta^2}. \tag{2.14}$$

A particle can move several times back and forth across the shock. Assuming an infinite plane shock results in an energy gain for each encounter[1].
Particle acceleration in internal and external shocks, e.g. in GRB jets, can be described by first order Fermi acceleration. The observed photon spectrum of GRBs can be explained by synchrotron radiation of shock accelerated electrons. Assuming that also protons are accelerated in the jets yields excellent conditions for neutrino production as described in the next chapter.

2.5 Neutrino Flux from GRBs

According to the fireball model discussed in Sec. 2.2.3 electrons and protons are shock accelerated in internal shocks within the jets of a GRB. Photons are produced by synchrotron radiation of the accelerated electrons. The protons interact with these photons and – if the center of mass energy of the photon-proton-system exceeds the rest mass of the Δ baryon – pions are produced in the following Δ-resonance process

$$p\gamma \to \Delta^+ \to \begin{cases} n\pi^+ \\ p\pi^0 \end{cases} \tag{2.15}$$

which has a very large cross-section of $\sigma_\Delta \sim 5 \times 10^{-28}\,\text{cm}^2$. Neutral pions are produced with a branching ratio of $2/3$ and immediately decay into two photons, while the charged pions created with a branching rate of $1/3$ subsequently produce neutrinos in the decay:

$$\pi^+ \to \nu_\mu \mu^+ \to \nu_\mu e^+ \nu_e \bar{\nu}_\mu\,. \tag{2.16}$$

Neutrinos can also be produced in pp collisions, but the target proton density in the ultra-relativistic flow of GRBs is too low to allow significant conversion of energy to neutrinos in this process. However this process will be relevant for neutrino production in soft relativistic jets of CCSN as will be discussed in Sec. 2.6.
Since the synchrotron photons are believed to be the target for pion production, from which the neutrinos stem, the neutrino emission is expected to take place in coincidence with the GRB. Yet, due to their finite mass, the neutrinos propagate slower than the GRB photons on their way from the source to the observer. For a typical expected neutrino energy of $10^{14}\,\text{eV}$ and neutrino mass m_ν, this delay however is only $\sim 10^{-11}(m_\nu/10\,\text{eV})^2\,\text{s}$ after traveling $100\,\text{MpC}$ [57]. Therefore, this coincidence is conserved on the way from the source to the observer.
Assuming that the photo-meson production is dominated by the contribution of the Δ-resonance, the neutrino energy spectrum can now be derived from the observed photon

[1] This is because $\cos(\theta'_{\text{out}})$ is always positive, while $\cos(\theta_{\text{in}})$ is always negative.

spectrum. To produce the Δ-resonance the center of mass energy of the photon-proton-system must exceed the rest mass of the Δ baryon of $m_\Delta = 1232\,\mathrm{MeV}$ [7]. Thus, momentum and energy conservation lead to the following equation relating the energy of the proton E'_p with the energy of the photon E'_γ and the scattering angle θ', where prime indicates the co-moving frame, i.e. the system of the jet (opposed to quantities in the observer frame, which are unprimed).

$$2E'_pE'_\gamma = (m_\Delta^2 - m_p^2)c^4 + 2\cos(\theta')E'_\gamma\sqrt{E'^2_p - m_p^2c^4}. \tag{2.17}$$

Inserting the relation $\cos(\theta') \leq 1$ yields a minimum proton energy of

$$E'_p \geq \frac{(m_\Delta^2 - m_p^2)c^4}{4E'_\gamma} + \frac{m_p^2E'_\gamma}{(m_\Delta^2 - m_p^2)}. \tag{2.18}$$

For a typical photon energy of $E'_\gamma \sim 1$ MeV the second summand is small ($1.4\,\mathrm{MeV}$) compared to the first summand ($160\,\mathrm{GeV}$). Thus the second summand can be neglected:

$$E'_p \geq \frac{(m_\Delta^2 - m_p^2)c^4}{4E'_\gamma}. \tag{2.19}$$

The charged pion decay in turn creates four leptons. Assuming equipartition of the initial energy among the decay products, each lepton has on average $\frac{1}{4}$ of the initial pion energy. The pion produced in the Δ-resonance process receives a fraction $\langle x_{p\to\pi}\rangle \simeq 0.2$ of the energy of the initial proton. To change from the co-moving frame to the observer's frame one has to correct for the ejection of the plasma (with the boost factor Γ) as well as for the expansion of the universe according to the Hubble law. Thus, the energy transformation is dependent on Γ and redshift z via $E' = E\frac{1+z}{\Gamma}$. Inserting $m_\Delta = 1232\,\mathrm{MeV}$ and $m_p = 938\,\mathrm{MeV}$ [7] and changing from the co-moving frame to the observer's frame yield the resulting neutrino energy

$$E_\nu = \frac{1}{4}\langle x_{p\to\pi}\rangle E_p \geq 7\times10^3\Gamma^2\frac{\mathrm{MeV}^2}{(1+z)^2E_\gamma}, \tag{2.20}$$

where Γ is the plasma expansion (bulk) Lorentz boost factor and z the burst's redshift. The boost factor is constrained to $100 < \Gamma < 1000$ [67] from two effects: For $\Gamma < 100$ the medium is optically thick to photons and for $\Gamma > 1000$ protons lose most of their energy to synchrotron radiation.

Equation 2.20 establishes the connection between the photon and the neutrino spectrum. The photon spectrum can be described by the Band function (see Sec. 2.2, Eq. 2.8) and has a characteristic break at E^b_γ. Hence the neutrino spectrum shows a break connected to the photon spectrum break at

$$E^b_\nu \simeq 7\times10^3\Gamma^2\frac{\mathrm{MeV}^2}{(1+z)^2E^b_\gamma}. \tag{2.21}$$

Additionally, modulation of the pion spectrum affects the neutrino spectrum. High energy pions may lose some energy by synchrotron radiation before they decay. Therefore, the neutrinos produced in the pion decay have reduced energy, which results in a second break of the neutrino spectrum at $E_\nu = E^s_\nu$. This synchrotron loss effect becomes important when - with increasing boost factor - the pion lifetime becomes comparable to the synchrotron loss time. Thus, accounting for the mean synchrotron lifetime reveals a second break in the neutrino spectrum at higher energy than the first break energy E^b_ν. Above this second break energy

$$E^s_\nu = \frac{10^{28}}{1+z}\sqrt{\frac{\varepsilon_e}{\varepsilon_B L_\gamma/\mathrm{ergs}}}\Gamma^4 t_v/\mathrm{s}\ \mathrm{MeV}, \tag{2.22}$$

the neutrino spectrum steepens by a factor E_ν^2. ε_e and ε_B are the fractions of the burst's internal energy converted to kinetic energy of electrons and to the magnetic field respectively. There is no good way of determining ε_e and ε_B theoretically yet, typically one assumes $\varepsilon = \varepsilon = 0.1$. L_γ is the observed gamma-ray luminosity and t_v the variability of the Lorentz factor within the jet giving rise to the variability of the light curve [68]. Finally, the relation between photon and neutrino energy $E_\nu \propto E_\gamma^{-1}$ (see Eq. 2.20) and the correction for the synchrotron energy loss of the pions yield the neutrino energy spectrum:

$$E_\nu^2 \frac{\mathrm{dN_{E_\nu}}}{\mathrm{dE_\nu}} \approx A_\nu \times \begin{cases} \left(\frac{E_\nu}{E_\nu^b}\right)^{\beta_\gamma+1} & E_\nu < E_\nu^b \\ \left(\frac{E_\nu}{E_\nu^b}\right)^{\alpha_\gamma+1} & E_\nu^b < E_\nu < E_\nu^s \\ \left(\frac{E_\nu}{E_\nu^b}\right)^{\alpha_\gamma+1} \left(\frac{E_\nu}{E_\nu^s}\right)^{-2} & E_\nu > E_\nu^s \end{cases}, \tag{2.23}$$

where the spectral indices α_γ and β_γ are the parameters used to describe the photon energy spectrum (see Eq. 2.8).The spectral indices of the neutrino spectrum can be obtained directly by the Band fit of the photon spectrum. The fit parameters are not universal. The parameters, and therefore the neutrino spectra, can differ significantly for individual bursts. Another essential parameter in the neutrino flux calculation is the redshift. A strong evolution of the GRB rate with redshift is expected if the GRB rate follows the star formation rate [67].
Finally the normalization of the neutrino spectrum is important to estimate the number of expected neutrinos per burst. The muon-neutrino spectrum is normalized to the photon fluence F_γ:

$$A_{\nu_\nu} = \frac{1}{8}\frac{1}{f_e}\frac{F_\gamma}{\ln(10)} f_\pi. \tag{2.24}$$

The factor $1/8$ is due to the fact that only half of the photo-hadronic interactions result in four leptons (see Eq. 2.15). f_e is the fraction of total energy in electrons compared to protons in the jet, f_π the fraction of proton energy transferred to the pions. This normalization is valid for the ν_μ flux at the source. The ν_e and $\bar{\nu}_\mu$ flux is approximately the same. As the distance of the source to the observer greatly exceeds the neutrino oscillation length, the flavor ratio at the source (ν_e:ν_μ:ν_τ)=(1:2:0) changes due to oscillations (see also Sec. 3.2) to (1:1:1) on Earth. The total all flavor neutrino flux at the source is ~3 times the ν_μ flux at the source. Only $\frac{1}{3}$ of this flux will reach the Earth in form of ν_μ or $\bar{\nu}_\mu$ flux. Therefore, the expected ν_μ or $\bar{\nu}_\mu$ flux on Earth is equal to the produced ν_μ-flux at the source. The muon neutrino flux is of special interest for this analysis since the long track of the neutrino induced muon allows the reconstruction of the neutrino direction (see chapter 3).
Figure 2.17 illustrates the expected neutrino flux for an average GRB (with typical values $\Gamma = 300$, $F_\gamma = 5 \times 10^{-5}\,\mathrm{erg/cm^2}$, $t_\nu = 10\,\mathrm{ms}$, $L_\gamma = 10^{52}\,\mathrm{erg/s}$, $E_\gamma^b = 250\,\mathrm{keV}$, $f_e = 0.1$ and $f_\pi = 0.2$). The IceCube detector (see Chap. 4) is most sensitive to neutrino energies around ~100 TeV, which typically is the energy where the first break is expected.

2.6 Neutrino Flux from CCSNs

Motivated by the GRB-SN connection Razzaque, Meszaros and Waxman [99] proposed a model for high-energy neutrino production in soft relativistic CCSN jets. Compared to GRB jets, SN jets are suggested to be equally energetic but more baryon-rich and hence only mildly relativistic. Such soft relativistic jets would become stalled in the outer layers of the progenitor star, leading to essentially full absorption of the electromagnetic radiation emitted by the jet and at the same time an efficient production of high-energy neutrinos. In

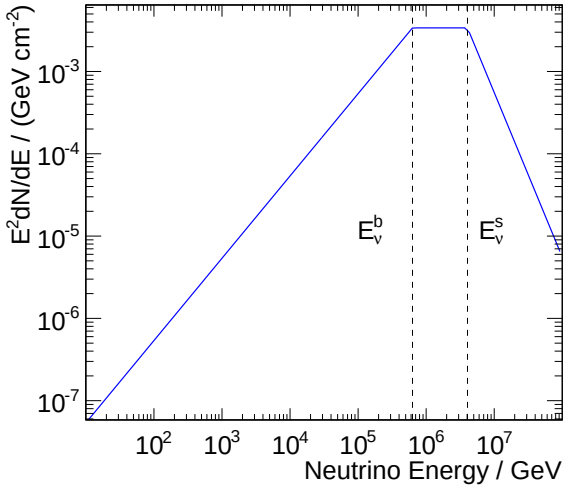

Figure 2.17: Muon-neutrino flux for an average GRB ($\Gamma = 300$, $F_\gamma = 5 \times 10^{-5}\,\mathrm{erg/cm^2}$, $t_\nu = 10\,\mathrm{ms}$, $L_\gamma = 10^{52}\,\mathrm{erg/s}$, $E_\gamma^b = 250\,\mathrm{keV}$, $f_e = 0.1$ and $f_\pi = 0.2$) at redshift z=1. Vertical dashed black lines indicate the two break energies E_ν^b and E_ν^s.

the same way as for GRBs, the protons in the jet are accelerated though Fermi acceleration in internal shocks. However, the baryon density is much larger in the SN jets and hence proton-proton-collisions producing kaons and pions dominate. The kaons and pions decay subsequently. Charged pions produce neutrinos following Eq. 2.16 and kaons decay either to a muon and a neutrino with a branching ratio of 63.4% or to a charged and a neutral pion with a branching ratio of 21.1%:

$$K^+ \rightarrow \begin{cases} \nu_\mu \mu^+ \\ \pi^+ \pi^0. \end{cases} \tag{2.25}$$

The initial formulation of the model only considered neutrino production through pion decay. It was extended by Ando and Beacom [100], who included neutrino production from kaons following Eq. 2.25, which yields a harder and hence more easily detectable neutrino spectrum. Ando and Beacom present the calculation of the neutrino spectrum for a fixed Lorentz factor of $\Gamma_0 = 3$ and a fixed jet energy of $E_{\mathrm{jet},0} = 3 \times 10^{51}\,\mathrm{erg}$. Here, in order to test a broader parameter space, the neutrino flux is calculated as a function of the Lorentz boost factor Γ, the jet energy E_{jet} and the density, ρ, of CCSN producing a jet following the prescription of Ando and Beacom. In the following the neutrino flux is derived for a SN at a distance of $10\,\mathrm{Mpc}$ assuming it hosts a jet pointing toward the Earth. Since high-energy photons are absorbed in the SN jet, a derivation of the neutrino spectrum from the photon spectrum as in the case of GRBs (see Sec. 2.5) is not possible. Instead the neutrino spectrum is derived from the expected proton spectrum. Protons are Fermi accelerated in internal shocks and are expected to follow an E^{-2} energy spectrum.
In the Ando and Beacom model, pions and kaons are produced with on average 20% of the parent proton energy and hence follow the proton spectrum with a relative offset. However, pions and kaons lose energy through synchrotron radiation and inverse Compton scattering (radiative cooling) and through πp and Kp processes (hadronic cooling) causing a steepening of the spectrum at higher energies. Above a certain break energy hadronic cooling becomes dominant and steepens the spectrum by a factor E^{-1} while radiative cooling dominates above a second break energy resulting in a total suppression factor of E^{-2}.

The daughter neutrino carries on average 25% of the pion energy or 50% of the kaon energy and its energy is related to the co-moving meson energy by

$$E_{\nu,\pi(K)} = \Gamma E'_{\pi(K)}/4(2). \tag{2.26}$$

The hadronic cooling break depends strongly on the jet Lorentz factor Γ and the jet energy $E_{\rm jet}$ (i.e. it depends on the number of protons, which is proportional to the jet energy $E_{\rm jet}$, and the energy of the protons, which depends on the Lorentz factor Γ):

$$E^{(1)}_{\nu,\pi(K)} = \left(\frac{E_{\rm jet}}{E_{\rm jet,0}}\right)^{-1} \left(\frac{\Gamma}{\Gamma_0}\right)^{5} 30(200)\,{\rm GeV}. \tag{2.27}$$

The radiative cooling break depends only on Γ (i.e. only on the energy of the protons, not on the number of protons):

$$E^{(2)}_{\nu,\pi(K)} = \frac{\Gamma}{\Gamma_0} 0.1(20)\,{\rm TeV}. \tag{2.28}$$

Finally the proton energy reaches its maximum at the photo-pion production threshold of $E'_{\rm p,max} = 7 \times 10^4\,{\rm GeV}$. Neutrino production from the resulting Δ decay is not considered by Ando and Beacom. They assume a cut-off of the neutrino spectrum at

$$E^{\rm cutoff}_{\nu,\pi(K)} = \frac{\Gamma}{\Gamma_0} 10.5(21)\,{\rm TeV}. \tag{2.29}$$

The normalization of the neutrino flux at 1 GeV scales with the total energy in the jet

$$F_{\nu,\pi(K),0} = \frac{\langle n\rangle\, B_{\pi(K)}}{8} \frac{E_{\rm jet}}{2\pi\theta d^2 \ln(E'_{\rm p,max}/E'_{\rm p,min})} \tag{2.30}$$

$$= \frac{E_{\rm jet}}{E_{\rm jet,0}} \left(\frac{\Gamma}{\Gamma_0}\right)^2 5\times10^{-5}(5\times10^{-2})\,{\rm GeV^{-1}cm^{-2}}, \tag{2.31}$$

$$\tag{2.32}$$

where $\langle n\rangle$ is the meson multiplicity (1 for pions, 0.1 for kaons), B is the branching ratio of the meson decay into a muon (1 for pions, 0.63 for kaons), d is the SN distance and $E'_{\rm p,max}$ and $E'_{\rm p,max}$ are the maximal and minimal proton energies in the source frame. The Γ^2 dependence results from the assumed collimation of the jet with an opening angle of $\theta \propto 1/\Gamma$. Note that the expected number of neutrinos does not simply scale with the jet energy because the first break energy shifts with the jet energy. The resulting neutrino energy spectrum follows a power law with two breaks:

$$E_\nu^2 \frac{{\rm dN_{E_\nu}}}{{\rm dE_\nu}} = \sum_{i=\pi,K} F_{\nu,i} \times \begin{cases} 1 & E_\nu < E^{(1)}_{\nu,i} \\ E^{(1)}_{\nu,i}/E_\nu & E^{(1)}_{\nu,i} < E_\nu < E^{(2)}_{\nu,i} \\ E^{(1)}_{\nu,i} E^{(2)}_{\nu,i}/E_\nu^2 & E_\nu > E^{(2)}_{\nu,i} \end{cases}. \tag{2.33}$$

Figure 2.18 illustrates the behavior of the neutrino spectrum for different jet energies and gamma factors separately for neutrinos from pion and kaon decay. In the energy range which IceCube is sensitive to (TeV to PeV), the spectrum is either hard and follows an E^{-2} spectrum of soft and follows an E^{-3} or E^{-4} spectrum depending on the choice of model parameters. Especially the inclusion of neutrinos from kaon decay makes the spectrum harder.

Although the flux of high-energy neutrinos from SN and GRBs is high, their detection is challenging due to very small cross sections of neutrino interactions with matter and thus requires very large detector volumes. The cross sections and signatures of high-energy neutrino interactions as well as the resulting detection techniques are discussed in Chap. 3.

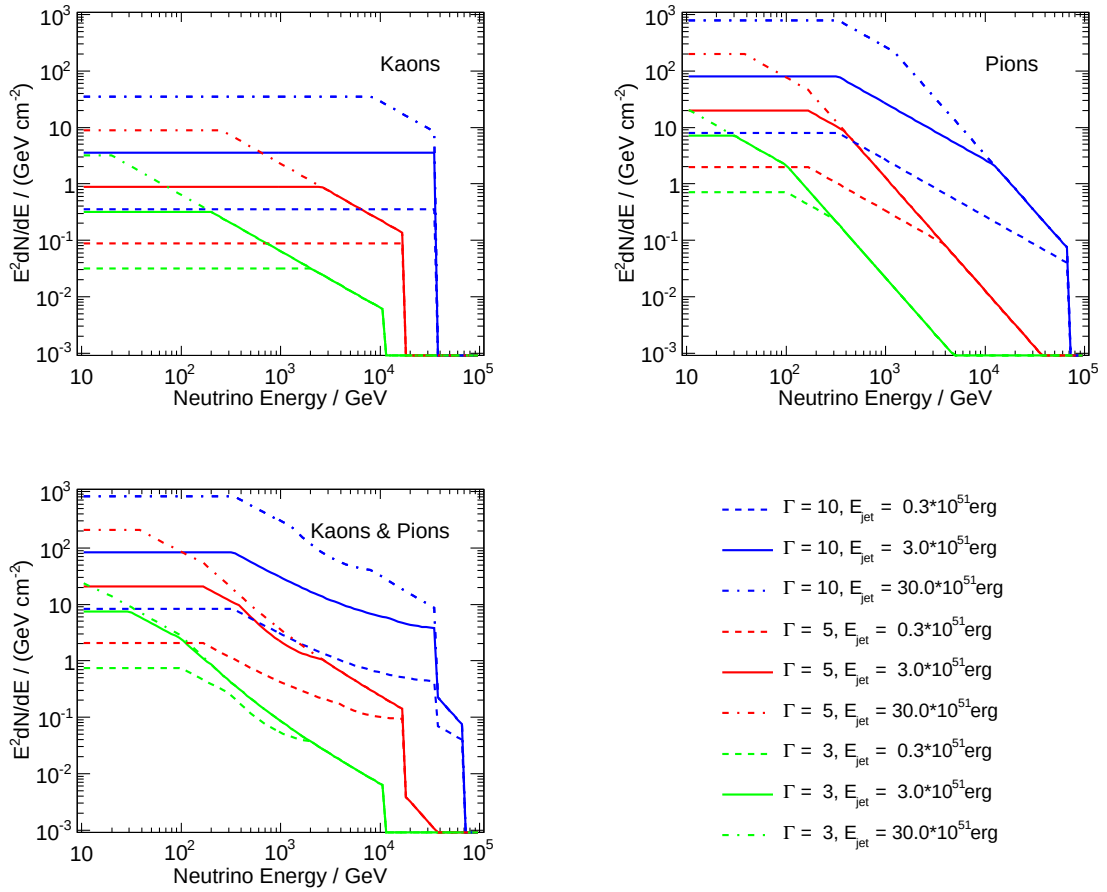

Figure 2.18: SN neutrino spectrum according to Ando and Beacom [100] for one SN at distance 10 Mpc with the jet pointing towards the Earth. Upper left: Kaon contribution. Upper right: Pion contribution. Lower left: Sum of pion and kaon contribution. Different colors indicate different Lorentz boost factors. Solid lines: $E_{\mathrm{jet}} = 3 \times 10^{51}$ erg. Dashed line: $E_{\mathrm{jet}} = 0.3 \times 10^{51}$ erg. Dashed-dotted line: $E_{\mathrm{jet}} = 30 \times 10^{51}$ erg.

Chapter 3

Neutrino Detection

High-energy neutrinos are hypothesized to be produced in violent astrophysical processes such as the death of a massive star (see Chap. 2.5). On one hand they represent perfect astronomical messengers because they reach us undeflected from magnetic fields and basically unaffected by absorption. On the other hand they are difficult to detect due to small cross sections of neutrino interactions with matter.
In order to be detected, neutrinos need to interact with the detector material in charged current (CC) or neutral current interactions (NC). The neutrinos cannot be detected directly but by secondary charged relativistic particles, which emit Cherenkov light (see Sec. 3.4). The Cherenkov photons can be detected by photo-sensors in a transparent medium (such as water or ice). The event signatures can be grouped into showers (also referred to as cascades) and tracks as illustrated in Fig. 3.1. Which of the signatures is observed will depend on the initial neutrino flavor.

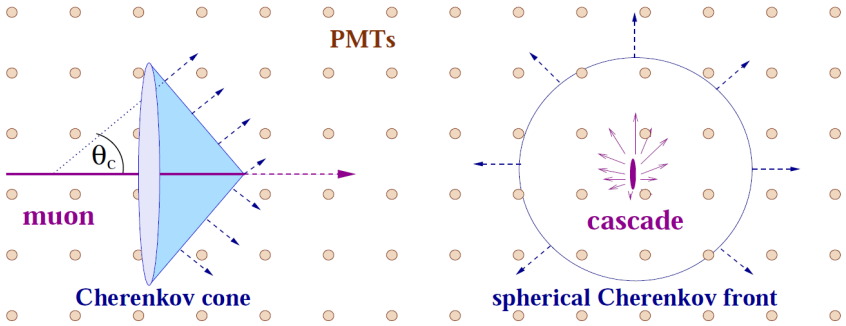

Figure 3.1: The event signatures are grouped as tracks (left) and cascades (right) [104].

Muons produced in CC interactions of muon neutrinos travel along a long track accompanied by a Cherenkov cone through the transparent medium, while electrons produced in CC interactions of an electron neutrino create an electromagnetic shower. The extension of the shower is small compared to the distance between the photo-sensors and thus the Cherenkov signature appears spherical. The tau produced in CC interactions of tau neutrino decays with a lifetime of only 2.9×10^{-13} s for low energies producing a result similar to the electron shower. However, at PeV energies the tau lives long enough to produce a detectable track. In addition, a hadronic shower from the disintegration of the nucleus is generated by all neutrino interactions.
This analysis only considers muon neutrino events, because the track signature allows an accurate reconstruction of the muon track direction. At the energies of interest here, the muon track is co-linear to the direction of the incoming neutrino (see Sec. 3.3). Hence, the

direction of a neutrino source can be obtained enabling the correlation with other, e.g. electromagnetic, observations.
Furthermore, the muon tracks are of special interest since their track length reaches several kilometers. Neutrino interactions outside the instrumented volume can still be detected if parts of the muon track enter the detector, thus leading to an increased effective detector volume. The propagation of these secondary muons through the medium is discussed in Sec. 3.3.
The relevant neutrino cross sections are very small (see Sec. 3.1) and thus cubic kilometer scale detector volumes are required. Such volumes consisting of a transparent medium can be built in water or ice. While water offers a large photon scattering length resulting in a good track resolution, radio-active decay of Potassium-40 creates a large background. In addition, sea currents represent a technical challenge, which can be solved by acoustic tracking of the sensor positions. Furthermore, bioluminescence produces light levels high enough to prohibit muon detection, hence cause additional detector downtime. In ice no radio-active and biologic background is present (except radio-active material, which might be inserted with the photo sensors), but the smaller scattering length does not allow equally good resolution compared to water detectors.
The first attempt to build a large scale neutrino detector was the Deep Underwater Muon and Neutrino Detector (DUMAND) [105] in the deep sea off-shore Hawaii's main island. It failed due to technical problems. A first successful construction took place in lake Baikal [106] followed by other detectors in the Mediterranean Sea [107, 108]. A cubic kilometer size detector, KM3NET [109], in the Mediterranean is planned but has not yet been funded. The first detector in ice was the Antarctic Muon and Neutrino Detector Array (AMANDA) [110] located at the South Pole, which proved the technology of neutrino detection in ice. Its successor is the cubic kilometer scale detector, IceCube, which is further described in Chap. 4.
In the following processes relevant for neutrino detection are discussed.

3.1 Neutrino Cross Section

Neutrinos interact weakly with matter in charged current (exchange of $W^{+/-}$-boson)

$$\nu_l N \xrightarrow{W^-} l^- + X \tag{3.1}$$

$$\bar{\nu_l} N \xrightarrow{W^+} l^+ + X \tag{3.2}$$

or neutral current interactions (exchange of Z^0-boson)

$$\nu_l N \xrightarrow{Z^0} \nu_l + X \tag{3.3}$$

$$\bar{\nu_l} N \xrightarrow{Z^0} \bar{\nu_l} + X, \tag{3.4}$$

where N represents the nucleus, l the leptonic flavor (e, ν or τ) and X is a hadronic cascade caused by the debris of the nucleus. The corresponding Feynman graphs are shown in Fig. 3.2. Since this analysis is only sensitive to charged current interactions of muon neutrinos, only the cross section for this interaction will be discussed further. A detailed presentation can be found in [111] and [112]. The differential cross section is given by

$$\frac{d^2\sigma}{dxdy} = \frac{2G_F^2 M E_\nu}{\pi}\left(\frac{M_W^2}{Q^2 + M_w^2}\right)^2 [xq(x,Q^2) + x\bar{q}(x,Q)(1-y)^2], \tag{3.5}$$

where $x = Q/2M\nu$ and $y = \nu/E_\nu$ are the Bjorken scaling variables, $-Q^2$ the invariant momentum transfer between incident neutrino and outgoing muon, $\nu = E_\nu - E_\mu$ is the

energy loss in the target frame, M and M_W are the nucleon and W-boson masses and finally $G_F = 1.16632 \times 10^{-5}\,\mathrm{GeV}^{-2}$ is the Fermi constant. The quark distribution functions $q(x, Q)$ and $\bar{q}(x, Q^2)$ can be written in terms of the quark distributions for different flavors u, d, c, s, t, b in a proton (subscripts v and s label valence and sea contributions):

$$q(x, Q^2) = \frac{u_v(x, Q) + d_v(x, Q^2)}{2} + \frac{u_s(x, Q) + d_s(x, Q^2)}{2} + s_s(x, Q^2) + b_s(x, Q^2) \tag{3.6}$$

$$\bar{q}(x, Q^2) = \frac{u_v(x, Q) + d_v(x, Q^2)}{2} + \frac{u_s(x, Q) + d_s(x, Q^2)}{2} + c_s(x, Q^2) + t_s(x, Q^2). \tag{3.7}$$

Figure 3.3 and shows the integrated neutrino and antineutrino cross sections σ for neutral current and charged current interactions as a function of energy. For small energies the cross section grows linearly with the energy, while it is damped by the W-boson propagator above $E_\nu = 10^4\,\mathrm{GeV}$. The mean distance that a neutrino travels before it scatters on a nucleon can be described by the water equivalent (we) interaction length L_{int} via

$$L_{\mathrm{int}} = \frac{1}{\sigma_{\nu N}(E_\nu) N_A}, \tag{3.8}$$

where $N_A = 6.022 \times 10^{23}\,\mathrm{mol}^{-1} = 6.022 \times 10^{23}\,\mathrm{cm}^{-3}$ (water equivalent) is Avogadro's constant. Figure 3.4 shows the neutrino and anti-neutrino interaction length as a function of energy for water with $\rho = 1\,\mathrm{g/cm}^3$ and $A = 18\,\mathrm{g/mol}$. At energies above $40\,\mathrm{TeV}$ the interaction length becomes smaller than the diameter of the Earth and the Earth becomes opaque for neutrinos. Thus, searches for ultra high-energy neutrinos can only be performed close to or above the horizon. However, this work focuses on the search for supernova neutrinos, which have on average much smaller energies.

3.2 Neutrino Oscillation

Due to oscillations, neutrinos produced at an astrophysical source change their flavor on their way to the Earth. The weak eigenstates ν_α ($\alpha = (e, \mu, \tau)$) are not identical to the mass eigenstates ν_i ($i = (1, 2, 3)$). They are connected by the unitary Maki-Nakagava-Sakata-matrix (MNS-matrix) U:

$$|\nu_\alpha\rangle = \sum_{i=1}^{3} U^*_{\alpha i} |\nu_i\rangle \,. \tag{3.9}$$

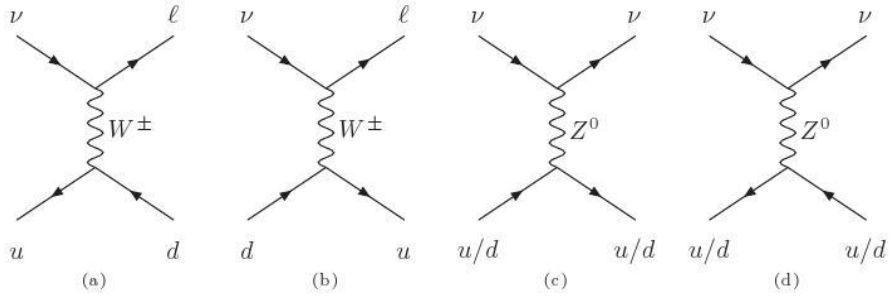

Figure 3.2: Feynman graphs: a) and b) charged current interactions, c) and d) neutral current interactions.

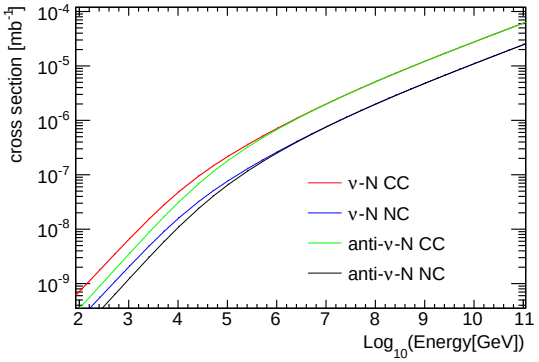

Figure 3.3: Muon-neutrino and anti-muon-neutrino charged current (CC) and neutral current (NC) cross sections as implemented in the neutrino generator ANIS [113] (based on CTEQ5 parton distributions [114]).

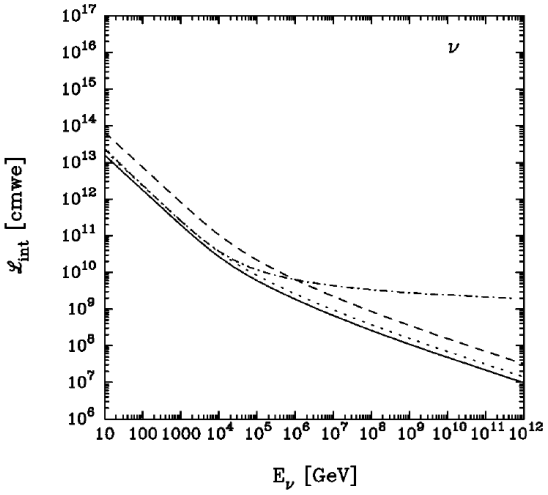

Figure 3.4: Muon-neutrino and anti-muon-neutrino charged current (CC) and neutral current (NC) water equivalent interaction length. The dashed line indicates the diameter of the Earth.

Assuming three neutrino flavors, U is given by

$$U = \begin{pmatrix} c_{12}c_{13} & s_{12}c_{13} & e^{-i\delta} \\ -s_{12}c_{23} - c_{12}s_{23}s_{13}e^{i\delta} & c_{12}c_{23} - s_{12}s_{23}s_{13}e^{i\delta} & s_{23}c_{13} \\ s_{12}s_{23} - c_{12}s_{23}s_{13}e^{i\delta} & -c_{12}s_{23} - s_{12}c_{23}s_{13}e^{i\delta} & c_{23}c_{13} \end{pmatrix} \times \begin{pmatrix} e^{i\alpha_1/2} & 0 & 0 \\ 0 & e^{i\alpha_2/2} & 0 \\ 0 & 0 & 1 \end{pmatrix}, \tag{3.10}$$

with $s_{ij} = \sin(\theta_{ij})$ and $c_{ij} = \cos(\theta_{ij})$ $(i, j = 1, 2, 3)$. θ_{ij} are the mixing angles and δ, α_1 and α_2 are CP-violating phases. The Majorana phases, α_1 and α_2, only have physical influences if neutrinos are identical to their antiparticles (Majorana particles), they do not affect neutrino oscillation. [115]
Experimental values for the mixing parameters are [7]

$$\begin{aligned} \sin^2(2\theta_{12}) &= 0.87 \pm 0.03 \\ \sin^2(2\theta_{23}) &> 0.92 \\ \sin^2(2\theta_{13}) &< 0.15 \\ \Delta m^2_{21} &= (7.59^{+0.19}_{-0.21}) \cdot 10^{-5}\,\mathrm{eV}^2 \\ \Delta m^2_{32} &= (2.43 \pm 0.13) \cdot 10^{-3}\,\mathrm{eV}^2 \\ \Delta m^2_{31} &\sim m^2_{32} \end{aligned}$$

Assuming that the oscillation length is very small compared to the distance between source and detector the probability of an oscillation from flavor α to flavor β after a distance L for a neutrino with energy E is:

$$P(\nu_\alpha \to \nu_\beta; L) = |\langle \nu_\beta | \nu_\alpha(x) \rangle|^2 = \delta_{\alpha\beta} - \sum_{i \neq j} U^*_{\alpha i} U_{i\beta} U^*_{\beta j} U_{j\alpha} \left(1 - \exp\left(\frac{-i\Delta m^2_{ij} L}{2E}\right)\right), \tag{3.11}$$

dependent on the neutrino mass difference Δm^2_{ij} between two mass eigenstates. Averaging over rapid oscillations yields in the limit $L \to \infty$

$$\langle P_{\alpha,\beta} \rangle = \langle P(\nu_\alpha \to \nu_\beta; L = \infty) \rangle = \delta_{\alpha\beta} - \sum_{i \neq j} U^*_{\alpha i} U_{i\beta} U^*_{\beta j} U_{j\alpha} = \sum_j |U_{\alpha j}|^2 |U_{\beta j}|^2. \tag{3.12}$$

A cosmic mixed flavor neutrino flux on Earth $(\Phi_{Earth}(\nu_e), \Phi_{Earth}(\nu_\mu), \Phi_{Earth}(\nu_\tau))$ can be calculated from the expected neutrino flux at the source $(\Phi_{source}(\nu_e), \Phi_{source}(\nu_\mu), \Phi_{source}(\nu_\tau))$ [116]:

$$\begin{pmatrix} \Phi_{Earth}(\nu_e) \\ \Phi_{Earth}(\nu_\mu) \\ \Phi_{Earth}(\nu_\tau) \end{pmatrix} = \begin{pmatrix} \langle P_{ee} \rangle & \langle P_{\mu e} \rangle & \langle P_{\tau e} \rangle \\ \langle P_{e\mu} \rangle & \langle P_{\mu\mu} \rangle & \langle P_{\tau\mu} \rangle \\ \langle P_{e\tau} \rangle & \langle P_{\mu\tau} \rangle & \langle P_{\tau\tau} \rangle \end{pmatrix} \begin{pmatrix} \Phi_{source}(\nu_e) \\ \Phi_{source}(\nu_\mu) \\ \Phi_{source}(\nu_\tau) \end{pmatrix} \tag{3.13}$$

The flavor ratio at a distant source (ν_e:ν_μ:ν_τ)=(1:2:0) changes due to neutrino oscillations[1] to (1:1:1) at Earth.
In matter the effect of forward scattering of electron neutrinos as a result of their charged-current interactions with electrons modifies the effect of neutrino oscillation [117]. This effect is called Mikheyev-Smirnov-Wolfenstein (MSW) effect, it can become important in media with very high electron densities, e.g. in the sun.

3.3 Muon Propagation

This analysis focuses on the muon-neutrino channel, because only this channel allows an accurate reconstruction of the neutrino direction. If a high-energy muon-neutrino interacts in a charged current interaction, a high-energy muon is created. The muon travels nearly co-linear to the direction of the incident neutrino with a mean angular difference, $\Delta\Psi_{\mu,\nu_\mu}$, between muon and neutrino direction, which can be approximated as a function of the neutrino energy E_ν by [118]:

$$\Delta\Psi_{\mu,\nu_\mu} = 0.7^\circ / (E_\nu / \text{TeV})^{0.7}. \tag{3.14}$$

The muon energy loss can be well approximated by

$$-\frac{dE_\mu}{dx} \simeq A + B \cdot E_\mu, \tag{3.15}$$

with $A = 2 \times 10^3\,\text{GeV}\,\text{cm}^2\,\text{g}^{-1}$ and $B = 4 \times 10^6\,\text{cm}^2\,\text{g}^{-1}$ [7]. The first term accounts for ionization losses while the second term describes radiation losses. The muon range R_μ, i.e. the distance after the muon energy drops below a threshold E^{th}_μ is given by

$$R_\mu = \frac{1}{B} \log\left(\frac{A + \beta \cdot E_\mu}{A + B \cdot E^{\text{th}}_\mu} \right). \tag{3.16}$$

Depending on the energy of the incoming neutrino the muon travels ~1 km (TeV neutrino energies) to ~10 km (PeV neutrino energies) through the ice. For low energy muons most of the energy is lost in ionization losses while for higher energies catastrophic energy loss via bremsstrahlung, pair production and nuclear interactions dominate. Figure 3.5 shows the different contributions to the muon energy loss in water ($\beta = v/c$ and $\gamma = 1/\sqrt{1-\beta^2}$). A similar behavior is expected in ice. The long muon track, which points into the direction of the neutrino, allows the reconstruction of the neutrino direction. Induced by a high-energy neutrino the muon will travel with relativistic speed and thus emits Cherenkov radiation.

[1] assuming distance to Earth $\gg$ oscillation length and maximal mixing angle

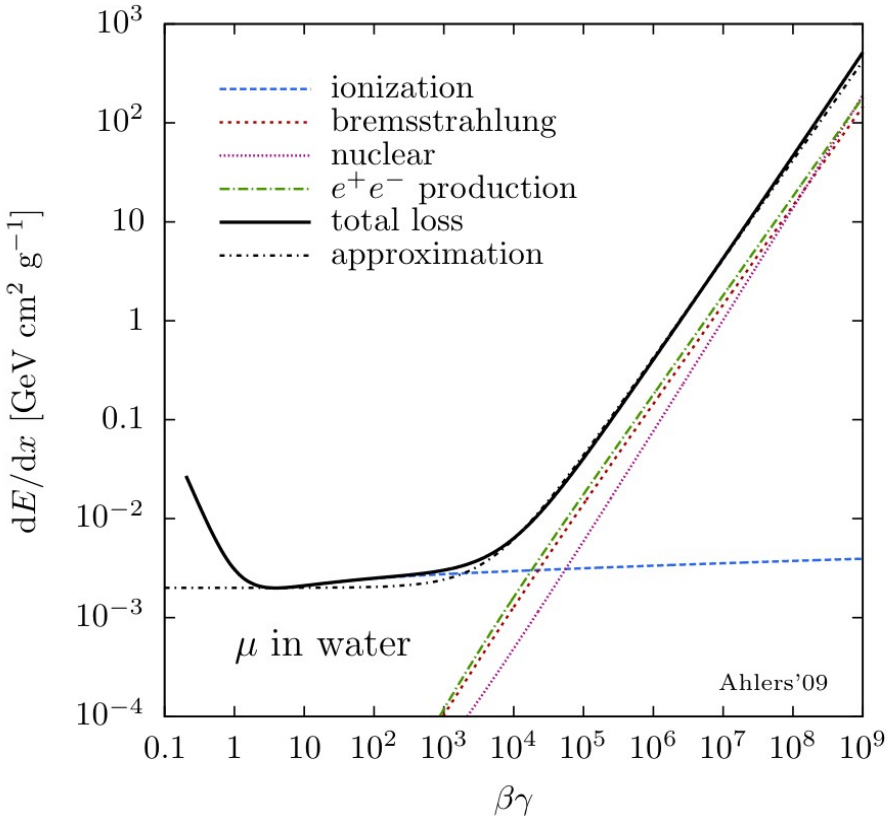

Figure 3.5: Muon energy loss in water using parametrization from [119]. Muons become minimal ionizing at about $\beta\gamma = 3$ corresponding to an energy of 350 MeV.

3.4 Cherenkov Effect

Cherenkov light is emitted when a charged particle travels through a dielectric medium with a velocity faster than the speed of light in this medium [120]. The molecules in the medium get polarized by the traversing charged particle. They rapidly fall back into their ground state emitting radiation. When the particle moves faster than the speed of light the emitted photons interfere constructively and the moving charged particle drags along a cone of Cherenkov light. The opening angle θ_c of the cone depends on the velocity v of the particle and the refractive index of the medium n:

$$\cos(\theta_c) = \frac{1}{n \cdot \beta}, \tag{3.17}$$

with $\beta = v/c$. For a high-energy particle with $\beta \approx 1$ and a refractive index of ice of $n_{\text{ice}} = 1.33$ the Cherenkov angle is $\theta_c = 41°$. The number of emitted photons per path length dx and wavelength band $d\lambda$ is given by the Frank-Tamm formula [121]

$$\frac{d^2N}{dxd\lambda} = \frac{2\pi\alpha Z^2}{\lambda^2}\left(1 - \frac{1}{\beta^2 n^2}\right), \tag{3.18}$$

where α is the electrical fine structure constant and Z the charge of the relativistic particle. Assuming a constant refractive index and the sensitive wavelength range of the IceCube photomultipliers (300-600 nm), yields a total of ~3×10^4 photons per meter for a highly relativistic muon ($\beta \approx 1$). IceCube, described in the next chapter consists of a grid of photosensors, which measure the arrival time of the Cherekov photons with high precision. Different arrival times recorded at different sensors allow the reconstruction of the muon track.

Chapter 4

IceCube

The neutrino observatory IceCube is located in the deep ice at the geographic South Pole. Constructions started in 2004/05 and finished during the austral summer of 2010/11. Section 4.1 gives a brief overview of the layout and the construction of the detector, followed by a description of the data acquisition system. The clear deep ice of the almost 3 km thick glacier is used as detector medium to observe Cherenkov light produced by charged particles traveling through the ice with relativistic speed. The blue and near-UV Cherenkov photons are recorded by photo multiplier tubes (PMTs) embedded in the ice. A good understanding of the properties of the ice, described in Sec. 4.2, is crucial for accurate track reconstruction (see Sec. 4.7) and an adequate description of the detector in the detector simulation as presented in 4.8.

4.1 IceCube Layout and Construction

Due to rough weather conditions (temperatures of $-30°$C to $-45°$C in summer and $-60°$C in winter) constructing a detector at the South Pole is difficult and construction is only possible from October to February. Furthermore, it is a remote place with limited logistics. However, the Amundsen-Scott South Pole Station and daily flights during the summer month from New Zealand (via McMurdo at the coast of Antarctica) provide sufficient infrastructure.
The completed detector consists of 5600 digital optical modules (DOMs), each housing a PMT in a 13 mm thick glass sphere. 86 cables, so-called *strings*, which each carry 60 DOMs, are deployed in the polar ice sheet. A string has a length of 2450 m. Figure 4.1 shows a schematic representation of the IceCube neutrino observatory. In order to deploy the strings in the ice boreholes of ~60 cm diameter have been drilled with a hot water drill. 5 MW of hot water ($88°$C) are pumped into the hole under 6.89 MPa pressure with a rate of 12 l/s. The drilling of one hole takes ~27 h and the deployment of the string another ~10 h [122]. After deployment of the string the water in the hole refreezes producing optical contact between the ice and the PMTs. 78 strings are arranged in a hexagonal shape with an inter-string spacing of 125 m. Only the last kilometer (1450 m - 2450 m) of each string is equipped with DOMs with a spacing of 17 m, because in this region the ice is especially clear and in addition the covering layers of ice operate as absorber for down-going muons produced in the atmosphere. Each string contains 30 twisted pair cables with each pair connected to two DOMs in parallel. Neighboring DOMs on the same string are directly connected with a cable, which is used for the trigger (see Sec. 4.4). Finally, all strings are connected to a counting house, the IceCube Laboratory (ICL), in the center of the array.
In addition to the 78 equally spaced strings, a densely instrumented core, called *DeepCore*, consisting of eight special strings with more closely spaced high-efficiency modules concen-

trated in the clearest ice towards the bottom was build in 2008-2011 [123]. DeepCore lowers the energy threshold of IceCube from ~100 GeV to energies as low as 10 GeV.
On the surface the observatory is completed by an air-shower detector IceTop to study cosmic rays and their composition [124].
This work is based on IceCube data during the construction phase of the detector. Each year additional string are deployed and added to the data acquisition at the end of the deployment season. Corresponding to the number of active strings of the period the detector configuration used here will be referred to as $IC40$ and $IC59$ (see Fig. 4.2).

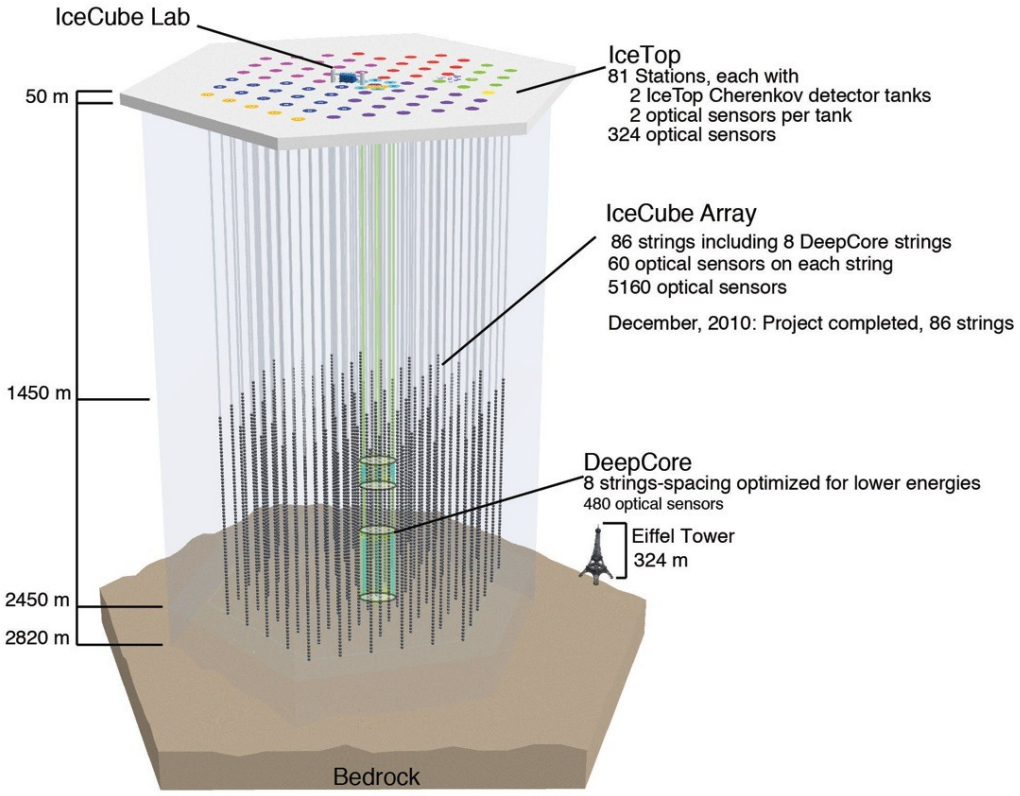

Figure 4.1: The IceCube neutrino observatory: The full detector consists of 86 strings with 60 DOMs attached to each string. Eight strings compose the low energy extension, DeepCore. The IceTop air shower detector is located on the surface.

4.2 Properties of the Antarctic Ice

The detection medium of IceCube is the glacial ice at the South Pole. A good understanding of the ice is crucial in order to correctly interpret the measurements and for an accurate modeling of the ice in the detector simulation. Absorption and scattering in the ice will influence the propagation of photons and thus the event reconstruction. Photons scatter on impurities in the ice, such as submillimeter-sized air bubbles and micrometer-sized dust grains. The geometric scattering length is small at IceCube depth (~1 m), but most of the scattering happens in forward direction with an average scattering angle of $\langle \cos(\theta) \rangle = 0.94$. Most of the photons scatter multiple times. It is useful to define an effective scattering length

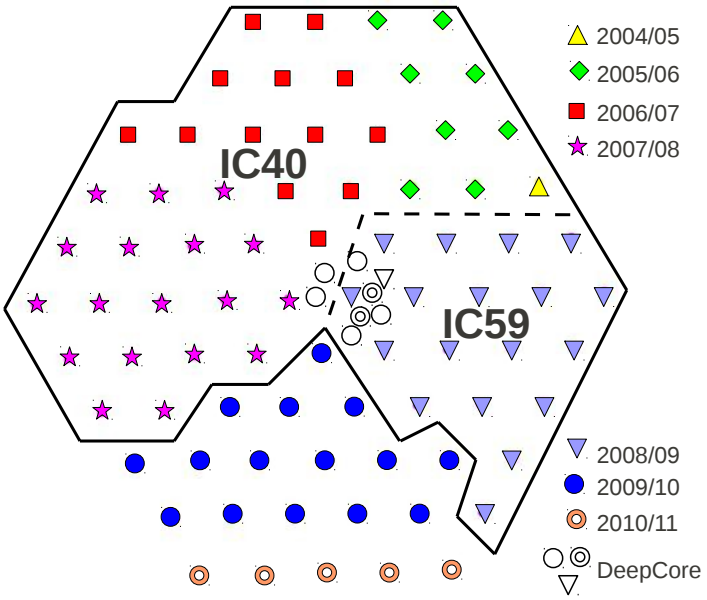

Figure 4.2: Top view of the IceCube detector: The full detector consists of 86 strings, 78 are arranged in a hexagonal shape, while 8 special strings make up the dense infill array DeepCore. Different colors indicate different deployment stages. Yellow: Season 2004/05, first string. Green: Season 2005/06, 9 strings. Red: Season 2006/07, 22 strings. Magenta: Season 2007/08, 40 strings. Purple: Season 2008/09, 59 strings, including first DeepCore string. Blue: Season 2009/10, 79 strings, including 6 DeepCore strings. Orange: 86 strings, including 8 DeepCore strings. The solid black line encircles the IC59 configuration, while the dashed line indicates IC40 string configuration, which is a subset of IC59.

$$\lambda_e = \lambda_s \sum_{i=0}^{n} \langle \cos(\theta) \rangle^i \xrightarrow{n\to\infty} \frac{\lambda_s}{1 - \langle \cos(\theta) \rangle}. \tag{4.1}$$

which describes the distance after which randomization occurs, e.g. the scattering becomes isotropic. It can also be interpreted as the distance that the center of gravity of the photon cloud advances in the limit of many scatters. The effective scattering coefficient is defined as $1/\lambda_e$. Although the geometric scattering length is small at IceCube depth, the effective scattering length is $\lambda_e \sim 25\,\mathrm{m}$.
The absorptivity a of a medium can be described by the reciprocal of the attenuation length λ_a, which is the distance at which the survival probability drops to $1/e$.

$$a = \frac{1}{\lambda_a}. \tag{4.2}$$

The average absorption length at IceCube relevant depth is $\lambda_a \sim 100\,\mathrm{m}$.
The optical properties of the ice have been measured carefully using two different methods: Artificial light sources (lasers and LEDs) [125] and the *dust logger* [126] described below. In IceCube and its predecessor AMANDA LEDs and lasers were used to emit light at several wavelengths. The photon delay times were measured by optical modules at different distances from the light source. A Monte Carlo, which models the propagation of photons through the ice, was compared to the data and the optical parameters were adjusted to bring the simulated photon arrival time distributions in agreement with the measurements. Figure 4.3 shows the absorptivity and the effective scattering coefficient obtained by measurements with artificial light sources. Both are strongly depth and wavelength dependent.

Strong vertical variations seen in both distributions are due to horizontal layers of dust impurities probably caused by massive historic volcano eruptions. Residual air bubbles cause strong scattering above 1300 m. At larger depth the air bubbles convert to non-scattering air hydrates.
The dust logger consists of a light source and a phototube. It is lowered down the IceCube boreholes before the IceCube string deployment. It emits light into the ice surrounding the borehole and measures the back-scattered photons. The fraction of back-scattered light is related to the amount of dust in the ice. The dust logger provides high resolution depth dependent results as displayed in panel c of Fig. 4.4. Similar features are found in ice cores from different places in Antarctica (panel a and d in Fig. 4.4) and AMANDA scattering measurements with artificial light sources (panel b).

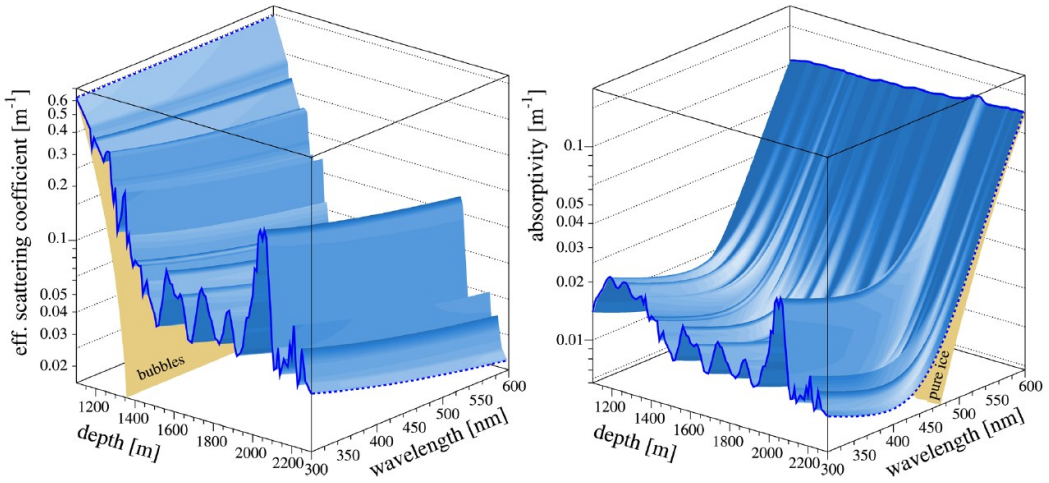

Figure 4.3: Scattering (left) and absorption (right) for deep South Pole ice as a function of depth and wavelength (from [125]).

4.3 Data Acquisition (DAQ)

The IceCube DAQ is designed to obtain high reliability with minimal on-site personnel interaction needed during operation. Only a brief summary is presented here, while a detailed description of IceCube's DAQ can be found in [127]. Its main task is to capture and timestamp the optical signal provided by the PMT with nanosecond timing accuracy. The optical signal is digitalized inside the DOM and is sent to the DAQ on the surface on request. The DAQ on the surface is located in the IceCube laboratory and consists of several components:

- The *DOMHub*, one computer for every string, that communicates with all 60 DOMs of one string. It controls the DOMs (e.g. calibration tasks) and collects data from the DOMs.

- The *Master Clock*, which distributes time calibration signals from a GPS receiver to the DOMHubs.

- The *StringHub*, a software element which synchronizes and sorts signals from all DOMs on one entire String according to the Coordinate Universal Time (UTC).

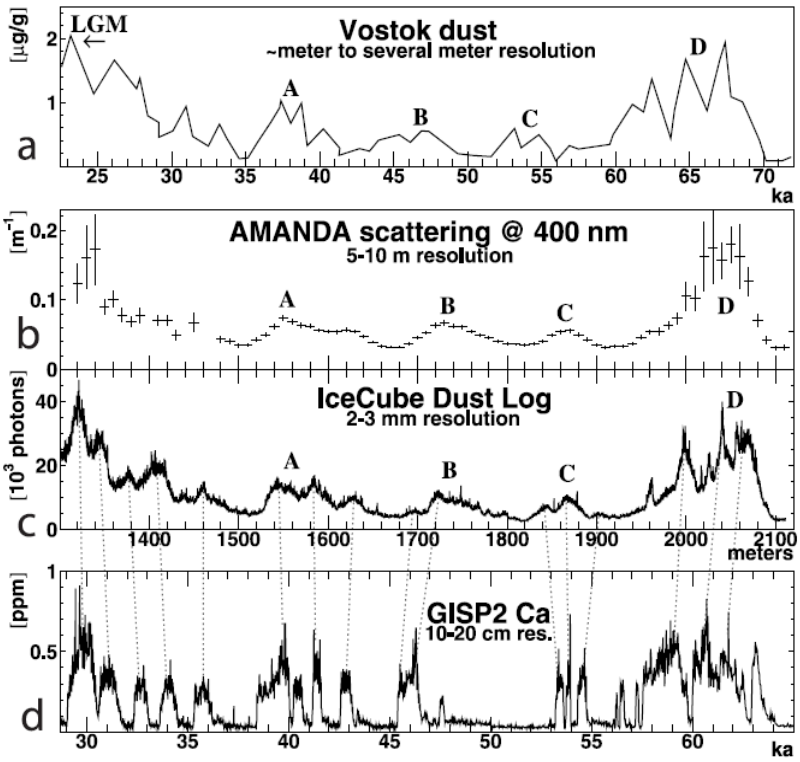

Figure 4.4: Dust measurements at (a) Vostok ice core; (b) AMANDA (flashers); (c) IceCube (dust logger); (d) Greenland Ice Sheet Project (GISP2) ice core (from [126]).

4.3.1 The Digital Optical Module (DOM)

The DOMs are designed to be extremely reliable, since they are inaccessible after deployment. Only 2% of the DOMs break during deployment and refreezing, 1% lose the connection to the neighboring DOM, but are still usable. A schematic view of the DOM is shown in Fig. 4.5. A 13 mm thick glass sphere hosts a 25 cm diameter PMT (Hamamatsu R7081-02), a 2 kV high voltage power supply, the DOM mainboard, a signal delay board and the flasher mainboard. The thick glass protects the electronics from the high pressure of 70 MPa. The glass was selected in order to minimize the contamination with Potassium-40, which produces dark noise in the PMT through radio-active decay. Electrons from β-decay produce photons by scintillation and Cherenkov radiation. The measured noise rate is 200-300 Hz at $-40°$C. A flexible gel is filled between PMT and the glass sphere to provide optical coupling. The PMT is sensitive to 300-650 nm and has a maximum quantum efficiency of ~25%. A mu-metal shield surrounds the PMT, reducing the Earth's magnetic field by a factor of two. The magnetic field modifies the electron trajectories in the PMT, especially for the slow photo electrons between the photocathode and the first dynode and degrades the uniformity of the response. The flasher-board contains 12 LEDs (with a peak wavelength of 400-420 nm) pointing radially outward from the DOM. 6 are oriented horizontally while the other 6 point upwards at an angle of 48°. The delay board introduces a delay of 75 ns to accommodate the delay in the trigger logic.

Each DOM receives power, control and calibration signals from the surface and returns digital data to the counting house. Core component of the DOM mainboard are two waveform digitization systems, the Analog Transient Waveform Digitizer (ATWD) and the fast Analog Digital Converter (FADC). The PMT signal is distributed to three separate amplifiers (with

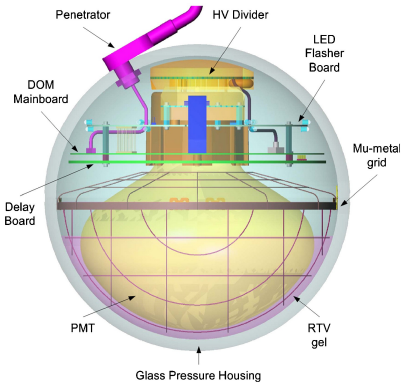

Figure 4.5: Digital optical module (DOM): Thick glass sphere hosts a photomultiplier tube and a mainboard for digitization of the data in the ice (from [127]).

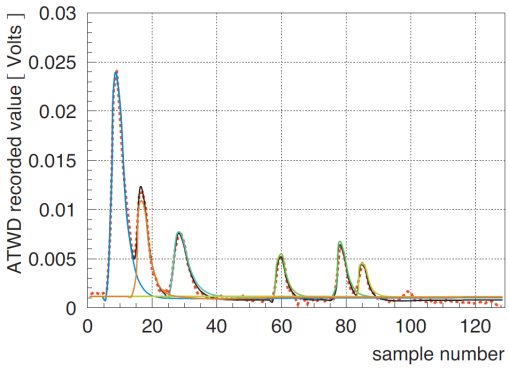

Figure 4.6: ATWD digitizer output from a typical event: 128 samples with 3.3 ns each. Each peak represents one photoelectron (from [122]).

amplification factors of $\times 16$, $\times 2$ and $\times 0.25$) before it is fed to the three input channels of the ATWD. The different amplification levels ensure on one hand a good resolution for weak signals and on the other hand avoid saturation for strong signals. The signal is stored in an analog array of 128 sampling capacitors. The charge stored on each capacitor corresponds to one time bin. The sampling rate is set to 3.3 ns per sample, thus providing a total memory of $0.42\,\mu$s. If the ATWD receives a trigger from the PMT discriminator, it is synchronized to a clock edge and the stored signal is digitized by 128 analog digital converters (ADC). The digitized data is buffered on the DOM mainboard until it receives a request to transfer the data to the surface. Two ATWDs are operated in parallel to minimize the dead time. While one is in the process of waveform digitization, which takes $29\,\mu$s, the other is available to capture a new signal. Because some physics signals last longer than $0.42\,\mu$s, the FADC provides a total memory of $6.4\,\mu$s with 256 samples and a coarser temporal resolution of 25 ns per sample. Figure 4.6 shows a typical waveform measured by the ATWD. Multiple photoelectrons were measured, each represented by a peak in the waveform. In the event processing (applied on a computer cluster in the ICL) the features of the waveform are extracted to obtain a list of photon arrival times, which is needed for the event reconstruction.

4.4 Trigger Condition

A hit is registered when a single DOM and its neighbor or next-to-neighbor DOM on the same string exceed their charge threshold of 0.25 PE within a time window of $\pm 1\,\mu$s (*hard local coincident (HLC) mode*). To suppress the background caused by PMT noise or radioactive decay, eight coincident hits are required within a time window of $5\,\mu$s to form a trigger. If this condition is fulfilled, the information of all hits within a time window of $\pm 10\,\mu$s is read out and merged to an event. The waveform of each DOM participating in the event is digitized and sent to the surface. In early 2009 the *soft local coincidence (SLC) mode* was introduced, which does not require the neighbor or next-to-neighbor DOM to be triggered, thus recording isolated hits. For those hits the complete waveform information is discarded and only a time and total charge stamp are transmitted to the surface. The SLC are recorded at the PMT dark noise rate of ~300 Hz (compared to 10 Hz in HLC mode). They might be useful for event selection in cascade analyzes and low-energy muon track reconstruction. However, at the time the online analysis presented here was developed, the SLC hits were

not correctly incorporated in the event simulation and inclusion of the SLC hits in the reconstruction was not well tested. Therefore, SLC hits information is not used in this analysis.

4.5 Calibration

Both timing and amplitude calibration are crucial to enable an accurate reconstruction of the event. To calibrate the local clock of each DOM relative to the master clock on the surface the *RapCal* (Reciprocal Active Pulsing) procedure is applied: A signal is sent down from the surface electronics to each DOM, which waits a known time period of a few microseconds and sends an identical signal back to the surface. RapCal measures the round-trip travel time and is repeated every few seconds. The mean of the round-trip travel time depends on the length of the cable and represents the delay relative to the master clock. The jitter in the round-trip travel time presents the uncertainty of the clock calibration and thus provides the basic measurement of the precision of the time calibration procedure. The *DOMCal* (DOM Calibration) software [128] is responsible for the calibration of the DOM front-end electronics. It translates the digital output into voltage and time waveforms and further measures the gain at various voltage settings. The transit time in the PMT and other delays in the photon signal path are measured by using the on-board LED on each DOM main board, which can be pulsed on command. The amplification is calibrated with an on-board pulser, which creates single-photo-electron like waveforms with known amplitudes. The obtained calibration constants are stored in a database. Since they are fairly constant over time, DOMCal is applied only monthly.
The 12 LEDs on the flasher board are used to measure the light travel time between the flashing and receiving sensor. The variation of the time delay reveals imprecision of drifts of the clock calibration. Furthermore local coincidence is verified and precise geometry measurements of the DOM positions are obtained. Flashing multiple DOMs in various combinations is used for linearity calibrations and to quantify saturation effects.
In addition to the DOM LEDs the *standard candle*, a $337\,\mathrm{nm}$ nitrogen laser mounted on a string between two DOMs, can be used to insert artificial light into the detector. The light output can be varied and is well-calibrated. The shape of the emitted light is that of a Cherenkov cone and represents a reasonable approximation of a cascade. It is run twice per year and is used to study energy reconstruction algorithms and detector simulations.

4.6 Online Data Processing

The IceCube data acquisition (DAQ) delivers the raw data to a central server. A single CPU could not process the incoming data in real time, therefore the processing is parallelized. The data stream is divided in $2\,\mathrm{GB}$ chunks of data. The data chunks get distributed to several machines (*filter clients*), where filtering and processing takes place. 50 filter clients were available in IC40, while the number was increased to 100 for IC59. Filtered data is sent back to the server. The SPADE (South Pole Archival and Data Exchange) system saves raw and filtered files to tape and transfers filtered data North (within a few days), where it is stored in the data warehouse [129]. Filtered data is also sent to dedicated machines (*analysis clients*) to be further processed at South Pole in form of an online analysis.
During the IC40 period $2\,\mathrm{GB}$ of data correspond to roughly five minutes (or 4×10^5 events) of detector lifetime, while the data volume increased for IC59 and $2\,\mathrm{GB}$ included three minutes of data (or 2.5×10^5 events). The processing per event takes about $30\,\mathrm{ms}$ not including input and output (I/O) times. Figure 4.9 shows the processing time distribution obtained from

data processing at the South Pole Test System (SPTS). SPTS is located in Madison Wisconsin and consists of a similar server machine and similar (but fewer) filter clients as running at South Pole and is used to test software before it is installed at South Pole. Including I/O operation times one node needs approximately 4 (2.5) hours to process 2 GB of data for IC40 (IC59). A problem arises due to varying processing times for each data chunk. Usually the last data chunk of a data run[1] is shorter than 5 (3) minutes, hence this chunk is processed in less than 4 (2.5) hours. Since the node sends the processed data chunk immediately back to the server, the varying processing times might cause a non-temporal arrival of the processed data at the analysis clients. For parts of the filtering the temporal order is crucial (see Sec. 5.3.4). To prevent the analysis client from reading data chunks in incorrect order an additional (artificial) delay of four hours is introduced in order to restore the temporal order, i.e. the analysis client waits 4 h before it starts to read the data chunks. This results in a total delay of approximately 8 (6.5) hours. The processing described above is referred to as *plan B* (illustrated in Fig. 4.7).

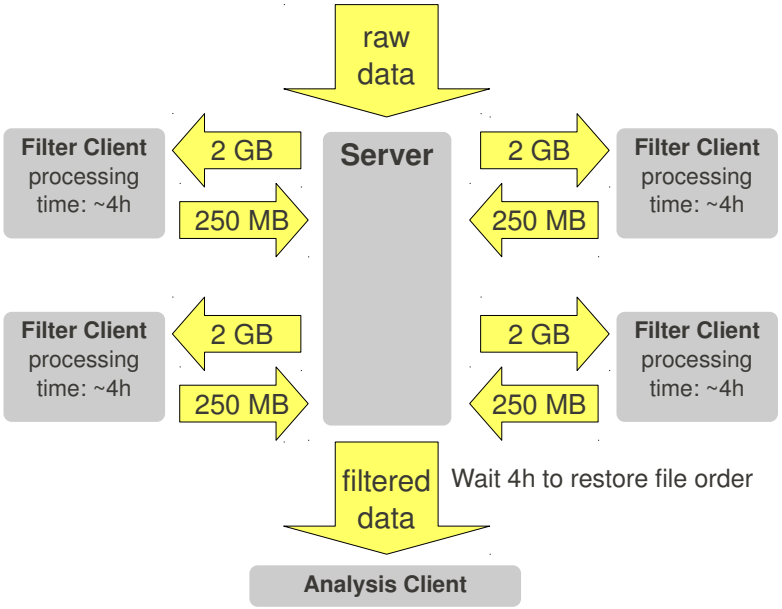

Figure 4.7: Online data flow and processing (**Plan B**): Raw data first arrives at the server. From there data chunks of 2 GB volume are distributed to the 50 (100) filter clients in IC40 (IC59). Each filter client takes approximately 4 h (2.5 h) to process the data. Reconstructions and filter information are added to the data before it is sent back to the server. Only events, which pass at least one filter are send back, hence the data volume is reduced from 2 GB to 250 MeV. The filtered data is transferred from the server to the analysis client with an additional delay of 4 h to restore the temporal file order.

A new scheme of parallel processing, *plan A*, was implemented with the transition from IC59 to IC79. Initially the processing was designed to operate in plan A mode. However, plan B was easier to implement and the original design was realized only later. Unlike plan B, plan A (illustrated in Fig. 4.8) sends single events from the server to the filter clients via a network connection. The average processing time for a single event is small (~30 ms). Single filtered events are merged to a continuous data stream on the server. This ensures a correct temporal order of all events and no additional delay for recovering the temporal order is

[1] A normal data run has a length of 8 hours

necessary. The average delay in the plan A configuration is ~5 min determined mainly by the size of the files written at the server and read by the analysis client[2].

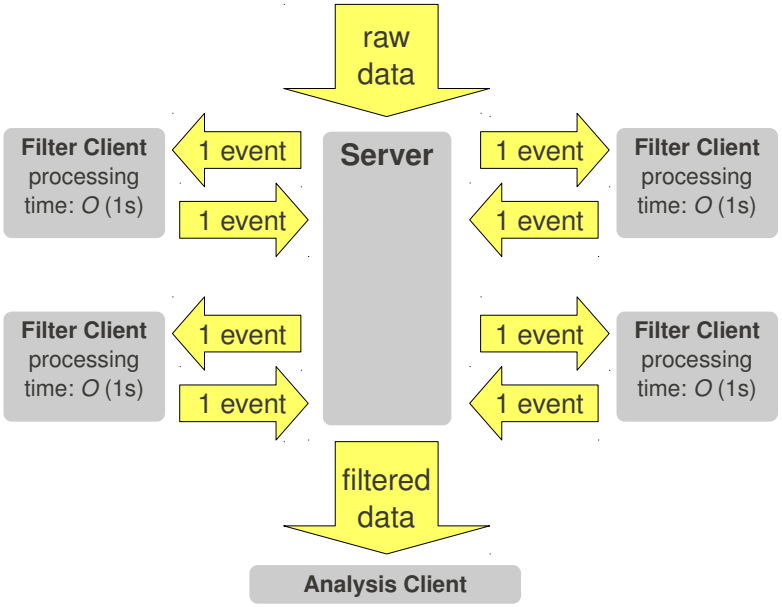

Figure 4.8: Online data flow and processing (**Plan A**): Different from plan B (figure 4.7) single events (instead of 2 GB chunks of data) are distributed to the filter clients over a network connection.

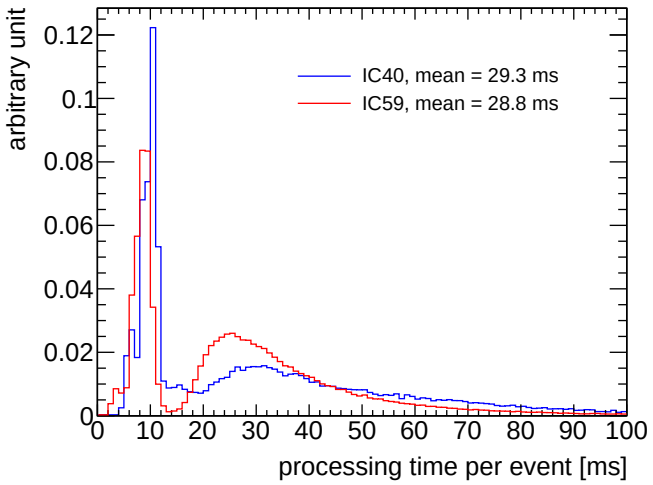

Figure 4.9: Processing time per event recorded on the South Pole test system (SPTS), machines at South Pole should behave similarly. I/O time is not included.

[2]Plans exist to avoid writing a file and instead sending single events via network to the analysis clients in order to reduce the latency to $\mathcal{O}$(s).

4.7 Event Reconstruction

The trigger condition defines a number of triggered DOMs N_{Ch}, which make up an event. Each hit consists of a time stamp, total charge and waveform. This information is used to reconstruct the direction of the muon track. A detailed description of the event reconstruction used in AMANDA, which is mostly still used in IceCube, can be found in [104].

4.7.1 Waveform Feature Extraction

The raw waveforms captured by the PMT in counts have to be calibrated to a charge in millivolt. The information needed for the calibration, such as signal transit time, baseline offset and gain for each single DOM, are stored in a database, which is updated after monthly DOMCal runs (see Sec. 4.5). Various waveform features, such as time, amplitude, width and area of the multiple pulses, are extracted from the calibrated waveforms based on an iterative Bayesian unfolding algorithm.

4.7.2 First Guess Algorithms

A first guess of the muon track is generated by a simple and fast pattern recognition algorithm. First guess algorithms are fast and coarse reconstructions that provide an identification of a large part of the muon background. To save CPU time, first guess reconstructions are used first to reduce the number of events running through the full reconstruction. Seeded on a first guess more CPU intensive maximum likelihood reconstructions can be applied. The most commonly used first guess algorithm for muon track reconstruction in IceCube is the *line-fit*. The line-fit generates an initial track on the basis of hit times. It does not take into account the Cherenkov cone geometry or the properties of the ice. Instead it assumes that the light travels along a straight line through the detector with constant velocity $\vec{V}$. The location of each DOM $\vec{r}_i$ hit at time t_i is given by

$$\vec{r}_i = \vec{R} + \vec{V} \cdot t_i, \tag{4.3}$$

where the vertex point $\vec{R}$ and the velocity $\vec{V}$ are free fit parameters, which can be obtained by minimizing

$$\chi^2 := \sum_{i=1}^{N_{\mathrm{NCh}}} (\vec{r}_i - \vec{R} - \vec{V} \cdot t_i), \tag{4.4}$$

where N_{NCh} is the number of hit DOMs. The minimization problem can be solved analytically by

$$\vec{r} = \langle \vec{r} \rangle - \vec{V} \cdot \langle t \rangle \text{ and } \vec{V} = \frac{\langle \vec{r} \cdot t \rangle - \langle \vec{r} \rangle \cdot \langle t \rangle}{\langle t^2 \rangle - \langle t \rangle^2}. \tag{4.5}$$

4.7.3 Likelihood Reconstruction

The track reconstruction gives an estimate of a set of track parameters $\{\mathbf{a}\}$ given a set of experimentally measured values $\{\mathbf{x}\}$. Assuming that the single components x_i of $\{\mathbf{x}\}$ are independent the corresponding likelihood reduces to

$$\mathcal{L}(\mathbf{x}|\mathbf{a}) = \prod_i p(x_i|\mathbf{a}). \tag{4.6}$$

$p(x_i|\mathbf{a})$ is the probability density function (PDF) of observing the measured value x_i for a given set of track parameters $\{\mathbf{a}\}$. The x_i measured by IceCube are the DOM positions $\vec{r_i}$, the hit times t_i, the charge and the waveform for each PMT pulse.
For simplification the muon track is assumed infinitely long and ultra-relativistic with $\beta = 1$. In this case the generated Cherenkov cone has a fixed angle of $\theta_c = 41^\circ$ and the track can be described by the following parameters:

$$\{\mathbf{a}\} = (\vec{R}, t_0, \vec{V}, E_0). \tag{4.7}$$

$\vec{R}$ is an arbitrary point on the track, which the muon passes at time t_0 with an energy E_0 along the direction $\vec{V}$ as illustrated in Fig. 4.10. The reconstruction is performed by minimizing $(-\log(\mathcal{L}))$ with respect to $\{\mathbf{a}\}$. The minimization is repeated n times in an *n-fold iterative likelihood* fit in order to overcome the problem of local minima. The algorithm is restarted with random track hypotheses to cover larger regions of the parameter space. This also leads to an improvement in the angular resolution.
A simple ansatz is to define a PDF, which only depends on the arrival time information. A relative arrival time, the time residual, can be defined as

$$t_{\text{res}} := t_{\text{hit}} - t_{\text{geo}}, \tag{4.8}$$

where t_{hit} is the measured hit time while t_{geo} is the expected arrival time for an unscattered photon according to the track geometry:

$$t_{\text{geo}} = t_0 + \frac{\vec{V} \cdot (\vec{r_i} - \vec{R}) + d \cdot \tan(\theta_c)}{c_{\text{vac}}}. \tag{4.9}$$

c_{vac} is the vacuum speed of light. On average t_{res} will be larger than zero due to scattering. Negative t_{res} can be caused by noise hits. The scattering strongly depends on the distance d of the DOM from the track (see Fig. 4.10 for illustration).
The arrival time distribution can be described by the *Pandel function* [130]

$$P(d, t_{\text{res}}) = \frac{1}{N(d)} \cdot \frac{1}{\Gamma\left(\frac{d}{\lambda}\right)} \cdot \frac{1}{t_{\text{res}}} \cdot \left(\frac{t_{\text{res}}}{\tau}\right)^{\frac{d}{\lambda}} \cdot \exp\left(-\frac{t_{\text{res}}}{\tau} - \frac{d + c_{\text{ice}} \cdot t_{\text{res}}}{\lambda_a}\right), \tag{4.10}$$

with normalization

$$N(d) = e^{-d/\lambda_a} \cdot \left(1 + \frac{\tau \cdot c_{\text{ice}}}{\lambda_a}\right). \tag{4.11}$$

$\Gamma(d/\lambda)$ is the Gamma function, $\lambda_a = 98\,\text{m}$ the average absorption length and c_{ice} the speed of light in ice. λ and τ are free parameter fixed by a fit to simulated photon arrival times. The fit obtained $\lambda = 33\,\text{m}$ and $\tau = 557\,\text{ns}$. The Pandel function describes the delay in the photon arrival due to scattering and absorption. Assuming homogeneous ice with constant absorption and scattering length individual hit probabilities can be calculated analytically and allow the calculation of the time likelihood [104].

4.7.4 Paraboloid Reconstruction

The muon track direction $(\theta_{\text{best}}, \phi_{\text{best}})$ obtained in a maximum likelihood fit corresponds to the maximum value on the likelihood surface $\mathcal{L}(\theta, \phi)$ or a minimum in $-\log(\mathcal{L})$.. The *paraboloid fit* [131] fits a paraboloid to this minimum as illustrated in Fig. 4.11. A least square fit is performed for $(\delta, \beta_1, \beta_2, c_{11}, c_{12}, c_{21}, c_{22})$ to determine the shape of a paraboloid:

$$f(\theta, \phi) = \delta + (\beta_1, \beta_2)^T (\theta, \phi) + (\theta, \phi)^T \begin{pmatrix} c_{11} & c_{12} \\ c_{21} & c_{22} \end{pmatrix} (\theta, \phi)\,. \tag{4.12}$$

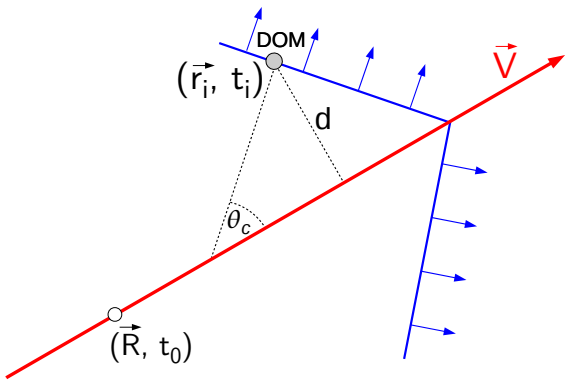

Figure 4.10: Track parameter definition: $\vec{R}$ is an arbitrary point on the track, which the muon passes at time t_0 along the direction $\vec{V}$. Cherenkov light is emitted at an angle $\theta_c = 41°$.

The width of the paraboloid provides an estimate for the reconstruction accuracy. An error ellipse is defined by slicing the paraboloid at

$$-\log(\mathcal{L}_{\text{ellipse}}) = -\log(\mathcal{L}_{\text{best}}) + \frac{1}{2}. \tag{4.13}$$

The half-axes of the ellipse, σ_x and σ_y (see Fig. 4.12 for illustration) serve as reconstruction uncertainty estimates. The paraboloid σ, which is used in this analysis to estimate the reconstruction accuracy, is defined as

$$\sigma = \sqrt{\frac{\sigma_x^2 + \sigma_y^2}{2}}. \tag{4.14}$$

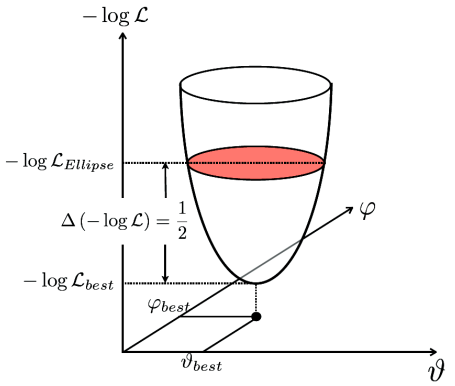

Figure 4.11: Illustration of paraboloid reconstruction: A paraboloid is fitted to the likelihood landscape centered around the best fit parameters (from [132]).

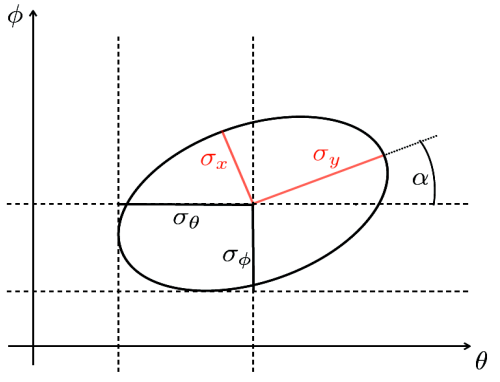

Figure 4.12: Ellipse received from slicing the paraboloid. The two half-axes σ_x and σ_y serve as reconstruction uncertainty estimates (from [132]).

4.7.5 Reconstruction Quality Parameters

A selection of good quality tracks is important for two reasons for the analysis presented here. First, only well-reconstructed events are useful to trigger optical telescopes with a

limited field of view. Second, mis-reconstructed muon events represent a background in every search for muon neutrinos and hence have to be suppressed. Usually mis-reconstructed muon events are characterized by a low track reconstruction quality. In the following the reconstruction quality parameters used in this analysis are presented.

Number of direct hits and track length

The number of direct hits, N_{Dir}, are defined as hits with a time residual (defined in Eq. 4.8) within $[-25\,\mathrm{ns}, 75\,\mathrm{ns}]$. A large number of direct hits ensures a good track reconstruction quality, since photons causing those direct hits are less affected by scattering. Furthermore, a large length of the projection of the direct hits on the track, L_{Dir}, indicates a high track quality. The definition of N_{Dir} and L_{Dir} is illustrated in Fig. 4.13.

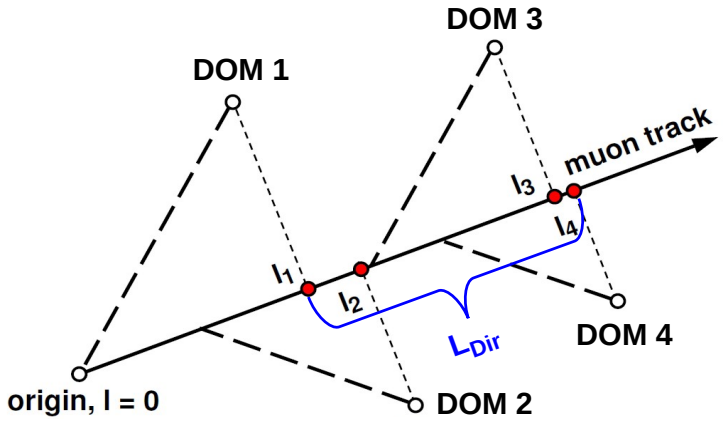

Figure 4.13: Direct hits are hits with a small time residual. Their projection on the track (represented by red dots) defines the track length L_{Dir}.

Reduced Maximum likelihood

The maximum likelihood evaluated in a likelihood reconstruction naturally indicates the quality of the reconstruction. The negative logarithm of the maximum likelihood, in the following referred to as $\mathcal{L}$, is expected to be large for mis-reconstructed events. Usually the reduced likelihood, $\mathcal{L}/(N_{\mathrm{Ch}} - 5)$ is used to inspect the track quality. $N_{\mathrm{Ch}} - 5$ is the number of degrees of freedom in the fit, i.e. $\mathcal{L}/(N_{\mathrm{Ch}} - 5)$ corresponds to the reduced χ^2 in case of a Gaussian probability distribution. However, other choices of p in $\mathcal{L}/(N_{\mathrm{Ch}} - p)$ sometimes result in better selection power.

4.8 Simulation

An accurate simulation of neutrino signal events is important for two reasons, first to develop selection criteria to separate signal from background and second to calculate the estimated flux according to a given model prediction. Simulated atmospheric muon background is used in this analysis to compare data rates with simulations at low filter levels. It is not used in the development of the selection criteria, where real data is used instead.

The simulation is divided in several steps:

- Simulation of neutrino interactions
- Muon propagation
- Photon propagation
- Detector simulation

A brief summary of these four steps is given in the following sections.

4.8.1 Neutrino Interactions

The *neutrino generator* software based on the program ANIS [113] generates neutrinos of any flavor according to a specified flux and propagates them through the Earth. It simulates neutrino interactions within a specified volume taking into account all relevant standard model processes. Primary neutrinos following a power law energy spectrum are randomly generated on the surface of the Earth. In the IceCube Monte Carlo production, neutrinos are injected from isotropic directions. The neutrinos are propagated through the Earth, where they can be absorbed in charged current interaction or are regenerated with lower energy in neutral current interactions. Once the detection volume is reached, a neutrino interaction is generated, i.e. the neutrino is forced to interact, and a neutrino or charged lepton and/or hadrons will be created according to the interaction probabilities. The detection volume used in this analysis is a cylinder of $2.0\,\mathrm{km}$ height and $1.2\,\mathrm{km}$ radius, centered around the center of the detector. For each generated neutrino, the cylinder is oriented around the incoming neutrino direction in order to provide an identical injection area. Those interaction probabilities are stored as a weight. Event rates for atmospheric and various extraterrestrial neutrino spectra are obtained by applying the appropriate weights to the events.
Neutrino generator calculates the quantity *OneWeight*, w_0, including all relevant factors such as generation volume, spectral index and interaction probabilities. The simulated events in a data set can be weighted in order to match a desired flux $F(\theta, E)$ by applying the following weight

$$w = F(\theta, E) \cdot w_0 / N_{\mathrm{gen}} \cdot \tau, \tag{4.15}$$

where τ is the livetime and N_{gen} the number of generated neutrino events in the data set. In this analysis a simulated neutrino data set it weighted in order to match the expected neutrino flux from soft jets in core-collapse SNe according to Ando and Beacom [100]. The same data set weighted with a different flux is used to study the expected atmospheric neutrino background.

4.8.2 Atmospheric Neutrinos

Atmospheric neutrinos are produced in cosmic ray interaction in the atmosphere [133]. Secondary mesons are created in proton interactions with the air molecules and produce neutrinos in their decay. Pion decay dominates the atmospheric neutrino production and determines the neutrino energy spectrum up to energies of $\sim 100\,\mathrm{GeV}$, while kaon decay plays a role at larger energies. The atmospheric muon neutrino spectrum follows a broken power law with spectral index ~ 3.7 up to an energy of $10^5\,\mathrm{GeV}$, above it steepens to a spectral index of ~ 4.0. The energy spectrum is zenith dependent, since inclined showers spend more time in the thin atmosphere, where they are more likely to decay rather than interact. The

neutrino flux arising from pion and kaon decay is reasonable well understood, with an uncertainty in the range $10\% - 20\%$ [133]. At high energies an additional component due to semi-leptonic decay of charged particles is expected, the so-called prompt-flux. Figure 4.14 shows the atmospheric neutrino spectrum measured by IceCube in its 40-string configuration [134] compared to neutrino flux models.

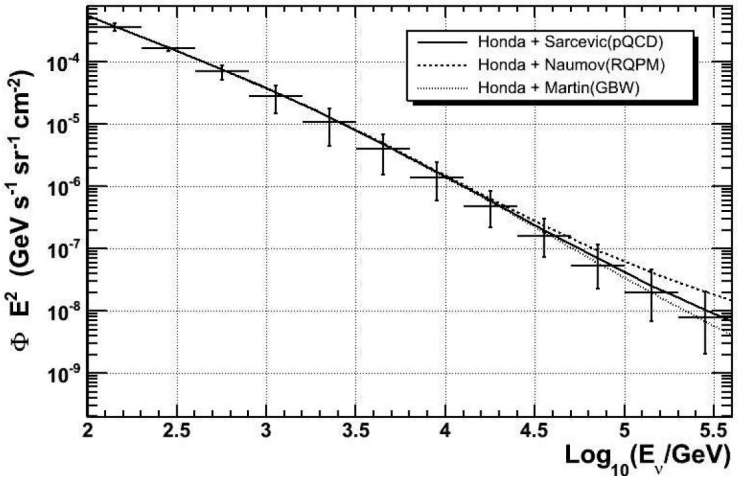

Figure 4.14: Atmospheric neutrino spectrum measured by IceCube in its 40-string configuration compared to various models: conventional flux as predicted by Honda [135], plus prompt flux predicted by Sarcevic [136], Naumov [137], or Martin [138]. Image taken from [134].

4.8.3 Muon Propagation

A muon generated in charged current neutrino interactions needs to be propagated from the interaction region through rock, ice and the detector volume. On its way it loses energy due to ionization losses, bremsstrahlung, photo-nuclear interaction and pair production. The process of muon propagation is simulated by the program MMC (Muon Monte Carlo) [139]. MMC treated energy loss event below an energy loss threshold as a continuous process, only secondaries with energies above the threshold are propagated as individual particles.

4.8.4 Photon Propagation

The Cherenkov photons emitted by neutrino induced muons and their secondaries are propagated through the ice with the PHOTONICS software package [140]. Direction and arrival time of Cherenkov photons are influenced by scattering and absorption in the medium. Usually the distance of the muon track from the optical modules is comparable or larger than the photon mean free path and scattering effects can neither be analytically calculated nor ignored. Furthermore, the ice is not homogeneous (as described in Sec. 4.2) causing a depth dependency of scattering and absorption coefficient. PHOTONICS determines the photon flux and time distributions throughout the instrumented ice through Monte Carlo simulation. The ice is described in vertical layers with varying optical properties. A dedicated ray tracing of each individual photon is not possible due to the large number of emitted photons by a single muon track and hence computing limitations. Therefore, pre-calculated tables containing photon propagation information are generated and are available for quick access during simulation or reconstruction. To create the PHOTONICS tables a large number of photons is generated and propagated through the detector volume. Their time distribution

is recorded on a cellular grid. To simulate a Cherenkov light source, photons are injected from a single point in space following the Cherenkov spectrum and angular emission profile. For each light source position and orientation one PHOTONICS table is generated.
For simulation and reconstruction the photon flux tables are converted to the mean number of photons detected in each detector module, as well as the arrival time distribution of these photons. The detector response, determined by absorption effects of the glass and gel layers of the DOM and the quantum efficiency of the PMT, are folded with the photon arrival time distributions. Dependency of the detector response on the incoming photon angle are taken into account.

4.8.5 Detector Simulation

The detector simulation computes the signal response of the DOM. The expected number of photo-electrons for a given Cherenkov source are provided by the PHOTONICS tables. A hit, i.e. a time series of detected photo-electrons, is generated and noise hits are added. The PMT response is simulated using a measured photo-electron spectrum and waveform response of the PMT. Effects of digitization and low level trigger logic performed on the DOM mainboard are simulated and electronic artifacts are added. Finally, the global trigger is simulated. Simulated and real data recorded by the IceCube DAQ appear in identical format to enable similar high level processing for real and simulated data sets.

4.8.6 Simulation of Atmospheric Muons

Atmospheric muon data sets are generated using the air shower simulation program CORSIKA (COsmic Ray SImulations for KAscade) [141]. High energy cosmic ray particles are propagated through the atmosphere where they interact with air nuclei creating a shower of secondary particles, which further interact in the atmosphere or eventually decay. Hadronic interactions at high energies are described by the QGSJET or SIBYLL model. Secondary high-energy muons can reach the Earth and are propagated through the ice using MMC. The Cherenkov light signal is generated using PHOTONICS. Two samples of CORSIKA generated events are used in this analysis. A sample of single muon events and a second sample containing coincident muons. Coincident muons are created in two different air showers and enter the detector simultaneously. Two coincident down-going muons can easily mimic an up-going neutrino and are thus an important class of background events.
The atmospheric muon background simulation is used in this analysis only to compare data rates with simulations at low filter levels. The experimental data itself can be exploited to develop selection criteria for separation of signal and background and to estimate the fraction of events from cosmic ray muons which remain in the data sample after the selection of neutrino induced events.

4.8.7 Doublet Signal Sample

To study the resolution of the combined direction of two (doublet) or more single reconstructed directions (multiplet) a simulated point source sample is needed. Since the resolution depends on the detector coordinates, samples for different detector direction need to be produced. Another option is to use the diffuse sample to construct point source samples [132]. The sample is divided into zenith bands to account for the zenith dependence of the point spread function. Pairs of events, which both lie in the same zenith band, are

shifted to their average direction:

$$\overline{\theta}_{\mathrm{true}} = \frac{1}{2}\left(\theta_{\mathrm{true},1} + \theta_{\mathrm{true},2}\right) \tag{4.16}$$

$$\overline{\phi}_{\mathrm{true}} = \frac{1}{2}\left(\phi_{\mathrm{true},1} + \phi_{\mathrm{true},2}\right) \tag{4.17}$$

Their reconstructed direction is shifted by the same amount as the true direction. The two events are now simulated to origin in the same true direction. Note that azimuth dependencies are not accounted for. Those are small compared to the zenith dependence.

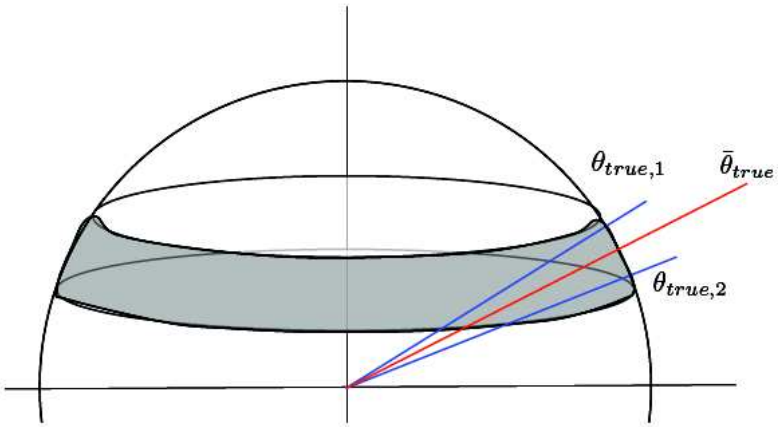

Figure 4.15: Point source factory: Two events with true zenith angles $\theta_{\mathrm{true},1}$ $\theta_{\mathrm{true},2}$ in the same zenith band are shifted to their average true zenith angle $\bar{\theta}_{true}$ (graphic taken from [132]).

Chapter 5

Online Neutrino Event Selection

The optical follow-up program aims for a fast detection of neutrinos from transient sources with IceCube in order to trigger optical telescopes, which then point towards the neutrino direction trying to observe an optical counterpart. To realize such a program, a fast analysis of IceCube data is required in order to rapidly trigger the optical observations. Furthermore, an accurate reconstruction of the neutrino direction is crucial to point the telescope in the right direction. To fulfill these requirements, the first online analysis of high-energy neutrinos detected by IceCube has been developed and implemented. This includes an online selection of neutrino candidates, the transmission of triggers to the telescopes and an extensive monitoring of the online system. Those three components are presented in this chapter.
Data recorded by IceCube is processed at the South Pole with a delay of $8\,\mathrm{h}$ ($6\,\mathrm{h}$) for IC40 (IC59) (see Sec. 4.6). The processing is preformed in a parallel manner on a computer cluster. In the following it is referred to as *online* processing. In contrast, the standard processing is performed on an entire dataset (usually ~ 1 year of data) with time consuming reconstructions on a large computer cluster, e.g. at the University of Wisconsin in Madison. Thus, the standard processing is referred to as *offline* processing.
The online processing comprises step wise filtering and track reconstruction. A high level event selection was developed in order to reduce the data stream to a reasonable rate to trigger optical telescopes (~ 25 per year). The event selection is responsible to filter well-reconstructed muon neutrinos from a large amount of background events. In order to find criteria to distinguish signal from background events, both a signal and background data set are needed. This way, characteristic parameter distributions can be studied to find a good classification of signal and background.

5.1 Background

The background in a search for muon-neutrinos of astrophysical origin can be divided into two classes. One consists of atmospheric muons created in meson decays in cosmic ray air showers entering the detector from above. The other is given by atmospheric neutrinos which originate in the same meson decays in cosmic ray air showers (see Fig. 5.1). Both are measured with IceCube and are well understood: The measurement of the atmospheric neutrino spectrum with IceCube in its 40-string configuration is discussed in [134] while the atmospheric muon energy spectrum measured by the 22-string configuration is presented in [142]. The zenith distribution of atmospheric muons and atmospheric neutrinos obtained from simulations are displayed in Fig. 5.2. The figure shows that the flux of atmospheric muons exceeds the flux of atmospheric neutrinos by 6 orders of magnitudes.
However, the muon flux is limited to the Southern hemisphere because muons from the

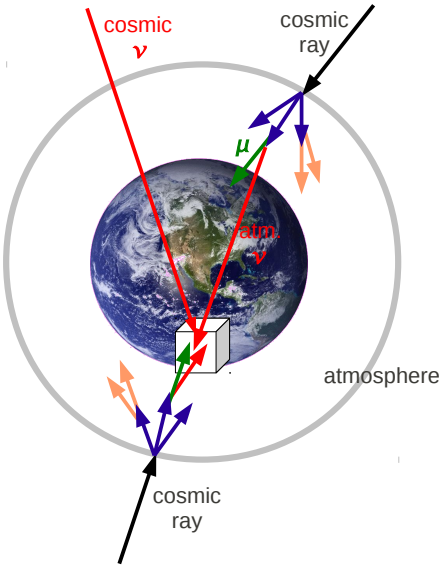

Figure 5.1: Background in search for cosmic muon neutrinos.

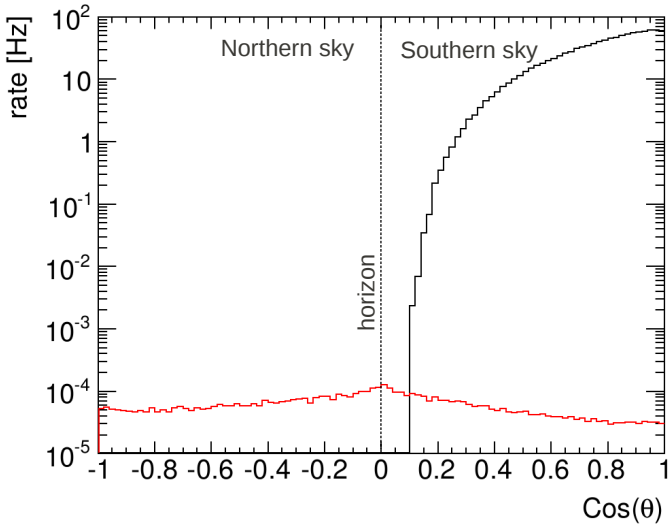

Figure 5.2: Simulated true zenith distribution of atmospheric muons (black) and atmospheric neutrinos (red).

northern hemisphere cannot penetrate the Earth and reach the detector. Therefore, the background of atmospheric muons can be reduced significantly by restricting the neutrino search to the northern hemisphere. Nevertheless, a small fraction of the Southern hemisphere muons are mis-reconstructed, e.g. truly *down-going* (entering the detector from above) but reconstructed as *up-going* (passing through the Earth). Due to the large flux of atmospheric muons these mis-reconstructed muons, although being only a small fraction of the total muons, represent a large contamination to the neutrino sample.

Atmospheric muons are simulated with the air shower simulation software CORSIKA (see Sec. 4.8.6). One distinguishes between single and coincident muons. Coincident muons are two single muons entering the detector at the same time from independent directions, i.e. are produced in two different air showers.

The atmospheric neutrino background is not obtained by the same air shower simulation, but by reweighting a muon neutrino data set as described in Sec. 4.8.2. The air shower simulation is time consuming and one has to generate comic rays hitting the atmosphere in a solid angle of 4π in order to generate atmospheric neutrinos. Most of the generated neutrinos would not even hit the detector. In contrast, the neutrino generator is very efficient and generates neutrinos close to the detector, forces every generated neutrino to interact and assigns a weight corresponding to the interaction probability to every event.

The data set was generated following an E^{-1}-energy spectrum and then reweighted with the expected atmospheric muon neutrino energy spectrum as predicted by Honda [135] and Naumov [137].

The background Monte Carlo, i.e. the sum of simulated atmospheric neutrinos and atmospheric muons, is only used to study the contribution of different background components. The CORSIKA simulations are very time consuming and since the background has to be suppressed by 6 orders of magnitude, one quickly runs out of atmospheric muon statistic preventing studies with background MC at high cut levels. Instead, IceCube data is used to represent the background in the development of selection criteria. This is a valid procedure, since the data stream at final cut level will still be largely background dominated and the

selection cuts developed here do not aim for a complete removal of the background, but to reduce the data stream to the atmospheric neutrino level.

5.2 Signal

The signal of interest in this work are neutrinos from core-collapse supernovae. The expected neutrino signal from a SN at a certain distance according to the soft jet SN model can be calculated as a function of two model parameters: the Lorentz boost factor Γ and the jet energy E_{jet} (see Sec. 2.6). Signal events are simulated following the predicted neutrino flux spectrum in order to develop and optimize selection criteria to distinguish signal and background events. The same neutrino data set as used to describe the atmospheric neutrino background (weighted with the atmospheric neutrino spectrum, see Sec. 5.1) is used to describe the SN neutrinos (weighted with the neutrino energy spectrum predicted by Ando and Beacom [100], see Sec. 2.6).
Note that this analysis is not explicitly optimized for neutrinos from GRBs because the delay introduced in the online processing is too large to allow the detection of an optical afterglow with small telescopes such as ROTSE. Such an analysis is only feasible after the delay caused by the online processing was reduced from 6-$8\,\text{h}$ to a few minutes, i.e. after the transition to IC79 (see Sec. 4.6).

5.3 Selection Cut Optimization

The character of signal and background events reflected by the distribution of certain variables is studied using the signal and background data sets described above. Requirements to the event reconstruction quality allow the suppression of the mis-reconstructed atmospheric muons. The parameters to estimate the track quality used in this work are (see Sec. 4.7.5 for a detailed description of the parameters and appendix A for plots comparing signal and background distributions as well as data and Monte Carlo):

- The number of direct hits, with a time residual within $[-15\,\text{ns}, 75\,\text{ns}]$, N_{DirC}, which is large for well-reconstructed and small for mis-reconstructed events.
- The track length between the first and the last direct hit, L_{DirC}, which is long for well-reconstructed and short for mis-reconstructed events.
- The negative logarithm of the maximum likelihood, $\mathcal{L}$, obtained in a likelihood reconstruction of the muon track, is small for well-reconstructed and large for mis-reconstructed events. Not $\mathcal{L}$ itself but the reduced likelihood $\mathcal{L}/(\text{N}_{\text{Ch}}-5)$ or a modified version $\mathcal{L}/(\text{N}_{\text{Ch}}-\text{p})$, with $p = 2$ or $p = 3.5$, is used.

In contrast to mis-reconstructed atmospheric muons, atmospheric neutrinos show a similar reconstruction quality as SN neutrinos and cannot be suppressed by requiring a good track reconstruction. However, atmospheric neutrinos are distributed isotropically, while SN explosions are point sources expected to emit bursts of neutrinos. Therefore, the detection of *multiplets* consisting of at least two events with an arrival time difference of $\Delta t \leq 100\,\text{s}$ and an angular difference between their two reconstructed directions of less than $\Delta\Psi \leq 4^\circ$ is required. The choice of the size of the time window is motivated by the duration of the jet, i.e. the activity of the central engine, which is typically $10\,\text{s}$ [99]. The observed gamma-ray emission from long GRBs has a typical length of $50\,\text{s}$ [63], which roughly corresponds to the

duration of a highly relativistic jet to penetrate the stellar envelope. The angular window $\Delta\Psi$ is determined by IceCube's angular resolution and is optimized along with the other selection parameters.
The final set of selection cuts has been optimized in order to reach a multiplet rate of ~25 per year corresponding to the maximal number of neutrino triggers accepted by the ROTSE telescopes. Note that this is not a hard limit and ROTSE would not refuse to observe a slightly larger number of triggers, e.g. caused by statistic fluctuations.
Compared to the neutrino point source analysis performed with IceCube data [143], which selects a nearly pure sample of neutrinos and searches for an excess in the isotropic background of atmospheric neutrinos, the combination of the neutrino measurement with the optical follow-up allows to relax the cuts in this analysis. This yields a larger background contamination but at the same time a higher signal passing rate. As such, the smallest multiplet, a *doublet*, consisting of two coincident events, is not significant by itself, but may become significant by adding the optical information.
Each multiplet is forwarded to ROTSE. Given the maximal number of guaranteed observations, this defines a maximal background multiplet rate of $R_{m\geq 2} = 25\,\mathrm{y}^{-1}$. In the following the corresponding maximal single event (*singlet*) rate R_1 is estimated from the maximal multiplet rate. The singlet rate is useful to estimate the necessary suppression of isotropic background. The probability to obtain a background *triplet* (three atmospheric neutrinos arriving by accident within 100 s and within $\Delta\Psi$) or any multiplet of higher order is negligible, hence we only consider doublets for the background estimation. Requiring no more than 25 background doublets per year ($R_2 \leq 25\,\mathrm{y}^{-1}$) corresponds to a rate of isotropic background events of:

$$\begin{aligned} R_1 &\lesssim \sqrt{R_2 \frac{\Omega_{\mathrm{north}}}{\Delta t \cdot \Delta\Omega}} \\ &= \sqrt{25\,\mathrm{year}^{-1} \frac{20627(^\circ)^2}{100\,\mathrm{s} \cdot (\Delta\Psi)^2 \cdot \pi}} = \frac{7.2\,\mathrm{mHz}}{\Delta\Psi[^\circ]} \end{aligned} \tag{5.1}$$

where $\Delta\Omega = \pi(\Delta\Psi)^2$ is the solid angle defined by the doublet condition and $\Omega_{\mathrm{North}} = 20627(^\circ)^2$ the solid angle of the northern sky [33]. Only the northern sky is considered in this analysis in order to suppress the background of atmospheric muons.
Note that Eq. 5.1 gives only an estimate on the relation of singlet and doublet rate. The singlet rate is integrated over the whole detector averaging over detector asymmetries. The effects of those asymmetries influence the singlet rate linearly, while they enter the doublet rate quadratically. Furthermore, the rate - especially of down-going atmospheric muons - is affected by seasonal variations. This inaccuracy in the estimated doublet rate does not propagate to the final result of this analysis, because the final expected multiplet rate, which is crucial for the final limit calculation presented in Sec. 9.2, is obtained accurately by scrambling the whole data set (see Sec. 5.8). However, for an online analysis the event selection has to be settled before the whole data set is available, leaving us with the rough estimate given by Eq. 5.1.
The event selection is optimized in order to restrict the singlet rate to $7.2\,\mathrm{mHz}/\Delta\Psi$ while obtaining the best signal passing rate. It consists of several steps as displayed in Fig. 5.3. It is divided in two parts: The first part of the filtering, which is not unique to this analysis but also of interest for other analysis, is applied as part of the parallel processing on the computer cluster, while the final part, which is unique to this analysis, is performed on a dedicated machine, the analysis client. A delay is introduced by the parallel processing and ordering of the data.
The filtering is based on the standard IceCube muon event filter (further referred to as

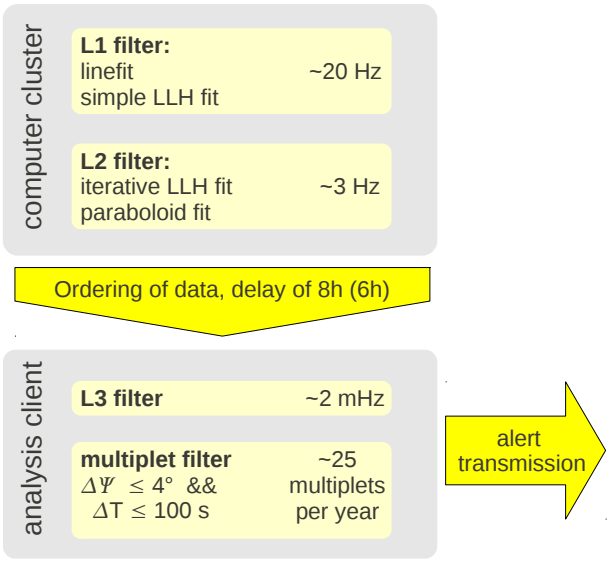

Figure 5.3: The event selection consists of several steps. On the computer cluster at South Pole based on the standard Level 1 filter a second more restrictive filter (Level 2) is applied. Together they reduce the rate in a first step to ~20 Hz and in a second step to ~3 Hz and thus allow the application of time consuming reconstruction algorithms. Then the data is transferred from the cluster to the analysis client. Processing and ordering of the data introduces a delay of 8 h (6 h) in IC40 (IC59). Optimized for the selection of SN neutrinos, a third filter (Level 3) reduces the rate further and finally the multiplet filter is applied, which selects 25 background multiplets per year that are forwarded to ROTSE.

Level 1), which is commonly used by several offline analysis. A second cut level (Level 2) reduces the data stream further in order to perform sophisticated track reconstructions with the limited CPU resources available at the South Pole. Based on those reconstructions further cuts are applied yielding the final cut level (Level 3). In the final step the multiplicity requirement is applied. The individual filter steps are described in the following sections. The cuts applied in each step are summarized in table 5.1. Table 5.2 shows the data passing rates and the expected number of detected SN neutrinos at different cut levels for a SN at distance $d_{\mathrm{SN}} = 10\,\mathrm{Mpc}$ with a jet of energy of $E_{\mathrm{jet}} = 3 \times 10^{51}\,\mathrm{erg}$ pointing toward the Earth and for Lorentz factors Γ of 4 and 10. The expected number of well reconstructed SN neutrinos (defined as $|\vec{\Psi}_{true} - \vec{\Psi}_{reco}| < 3^\circ$ and $\theta_{true} > 90^\circ$, where the unit vector $\vec{\Psi}$ indicates the track direction) is given in brackets since only these events are useful to trigger optical telescopes.

5.3.1 Muon Level 1 Filter

The neutrino event selection for this analysis is based on the muon Level 1 filter, which is IceCube's primary filter for rejecting down-going, atmospheric muons and retaining generic muon events from near or below the horizon. Therefore, it selects muon tracks, that are reconstructed as up-going (passing through the Earth) based on fast and simple algorithms (for details see [143]). It selects ~2% of all triggered events and is still largely dominated by atmospheric muons (99.97%). The selected events are transferred to the data archive in Madison via a broad-band satellite connection within a few days. There it is used for a variety of different offline analyses, such as the point-source analysis [143], atmospheric neutrino spectrum unfolding [134] or the WIMP search [144] among others. The filter is

Table 5.1: Cuts used to reduce the data to the neutrino level. The reduction is done in three levels - see text for details.

Cut Level	Cuts
IC40 Level 1	$\theta_{\mathrm{llh1}} \geq 70^\circ$ && $\theta_{\mathrm{llh2}} \geq 70^\circ$ && $\mathrm{N_{Ch}} \geq 10$
IC40 Level 2	$\theta_{\mathrm{llh1}} \geq 80^\circ$ && $\theta_{\mathrm{llh2}} \geq 80^\circ$ && $\theta_{\mathrm{lf}} \geq 70^\circ$ && $\mathrm{N_{DirC}} \geq 5$ || $\mathcal{L}/(\mathrm{N_{Ch}} - 5) \leq 10$
IC40 Level 3	$\theta_{\mathrm{llh1}} \geq 85^\circ$ && $\theta_{\mathrm{llh2}} \geq 85^\circ$ && $\theta_{\mathrm{10it}} \geq 85^\circ$ && $\mathcal{L}/(\mathrm{N_{Ch}} - 5) \leq 8.85$ && $(\mathrm{N_{DirC}} \geq 7$ && $\mathrm{L_{DirC}} \geq 225)$ || $\mathrm{N_{Ch}} \geq 200$
IC59 Level 1	$\mathrm{N_{Ch}} \geq 8$ && $(\mathrm{N_{Ch}} \geq 10$ || $\theta_{\mathrm{lf}} \geq 70^\circ)$ && $\theta_{\mathrm{llh1}} \geq 80^\circ$ && $\mathcal{L}/(\mathrm{N_{Ch}} - 2) \leq 8.2)$
IC59 Level 2	$\mathrm{N_{DirC}} \geq 5$ || $\mathcal{L}/(\mathrm{N_{Ch}} - 2) \leq 7.38$ || $\mathrm{N_{Ch}} \geq 80$
IC59 Level 3	$\theta_{10it} \geq 90^\circ$ && $\mathcal{L}/(\mathrm{N_{Ch}} - 3.5) \leq 7.7$ && $(\mathrm{N_{DirC}} \geq 7$ && $\mathrm{L_{DirC}} \geq 250)$ || $\mathrm{N_{Ch}} \geq 100$

Table 5.2: Data and Signal Passing Rates at Different Cut Levels. Values in brackets refer to well reconstructed events - see text for details.

Cut Level	Event Rate		Neutrino events for SN at $d_{\mathrm{SN}} = 10\,\mathrm{Mpc}$			
			$\Gamma = 4$, $E_{\mathrm{jet}} = 3 \times 10^{51}$ erg		$\Gamma = 10$, $E_{\mathrm{jet}} = 3 \times 10^{51}$ erg	
	IC40	IC59	IC40	IC59	IC40	IC59
Level 1	20.7 Hz	22.7 Hz	68.0 (18.6)	133.3 (34.7)	3385.5 (1081.3)	5304.0 (1877.7)
Level 2	2.74 Hz	3.32 Hz	48.1 (17.6)	100.0 (32.9)	2544.6 (1076.0)	4225.9 (1801.1)
Level 3	2.17 mHz	1.86 mHz	13.3 (8.7)	22.4 (16.3)	947.4 (674.6)	1441.7 (1153.0)

developed to fulfill the needs of these various analyses. Therefore, it uses soft, simple and robust cuts and has a high signal passing rate over a broad energy range. At the same time the background passing rate is high (~20 Hz). Hence, it requires a lot of satellite bandwidth (~7 GB per day).

The selection criteria of the Level 1 filter are based on a single iteration likelihood fit (*llh*) seeded with a linefit first guess, which is applied to all triggered events. In IC40 a two iteration likelihood fit *llh2* was applied in addition to the single iteration fit. In the first iteration it is seeded with the linefit and in the second iteration with the inverted linefit result and the best fit result is kept. Due to computing time restrictions the *llh2* reconstruction was not applied in IC59.

Based on the reconstructed zenith obtained by *llh1* (*llh1* and *llh2* in IC40) the Level 1 filter is divided into two complementary branches: The first branch selects events with a zenith angle of $\theta > 70^\circ$ for IC40, $\theta > 80^\circ$ for IC59, and a maximum of 10 hit DOMs, $\mathrm{N_{Ch}} \geq 10$. Note that $\theta = 90^\circ$ corresponds to the equator in the IceCube coordinate system as illustrated in Fig. 5.2. Events with $\theta = 0^\circ$ enter the detector from above, i.e. from the South, and events with $\theta = 180^\circ$ from the North.

The second branch represents a high energy extension to the Southern hemisphere, where

ultra high-energy events can be distinguished from atmospheric muons by using energy estimators, such as the number of hit DOMs $\mathrm{N_{Ch}}$ or the total charge recorded at the hit DOMs, $\mathrm{Q_{tot}}$. Only hard energy cuts allow a reasonable separation of signal and background above the horizon. Since this analysis focuses on the search for SN neutrinos with an expected soft energy spectrum, it is restricted to the northern hemisphere. Note that for a future high-energy extension of the optical follow-up program (see Chap. 12) aimed for the detection of GRB neutrinos in coincidence with their optical afterglow the high-energy extension of the filter will be useful. In the following the term Level 1 refers to the first branch.
Since IC59 is ~50% larger than IC40, the zenith cut is tightened and an additional cut on $\mathcal{L}/(\mathrm{N_{Ch}}-2)$ is applied in order to obtain a similar passing rate to fulfill the satellite bandwidth requirements.
Based on the Level 1 filter further selection criteria mainly based on the reconstruction quality of the likelihood fit are applied. Those have been developed to fulfill the special requirements of an online analysis, i.e. reduction of the rate to allow sophisticated reconstructions while keeping a high fraction of well-reconstructed signal events. This yields the so-called (online) Level 2 filter stream.

5.3.2 Level 2 Filter

The aim of the Level 2 filter is to provide a good resolution of the reconstructed neutrino event direction, which is crucial in order to provide an accurate pointing for the optical follow-up. The likelihood reconstruction available at Level 1 is not sufficient. An improvement of the resolution can be reached by applying iterative likelihood methods. However, those are time consuming and computing resources are limited at the South Pole. It is not possible to apply such time consuming reconstructions to all events, which pass the muon Level 1 filter. Additional filtering is needed to select good quality neutrino candidates before additional reconstructions can be applied. Since an online data stream of well-reconstructed events is of generic interest for future online analyses, the online Level 2 filter was established. It reduces the Level 1 filter stream based on the available reconstruction results.
First, an additional zenith cut ($\theta \geq 80^\circ$) is applied to reduce the background of atmospheric muons further. Second, a good reconstruction quality needs to be ensured. The likelihood value (more specifically, the negative logarithm divided by the number of degrees of freedom, $\mathcal{L}/(\mathrm{N_{Ch}}-5)$, i.e. reduced likelihood) and the direct hit variable, N_{DirC}, serve as a proxy of the quality of the reconstruction as illustrated in Fig. 5.4 and Fig. 5.5. Small values of $\mathcal{L}/(\mathrm{N_{Ch}}-5)$ correspond to good track reconstruction quality. In IC40 $\mathcal{L}/(\mathrm{N_{Ch}}-5)$ was used, while a modified version $\mathcal{L}/(\mathrm{N_{Ch}}-2)$ was shown to be more efficient in IC59.
A large number of $\mathrm{N_{DirC}}$ indicates a good track reconstruction quality, since photons causing direct hits are less likely to have been scattered. However, the $\mathrm{N_{DirC}}$ cut introduces a considerable energy dependence as illustrated in Fig. 5.6. A large fraction of high-energy events have zero direct hits. The reason for this behavior is an inaccuracy in the used photon PDF. For high energy events many photons arrive at each DOM. The first one is fitted with a single photon PDF. Since most photons are expected to arrive well after the first hit, the actual peak of the time PDF occurs later. The reconstruction algorithm however tries to match the first photon with the later peak which introduces a time shift. Therefore, truly direct hits get shifted to larger time residuals. Using a multi-photon PDF would solve the problem, but multi-photon reconstructions are too time consuming to be applied online.
To circumvent the problem of energy dependence, the $\mathrm{N_{DirC}}$ cut is combined in an or-condition with an $\mathrm{N_{Ch}}$ cut. The $\mathrm{N_{Ch}}$ cut also introduces an energy dependence preferring high-energy events as shown in Fig. 5.7, since high energy events lead to more hit DOMs in the detector. The energy dependence is inverted compared to the N_{DirC} energy dependence.

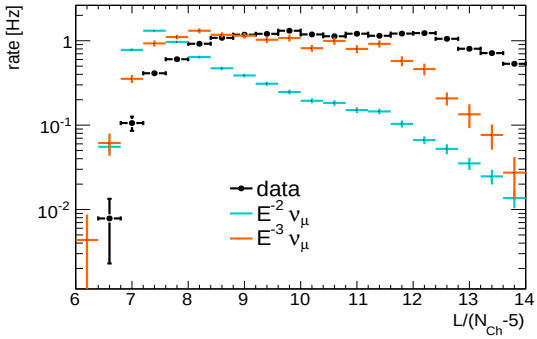

Figure 5.4: Distribution of reduced likelihood, $\mathcal{L}/(\mathrm{N_{Ch}} - 5)$, (after application of Level 1 filter cuts, IC40) for background (black), neutrino signal following an E^{-2}-spectrum (cyan) and an E^{-3}-spectrum (orange).

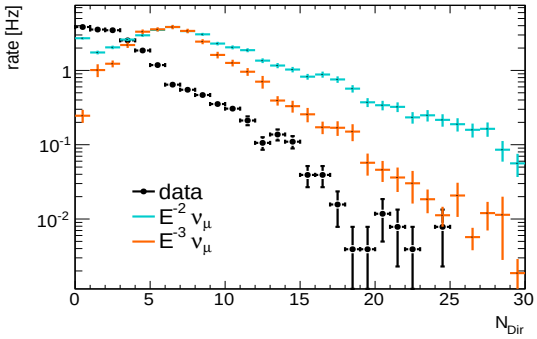

Figure 5.5: Distribution of number of direct hits, $\mathrm{N_{DirC}}$, (after application of Level 1 filter cuts, IC40) for background (black), neutrino signal following an E^{-2}-spectrum (cyan) and an E^{-3}-spectrum (orange).

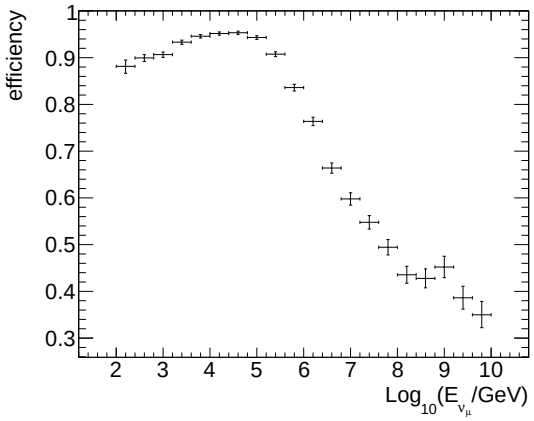

Figure 5.6: Signal efficiency as a function of the neutrino energy after applying the cut $\mathrm{N_{DirC}} \geq 5$ (IC59, well-reconstructed events). An energy dependency is introduced preferring low energy events due to an inaccuracy in the photon PDF.

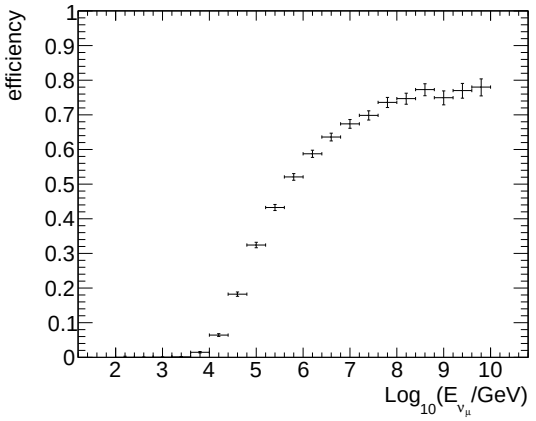

Figure 5.7: Signal efficiency as a function of the neutrino energy after applying the cut $\mathrm{N_{Ch}} \leq 80$ (IC59, well-reconstructed events). An energy dependency is introduced preferring high energy events.

The or-combination of the direct hits and the $\mathrm{N_{Ch}}$ condition keeps the high energy events, which are mistakenly discarded by the direct hits cut and thus results in a flat energy dependence of the filter efficiency over a broad energy range as illustrated in Fig. 5.8.

After applying the selection criteria described above, the rate is reduced to ~3 Hz at Level 2. This significantly smaller rate, compared to the Level 1 rate of ~20 Hz, allows the application of time consuming reconstructions online. These reconstructions are an iterative likelihood reconstruction (10 iterations) and a paraboloid reconstruction (see Sec. 4.7 for more details on the event reconstruction). They provide a more accurate reconstruction of the event direction compared to the single iteration likelihood fit available at Level 1.

The Level 2 filter fulfills the needs of an online analysis: fast online event selection and accurate track reconstruction. Based on the results of the more sophisticated reconstruction algorithms the final event stream, Level 3, is selected.

5.3.3 Level 3 Filter

The Level 3 selection is optimized for the expected neutrino signal of the optical follow-up program, i.e. core-collapse supernova (CCSN) neutrinos. The event selection takes place on a dedicated analysis client for the optical follow-up program. The analysis client receives a time-ordered data stream from the central server as discussed in Chap. 4.6. The sophisticated reconstructions available for all events, which passed the Level 2 filter, allow a further event selection, reducing the remaining background events to mainly atmospheric neutrinos. Therefore, only well-reconstructed up-going events with zenith angle $\theta \geq 85^\circ$ (IC40) and $\theta \geq 90^\circ$ (IC59) are selected. Furthermore, a strict selection of well-reconstructed events is performed using similar variables, but harder cuts as used for the Level 2 filter. One additional variable is added, namely $\mathrm{L_{DirC}}$, which is defined as the length of the projection of the direct hits onto the track (see chapter 4.7.5 for details). A long $\mathrm{L_{DirC}}$ indicates a good reconstruction quality and thus provides a good separation between signal and background as illustrated in Fig. 5.9. A summary of the distributions of all used cut parameters can be found in appendix A.

In contrast to Level 2, the variables are calculated based on the 10-fold iterative llh fit, which provides a more accurate event reconstruction and hence a better discrimination between signal and background.

The event selection is optimized in order to restrict the singlet rate to $7.2\,\mathrm{mHz}/\Delta\Psi$, corresponding to 25 doublets per year according to Eq. 5.1, while obtaining the best signal passing rate. Possible combinations of cut values are tested by varying the cut values in small steps. For each combination the background and signal passing rates are computed. All combinations which yield an expected background rate of less than $7.2\,\mathrm{mHz}/\Delta\Psi$ are compared. The best set of cuts depends on the assumed signal neutrino energy spectrum. The SN neutrino spectrum obtained from the Ando and Beacom model can be either hard or soft depending on the choice of model parameters. Therefore, the combination of cut values that led to the best compromise between high passing rates for hard spectra and high passing rates for soft spectra is chosen in order to provide good passing rates for all choices of model parameters. The final filter obtained at Level 3 is nearly energy independent above neutrino energies of $100\,\mathrm{TeV}$ as illustrated in Fig. 5.10. For high energies above $100\,\mathrm{TeV}$ the filter is 90% efficient,

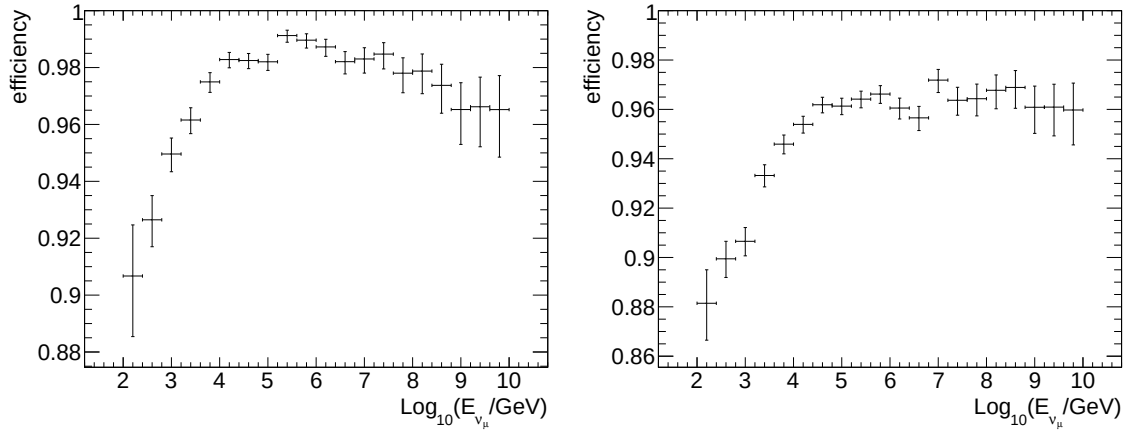

(a) IC40 (b) IC59

Figure 5.8: Filter efficiency of Level 2 relative to Level 1 as function of the neutrino energy for well-reconstructed events.

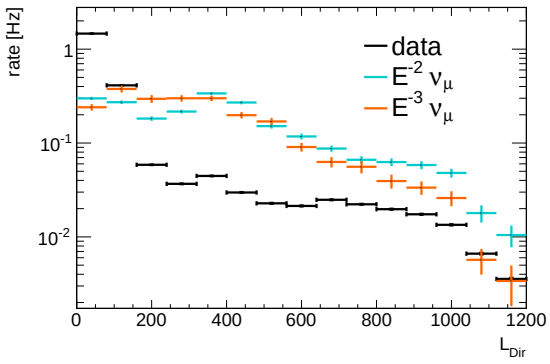

Figure 5.9: Distribution of L_{DirC} (after application of Level 2 filter cuts, IC40) for background (black), neutrino signal following an E^{-2}-spectrum (cyan) and an E^{-3}-spectrum (orange).

while for smaller energies the efficiency decreases to 50% at $1\,\text{TeV}$ and 20% at $100\,\text{GeV}$.
$\Delta\Psi = 4^\circ$ was found to be the best choice by the optimization process. This corresponds to a maximal singlet rate of $1.8\,\text{mHz}$. In the case of IC40 the initially estimated event rate ($1.8\,\text{mHz}$) was smaller than the average of the measured rate ($2.17\,\text{mHz}$, see table 5.2). This deviation can be explained by detector asymmetries and seasonal variations, which were not taken into account in the initial estimate. This effect is strongest close to the horizon, where atmospheric muons dominate. In order not to exceed the maximal number of doublets, an additional cut was applied on the doublet direction selecting only doublets with a combined zenith of $\theta_{\text{Doublet}} \geq 90^\circ$. For comparison, a simple cut on the single event zenith angle at 90° reduces the rate to $1.59\,\text{mHz}$. The additional cut was introduced when the program has already been running for two month. Doublets with $\theta_{\text{Doublet}} < 90^\circ$, which had already been forwarded to ROTSE, did not enter the final analysis to ensure a homogeneous analysis.
The deviation between measured and expected doublet rate (as obtained by Eq. 5.1) was ascribed to contamination by atmospheric muons. Atmospheric neutrino Monte Carlo is used to estimate the fraction of atmospheric neutrinos in the final event sample, i.e. at Level 3.

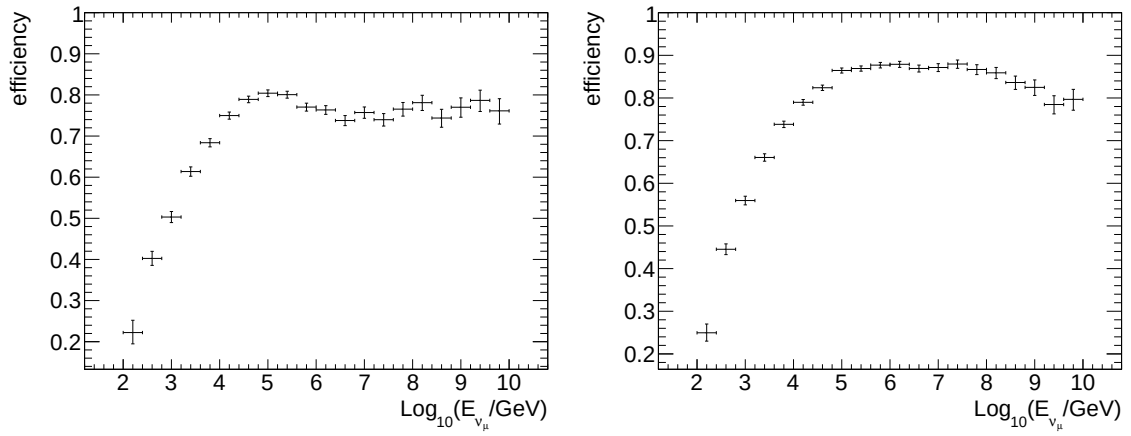

(a) IC40 (b) IC59

Figure 5.10: Filter efficiency of Level 3 relative to Level 2 as function of the neutrino energy for well-reconstructed events.

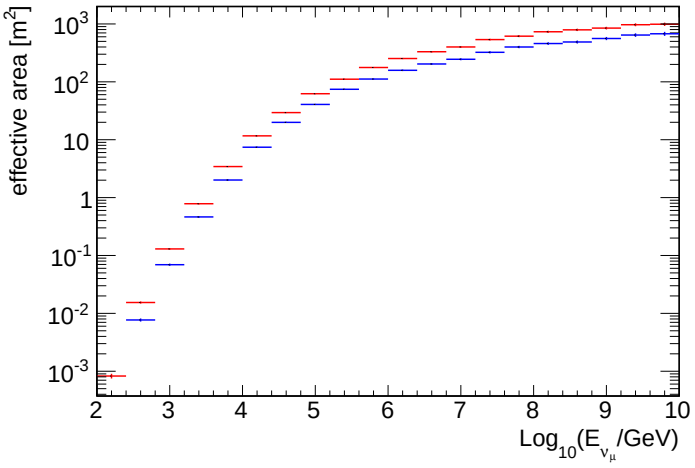

Figure 5.11: Effective area for well-reconstructed neutrino events for IC40 (blue) and IC59 (red).

The filtered data stream consists of 37% (70%) atmospheric neutrinos for IC40 (IC59), while the rest are atmospheric muons. The neutrino sample became cleaner, because the cuts are harder in order to retain a similar doublet rate. Nevertheless, the signal efficiency increased due to improved event selection and better reconstruction.
To compare the sensitivity for neutrino searches between different detector configurations, separate analyses or even different experiments, it is useful to introduce the effective area, A_{eff}. It is defined as the area of an ideal detector, which is capable of detecting neutrinos with 100% efficiency and can be obtained from simulation:

$$A_{\text{eff}}(E,\theta) = \frac{N_{\text{obs}}}{N_{\text{gen}}} \cdot A_{\text{gen}}, \tag{5.2}$$

where N_{obs} are the number of detected signal events after all cuts are applied, N_{gen} the number of generated events and A_{gen} the generation area over which the simulated events have been distributed. The effective area for well-reconstructed events at Level 3 is shown in Fig. 5.11 for IC40 and IC59. The increased detector volume yields an improved effective area in all energy bins.

The improved performance due to the increased detector volume is also reflected in the signal passing rate. The volume increase is roughly 50%, however, due to improved performance of the reconstruction algorithms applied to data of the larger detector, the signal passing rate at Level 3 increased by 52% ($\Gamma = 10$) and 68% ($\Gamma = 4$) (see table 5.2). The increase for well-reconstructed events is even better (71% for $\Gamma = 10$ and 87% for $\Gamma = 4$), showing that the selection of good reconstructed events is very efficient with the larger detector.
Furthermore, table 5.2 compares the signal expectation for two different choices of the Lorentz boost factor ($\Gamma = 4, 10$) in the model prediction. It shows that much more neutrino events are expected for SNe with a high boost factor. On the other hand a large boost factor implies a small jet opening angle ($\theta \propto 1/\Gamma$) and hence a smaller probability of the jet pointing toward Earth. While table 5.2 shows the expected number of SN neutrinos for two choices of model parameters, Fig. 5.12 displays the number of SN neutrinos for a broad selection of model parameter configurations. The figure shows that the number of expected neutrinos per SN increases with an increased jet energy and an increased Lorentz boost factor. The larger number of neutrinos per SN expected to arrive within $10\,\text{s}$ motivates the search for neutrino multiplets as described in the next section.

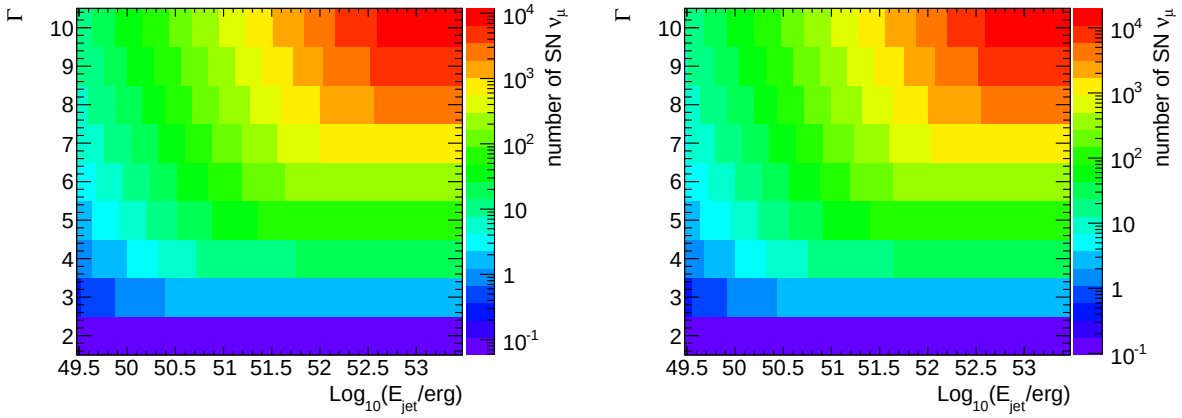

(a) IC40 (b) IC59

Figure 5.12: Expected number of SN neutrinos from a SN at distance 10 Mpc for different model parameter combinations.

5.3.4 Multiplet Filter

The selection criteria above (Level 1 to Level 3) reduce the data stream to ~1.8 mHz. A large fraction (30% in IC40 and 70% in IC59) is represented by atmospheric neutrinos, which are distributed isotropically. This background can be suppressed by requiring the detection of multiplets, consisting of at least two events, which arrive in a time window of $\Delta T \leq 100\,\mathrm{s}$ and with an angular difference between their two reconstructed directions of $\Delta\Psi \leq 4^\circ$.

$$\Delta T \leq 100\,\mathrm{s} \;\;\&\&\;\; \Delta\Psi \leq 4^\circ. \tag{5.3}$$

This requirement results in roughly 25 doublets per year from atmospheric background. The efficiency of the angular coincident cut $\Delta\Psi \leq 4^\circ$ depends on the model parameters. The average passing rates range from 56-69% (IC40) and 60-74% (IC59) depending on the choice of model parameters as displayed in Fig. 5.13. This can be explained by the fact that different model parameters imply a different energy spectrum. Moreover, the angular resolution depends on the energy spectrum, since high energy events tend to produce more photons and thus more modules are hit in the detector, which improves the reconstruction accuracy. Figure 5.14 shows an example for the energy dependence of the angular resolution. Hard spectra yield a better angular resolution.

The technical implementation of the multiplet filter is as follows: Incoming events are stored in a buffer. For each incoming event the buffer is updated and events, which have a time difference compared to the newest incoming event of more than 100 s, are deleted. Then the angular difference between the reconstructed direction of the incoming event and the direction of all events in the buffer is calculated. If one or more events from the buffer have an angular difference to the incoming event of less than 4°, a multiplet is found. To improve the accuracy of the direction forwarded to the telescopes, the multiplet direction is calculated as a weighted mean from the single reconstructed directions comprising the multiplet. The single events are weighted with $1/\sigma^2$, where σ is the reconstruction error estimated by the paraboloid fit, i.e. large weights are assigned to well-reconstructed events with a small angular error estimate σ.

$$\vec{\Psi}_{\mathrm{comb.}} = \frac{\sum_i \frac{1}{\sigma_i^2}\vec{\Psi}_i}{|\sum_i \frac{1}{\sigma_i^2}\vec{\Psi}_i|}, \text{ with } \sigma_i^2 = \frac{\sigma_{x,i}^2 + \sigma_{y,i}^2}{2}, \tag{5.4}$$

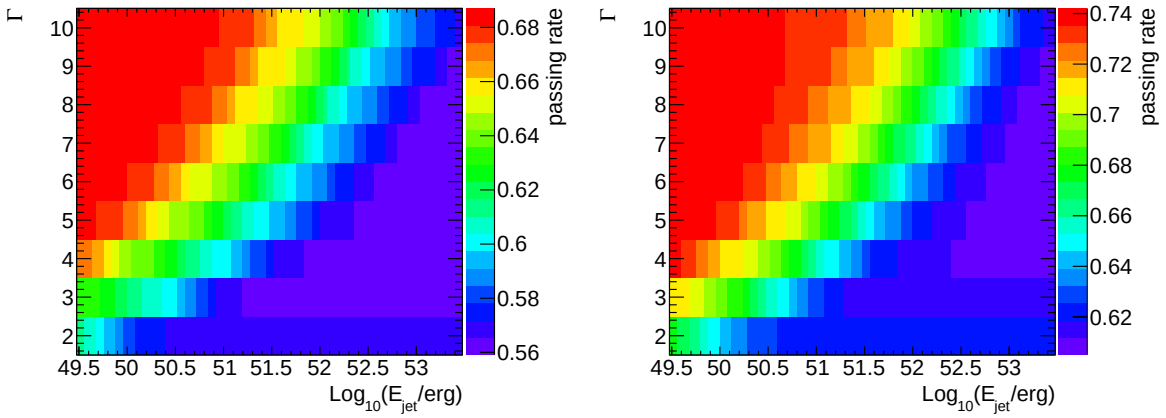

(a) IC40 (b) IC59

Figure 5.13: Signal passing rates of the angular coincidence cut ($\Delta\Psi \leq 4°$) for different Lorentz boost factor Γ and different jet energies E_{jet}. IC59 performs better since the reconstruction accuracy has improved due to the increased detector volume.

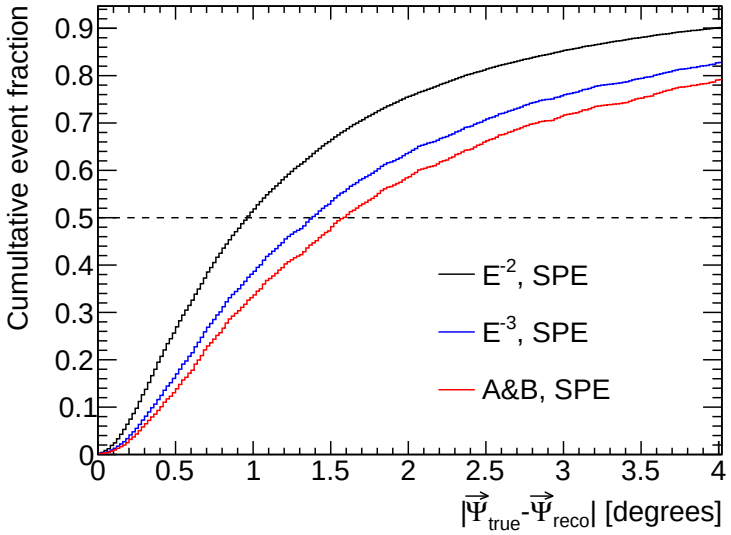

Figure 5.14: Angular difference, $|\vec{\Psi}_{\mathrm{true}} - \vec{\Psi}_{\mathrm{reco}}|$, between true and reconstructed direction for different energy spectra (IC59). Black: E^{-2}-spectrum, blue: E^{-3}-spectrum, red: Ando and Beacom SN spectrum. The horizontal black line marks the median. The angular resolution is defined as the median. Hard spectra yield a better angular resolution.

where the unit vector $\vec{\Psi}$ indicates the track direction. Compared to single events, doublets have a better resolution. The weighting improves the doublet resolution as illustrated in Fig. 5.15. The resolution is defined as the median angular difference between true and reconstructed direction, i.e. $median(|\vec{\Psi}_{\mathrm{true}} - \vec{\Psi}_{\mathrm{reco}}|)$. It improves further after applying the directional coincidence condition $\Delta\Psi \leq 4°$. The weighted mean direction is transmitted to the telescopes.

Large reconstruction uncertainties might lead to mis-pointing of the telescope and in the worst case the real source position might lie outside ROTSE's field of view (FoV) of $1.85° \times 1.85°$. Figure 5.16 shows the doublet point spread function in θ-ϕ-space compared to

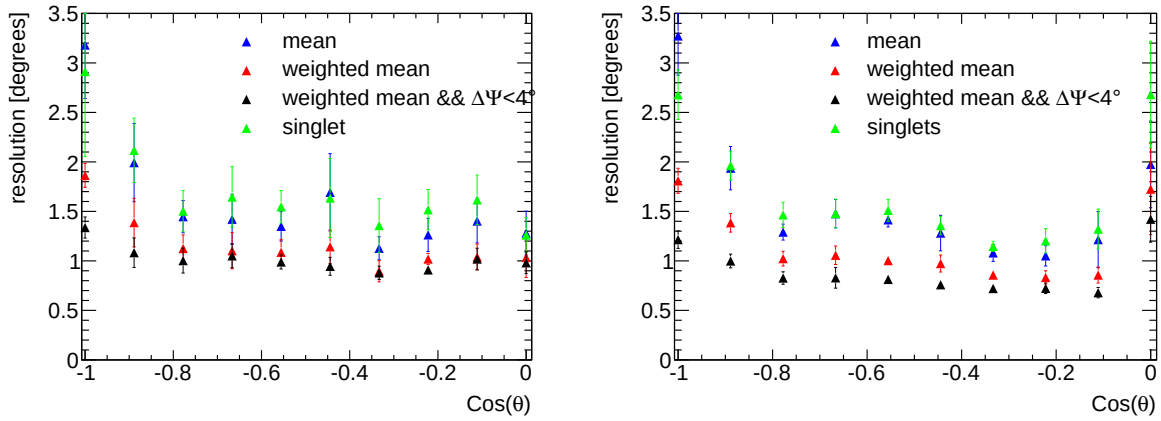

(a) IC40 (b) IC59

Figure 5.15: Doublet resolution using an ordinary mean (blue) and a weighted mean (red) compared to the singlet resolution (green) for signal neutrinos ($\Gamma = 3$, $E_{\rm jet} = 3 \times 10^{51}$ erg). Applying the directional coincidence cut $\Delta\Psi \leq 4^\circ$ (black) keeps mainly well-reconstructed doublets and yields a further improvement of the doublet resolution.

ROTSE's FoV. The zenith and azimuth projections of Fig. 5.16 displayed in Fig. 5.17 reveal the large tails of the angular resolution. Depending on the model parameters 41-53% (IC40) and 44-61% (IC59) of all doublet events (see Fig. 5.18 illustrating the passing rates for various model parameter combinations), which pass the selection cuts, lie within ROTSE's FoV. ROTSE provides a relatively good match for this search without requiring multiple pointings of the telescope (so-called tiling). Tiling would imply to point the telescope several times to cover the point spread function of IceCube. It would require significantly higher observation time and would complicate the optical data analysis.

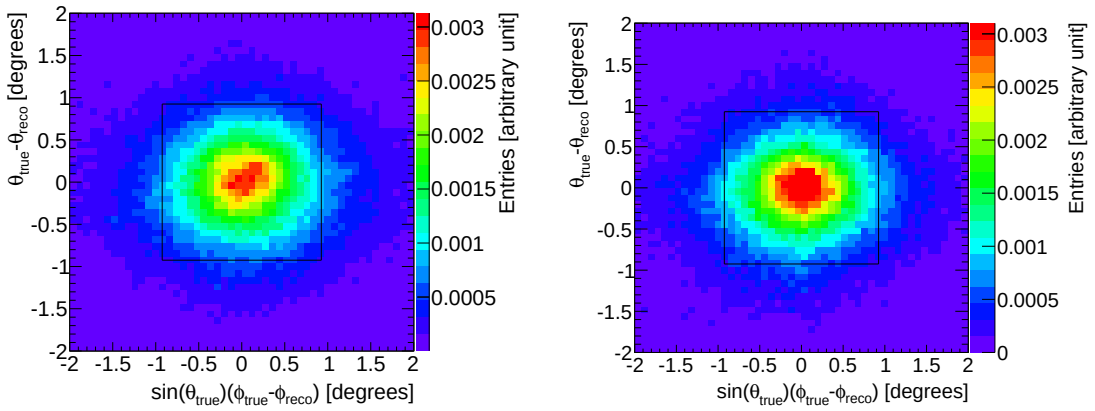

(a) IC40 (b) IC59

Figure 5.16: Deviation of the reconstructed multiplet direction from the true direction. The black box shows ROTSE's FoV of $1.85^\circ \times 1.85^\circ$.

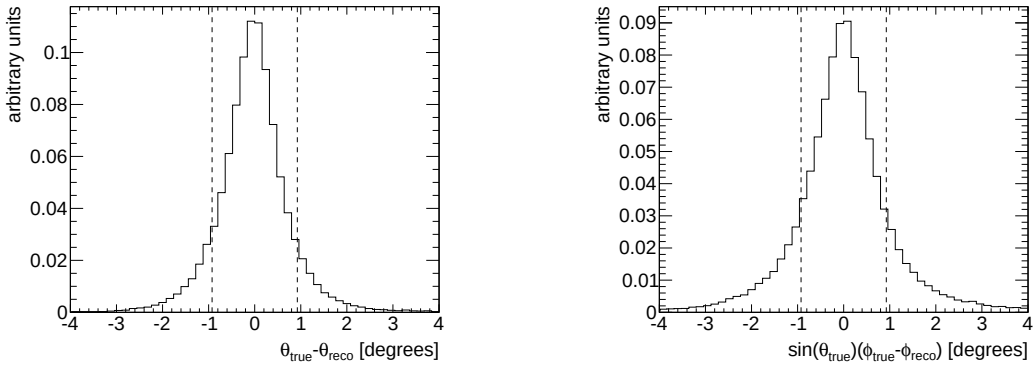

(a) zenith angle (b) azimuth angle

Figure 5.17: One dimensional deviation of the reconstructed multiplet direction from the true direction (projection of Fig. 5.16(b)). Dashed lines show ROTSE's FoV of $1.85° \times 1.85°$ (IC59).

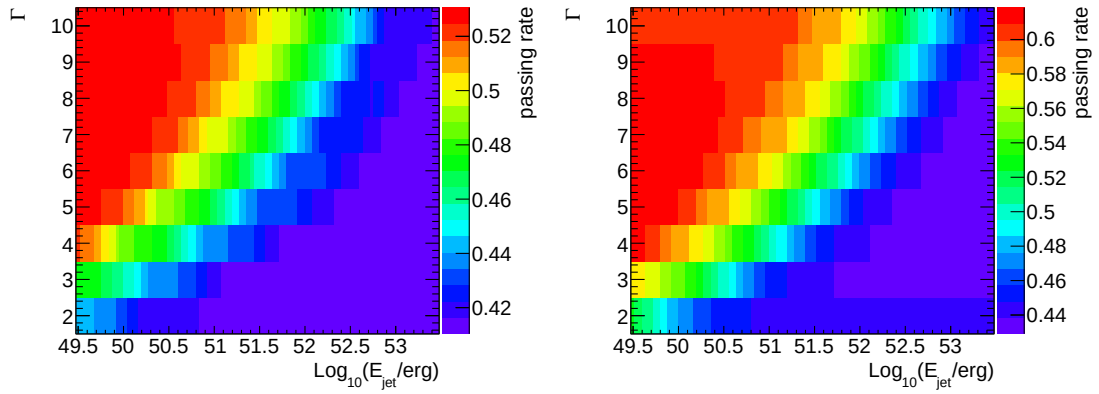

(a) IC40 (b) IC59

Figure 5.18: Fraction of doublets lying in ROTSE's FoV. IC59 performs better than IC40 since the reconstruction accuracy has improved due to the increased detector volume.

5.4 Alert Transmission

The filtering described above suppresses the background and selects the most interesting neutrino burst candidates providing accurate directional information. An expected number of 25 multiplets is produced per year. Once a multiplet is detected by IceCube, an *alert* containing the directional information needs to be transferred to the telescopes. If a multiplet is found, a text file is written to disk by the IceCube software running at the analysis client. The alert information is stored using the JSON (JavaScript Object Notation) format, which has a dictionary structure and is compatible with various programing languages. An example JSON alert is shown below:

Listing 5.1: Exampe JSON alert

```
{"vars": {"deltaPsi": 1.5164531957991041,
          "deltaT": 43.161582946777337,
          "eventIDs": [9083385, 9171800],
          "version": 6,
          "ra": 102.94827719308169,
          "dec": 4.4115299920714088,
          "eventTm": "2009-12-10T14:25:15.416181948Z",
          "runID": 114998},
 "debug": {"NTestAlerts": 0,
           "NAlerts": 1,
           "sendTm": "2009-12-10T20:07:51.Z+0000"},
 "id": 3,
 "condition": "alert"}
```

The file contains the doublet direction (right ascension (ra) and declination (dec)) obtained by calculating the weighted mean according to equation 5.4. Furthermore, the temporal difference between the first and the last event of the multiplet ΔT and the spacial difference $\Delta\Psi$ are written to the alert file. Other important variables are the event time of the first event of the multiplet, the event IDs (the length of the event ID array indicates the multiplicity), the run ID and an alert ID, which is increased for every found multiplet. A version number allows to keep track of updates of the alert file structure. Every time new variables have been added to the alert the alert version number was increased. Finally a condition flag is added, which can be set to *alert* or *test*. Alerts get forwarded to the telescopes while test alerts are only used for monitoring purposes (see Sec. 5.5).
The alert transmission is sketched in Fig. 5.19. The text files are picked up by a python script, which adds further monitoring variables to the alert file and hands it over to the IceCube Teleport System (ITS), an interface for IceCube software to the Iridium satellite system. These variables are the number of alerts and test alerts (see Sec. 5.5) written to disk but not yet transmitted and the time of transmission. ITS is contacted in an xmlrpc call. It sends the information over the network of Iridium satellites, which allow a 24 hours coverage, but at the same time have a strict bandwidth limitation of maximal 1800 bytes per transmission. Another instance of ITS receives the messages from Iridium in Madison and delivers them to a server set up at a dedicated machine at University of Wisconsin, Madison (UW). The server script saves the alert to a text file and issues a trigger to the ROTSE telescopes. A socket connection is established to the telescope computers at the four different telescope sites in order to insert the requested observation to the observation schedule. In contrast to ITS, which is fast but limited in bandwidth, the broad-band satellites which are used by SPADE (South Pole Archival and Data Exchange, see Sec. 4.6) to transfer the filtered data to the data warehouse at UW supply much more bandwidth, but are only visible from the South Pole for less than 50% of the day and therefore are not suitable for a

fast alert transmission. A back-up of all alerts is sent to UW via SPADE to be stored in the data warehouse.

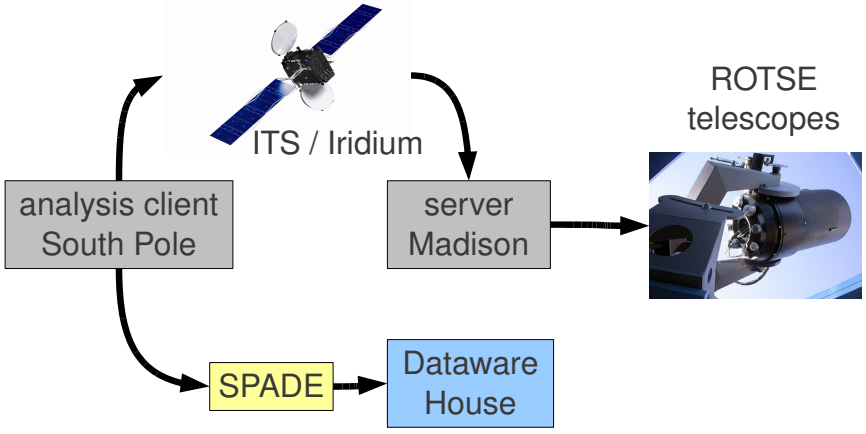

Figure 5.19: Alerts produced at the South Pole are transfered North via the Iridium satellite system using the ITS interface and SPADE (as back-up). They are delivered to a server at UW and forwarded to the ROTSE telescopes.

5.5 Monitoring

The stability of the online system is crucial on the one hand to ensure fast reaction to problems in order to minimize down time of the system and on the other hand to avoid sending triggers to the telescopes during times of unstable detector behavior (e.g. calibration runs, see also Sec. 5.5.1). Hence, the stability of the system is constantly monitored. The alert rate itself is too small (two alerts per month) to allow fast discovery of problems. Therefore, so called *test alerts* are selected, processed and transmitted by the same pipeline as the real alerts. The test alerts have to pass looser quality cuts (see table 5.3 compared to the original Level 3 cuts in table 5.1) in order to obtain a higher event rate and pass modified angular multiplicity criteria:

$$4^\circ < \Delta\Psi \leq 8^\circ \;\&\&\; \Delta T \leq 100\text{s}. \tag{5.5}$$

This ensures that no overlap between test and real alerts occurs. The definition of real and test alerts is illustrated in Fig. 5.20.

Table 5.3: Looser Event Selection Cuts for Test Alert Selection

Detector Configuration	Cuts
IC40	$\theta_{\text{llh1}} \geq 85^\circ \;\&\&\; \theta_{\text{llh2}} \geq 85^\circ \;\&\&\; \mathcal{L}/(\text{N}_{\text{Ch}} - 5) \leq 9.2 \;\&\&$ $\text{N}_{\text{DirC}} \geq 6 \;\|\|\; \text{N}_{\text{Ch}} \geq 200$
IC59	$\theta_{\text{10it}} \geq 90^\circ \;\&\&\; \mathcal{L}/(\text{N}_{\text{Ch}} - 3.5) \leq 7.8 \;\&\&$ $\text{N}_{\text{DirC}} \geq 6 \;\|\|\; \text{N}_{\text{Ch}} \geq 100$

Due to the looser quality cuts the rate of test alerts is much higher than the real alert rate and

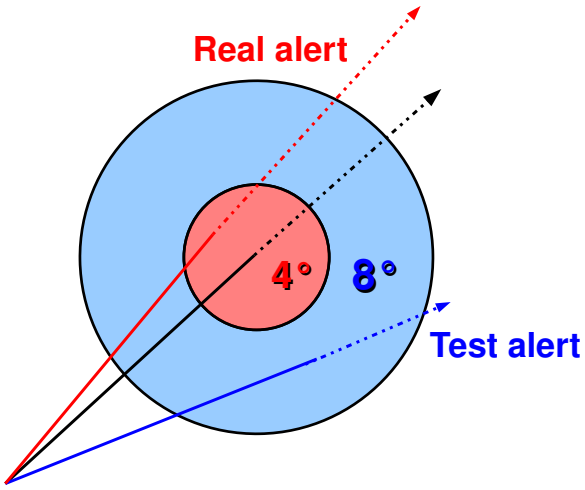

Figure 5.20: Real alerts have to fulfill $\Delta\Psi \leq 4^\circ$ while for test alerts $4^\circ < \Delta\Psi \leq 8^\circ$ is required. The temporal coincidence requirement is $\Delta T \leq 100\,\mathrm{s}$ in both cases. To build a real alert with the black event the second event has to arrive within the red area, while for a test alert the second alert may not hit the read area but must arrive within the blue area.

about 100 test alerts are expected per day. If no test alert arrives for more than two hours, an email is sent to persons in charge of checking for potential problems.
A web page[1] is created automatically at the machine at UW using the test alert information to display basic distributions. The plots displayed on the web page are automatically generated every 5 min. Two of them allow the monitoring of the rate by showing a histogram of the event rate, one on a short time scale (120 h with 8 h bin length) and the other one on a longer time scale of ninety days (with three days bin length). Potential problems would cause a variation in the event rate. For example a sudden increase in the rate could be caused by an artificial light source (e.g. flashing LED) in the detector. On the other hand a low rate hints at a detector outage or problems in the alert transmission. Examples of the two event time histograms are displayed in Fig. 5.21 and Fig. 5.22. The x-axis shows the trigger time relative to the trigger time of the latest arrived test alert. In addition, the processing time or *latency* - defined as time difference between the time when the event triggered the detector and the time when the alert was written to disk at South Pole - is shown on the web page. It is displayed as a function of the trigger time (again, relative to the latest event) for the past 140 h. Figure 5.23 shows an example for the latency plot during IC59. The average latency was ~6 h (~8 h for IC40). The peak in the latency at -60 h indicates an outages of the processing and filtering system (PnF), which can cause data backlogs. Once PnF is running again it needs some time to catch up, but no data will be lost.
Finally, the number of test alerts per run is shown on the web page. A normal physics run has a length of eight hours and contains on average ~30 test alerts. However, if the DAQ runs in test mode (e.g. during calibration runs), test data is produced, which is not read by the analysis client, because it can contain events triggered by artifical light produced by LEDs on the DOMs and hence is not save to use in physics analyses. Gaps in the test alerts per run distribution as illustrated in Fig. 5.24, which shows many empty bins, give a hint to ongoing tests at the South Pole usually resulting in many short runs taken in test data mode.

[1] http://internal.icecube.wisc.edu/rotse/ofu_monitoring/ofu-monitoring.html (IceCube internal)

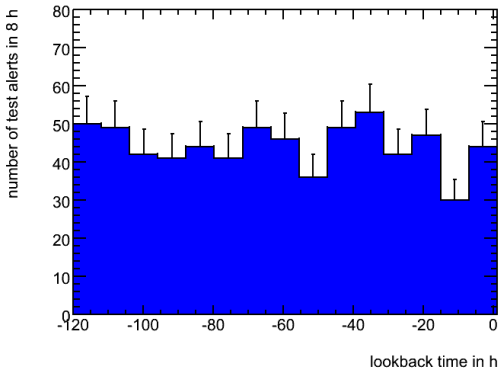

Figure 5.21: Event time histogram on short time scale: 120 h with 8 h bin length. Stable behavior of the rate on short time scales is monitored.

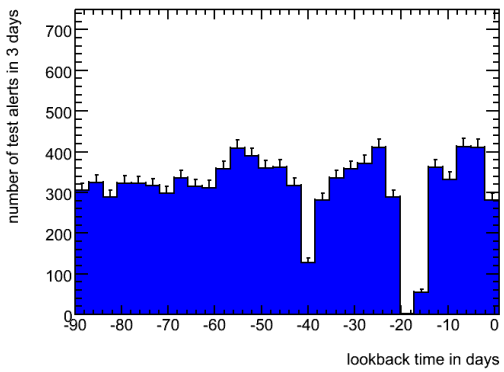

Figure 5.22: Event time histogram on long time scale: 90 days with three days bin length. The drop in the rate at -40 d was due to an ITS outage, while the second drop at -20 d is connected to a crash of the filtering system on the analysis client due to a failed connection to the database, which contains run and geometry information.

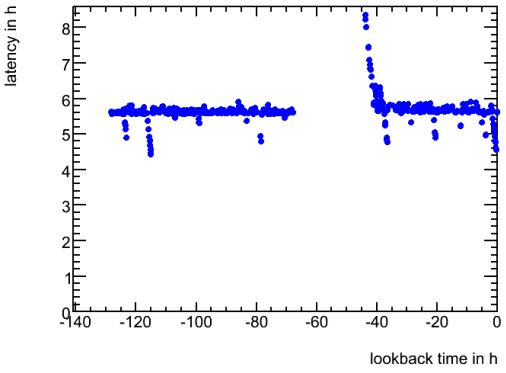

Figure 5.23: Latency: Time difference between the time when the event triggered the detector and the time when the alert was written to disk at the South Pole. The average processing time during the IC59 period was ~6 h.

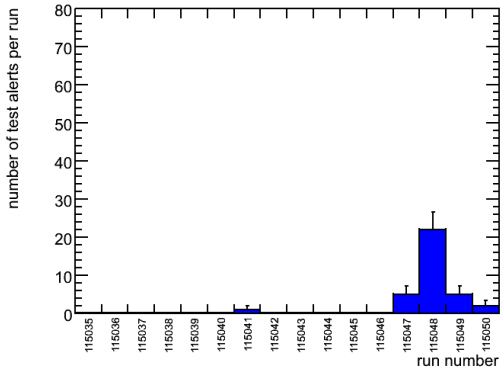

Figure 5.24: Number of test alerts per run: An average run of 8 h lenght contains ~30 test alerts, while runs taken in test data mode are not read by the analysis client. Many empty bins indicate a test period, which usually results in many short runs.

5.5.1 Problems Found by Monitoring System

While the last section described the general setup of the monitoring system and presented ways to indicate potential problems, concrete examples of discovered problems are discussed here.
The study of the test alert rate has been a reliable tool. In several cases a drop in the test alert rate was encountered. This can occur for several reasons:

- Calibration runs are performed, i.e. IceCube is not taking data in physics data mode. The test data taken during calibration runs is not read by the analysis client.
- The ITS modem is down and needs to be restarted manually by somebody at South Pole. By now the heartbeat of ITS is constantly monitored and an alert is issued to the IceCube winter-overs, but in the beginning of the optical follow-up program no such monitoring was available. Here the test alert rate helped to ensure a quick restart of the ITS modem.
- The processing script running at the analysis client encountered a problem, e.g. a failed connection to the database, which contains run and geometry information.
- The python script responsible for transmitting alerts to ITS encountered a problem, e.g. after a power outage.

It is crucial to find these problems fast in order to ensure a high uptime of the online system. However, a sudden large increase in the test alert rate indicates even more critical problems. During one year of operation three such cases were encountered, all caused by light in the detector.
In the first two cases calibration runs (so-called flasher runs) were started at pole. During a calibration run LEDs, which are attached to each DOM (see Sec. 4.3.1), are flashed on certain DOMs and the light received by the neighboring DOMs is evaluated. Many events are registered due to the bright artificial light source active in the detector, resulting in a large number of alerts and test alerts.
Usually, flashers are only operated during dedicated test data runs and an LID (light in the detector) flag needs to be set. To avoid reading flasher data two filters were implemented checking for the data taking mode (*test* or *physics*) and requiring the LID flag to be set to *dark*. However, it was possible for an operator to start flasher runs even if the LID flag was not set and the detector was running in physics data mode. Flashers were accidentally activated twice during physics data taking and with the LID flag set to status *dark*. To prevent this kind of unavoidable human failures, the calibration software was adjusted in order to prohibit the start of flashers without the LID flag being set to status *bright*.
However, a third incident occurred when the standard candle (see Sec.4.5), a single very bright laser light source used for energy calibration, was switched on by accident during a software crash. The standard candle and its operating software is an independent component not included in the flasher calibration system.
In each case the event rate increased rapidly causing an increase in the event rate (see Fig. 5.25). To avoid sending such fake alerts to the telescopes we implemented a lock to the forwarding of alerts. An alert is not sent automatically to the telescopes if the previous alert was received less than $24\,\mathrm{h}$ ago. Instead a notification is sent by email. The alert can still be manually forwarded to the telescopes, if no problem indicating an instability of the detector was found. This ensures that, in the worst case, only one fake alert is send to the telescopes. If an observation triggered by a false alert has already started it can be canceled manually.

After the standard candle incident, an additional check was implemented: The number of alert and test alert files produced at South Pole is checked before notifying the telescopes. If the standard candle or a flasher are active one expects to receive hundreds of alerts and test alerts within seconds. A very strong astrophysical source could produce many alerts, but would not produce a lot of test alerts at the same time. However, the flasher or standard candle events show cascade like signatures and cause alerts and test alerts at the same time. Hence it is required:

$$!(\mathrm{N_{alert}} > 10 \;\&\&\; \mathrm{N_{test}} > 20), \tag{5.6}$$

where $\mathrm{N_{alert}}$ is the number of alerts and $\mathrm{N_{test}}$ the number of test alerts produced at Pole at the time of transmission. The number of alerts could increase in case of a very strong signal, but a simultaneous increase of both numbers at the same time indicates a problem.
After the implementation of all stability filters and checks mentioned above, no further problems occurred.

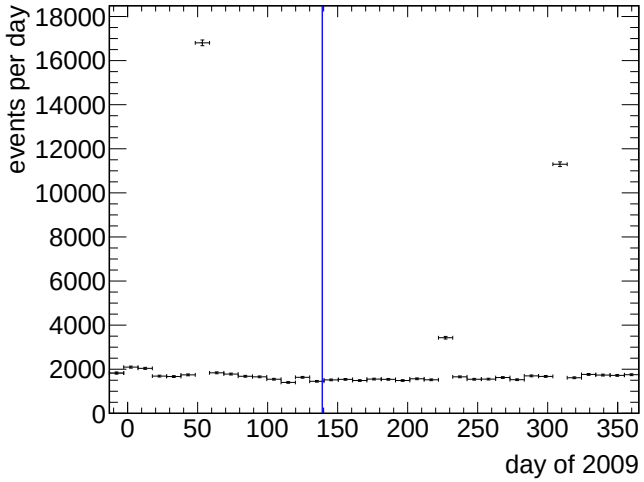

Figure 5.25: Event rate at Level 3 as a function of time. During the first year of data taking (December 16, 2008 to December 31, 2009) the rate shows three distinct peaks. The first two peaks are caused by incorrectly flagged flasher runs, while the last peak is due to an accidental standard candle run. The vertical blue line marks the transition from IC40 to IC59.

5.6 Lifetime

The monitoring system presented above is responsible for fast identification of possible problems in order to have them fixed rapidly to ensure a high up-time. A good knowledge of the final lifetime of the final data set becomes important to estimate the number of expected signal events, which enters the limit calculation (see Sec. 9.2).
First, the lifetime of the data acquisition and the processing and filtering system is estimated. For the final analysis only runs from the good run list [145] are considered. The good run list is maintained by the verification group and the run coordinator. Bad runs such as calibration runs or short runs (duration smaller than 5 min) are removed from the list. The sum over all good run durations yields the lifetime of data taken at South Pole: 130.8 d for IC40 and 206.31 d for IC59, i.e. a total of 337.1 d.
Second, the downtime of the online system needs to be considered, including the alert transmission. Sometimes the alert transmission fails, e.g. if the ITS modem is down, and alerts

can be lost. Here the test alerts serve as a useful tool again. Test alerts are produced at a rate of ~100 per day and are transferred to UW with the same pipeline as the real alerts. To check how many test alerts are lost the entire data set is processed again offline. By now all filtered data has been transferred to the data warehouse. The same selection criteria are applied in the offline processing as in the online processing at the South Pole. If the online system was operating without any failure the same number of test alerts are expected from the offline processing as have been received online via ITS. The test alerts are referred to as *offline test alerts* and *online test alerts* respectively. However, the online system, especially ITS, does not have an uptime of 100%. Comparing the number of online and offline test alerts gives a good estimate of the downtime of the online system. Figure 5.26 shows the number of online and offline test alerts as a function of time during the period of this analysis. Obviously a few test alerts get lost in the online processing and transmission. This can be explained by ITS outages or incorrect order of the read in input files. Although the additional delay has been added to recover the temporal order of the files (see Sec. 4.6), in a few cases the delay of 4 h is not sufficient and some data is lost. The fraction of lost test alerts is displayed in Fig. 5.27. In total a fraction of 6.8% of all test alerts are lost. Combining this with the good runs lifetime of 337.1 d yields a total lifetime of 314.2 d.

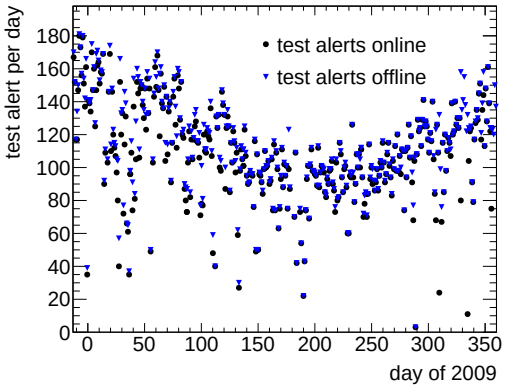

Figure 5.26: Online test alerts (black) compared to offline produced alerts (blue). Some test alerts get lost in the online analysis pipeline.

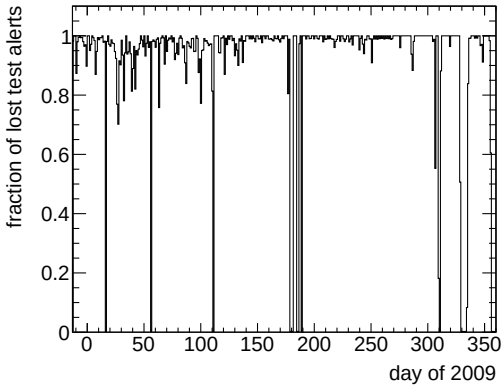

Figure 5.27: Fraction of test alerts, which get lost in the online analysis pipeline. The fraction of lost test alerts is an estimate for the downtime of the online system.

5.7 Stability of the Rate

Another check for long term stability is conducted by inspection of the long term rate over the time period of this analysis. The rate is inspected at different filter levels. Fig. 5.28 shows the rate at filter Level 2. There is a step in the rate at the transition from IC40 to IC59 marked by a blue line. The increase in rate can be explained by the increased detector volume an the modified filter logic.
The Level 2 rate is used to create a *mask*, which corrects for deadtime. Therefore, a very fine binning of 10 s bins has been selected. The corresponding mask histogram bin is set to 0 or 1 if the number of entries in the 10 s bin is smaller or larger than 10 respectively (~30 entries are expected at a rate of ~3 Hz). The original rate histogram can now be divided by the mask histogram (rebinned to match the number of bins in the rate histogram). The deadtime corrected rate histogram is displayed in Fig. 5.29, which is very smooth compared

to the not corrected histogram in Fig. 5.28. Features in the temporal behavior of the rate are now easier to identify. For example, seasonal variations cause a sinus-shaped variation of the rate with a minimum in summer and a maximum in winter. The variations in the rate arise from temperature variations, which cause density variations in the atmosphere. Due to a reduced atmosphere density in the antarctic summer a larger fraction of cosmic ray pions and kaons decay to muons (instead of losing all their energy in the atmosphere before decaying) and reach the detector. Therefore, the atmospheric muon rate is enhanced during the antarctic summer [146]. Variations on smaller time scales are due to short term weather changes.

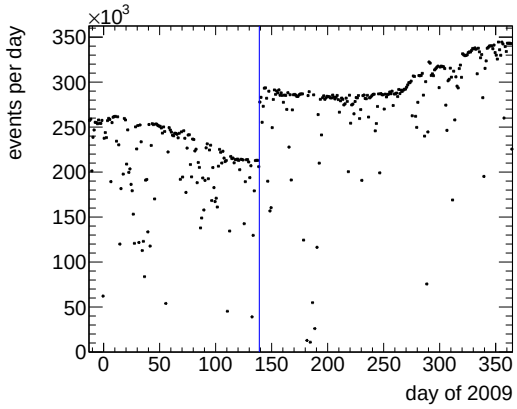

Figure 5.28: Rate at Level 2.

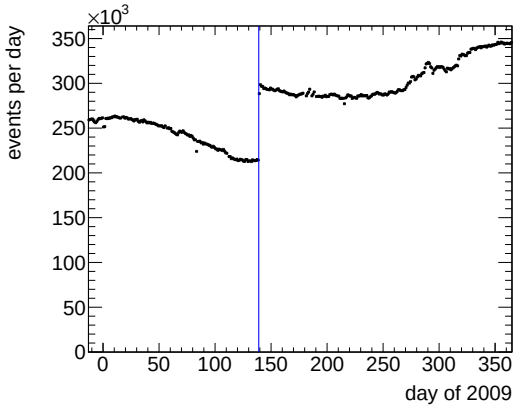

Figure 5.29: Rate at Level 2 corrected with mask.

The same mask created from the Level 2 rate is used to correct the Level 3 rate. Compared to the uncorrected histogram the corrected histogram is smooth as illustrated in Fig. 5.30 and Fig. 5.31. The Level 3 rate shows less seasonal variations compared to the Level 2 rate, because it contains a smaller fraction of atmospheric muons. Atmospheric neutrinos are less effected by seasonal variations since they arrive from random directions in the northern hemisphere washing out seasonal effects, while the atmospheric muons entering the detector originate in a small solid angle directly above the detector.
No significant deviation from a smooth distribution has been discovered.

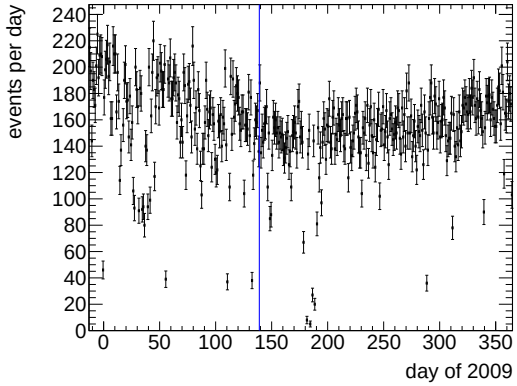

Figure 5.30: Rate at Level 3.

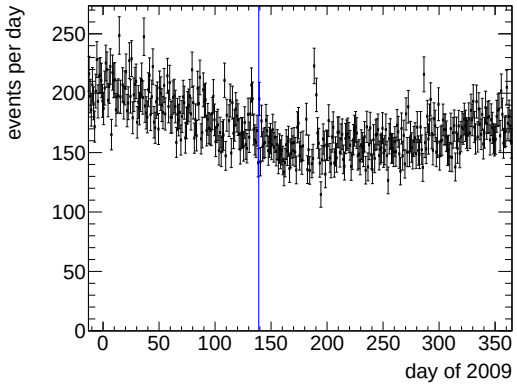

Figure 5.31: Rate at Level 3 corrected with mask.

5.8 Background Estimation

The number of expected background multiplets is very important to compute the significance of the measurement or to compute a final limit. In order to estimate the expected number of background multiplets, experimental events from the two data sets (IC40 and IC59) are used to estimate the multiplet background expectation in a process called *scrambling*. The process is described in the following, it is illustrated in Fig. 5.32.
Because of different detector geometry and different selection criteria in IC40 and IC59 the data sets are scrambled separately. To correctly incorporate detector asymmetries, seasonal variations and up-time gaps the entire dataset is used and the event directions are exchanged randomly by keeping the event times fixed. After the exchange of directions, one counts the number of multiplets. The process is repeated many times to obtain the background expectations. To take into account detector asymmetries the event directions are compared in detector coordinates instead of using celestial coordinates, which wash out detector asymmetries after scrambling. This is justified because the angular difference of two events within $100\,\mathrm{s}$ calculated in detector or celestial coordinates is very small, since the rotation of the Earth can be neglected at such a short time scale. As the Earth rotates $0.42°$ in $100\,\mathrm{s}$, the effect is small compared to the required angular coincidence of $\Delta\Psi \leq 4°$.

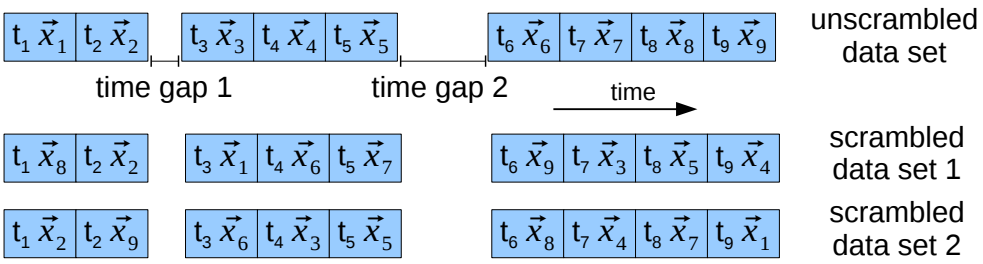

Figure 5.32: Illustration of scrambling procedure: Event directions are exchanged randomly by keeping the event times fixed. This incorporates detector asymmetries, seasonal variations and up-time correctly. The entire IC40 and IC59 datasets are used.

Both data sets, IC40 and IC59, were scrambled 10^6 times. For each scrambled data set the number of doublets and triplets is obtained, the corresponding errors are small due to the large number of scramblings. The distribution of the number of doublets is displayed in Fig. 5.33. The arithmetic mean over all scrambled data sets is calculated to determine the expected numbers of doublets and triplets for each dataset, which are summarized in table 5.4. A detailed discussion on the effect of seasonal variations to the scrambling results is presented in the next section.

Table 5.4: Lifetime and Expected Number of Multiplets Obtained from Scrambling.

Detector configuration	Lifetime	Doublets	Triplets
IC40	121.9 d	8.546 ± 0.009	$2.803 \times 10^{-3} \pm 0.003 \times 10^{-3}$
IC59	192.3 d	15.660 ± 0.012	$3.948 \times 10^{-3} \pm 0.003 \times 10^{-3}$

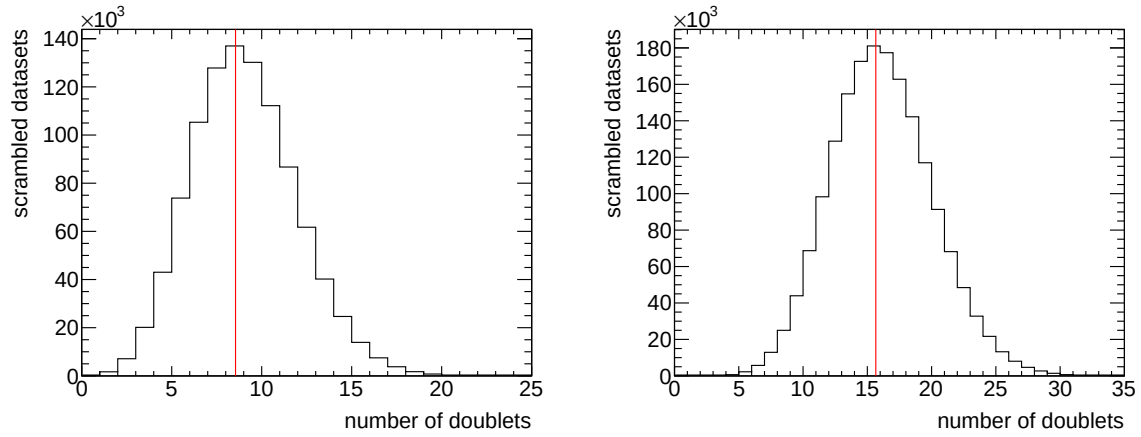

(a) IC40 (b) IC59

Figure 5.33: Number of doublets from scrambling with mean (red line).

5.8.1 Seasonal Variations in Background Estimation

Seasonal temperature variations cause a variation in the event rate detected by IceCube. Mainly down-going muons are affected. Since the final data sample, Level 3, is still contaminated by mis-reconstructed down-going muons, seasonal variations are expected to occur. It is therefore crucial to include this effect in the background estimation. The scrambling method takes into account the absolute change in the event rate over time, because event times stay fixed while only event directions get randomized. A secondary effect not considered in the scrambling is a possible θ dependence of seasonal variations. It is shown here, that this secondary effect is negligible. Figures 5.34(a) and 5.34(b) show the singlet event rate as a function of $\cos(\theta)$ for the IC40 and IC59 period respectively. Winter, summer and total rate is displayed in blue, red and green. All histograms are normalized to an area of one. The normalized histograms are squared (see Fig. 5.35(a) and Fig. 5.35(b)) since the doublet rate is proportional to the square of the singlet rate. The cumulative distribution (see Fig. 5.36(a) and Fig. 5.36(b)) of the square of the normalized singlet distribution gives an estimate on the influence of the θ dependent seasonal variation to the background estimation. No offset between the summer and winter distribution is visible in the last bin, zooming in reveals a tiny offset of 0.2%. Hence, the effect can be neglected.

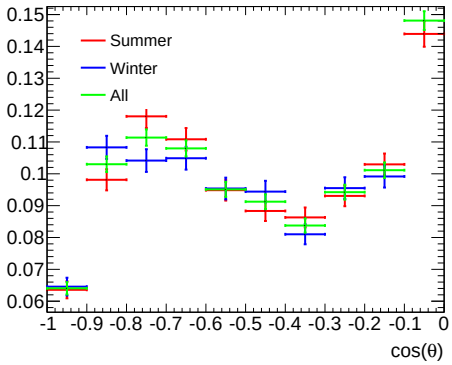

(a) IC40

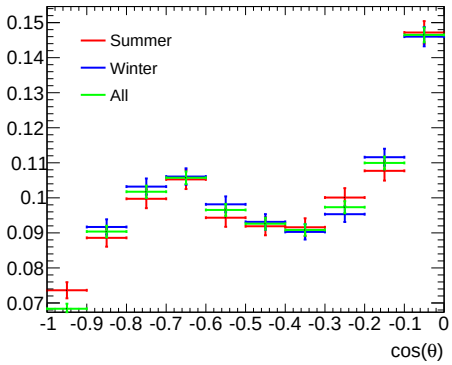

(b) IC59

Figure 5.34: Singlet rate as a function of $\cos(\theta)$ normalized to an area of one. Blue: winter, red: summer.

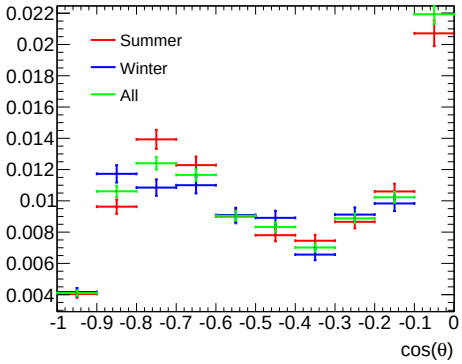

(a) IC40

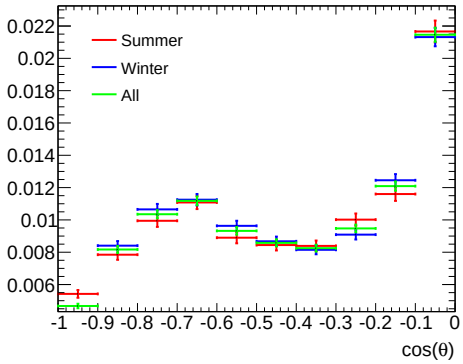

(b) IC59

Figure 5.35: Squared singlet rate as a function of $\cos(\theta)$. Blue: winter, red: summer, green: all.

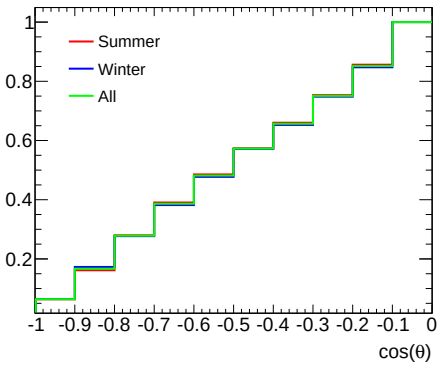

(a) IC40

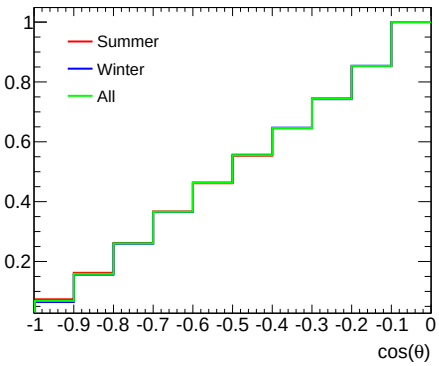

(b) IC59

Figure 5.36: Cumulative squared singlet rate as a function of $\cos(\theta)$. Blue: winter, red: summer, green: all. The offset between the summer and winter distribution in the last bin shows the influence of seasonal variations in the background estimation by scrambling. Zooming in reveals a small offset of 0.2%. Hence, the effect is negligible.

Chapter 6

The ROTSE Telescopes

In order to perform an optical follow-up of IceCube neutrino multiplets, which have an angular resolution of ~1°, wide field telescopes are needed. Furthermore, a fast response is required to catch the rapidly decaying optical GRB afterglow and to provide early data points of a SN light curve. An excellent match for those requirements is the *Robotic Optical Transient Search Experiment* (ROTSE) consisting of four identical telescopes located in Australia, USA, Namibia and Turkey. Since this is the third generation of ROTSE the four telescopes are called 3a (Australia), 3b (USA), 3c (Namibia) and 3d (Turkey). Table 6.1 shows the coordinates of each telescope. The telescopes stand out because of their large field of view (FoV) of $1.85^\circ \times 1.85^\circ$ and a rapid response of typically $4\,\mathrm{s}$ to slew the telescope from the standby position to any desired position. In the following, a brief overview of the telescope set-up (see also [147] for a details) is given followed by a detailed description of the image processing used in this analysis (see Chap. 7).
Each telescope is installed within a steal enclosure (see Fig. 6.1), which is closed automatically in case of bad weather (rain or heavy wind). Figure 6.2 shows the Cassegrain configuration of the optics. The telescopes have a parabolic primary mirror with a diameter of 45 cm. A flat secondary mirror before the focal point (Cassegrain configuration) allows a compact design of the optical system. A refracting corrector consisting of four glass lenses achieves aberration control and color correction. To be sensitive also to weak sources, no bandwidth filter is used. Peak sensitivity is reached in the R-band (600-700 nm). The wide field of view is imaged onto a back-illuminated thinned CCD with 2048×2048 pixels with a pixel size of $13.5\,\mu$m. Backside illumination implies that light enters the chip from the rear, i.e. after passing the lenses it directly hits the sensor and does not have to pass the wiring first, where photons could be absorbed or reflected. Thinning is a process, which reduces the amount of silicon yielding an increased efficiency for blue photons, which would be absorbed in thick layers of silicon before they reach the depletion region [148].
The camera has a fast readout cycle of $6\,\mathrm{s}$ and is cooled to $-40°$C to reduce thermal noise.

Table 6.1: Locations of the four ROTSE telescopes.

Telescope	Location	Longitude	Latitude	Altitude [m]
3a	Coonabarabran, Australia	$-149^\circ\ 03'\ 40.3''$ E	$-31^\circ\ 16'\ 24.1''$ S	1149
3b	Fort Davis, Texas, USA	$104^\circ\ 01'\ 20.1''$ W	$30^\circ\ 40'\ 17.7''$ N	2075
3c	Mt. Gamsberg, Namibia	$-16^\circ\ 30'\ 00''$ E	$-23^\circ\ 16'\ 18''$ S	1800
3d	Bakirlitepe, Turkey	$-30^\circ\ 20'\ 00'$ E	$36^\circ\ 49'\ 30'$ N	2550

Figure 6.1: Photograph of the ROTSE enclosure in Australia. Top right: Photograph of the ROTSE telescope.

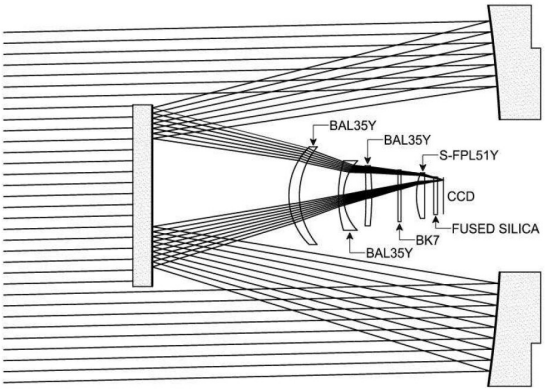

Figure 6.2: Illustration of ROTSE's optics arranged in Cassegrain configuration with a parabolic primary mirror and a flat secondary mirror before the focal point [147].

For a $60\,\mathrm{s}$ exposure under optimal conditions the limiting magnitude is around $m_R \approx 18.5$, which is well suited for a study of GRB afterglows during the first hour or more (see e.g. Fig. 2.13) and SN light curves with peak magnitude ≤ 16. The corresponding *FWHM* (Full Width at Half Maximum) of the point spread function in stellar images is ~2.5 pixel (8.1 arcseconds). The telescopes are operated robotically and managed by a fully-automated system of interacting daemons within a Linux environment. Observations are scheduled in a queue and are processed in the order of their assigned priority. A scoring algorithm decides which schedule item should be carried out next. The four primary types of schedule items are listed below in decreasing priority:

1. **Prompt burst observations**: GRB alerts received by the GRB coordinate network (GCN)[1] are automatically put in front of the queue and are processed immediately if the weather is dry, the sun is down and the burst is above the horizon. If any of these conditions is not met, the schedule item remains at front of the queue until it can be imaged or its lifetime of $3\,\mathrm{days}$ expires.

2. **IceCube prompt follow-up**: If an IceCube alert is received, the telescopes start immediately to record 30 consecutive $60\,\mathrm{s}$ exposures, if no GRB alert is in the queue and the coordinates are above the horizon, the sun is down and the weather is dry.

3. **Late burst follow-up observations**: At later times after the GCN burst alert was received, the location is repeatedly imaged with increasing exposure time, because the afterglow is expected to fade.

4. **IceCube late follow-up**: Every night continuing for two weeks after the IceCube alert arrived 8 consecutive $60\,\mathrm{s}$ exposures are recorded. This was extended on October 27, 2009 to daily observations for 12 nights and then observations during every second night up to day 24 after the trigger was received.

5. **Target Observations**: Specific fields can be named as targets.

6. **Sky Patrol** (default mode of operation): Regularly spaced fields of the sky are observed in two consecutive $60\,\mathrm{s}$ exposures.

[1] A system which distributes locations of GRBs and other transients detected by spacecrafts in real-time and in addition reports on ground or space-based follow-up observations.

Exposures are made according to the observation schedule. Multiple exposures are taken by adding a random offset of up to 10 pixels to the position of each image. This so called jiggling mode reduces the number of false detections due to hot pixels, i.e. individual pixels with a high dark current. Images are stored in the fits-format [149], which is commonly used among astronomers. Each file consists of an `ASCII` image header and one or several binary extensions.
As discussed above, IceCube alerts are placed below the GCN alerts in the priority queue and above every other observation. The late follow-up of the IceCube alerts is placed behind the late burst follow-ups. IceCube triggers are sent to the telescope computer via a TCP-socket connection from the same IceCube machine in Madison, which receives alerts from South Pole via the IceCube teleport system, ITS. Sometimes the connection is refused and the alert cannot be transmitted due to network or technical problems at the telescope site. However, we have the option to resend the alert by hand once the telescope is back online. A real time operation web page[2] operated by the ROTSE collaboration allows us to check the current status of each individual telescope. It also provides local weather information. Figure 6.3 is taken from this web page and shows the four ROTSE telescopes as a colored dot at their location on a world map. Green indicates that the telescope is currently active and taking data. Yellow indicates an active telescope which is not taking data, usually because the sun is up or the weather is bad. Red means the telescope is offline and cannot receive any alerts. Detailed information about the telescopes' components and operation can be found in the ROTSE manual [150].
The processing of the optical data in order to find an optical counterpart of the neutrino detection is presented in the next chapter.

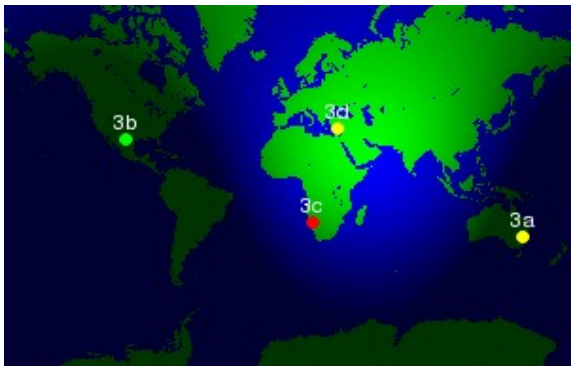

Figure 6.3: ROTSE telescopes: Green: active and taking data. Yellow: active but currently not taking data due to bad weather or day light. Red: offline, no alerts can be received.

[2] http://www.rotse.net/operation/

Chapter 7

Optical Image Analysis

The data collected by the ROTSE telescopes following an IceCube trigger are analyzed in order to find an optical counterpart of the neutrino detection. In contrast to a SN light curve, which rises slowly and reaches its maximum after ~20 days, the GRB afterglow decays rapidly and falls below the detection threshold of ROTSE within hours. However, the IceCube data used for this analysis were taken with a delay of 6-8 h, which makes the detection of an optical GRB afterglow unfeasible. Hence, this work focuses on the detection of an optical supernova counterpart.
The image processing consists of several steps as illustrated in Fig. 7.1:

- Correction and calibration
- Source extraction
- Co-adding
- Image subtraction
- Candidate identification

Each step is described in the following. The entire image processing software is written in `IDL` (interactive data language).
In the following the image, which is searched for a transient object will be referred to as the *new image*.

7.1 Correction and Calibration

Image correction and calibration is done at the telescope site. Each image is dark and flat field corrected and subtracted by a fringe map as described below. The calibrated and corrected images contain the number of counts for each pixel after dark image and fringe map subtraction and flat field division.

7.1.1 Dark Fields

A dark image is a measure of the dark current in the CCD at a specific temperature for a specific exposure length. It is taken for a configured exposure lengths (60 s) while the shutter is closed. The dark image is subtracted pixel by pixel from the new images to remove the bias level, as well as the dark level and to subtract hot pixels. The bias level is a low level electrical signal fed to each pixel to "bias" the semiconductor in order to prevent negative

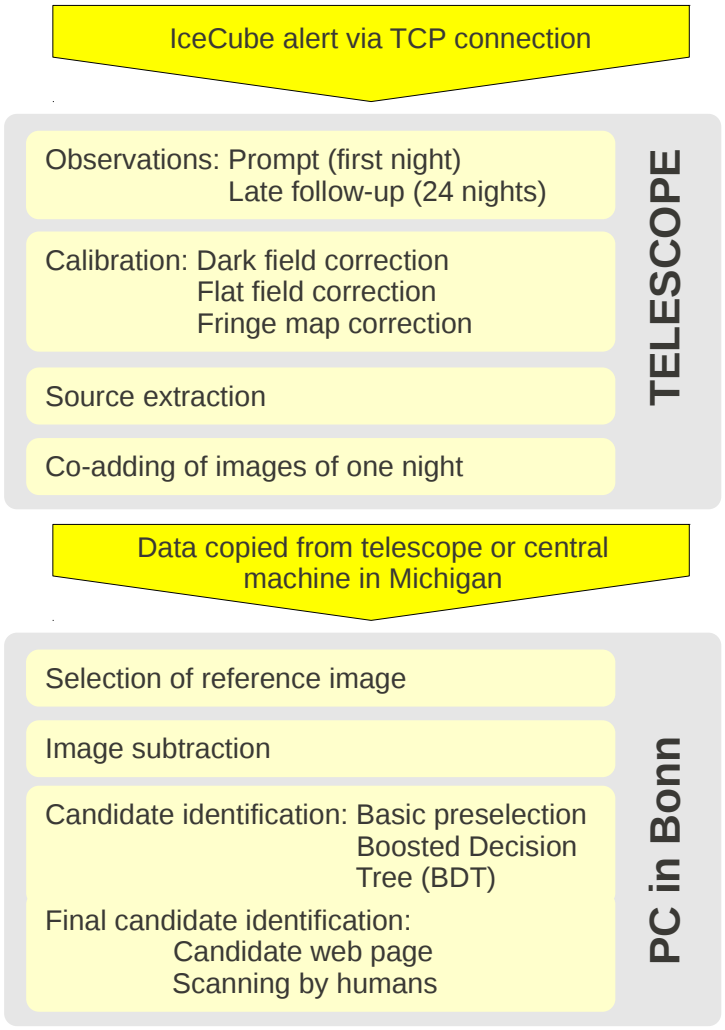

Figure 7.1: Image processing pipeline.

ADC signals, while the dark current is caused by thermal electrons. Usually, one dark run per night is performed. A dark field example taken by ROTSE 3b is displayed in Fig. 7.2.

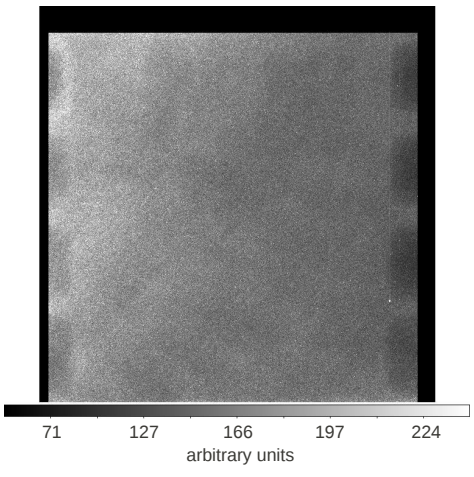

Figure 7.2: Dark field taken by ROTSE 3b.

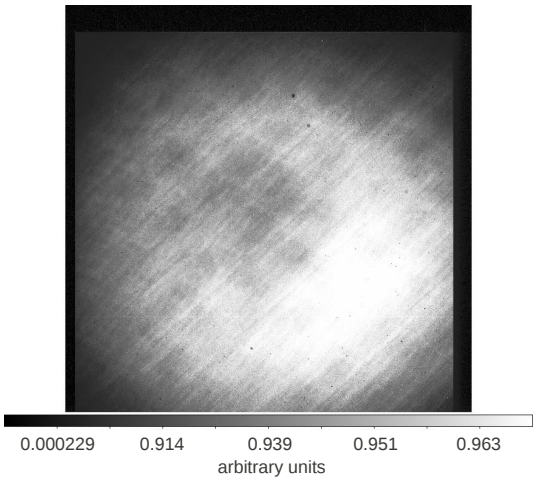

Figure 7.3: Twilight flat taken by ROTSE 3b.

7.1.2 Flat Fields

The pixel responsivity is not uniform for all pixels of the CCD. To determine the responsivity for every pixel, the CCD is exposed to an object of uniform intensity. Such an exposure is called flat field. ROTSE records flat fields during twilight at high elevation away from the setting sun. At this time the sky is uniformly illumated with the expection of a few bright stars. The median of several images (at least 30) is taken to remove the stars. A field is imaged several times with more than 5 min between the single exposures to allow the stars to drift and prevent them from being imaged with the same pixel from image to image. New images are divided by the flat field image to correct for non uniform pixel responsivity. A twilight flat field taken by ROTSE 3b is shown in Fig. 7.3. It shows that the center of the CCD is more sensitive than the edges.

7.1.3 Fringe Maps

Fringing is an interference between the incident light and the light internally reflected at the interfaces between the thin layers of the CCD chip. The fringe pattern is stable, although the amplitude varies. The scale of the fringe pattern is wavelength dependent (like the rainbow on an oil slick), it further depends on the sky brightness, lunar illumination, and cloud coverage. A fringe map is created by subtracting a twilight flat, which does not display a fringe pattern, from a sky flat, which does show fringing. Sky flats are generated from the whole night of exposures. If the telescope points at a large number of random directions during the night, each pixel will record empty sky most of the time and only sometimes points at an object. The median of all images yields the response to the actual sky background. Most of the night sky brightness is contained in emission lines. Some of these lines create a strong fringe pattern. In contrast, light from the sun, which dominates the twilight flat, is broadband and hence does not cause fringing.
To correct an image for fringing, the fringe pattern is scaled and is then subtracted from the image. First, the image is flat field corrected. To obtain the scaling factor, contamination from star light needs to be removed, since the fringe pattern is contained in the background sky. Therefore, all pixels which deviate more than 3σ from the mean, are excluded from the scaling process, since they likely contain star light. The remaining pixels are fit via linear regression with the corresponding pixels in the fringe pattern. A linear correlation between pixel values and fringe map values is expected:

$$p_i = s \cdot f_i + C, \tag{7.1}$$

where p_i is the image pixel value and f_i the corresponding pixel value of the fringe map. The slope s is obtained in a fit and represents the fringe scaling factor. If the fit is poor (reduced $\chi^2 > 3$), due to scattered moonlight or clouds in the image, the fringe pattern is not subtracted. In the worst case the fringe pattern can introduce photometric errors of up to 5% and can produce occasional false detections of faint objects. A fringe map used to correct ROTSE 3b images is shown in Fig. 7.4.

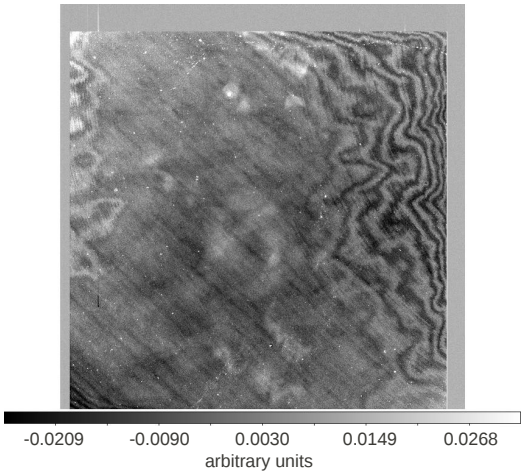

Figure 7.4: Fringe map used to correct ROTSE 3b images.

7.2 Source Extraction

Once the image is corrected and calibrated as described above, the software `SExtractor` (source extractor) [151] extracts objects from the image. First it determines the background and selects pixels above a certain threshold (1σ above the background level in the ROTSE image processing). Pixel clusters are identified and define the found objects. Properties of each object are calculated and written to a fits file.

7.2.1 Background Estimation

An area of $N_{\mathrm{bg}} \times N_{\mathrm{bg}}$ pixels is defined in which the mean and the standard deviation σ are calculated. The pixel which deviates most is removed and mean and σ are computed again. This procedure is repeated until all remaining pixel values deviate less than 3σ from the mean. The mean after removal of the deviating pixels defines the background of the field. The size of the background field has to be larger than the average point spread function. It is set to 32×32 pixels for the ROTSE image processing. The background is smoothed over $N_{\mathrm{smooth}} \times N_{\mathrm{smooth}}$ background fields ($N_{\mathrm{smooth}} = 3$ for ROTSE) by applying a median filter[1] and a spline interpolation over all smoothed background fields of the image defines the background map.

7.2.2 Object Detection

First the image, i.e. the pixel values, are smoothed according to a filter. Here, a Gaussian filter is applied with a FWHM of 2 pixels to 3×3 pixels fields. Each pixel in the smoothed image above a threshold T is considered in the object detection. The threshold is defined as a multiple of the background mean as obtained from the background map (1σ for ROTSE images). If the number of adjacent pixels above the threshold is larger than a minimal value A_{min}, an object is found ($A_{\mathrm{min}} = 5$ pixels for ROTSE images). `SExtractor` decides if the cluster of pixels represents one or several objects close to each other. This process is called *deblending*. The threshold is lowered from the maximal pixel value in 32 exponential steps. Each time the cluster identification is repeated. If more than one cluster is found, they are

[1] The median filter replaces neighboring entries with their median.

considered as two objects if the number of counts in both clusters is greater than a fraction δ_c of the total counts of the initial cluster ($\delta_c = 0.0001$ for ROTSE). A simplified example of the deblending process is illustrated in Fig. 7.5.

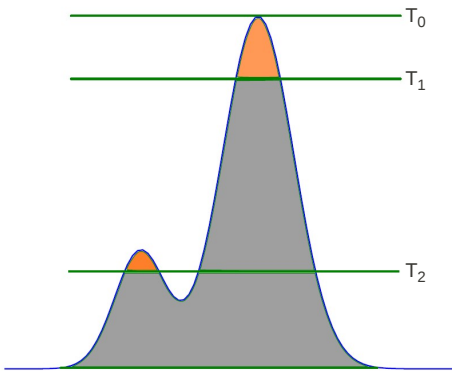

Figure 7.5: Deblending: The threshold is lowered starting from the maximal pixel value T_0 in exponential steps. Two steps are illustrated here. In the first step the threshold is lowered from T_0 to T_1. One cluster is found. If the orange area is larger than a certain fraction δ_c of the total area it is considered an object. In the second step the threshold is lowered further to T_2. An additonal cluster is found, which is separated from the first cluster by pixels below the threshold. Again, if the orange area of this second cluster is larger δ_c the cluster is considered a separate object.

`SExtractor` computes several geometric parameters for each found object. Assuming a Gaussian profile of the object the FWHM can be obtained as the diameter of the disk containing half of the object's flux. The ellipticity ε of an object is defined as

$$\varepsilon = 1 - \frac{b}{a}, \tag{7.2}$$

where a is the major and b the minor axis. Finally, the number of pixels belonging to the object above the detection threshold is called the isophotal area A_{iso}.
For each found object, `SExtractor` measures the flux F_c (in counts) above the background within a circle, the aperture. The diameter of the aperture is set to 5 pixels for the ROTSE image processing, which is slightly larger than the typical point spread function (PSF). An estimate of the magnitude is given by

$$m_{\text{aper}} = -2.5 \cdot \log(F_c) - m_0, \tag{7.3}$$

where m_0 is the zero-point magnitude containing a number of instrument specific constants. m_0 is set initially to 23, but is not relevant later since the magnitude calibration corrects for an absolute offset. `SExtractor` only provides only a rough estimate of the magnitude and the objects coordinates are given in pixel coordinates. An estimate of equatorial coordinates is obtained from a linear transformation using the known equatorial center coordinate of the image ignoring optical distortion. To obtain accurate equatorial coordinates and a more accurate magnitude information the source list needs to be calibrated against a catalog of known bright stars. The ROTSE images are calibrated against the USNO A2.0 catalog [152]. First the closest match between the catalog and the image coordinates is found. A *polynomial spatial warping* is applied to the matching pairs to compute two conversion matrices K_x and K_y, which allow a transformation from image coordinates $\vec{A}$ and $\vec{B}$ to catalog coordinates

$\vec{X}$ and $\vec{Y}$. Catalog coordinates can be expressed as polynomials of the image coordinates:

$$X_i = \sum_{u,v=0}^{N} K_x[u,v](A_i)^u(B_i)^v \tag{7.4}$$

$$Y_i = \sum_{u,v=0}^{N} K_y[u,v](A_i)^u(B_i)^v, \tag{7.5}$$

where N is the degree of the polynomial fit ($N = 3$ the ROTSE). The polynomial conversion matrices are calculated in a least square method and allow to obtain the calibrated coordinates for every pixel of the image.
For the magnitude calibration the difference between the `SExtractor` magnitude and the catalog magnitude is computed for every matching pair. The median difference is added to the `SExtractor` magnitude of every extracted object to obtain a calibrated source list. The magnitude calibration is not applied to the whole image but to several sub-images to account for brightness variation through out the wide field of view.

7.3 Co-Adding

The calibrated images of each night (usually 8) are co-added in order to obtain a deeper image (i.e. with a larger limiting magnitude allowing the detection of dimmer objects). Three co-added images are created: one consisting of all images taken during this night, one of the first half of the images and the third one of the second half of the images. Those co-added images will be referred to as 0, 1 and 2 respectively.
Before the pixel values can be added, the images need to be aligned. First the sources are extracted from each individual image following the procedure explained in Sec. 7.2 and polynomial conversion matrices are computed similarly to the conversion from image to catalog coordinates described above. Since the images are taken within a short time period (the exposure length is $60\,\mathrm{s}$ and only a few seconds pass between the single exposures) the point spread function is assumed to be stable and no time consuming kernel convolution is necessary to match the different PSFs. This is different in case of the image subtraction (as described in the next section), where the co-added images of one night are subtracted from a reference image of a different night and sometimes even from a different ROTSE telescope.

7.4 Image Subtraction

The three co-added images of each night get subtracted by a reference image. Usually deep images are not available for the positions given by the IceCube triggers. Therefore, initially the best image of our observing sequence is chosen as the reference. If no early image of good quality is available (30% of the alerts) another deep reference is taken several months later. Both SN light curves and GRB afterglows would have faded after a few weeks and would not be present in the newly taken reference. If the reference is from the observation sequence, a rising SN would be present in the reference too. However, it would be brighter or dimmer than the SN detection in the other images depending on where in the light curve the reference was taken. Therefore, it is essential to detect also negative changes with respect to the reference. Since the `IDL` detecting routine is only sensitive to positive changes, the reference is subtracted from the new image and vice versa in the same way. Both subtracted images are then processed in the same way by the candidate detection algorithm.

Image subtraction is not a simple pixel by pixel operation. Each image is taken under slightly different conditions resulting in a different PSF in each image for the same object. Both images need to be folded with a kernel function to match their point spread functions. The convoluted images allow a pixel by pixel subtraction. The algorithm was developed by [153] and is described below.

7.4.1 Image Convolution

To subtract two optical images a kernel convolution is necessary to match their different point spread functions. The basic mathematical method for optical image subtraction is described by Alard and Lupton [154]. Starting with a reference image $R(x, y)$ and a new image $I(x, y)$ the reference image has to be smeared in order to match the new image to perform a pixel by pixel subtraction. Both images have $N_x \times N_y$ pixels. x, y denote pixel coordinates, $x \in \{1, 2, ...N_x\}$, $y \in \{1, 2, ...N_y\}$. The convolution can be written as:

$$R(x, y) \otimes K_R(u, v) = I(x, y), \tag{7.6}$$

where $K_R(u, v)$ is the point spread function smearing kernel, which needs to be determined from the images. The kernel is of the size $k_x \times k_y$, with $u \in \{1, 2, ...k_x\}$ and $v \in \{1, 2, ...k_y\}$. Usually it is $k_x \leq N_x$ and $k_y \leq N_y$.
The symbol $\otimes$ denotes *convolution*, which is defined as:

$$R(x, y) \otimes K_R(u, v) = (R \otimes K_R)(x, y) = \sum_{u=-k_x/2}^{k_x/2} \sum_{v=-k_y/2}^{k_y/2} R(x - u, y - v) K_R(u, v) \tag{7.7}$$

An example convolution is displayed in Fig. 7.6. The kernel can be composed as a linear combination of some basis functions. The basis functions to model the PDFs are chosen to be Gaussian functions multiplied with a polynomial in order to have finite sums and to drop rapidly beyond a given distance:

$$K_R(u, v) = \sum_i \exp\left\{-(u^2 + v^2)/2\sigma_i^2\right\} \sum_{j=0}^{p_i} \sum_{l=0}^{p_i - j} a_{ijl} u^j v^l, \tag{7.8}$$

where the range of i, the degree of the polynomial, p_i, corresponding to each i and the choice of the Gaussian width σ_i depend on the characteristic PSFs of the instrument. A composition of three Gaussians (i.e. $i \in \{1, 2, 3\}$) with width σ_i of 1, 3 and 9 pixels and p_i of 6, 4 and 2

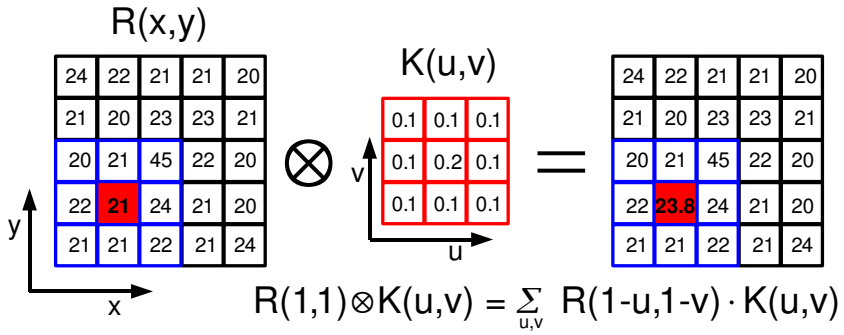

Figure 7.6: Example convolution of one point $(x = 1, y = 1)$ in the reference image $R(x, y)$ with the smearing kernel $K(u, v)$

respectively is proposed in [154].
The coefficients a_{ijk} are derived from the difference image $D(x, y)$ by solving the least square problem ([154, 155]):

$$\chi^2 = \sum_{x,y} \frac{1}{\sigma^2_{x,y}} D(x,y)^2 \stackrel{!}{=} \text{min, with } D(x,y) = (R \otimes K_R)(x,y) - I(x,y), \tag{7.9}$$

where $\sigma^2_{x,y}$ is the variance, e.g. if assuming Poisson statistics for the number of counts measured at each pixel: $\sigma(x, y) \propto \sqrt{I(x, y)}$.
This image subtraction method works well if the reference image is of high quality compared to the new image. Yuan and Akerlof [153] extended the method described above to optimize it for cases with reference images of varying quality. The method, referred to as *cross-convolution*, symmetrizes Eq. 7.6 by adding a second kernel $K_I(x, y)$, smearing also the new image:

$$R(x,y) \otimes K_R(u,v) = I(x,y) \otimes K_I(u,v). \tag{7.10}$$

Flux conservation $\sum K_R(u, v) = \sum K_I(u, v) = 1$ is required for both kernels to avoid possible scaling by arbitrary constants. Including a second kernel increases the number of degrees of freedom by a factor of two.
The minimization criterion used above is not sufficient in the case of two kernels, since it does not provide unique solutions. Smearing both reference and new image stronger, could yield similarly good results in the least square solution. Obviously, the convoluted image should not be smeared any further than necessary. Therefore, an additional penalty term, suppressing this so-called radial scaling, is added to the term to be minimized. The penalty term depends on the total number of pixels in the image and the pixel amplitude variance scaled with the characteristic stellar PSF (see [153] for a detailed description).
To take into account variations of the PSF throughout the image plane, each image is subdivided into 6×6 equally sized sub-images. The convolution kernels are calculated separately for each sub image. The two convoluted images can then be subtracted pixel by pixel.

7.5 Candidate Detection

Steady sources such as galaxies and non-variable stars are equally bright in the new and in the reference image and hence disappear in the subtraction. However, variable or transient sources such as GRBs and SNe would appear as sources in the subtracted image.
For each subtracted image the list of sources is extracted by `SExtractor`. The parameter for the source extraction in subtracted images are slightly different compared to the source extraction in the original image: The detection threshold is increased from 1σ to 1.5σ and the aperture diameter is extended from 5 to 7 pixels. The increased detection threshold suppresses faint subtraction artifacts, while the larger aperture accounts for larger PSFs after the cross-convolution.
Extracted sources in the subtracted image are candidates for variable sources, but are also frequently caused by mis-subtractions. The detection routine adopted from the ROTSE SN search requires the following criteria for an object to be considered as a candidate:

- Objects with saturated pixels are discarded.
- The object has to be detected by `SExtractor` in subtraction 0, 1 and 2 (corresponding to the three coadded images 0, 1 and 2).
- Objects closer than 20 pixels to the image edge are removed.

- Signal-to-noise ratio (S/N) criterion:
  in subtraction 0: $S/N > 5$
  in subtraction 1, 2: $S/N > 2.5$
- Isophotal area (number of adjacent pixels above threshold) criterion:
  in subtraction 0, 1 and 2: $A_{\mathrm{iso}} > 5\,\mathrm{pixel}$
- Change (relative to reference image) criterion:
  in subtraction 0: $change > 5\%$
  no requirement to subtraction 1 and 2.
- FWHM criterion (in pixels):
  $1.01 < \mathrm{FWHM_i} < \mathrm{FWHM_{lim,i}}$, where $i = 0, 1, 2$. The definition of the upper limits takes into account the image quality measured by the average FWHM:

$$\mathrm{FWHM_{lim,0}} = \begin{cases} 7, \text{ if } \mathrm{FWHM_{ref}} \geq 7.0 \\ \mathrm{FWHM_{mean,ref}} \cdot 2, \text{ if } 1.5 < \mathrm{FWHM_{mean,ref}} < 7.0 \\ (\mathrm{FWHM_{mean,ref}} + \mathrm{FWHM_{mean,0}}) \cdot 1.5, \text{ if } \mathrm{FWHM_{mean,ref}} \leq 1.5 \end{cases}$$

$$\mathrm{FWHM_{lim,1}} = (\mathrm{FWHM_{mean,1}} - \mathrm{FWHM_{mean,0}}) \cdot 1.5 + \mathrm{FWHM_{lim,0}}$$

$$\mathrm{FWHM_{lim,2}} = (\mathrm{FWHM_{mean,2}} - \mathrm{FWHM_{mean,0}}) \cdot 1.5 + \mathrm{FWHM_{lim,0}}$$

In addition to these standard ROTSE requirements, every candidate is required to be detected in at least two nights of the observation sequence to reduce the number of subtraction artifacts. In a search for SN light curves this is a valid criterion, since typical supernovae light curves rise slowly for ~20 days and are thus most likely detectable in several nights. In contrast, a GRB afterglow decays rapidly and might only be detected in a single night. However, this work focuses on the detection of SN counterparts as mentioned above.

7.5.1 Catalog Information

Furthermore, information from the two micron all sky survey (2MASS) [156] [157] is added to the candidate identification chain. This survey imaged 99.998% of the sky in three different near infrared bands: $J(1.25\,\mu\mathrm{m})$, $H(1.65\,\mu\mathrm{m})$, $K_s(2.16\,\mu\mathrm{m})$. The catalog distinguishes between point and extended sources. Extended sources are resolved relative to a single point spread function. The 2MASS point source catalog is complete down to $J < 15.8$, $H < 15.1$ and $K_s < 14.3$mag[2]. Most point sources are stars in the Milky Way while the majority of the extended sources are galaxies. Candidates extracted by `SExtractor` from the subtracted image, which passed above criteria, are compared to 2MASS point sources. If a candidate is found closer than 3 pixels (9.7 arcsec) next to a point source with small photometric uncertainty (indicated by the 2MASS photometry quality flag), it will be rejected. Table 7.1 shows the possible photometry flag values. Only objects with photometry flag AAA (one value for each band) are rejected automatically. Those objects are most probably Milky Way stars, which were extracted in the subtracted ROTSE image, because they are either variable or mis-subtracted. Stars are not considered to be transient high-energy neutrino sources. The SN rate in the Milky Way is very low ($1 - 2$ per century [158]) and such a Milky Way SN would be exceptionally bright in the optical and also in neutrinos, i.e. impossible to miss. SNe outside of our galaxy will always be associated with a galaxy.
Unresolved galaxies constitute a non-negligible fraction of the 2MASS point source catalog (1%). Since unresolved galaxies are most prominent at faint magnitudes ($K_S > 14.0\,\mathrm{mag}$) and red colors ($J - K_S > 1.0\,\mathrm{mag}$), candidates are not excluded, if they fulfill ($K_S > 14.0\,\mathrm{mag}$ && $J - K_S > 1.0\,\mathrm{mag}$).

[2]Note that infrared magnitudes are not directly comparable to optical magnitudes.

Table 7.1: 2MASS catalog: Photometric quality flag

Photometric quality flag	Meaning
A	detected with $S/N > 10$
B	detected with $S/N > 7$
C	detected with $S/N > 5$
D	detected, no S/N requirement
E	detected, but poor photometry (e.g. unresolved double stars)
F	no reliable estimate of photometric error
U	Upper limit on magnitude, either not detected or not consistent with other bands
X	detected, but no useful brightness estimation

7.5.2 Machine Learning Classification

After applying the 2MASS criteria, the background mainly consists of mis-subtracted objects and a very small amount of signal-like background (e.g. variable stars). Mis-subtractions are easily identified by eye in most cases. Inspecting thumbnail images of the new image, the reference and the subtraction zoomed in to the candidate's coordinates is a common way to classify objects among astronomers. But if many candidates are left after the subtraction, a scanning by eye can become tedious, especially in wide-field astronomy. Therefore, the automatic elimination of as many subtraction artifacts as possible is aimed. Multivariate analysis techniques (see appendix B) are very powerful in solving such classification problems. Therefore the TMVA package [159] embedded in the analysis software ROOT [160] is used. TMVA provides a large variety of different multivariate classification algorithms. Training, testing and performance evaluation is done simultaneously. A signal and a background sample are needed to train the classification algorithms.

Background Sample

The number of detected candidates in the ROTSE images after the application of the criteria described above is still largely dominated by background caused by mis-subtraction. It would be very difficult if not impossible to simulate the different sources of background, especially the mis-subtractions. Hence, all found candidates are used to represent the background sample. Note that also candidates, which were detected only in a single night are included in the background sample to increase the statistic of mis-subtraction artifacts. 11680 background events have been used, half of them for training and the other half for testing.

Signal Sample

This search is focused on the detection of core-collapse supernovae as high-energy neutrino sources. Our expected optical signal is therefore a supernova light curve. A SNIbc template light curve [39] based on SN1999ex [161] is used. SN1999ex exploded three weeks after a SN type Ia in the same galaxy. Since the type Ia SN was observed nightly, very early data is available for SN1999ex [162]. Figure 7.7 shows the template light curve in five different bands. The magnitude relative to the peak magnitude in B-band is plotted as a function

of time in days, where time=0 corresponds to the time when the B-band peak is reached. ROTSE operates without any filter but is mainly sensitive to the R-band.

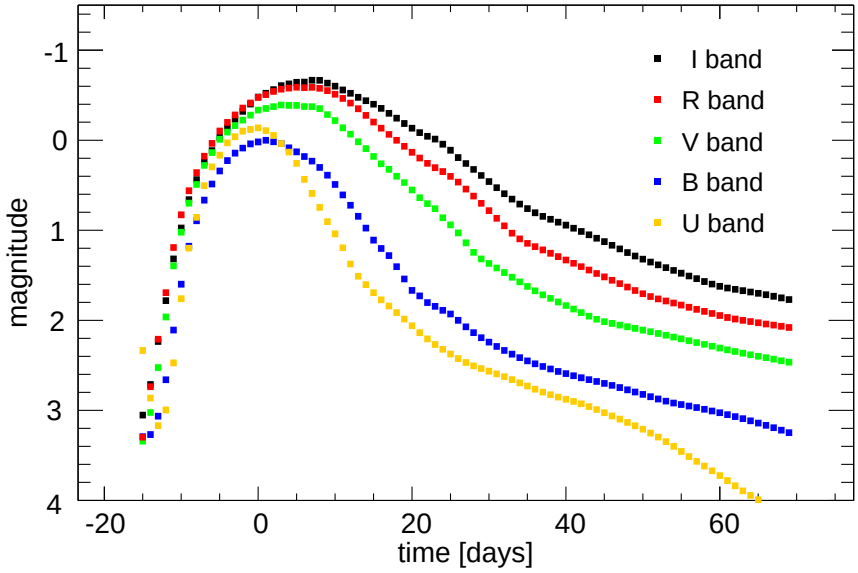

Figure 7.7: Template SN light curve for different bands. The magnitude difference relative to the B-band maximum is displayed as a function of the time in days relative to the time when the B-band peak is reached. ROTSE is most sensitive to the R-band, shown in red.

To simulate our expected signal, a fake star is inserted to every single image from the observation sequence. The brightness of the star changes according to the R-band SN light curve template. The neutrino detection, which triggered the optical observation, defines the start time of the light curve. The magnitude of the fake star in each image can then be calculated as the peak magnitude plus the shift given by the template at the observation time. The light curve template is binned in one day steps, linear interpolation is used to calculate the template shift at any given time. The peak magnitude is generated randomly following a uniform distribution between magnitudes of 12 and 18. Smaller magnitudes would be extremely bright and should be always detected by the image processing and candidate identification algorithm. Dimmer objects ($\mathrm{mag} > 18$) fall below the limiting magnitude and can not be detected at all. The signal events are weighted in the TMVA training process with the reciprocal of the flux, F,

$$w = \frac{1}{F} = 10^{0.4 \cdot mag} \tag{7.11}$$

to ensure that the classification is not optimized for the detection of bright objects. More distant and thus dim signal objects are expected due to an increasing volume for increasing distances. 100 fake supernovae are inserted in every optical dataset. One dataset corresponds to one neutrino trigger sent to ROTSE. Fake stars are inserted on top of galaxies if the corresponding field overlaps with the SDSS [163] or NED [164] catalogs, which provide galaxy coordinates. Otherwise, fake stars are inserted to random positions (30% of all alert fields are not covered by the catalogs). The catalogs provide a classification of objects in stars and galaxies. 50% of the fake stars are inserted on top of bright galaxies ($\mathrm{mag_G} < 16$) while the rest is placed on dim galaxies. The star is not inserted directly on the center of the galaxy but randomly shifted according to a Gaussian distribution with width of the galaxy's major axis, which is defined as the FWHM along the direction of the major axis, divided by

2.35. This scaling is motivated by the relation between FWHM and standard deviation σ of $\sigma = \mathrm{FWHM}/(2\sqrt{2\log 2}) = \mathrm{FWHM}/2.35$. In most cases the shift is negligible compared to ROTSE's resolution.
Crucial for a realistic modeling of the signal is the PSF of the inserted star. It has to be similar to the PSF of existing objects in the image. In a bad quality image, for example, all observed objects might appear elongated, which complicates the image subtraction significantly. To make sure that the inserted PSF reflects all the features of other objects found in the image, we calculate the mean PSF of all objects in a 291×291 pixels box around the insertion coordinates. The PSF of a single star is defined in a box of 15×15 pixels around the star's center. The fake star is inserted to every single image before the images get coadded and further processed by the procedure described above. 4472 single signal candidates are available after the preselection cuts, half of them are used for training while the other half is used for testing.

Input variables

To train the multivariate classifier it has to be fed with input variables, which show different distributions for the signal and the background sample. The chosen input variables are obtained from the subtracted image and can be divided into two classes: geometric parameters describing the shape of the found object in the subtracted image

- Minor axis normalized with the average FWHM of the image, $b/\langle\mathrm{FWHM}\rangle$
- Ellipticity, ε
- Normalized full with half maximum, $\mathrm{FWHM}/\langle\mathrm{FWHM}\rangle$
- Normalized isophotal area $A_{\mathrm{iso}}/\langle\mathrm{FWHM}\rangle^2$
- Number of pixels 5σ below zero in a 15×15 pixel box, $N^{5\sigma}_{\mathrm{pixel}}$

and parameters indicating the variability of the object

- Change with respect to the reference image
- Signal-to-noise ratio

The choice of the geometric variables is motivated by the typical shape of subtraction artifacts. Mis-alignment of new and reference image results in dipole pattern of positive and negative pixels, while mis-subtracted cores of bright, but not saturated, stars cause 'bullseye' patterns. A selection of mis-reconstructed objects is displayed in Fig. 7.8 compared to a successful subtraction of an inserted star in Fig. 7.9.
The input variable distributions for signal and background are displayed in figure 7.10. The FWHM, the minor axis b and the isophotal area A_{iso} are scaled with the average FWHM of all objects in the image to be able to compare images of varying quality. The input variable distributions show that signal events are less elliptic and hence have a larger minor axis compared to background events. Furthermore, signal events have a smaller FWHM, but more pixels above the threshold, i.e. are brighter but more peaked. Subtraction artifacts tend to have more negative pixels, which can be explained by the characteristic dipole or bullseye pattern. Finally, signal events stand out by a larger signal-to-noise ratio and a larger change relative to the reference image.
The correlation coefficient between the input variables is given by

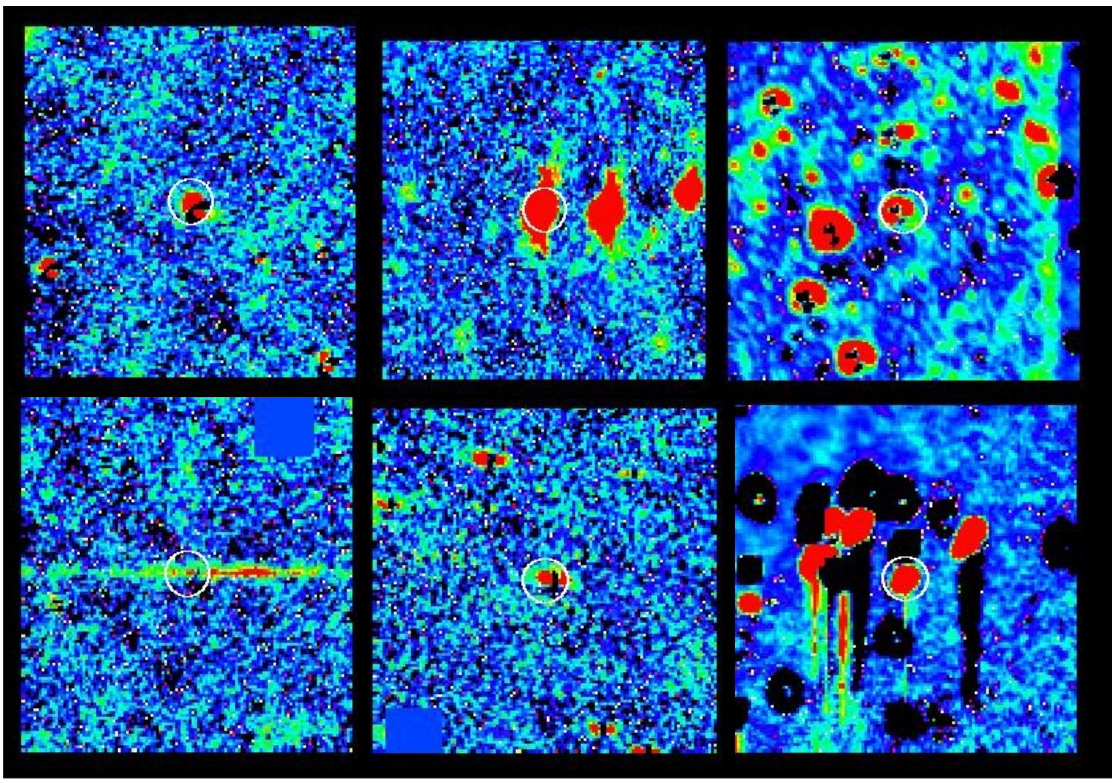

Figure 7.8: Bad subtracted objects (colors indicate brightness): Negative values appear black. Dipole pattern appears in top left and bottom middle. Bullseye pattern shows up in top right. Top middle shows strong elongation of all objects. Bottom right shows bleeding pixels (overflowing pixels which collected too many photoelectrons). Bottom left shows a bright moving object. Saturated objects are removed (blue boxes).

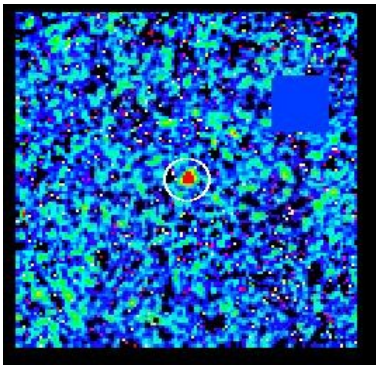

Figure 7.9: Successful subtraction of an inserted star.

$$\rho(X,Y) = \frac{\mathrm{cov(X,Y)}}{\sigma_X \sigma_Y} \tag{7.12}$$

where X and Y are two input variables, σ_X and σ_Y are the standard deviations of the sample and $\mathrm{cov}(X,V)$ is the covariance [165]. The correlation coefficients are shown for the input variables listed above in Fig. 7.11 for signal and Fig. 7.12 for background. Some of the geometric input variables are correlated, e.g. the normalized isophotal area $A_{iso}/\langle FWHM\rangle^2$ and the normalized minor axis $b/\langle FWHM\rangle$. However, removing one of the variables from

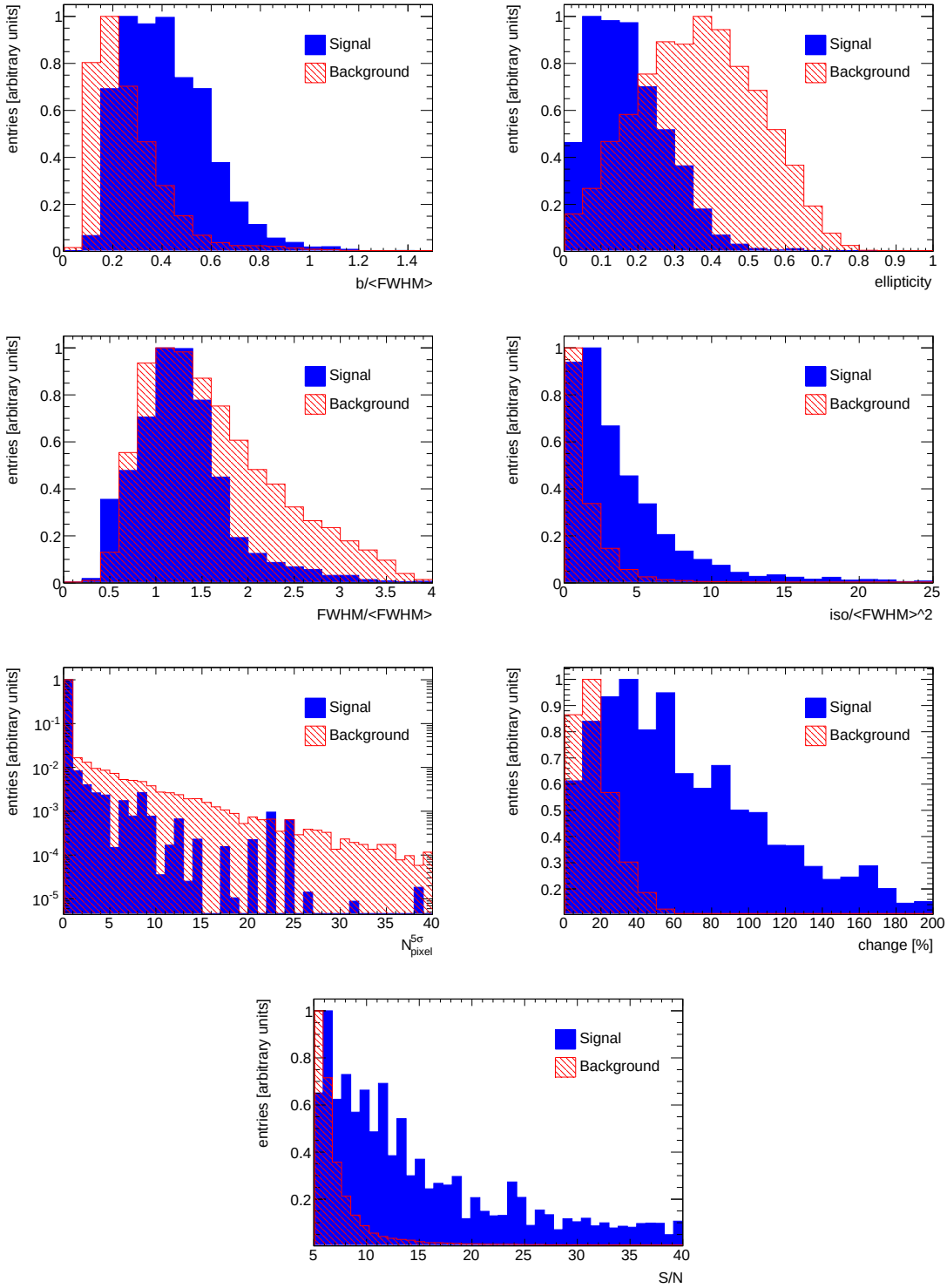

Figure 7.10: TMVA input variables - see text for details.

the list of input variables slightly decreased the selection power of the TMVA output variable.

Different multivariate classifiers have been tested:

- Boosted decision tree (BDT), which consists of a binary tree of several yes/no decisions

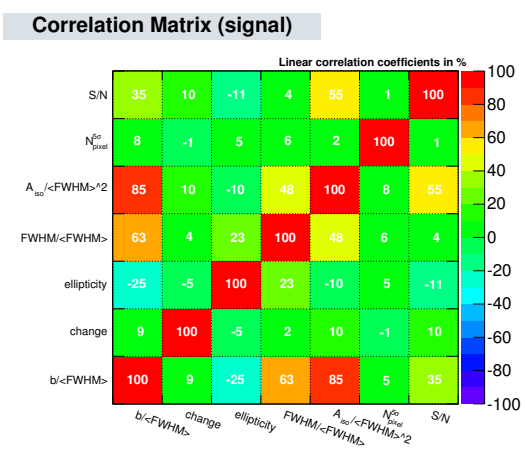

Figure 7.11: Correlation coefficient for input variables of the signal sample.

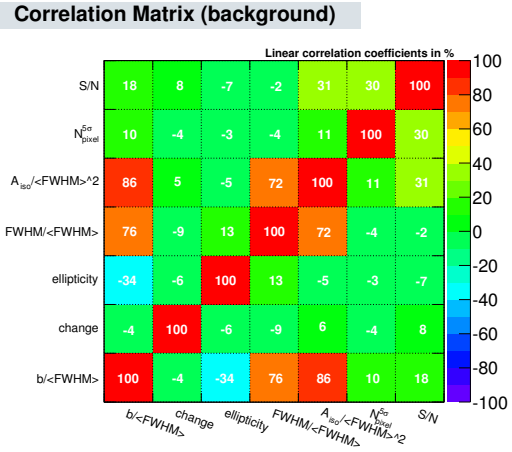

Figure 7.12: Correlation coefficient for input variables of the background sample.

- Maximum likelihood method, which uses probability density functions to build a model that reproduces the input variables for both signal and background
- Fisher method, which performs event selection in a transformed variable space with no linear correlations.
- Support Vector Machine (SVM), which builds a hyperplane to separate signal and background
- Rectangular cuts

A detailed description of all classifiers can be found in [165].
Several classifiers perform well as illustrated in Fig. 7.13, which shows the signal efficiency, ε_s, vs. the background rejection, $1 - \varepsilon_b$. The boosted decision tree (BDT) is chosen for this analysis since it provides high signal efficiency ($90-95\%$) in the region of strong background rejection ($85 - 90\%$). SVM also performs well in this region. However, each step of the BDT method involves only one-dimensional cut optimization and the method is thus simple and robust, while SVM is considered as a "black box". Furthermore, in contrast to the SVM method, the BDT method is not sensitive to poorly or non-discriminating variables, which are simply not used.
Different boosting algorithms were tested. BDT uses adaptive boosting, while BDTG uses gradient boosting and BDTB bagging (see appendix B for more details on the different boosting algorithms). BDT and BDTG show similar performance, while BDTB performs worse (see Fig. 7.14). Comparisons of BDT and BDTG showed that the first is much more affected by over-training. Figure 7.16 and 7.17 show the TMVA output value, i.e. the BDT response, for the test and the training sample. The BDTG distributions for test and training sample agree well, while the BDT distributions deviate strongly, clearly indicating over-training. Therefore, the BDTG algorithm was used. The number of trees N_{tree}, the number of cuts N_{cuts} and the number of maximal nodes $N_{\text{nodes}}^{\text{max}}$ was varied. The best choices were $N_{\text{tree}} = 400$, $N_{\text{cuts}} = 35$ and $N_{\text{nodes}}^{\text{max}} = 3$. Larger values of $N_{\text{nodes}}^{\text{max}}$ showed slightly better signal efficiency for equal background rejection, but at the same time introduced over-training effects. All objects with a BDTG value of smaller than -0.5 are removed. This yields a background rejection of 90% while keeping 90% of the signal. The chosen cut reduces the number of mis-subtractions sufficiently to perform the visual scanning of the remaining candidates.

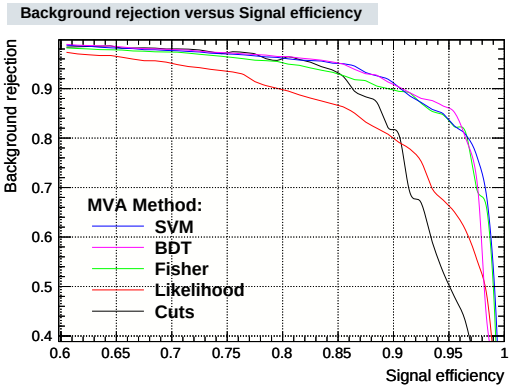

Figure 7.13: Background rejection vs. signal efficiency curve for different classifier methods. BDT provides high signal efficiency in the region of strong background rejection.

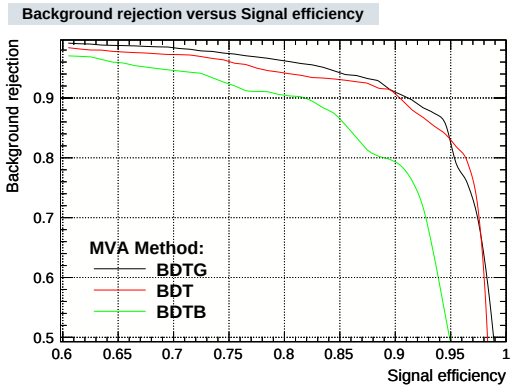

Figure 7.14: Background rejection vs. signal efficiency curve for different BDT boosting algorithms.

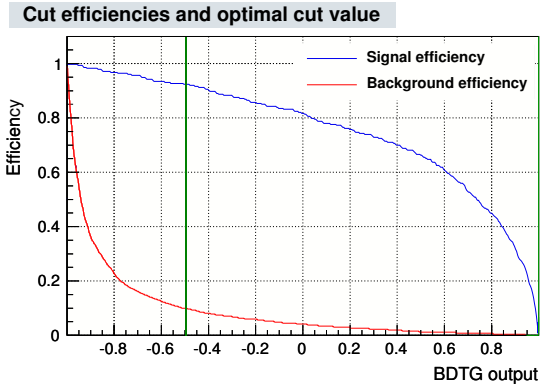

Figure 7.15: Signal efficiency (blue) and background rejection (red) of BDTG. The green line indicates the chosen cut value.

7.5.3 Visual Scanning

After applying the BDTG selection cut, the number of candidates per alert is reduced to 10-200 depending on the quality of the images and the galactic latitude. Fields close to the galactic plane contain a large number of stars, which complicates the subtraction. Tightening the cuts would reduce the number of candidates but at the same time reduce the sensitivity.

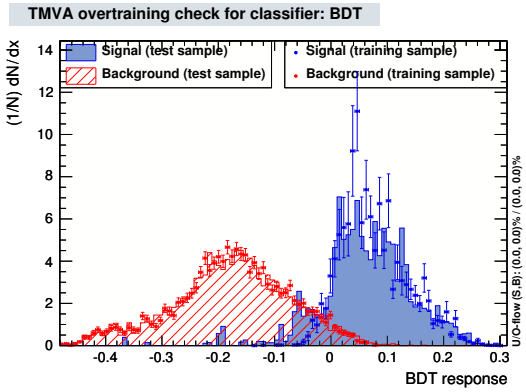

Figure 7.16: BDT response distribution for signal and background for test and training sample. Over-training effects are visible, e.g. test and training distribution do not match.

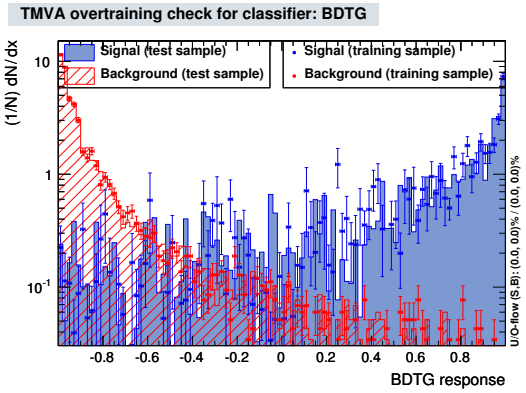

Figure 7.17: BDTG response distribution for signal and background for test and training sample. Less over-training appears.

The final candidates are summarized on the scanning web page. For each candidate the web page shows a light curve as illustrated in Fig. 7.18. The light curve consists of squares indicating the magnitude of the detected object. In addition, the limiting magnitude is displayed (triangles in Fig. 7.18) for each night with a successful observation and subtraction[3]. The limiting magnitude indicates how deep the image is, i.e. at which magnitude an object can still be detected. Different colors mark different telescopes. For each square in the light curve, i.e. each detection of the object (at least two), the web page provides further information: It shows a 100×100 pixels extract, centered around the object's position, of the new, the reference and the subtracted image as illustrated in Fig. 7.19. An image taken by the deep sky survey (DSS), which is deeper than the ROTSE images, of the same patch of the sky is shown for comparison. In addition, links to databases, such as SDSS, NED, 2MASS, SIMBAD [166] and MPChecker[4] are provided. SDSS was a large sky survey covering $8000(^\circ)^2$. It provides high resolution images and a classification of objects, i.e. identifies them as stars or a galaxies. NED is a database of cross-correlated multi-wavelength data for extragalactic objects. It integrates the information from several large sky surveys and many publications. 2MASS is an infrared sky survey as mentioned above. The SIMBAD astronomical database [166] provides basic data, cross-identifications, bibliography and measurements for astronomical objects outside the solar system. MPChecker needs the observation date and the candidate coordinates as input and looks for the transit of minor planets. On the basis of this information, the human scanners have to decide whether the candidate is a supernova, a variable star or a subtraction artifact. The visual scanning was performed by three individual persons to ensure that no good candidate was missed and to avoid false positives.

[3] If the image is of very bad quality, the subtraction algorithm sometimes fails.
[4] `http://scully.cfa.harvard.edu/cgi-bin/checkmp.cgi`

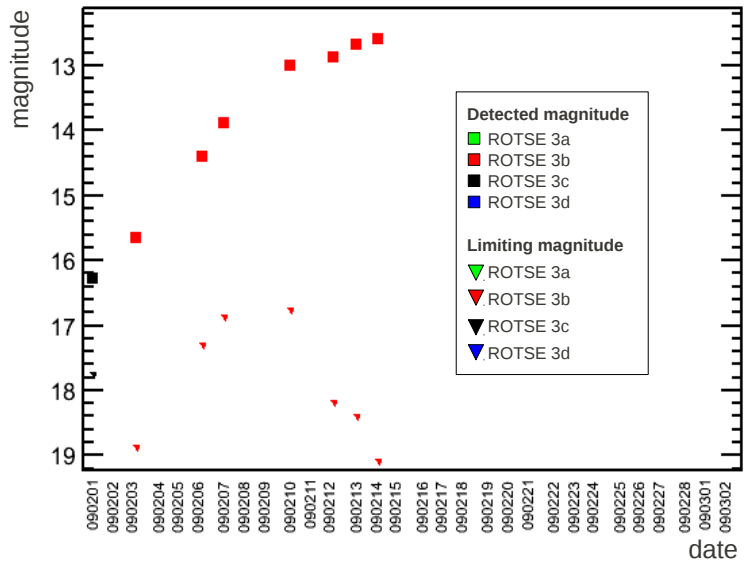

Figure 7.18: Light curve of an inserted SN as shown on the web page. The date is in YYMMDD format. For each night with a successful observation, the limiting magnitude of that night is indicated by a triangle and if the object was detected in that night the found magnitude is shown as a square. Different colors indicate different telescopes. The inserted rising SN light curve is clearly visible.

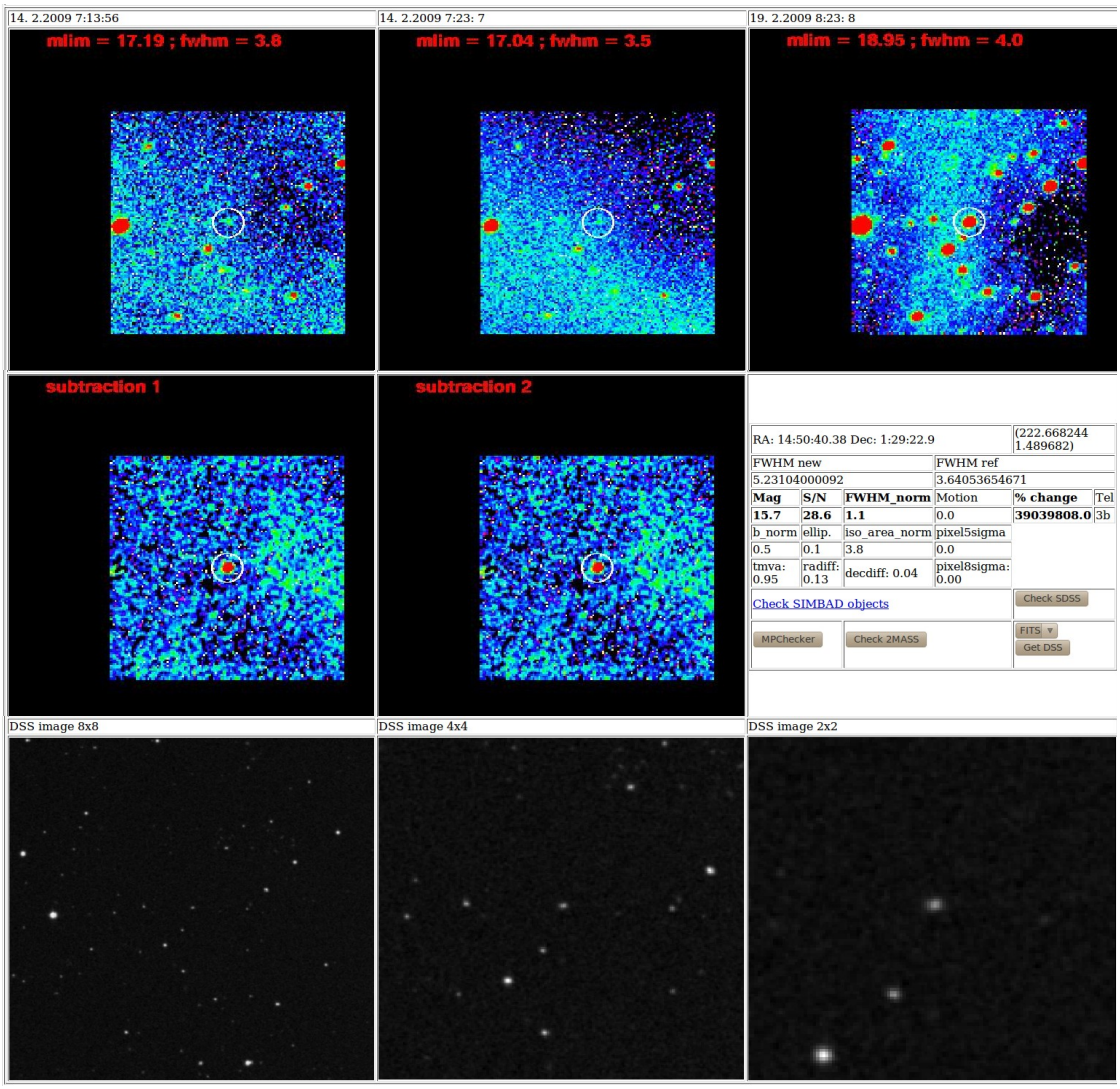

Figure 7.19: Detection of the inserted candidate in one night: The subtraction was successful and the inserted star was found. The first row shows an extract of the new images 1, 2 and the reference image on the right. The second row shows images 1 and 2 after subtraction. On the right more details on the found candidate are provided. The third row contains the DSS image with increasing zoom factor from left to right. The star was inserted on top of a galaxy, which is visible in the DSS image.

7.6 Efficiency

Not all supernovae will be detected by ROTSE and pass the candidate selection criteria presented above. It is important to quantify the efficiency of the optical follow-up to detect a SN, to estimate the background and also to compute the signal expectation. This efficiency will depend on the brightness and thus the distance of the SN.
To estimate ROTSE's efficiency, the simulated signal sample is used consisting of inserted fake SNe as described in Sec. 7.5.2. The efficiency is given by the fraction of inserted SNe, that has been detected by the processing and candidate identification. For some inserted SNe the detection algorithm fails: If the quality of the image is bad (e.g. large average FWHM or small limiting magnitude) the image convolution performs badly. Candidates close to saturated objects or close to objects listed in the two micron all sky survey (2MASS) point source catalog are removed automatically. Figure 7.20 shows the fraction of simulated SNe that are found by the algorithm as a function of the inserted peak magnitude. The efficiency as a function of the peak magnitude can be converted to the efficiency as a function of SN distance $\varepsilon_{\mathrm{ROTSE}}(d)$ (see Fig. 7.21) by Monte Carlo sampling, assuming an absolute R-band magnitude of -18 ± 1 mag for core-collapse SNe [167].

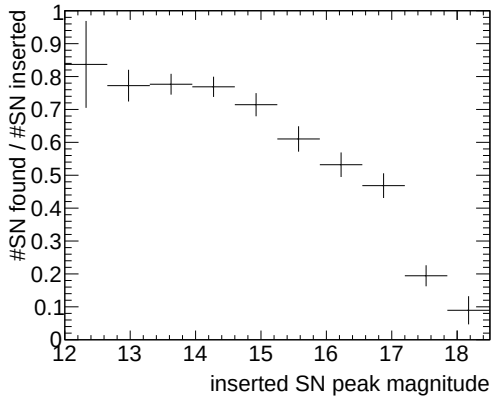

Figure 7.20: Efficiency to find inserted SNe as a function of the peak magnitude.

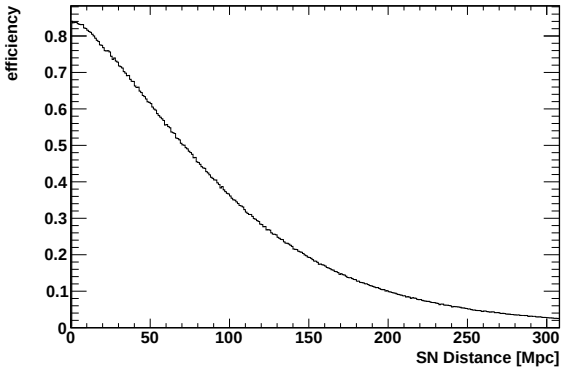

Figure 7.21: Efficiency to detect core-collapse SN as a function of the distance to the SN.

A correction factor of 55% has to be added to obtain the final efficiency, because 45% of all alerts forwarded to ROTSE could not be observed (because they were too close to the sun or due to technical problems, see chapter 11 for more details). As not all SNe will be detected, the efficiency is used to calculate the number of expected SNe detections for a given signal neutrino prediction. Furthermore, it is essential to estimate the number of background SNe, i.e. the number of SNe, which are detected in coincidence with a neutrino doublet by accident.

7.7 Background Expectation

To estimate the expected number of accidentally detected SNe, a core-collapse SN rate of 1 per year within a sphere of radius 10 Mpc, i.e. $2.4 \times 10^{-4}\,\mathrm{y}^{-1}\,\mathrm{Mpc}^{-3}$, and a Gaussian absolute magnitude distribution with a mean of -18 mag and a standard deviation of 1 mag [167] are assumed. Based on the efficiency estimated in Sec. 7.6 the rate of core-collapse SNe, which

can be detected by ROTSE, can be calcualted: $\rho_{\mathrm{CCSN}}^{\mathrm{ROTSE}} = 3823\,\mathrm{y}^{-1}$ (i.e. if ROTSE would survey the full sky). The number of expected accidental SNe detections is

$$N_{\mathrm{SN,exp}} = \Delta T_{\mathrm{SN}} \cdot N_{\mathrm{alerts}} \cdot \frac{\Omega_{\mathrm{ROTSE}}}{\Omega_{\mathrm{sky}}} \cdot \rho_{\mathrm{CCSN}}^{\mathrm{ROTSE}} = 0.074 \tag{7.13}$$

where $N_{\mathrm{alerts}} = 17$ is the number of multiplet alerts followed-up by ROTSE (see chapter 11). $\Omega_{\mathrm{ROTSE}} = 1.85^\circ \cdot 1.85^\circ$ is the solid angle covered by ROTSE's field of view and $\Omega_{\mathrm{sky}} = 41253(^\circ)^2$ is the all sky solid angle. ΔT_{SN} is the time window in which a coincidence of neutrino and optical signals is accepted. It has to be larger than the uncertainty of the SN explosion time. In the next chapter it is shown, that the explosion time can be estimated with an accuracy of ~1 day if early data are available. Hence, to be conservative $\Delta T_{\mathrm{SN}} = 5\,\mathrm{days}$ is assumed.

Chapter 8

Estimation of the Explosion Time from Supernova Light Curves

If the optical follow-up performed by ROTSE detects an optical SN light curve triggered by a neutrino multiplet, it will be crucial to establish the coincidence between the neutrino detection and the optical SN. A neutrino doublet itself is not a significant detection due to the high rate of background doublets caused by random coincidences of atmospheric neutrinos, which are indistinguishable from SN neutrinos. However, if a supernova from the same direction is observed optically within a coincidence time window, the significance of the observation rises dramatically. The neutrinos are expected to be produced directly in the explosion and hence their arrival time should be in coincidence with the explosion time estimated from the SN light curve. The time window to accept a coincidence has to be chosen carefully. On one hand it should be as short as possible to reduce the expected background and on the other hand it has to be large enough not to lose any signal, i.e. it has to be larger than the uncertainty of the explosion time estimation and larger than the theoretical uncertainty of the neutrino arrival time relative to the explosion time. This chapter presents the first study of the determination of the explosion time, t_0, from fitting the optical supernova light curve, and a study of the corresponding uncertainty. It has been published in [168].

8.1 Supernovae with Known Explosion Time

The estimation of the explosion time from SNe light curves became attractive in the last few years due to the recent fortuitous discoveries of two nearby type Ibc SNe, SN2008D [93] and SN2006aj [92], each with an associated X-ray flash (XRF) presumably from the shock breakout. The short XRF provides a time stamp for the explosion that can be compared to the one obtained from fitting the optical light curve data. Furthermore, for obvious reasons the light curve data for these SNe begin very early after the XRF, and as such are well-suited to the method described below, because as with an XRF, a neutrino trigger will enable early optical observation of the target SN.
The only other SN that has an explosion time known with even better precision is SN1987A. It is a low-luminosity type IIP SN with a light curve very different from that of SN2008D and SN2006aj. Nevertheless, the physics of the early part of the light curve is similar enough that the analysis presented here can be successfully extended to SN1987A as well. The explosion time of SN1987A is taken to be the time of the MeV neutrino burst. For SN2008D and SN2006aj, the time of the XRF is used as a rough proxy for the explosion time. The XRF is expected to happen after the actual explosion, because the shock wave has to prop-

agate through the star first before it "breaks out" of the stellar surface producing the XRF. However, the propagation time of the shock is expected to be small considering both radius and shock velocities for these SNe. The XRF is emitted when the shock wave reaches a radius, where the system becomes optically thin. The progenitor system of SN2008D becomes optically transparent to X-rays at a relatively small radius of $r_* \lesssim 10^{12}$ cm [93, 169]. For SN2006aj, a larger radius of $r_* \sim 5 \times 10^{12}$ cm is estimated [43, 170], while for SN1987A a photospheric radius of $r_* \sim 2 \times 10^{12}$ cm is assumed [171]. The maximum shock velocity at the shock breakout has been computed as a function of radius, energy and mass in [172, 173]. Inserting parameters for the SNe at hand one obtains $\sim 0.5\,c$ for SN2008D and $\sim 0.1\,c$ for SN1987A. The non-relativistic theory in [172, 173] yields a maximum shock velocity for SN2006aj that exceeds the speed of light. The authors in [170] do a relativistic treatment and estimate $0.85\,c$. The minimum time scale is given by

$$t_{\min} = r_*/v_s^{\max}. \tag{8.1}$$

One obtains $t_{\min} = 70\,\mathrm{s}$ for SN2008D, $t_{\min} = 200\,\mathrm{s}$ for SN2006aj and $t_{\min} = 1300\,\mathrm{s}$ for SN1987A. While this crude calculation underestimates by a factor of five the 6×10^3 s delay time between explosion and shock breakout predicted by a detailed simulation of SN1987A [171], it indicates that for SN2008D and SN2006aj, the shock breakout is not expected to appear much later than $5 \times t_{\min} \sim 10^3$ s after the explosion. As will be shown in Sec. 8.3, this theoretical time scale for the shock propagation is much shorter then the resolution of the fit on the time of explosion t_0 that we obtain for SN2008D. For SN2006aj, it is comparable to the resolution of the light curve fits.

8.2 Light Curve Data and Model

The SN2006aj and SN2008D light curves contain data from times exceptionally soon after their putative explosions, making an accurate estimation of SN explosion times feasible. For SN2006aj the U, B and V band data from the SWIFT UVOT [43] and for SN2008D the B, V, R and I band data from FLWO [169] are used. Additionally, data from other telescopes are available, but in order to avoid calibration problems arising from different filter and instrument pass bands, this study is performed only with data from a single source[1]. For SN 1987A, the photometric B, V, R, and I band data compiled and analyzed consistently by Hamuy et al. [175] is used. The first data point is $1.14\,\mathrm{d}$ after the explosion. Again, to avoid calibration problems, the earlier discovery data points that exist for the V-band are not used. The explosion time is estimated by fitting light curves under the assumptions of an initial blackbody emission from the rapidly cooling shock breakout, followed by a phase dominated by the expansion of the luminous shell. For the latter two distinct models are tested.

8.2.1 Shock Breakout Phase

To represent the shock breakout phase the formulation from Waxman et al. [170] is used. The flux during the shock breakout phase of the SN light curve is approximated by $\Phi_{BB} = IA$, where $A = 4\pi r^2$ is the area, r is the radius of the expanding photosphere and I is the intensity. The intensity is taken as proportional to that produced by a blackbody, which is

[1] Ref. [174] provides a V band data point $4\,\mathrm{h}$ after t_0. While it was not included in the light curve fits, it could be shown to fit the model prediction well.

given by Planck's law

$$I(\lambda, T) = \frac{2hc^2}{\lambda^5} \frac{1}{e^{\frac{hc}{\lambda kT}} - 1}, \tag{8.2}$$

with h being the Planck constant and k the Boltzmann constant. T is the temperature and λ the wavelength. In the following a fixed wavelength of $\lambda = 600\,\text{nm}$ is assumed. Note that this reference wavelength is not relevant for the results presented here since it appears as multiplicative factor to the fitted temperature. In addition to the explosion time t_0, the other free parameters of the model are the radius and temperature at a fixed reference time. Waxman et al. [170] give the SN radius $r \propto \delta_t^{0.8}$ and the shock breakout temperature $T \propto \delta_t^{-0.5}$, where $\delta_t = (t - t_0)$ is the elapsed time since the explosion. Inserting these relations in the flux equation yields:

$$\Phi_{BB} = \frac{a_1}{\exp(a_2 \delta_t^{0.5}) - 1} \delta_t^{1.6}, \tag{8.3}$$

with a_1, a_2 and t_0 free parameters.

8.2.2 Expansion Phase

For the expansion phase either a simple expanding photosphere model is used for the behavior of the light curve or the more complex description from Arnett [176] that includes a time-dependent diffusion equation. In the first model, the flux in the pure expansion phase is approximated as

$$\Phi_{t^2} = a_3 \delta_t^2, \tag{8.4}$$

with δ_t defined above and a_3 and t_0 free parameters. This t^2 assumption treats the SN photosphere as represented by a blackbody of constant temperature, which expands with constant velocity v [177, 178]. The area of the photosphere, which is directly proportional to the photon flux, then increases $\propto (v\delta_t)^2$. This *ansatz* works remarkably well for the rising part of type Ia SN light curves [179]. The model has one free parameter (a_3) and, when combined with the blackbody emission model, there are a total of four parameters (a_3, a_1, a_2 and t_0) in the fit to the light curve.
As an alternative to the expanding photosphere model, the light curve model of Arnett [176] (also used by Soderberg et al. in [93]) is applied, that assumes homologous expansion, i.e. the fractional rate of change in the star is a constant

$$\frac{\dot{r}}{r} = const. \tag{8.5}$$

Furthermore, it assumes radiation pressure dominance, and the presence of ^{56}Ni in the ejected matter, which is distributed peaked toward the center of the ejected mass. The light curve is described by

$$\phi_{\text{Arnett}} = M_{\text{Ni}} e^{-(t-t_0)^2/\tau_m^2} \epsilon_{\text{Ni}} \int_0^{t-t_0/\tau_m} \exp\left(z^2 - z\frac{\tau_m}{\tau_{\text{Ni}}}\right) 2z dz, \tag{8.6}$$

where the nickel mass, M_{Ni}, is a free parameter. $\tau_{\text{Ni}} = 8.8\,\text{d}$ is the half-life of ^{56}Ni and $\epsilon_{\text{Ni}} = 3.9 \times 10^{10}\,\text{erg}\,\text{s}^{-1}\,\text{g}^{-1}$ the energy released per unit mass in radioactive decay of nickel. The light curve time scale τ_m depends on the opacity κ, the ejected mass M_{ej} and the kinetic energy E_k via

$$\tau_m = 0.36 \left(\frac{\kappa^2 M_{\text{ej}^3}}{c^2 E_k}\right) \tag{8.7}$$

and is also treated as a free parameter. Thus, the Arnett formulation introduces two free parameters (M_{Ni} and τ_m). Combined with the rising part of the light curve described by equation 8.3, which has three additional free parameters (a_1, a_2 and t_0), this alternative model has a total of five free parameters in the fit to the light curve.
As an example, Fig. 8.1 shows the results of the fits to R-band light curve data of SN2008D. The full set of light curves for SN2006aj, SN2008D and SN1987A is shown in figures 8.2, 8.3 and 8.4 respectively. A systematic evaluation of fits to all available bands is the subject of the next section.

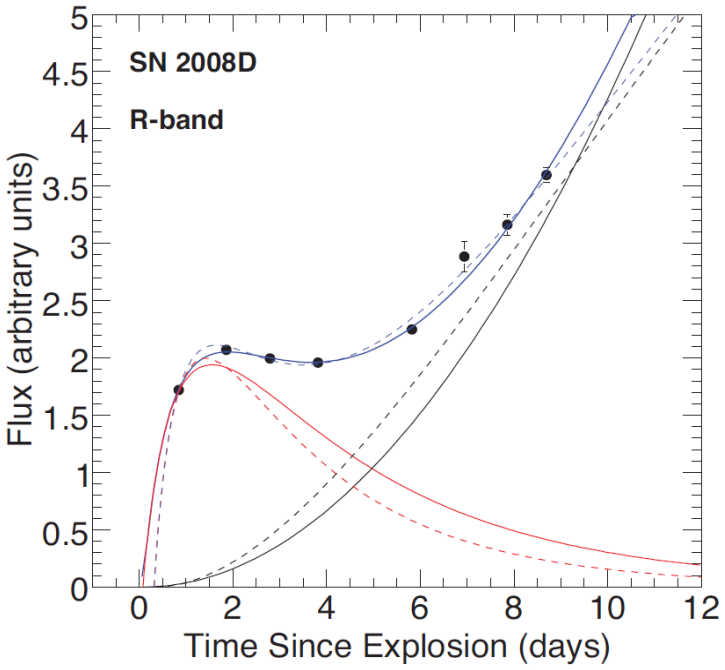

Figure 8.1: The rising part of the R-band light curve data for SN2008D from [169] is shown along with the fit results. The fit model consists of a superposition of a blackbody spectrum (the initial "bump" of the curve) and a model for the later emission (the rising part of the curve). The solid lines represent the fit results using the t^2 dependence for the late time emission; the dashed lines the Arnett model (the t^2 formulation, which here gives $t_0 = 2 \pm 3\,\mathrm{h}$, is preferred due to a better fit; see text in Sec. 8.3 for details).

8.3 Fit Results

The two models described above are fitted to the light curve data in multiple bands for SN2006aj, SN2008D and SN1987A, as shown in Fig. 8.2, 8.3 and 8.4. For each fit the initial explosion time, t_0, the error on t_0, and the χ^2 of the fit are extracted. The results are summarized in table 8.1.

8.3.1 SN2006aj

For SN2006aj, only a marginal difference in the accuracy of the fitted t_0 is found, if the more complex Arnett formulation is used instead of the simpler t^2. For the comparison, the fit was restricted to the first six days, since the light curve of SN2006aj evolves faster than other SNe, and for later times the t^2 approximation does not hold. The agreement between both

Table 8.1: Fit result summary.

Supernova	t_0	χ^2
SN2006aj	$-1.0 \pm 0.1\,\mathrm{h}$	$23.6/27$
SN2008D	$3.0 \pm 1.4\,\mathrm{h}$	$15.9/16$
SN1987A	$0.1 \pm 2.6\,\mathrm{h}$	~1

fit models is due to the fact that the earliest part of the light curve is entirely dominated by emission from the shock breakout and hence already strongly constrains t_0. The fit yields an average t_0 that is shifted by $-1\,\mathrm{h}$ relative to the XRF, with a statistical error of about $0.1\,\mathrm{h}$.

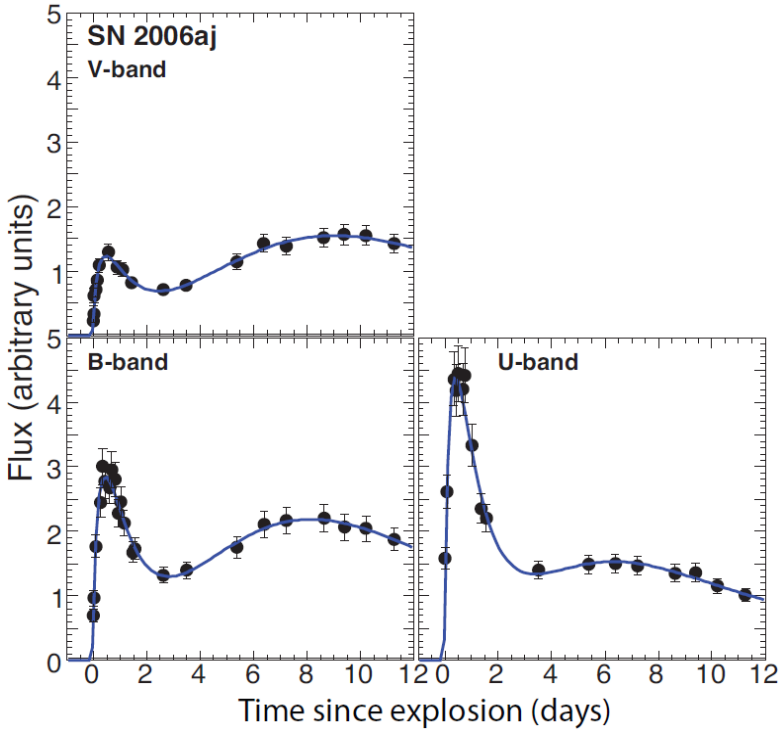

Figure 8.2: Early light curve data for type Ibc SN2006aj from [43] are shown and the fit performed for several optical bands. The fit function is an initial blackbody spectrum followed by the Arnett formulation (for illustration purpose). In the t_0 analysis, the Arnett formulation is replaced with the t^2 dependence, which results in an improved fit result. Arnett formulation is shown. The fit result is displayed as a solid line.

8.3.2 SN2008D

The light curve data of SN2008D have also been fit by both the t^2 and Arnett formulations. However, the early data shown in figures 8.1 and 8.3 are better represented by the t^2 model, as determined by the quality of the fit. For the sum of all four bands the fit has a $\chi^2/\mathrm{NDF} = 15.9/16$. Fitting with the Arnett formulation instead of t^2 one obtains, with one additional fit parameter per band, a χ^2 that is significantly worse ($\chi^2/\mathrm{NDF} = 18.6/12$ for the sum of χ^2 for all bands). Hence the t^2 fit model is used as the default fit method in the following. The fit results for all bands using the t^2 formulation are shown in Fig. 8.5.

For SN2008D, whose light curve data do not start so soon after the explosion time, the fitted t_0 is found to be consistent with zero for two out of four bands (90% CL), with an average t_0 of about 3 h. The largest outlier is the I-band, with $t_0 = 5.8 \pm 1.9$ h. If the Arnett formulation is used instead of the default t^2 formulation, the estimated t_0 would be shifted by ~7 hours to later times (see also Fig. 8.1) .

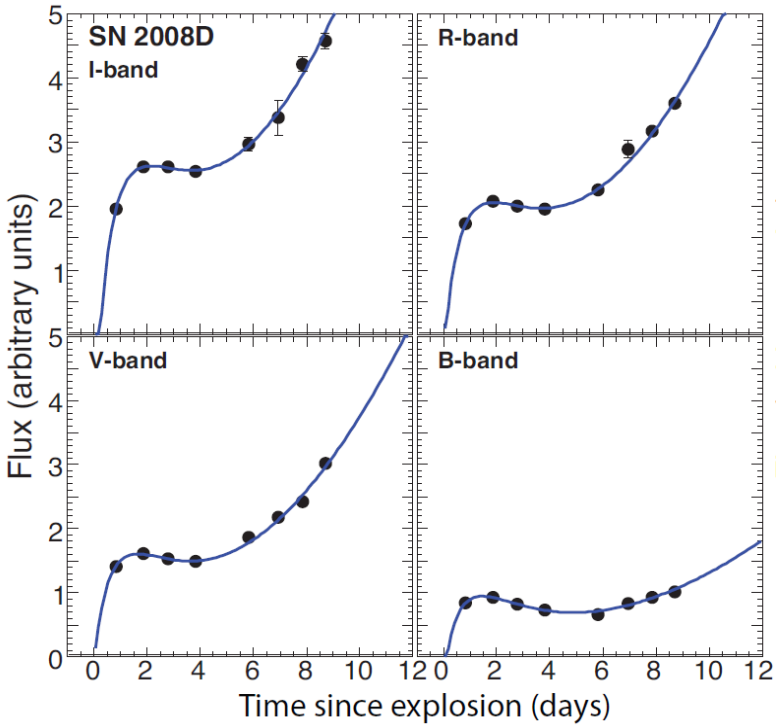

Figure 8.3: Early light curve data for type Ibc SN2008D from [169] are shown and the fit performed for several optical bands. The fit function is an initial blackbody spectrum followed by a t^2 dependence. The fit result is displayed as a solid line.

8.3.3 SN1987A

In contrast to SN2006aj and SN2008D, SN1987A has its date of "birth" clearly marked by the observation of a short burst of neutrinos. Since its detection, SN1987A has been studied in great depth, both observationally and theoretically. One cannot expect to have such detailed information for future SNe unless they appear in our own galaxy and hence, for the sake of simplicity, the methodology already used above is adopted. The light curve data of SN1987A are fitted with the model composed of the shock breakout according to Eq. 8.3 and the t^2 dependence for the expansion phase. The first eight days of data are fitted. Since the photometric data [175] do not come with estimated uncertainties, they were chosen to be 0.03 mag to achieve $\chi^2/\mathrm{NDF} \approx 1$ in the fits. The size of this assumed uncertainty roughly matches the largest scatter of photometric data points observed during a single night. The fit results for four bands are shown in Fig. 8.5. In the figure, the larger error bar for the V, R and I-band fits with respect to the B-band fits reflects the fact that the shock breakout feature is not very evident for the redder bands, as can be seen in Fig. 8.4. For all bands except the B band the obtained t_0 is consistent with zero. The B band shows a shift of 7.2 ± 2.4 h.
It was explored whether the fits can be improved by incorporating some key observations for SN1987A into the model, for example that an almost constant bolometric luminosity

was observed after the first day after the explosion. In this simple picture, this is achieved by making the photosphere radius expand linearly with time, $r \propto \delta_t$, while keeping the photosphere temperature dependence as before: $T \propto \delta_t^{-0.5}$. Reinserting this into Eq. 8.3 provides a slightly modified model for the shock breakout phase. Fitting this shock breakout model results in a systematic shift of $-7.2\,\mathrm{h}$ for all bands. While the B-band result is now consistent with the explosion time obtained from the neutrino burst, the fits of the redder bands appear systematically shifted. Either way, the observed deviation is of the order of $7.2\,\mathrm{h}$ for one of the bands indicating the size of the systematic uncertainty involved in the extrapolation.
Summarizing, for SN1987A the light curve data starting $1.14\,\mathrm{d}$ after the neutrino burst allows to fit the explosion time with a fitting error of about $5\,\mathrm{h}$ and a systematic error of about $7\,\mathrm{h}$. The systematic uncertainty reflects the crudeness of the light curve model employed. Nevertheless, relative to simply using the first data point at $t_0 = 1.14\,\mathrm{d}$, the fitting technique yields a factor of ~4 improvement in the t_0 measurement.

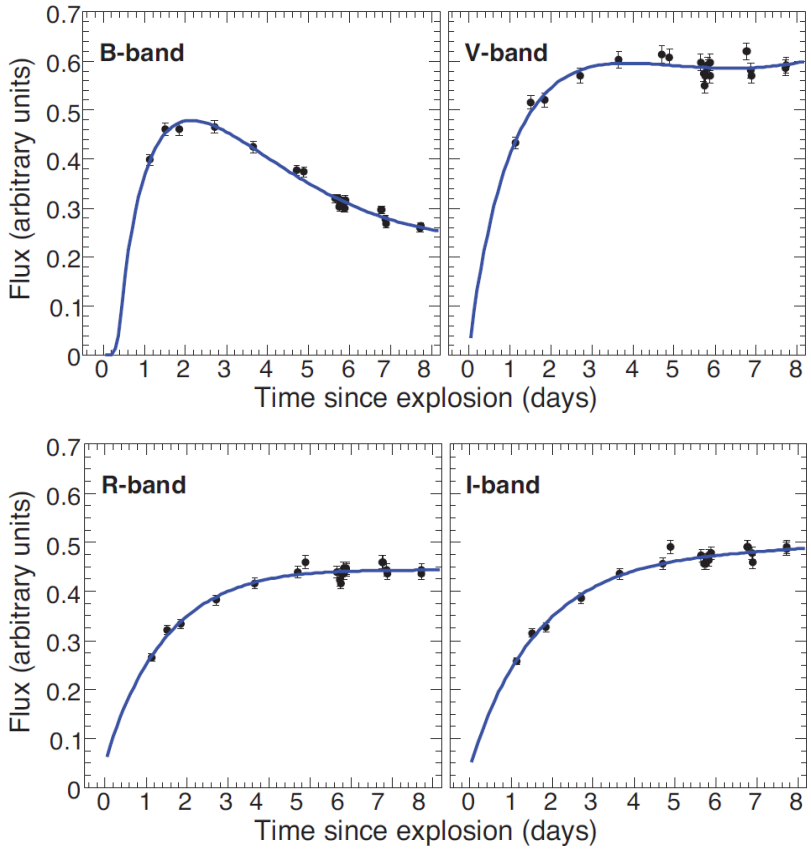

Figure 8.4: Early light curve data for the type II SN1987A from [175] are shown. For the fit function the initial blackbody spectrum followed by a t^2 dependence is used.

8.4 Conclusion from Light Curve Fits

The fitted t_0 values demonstrate that an estimate of the explosion time with an accuracy of less than one day can be made using simple analytic light curve models. The estimates are robust on the scale of a few hours across several independent optical bands. As shown in Fig. 8.5, the estimated t_0 and its error, averaged over all available bands, is about $3.0 \pm 1.4\,\mathrm{h}$

for SN2008D, -1.0 ± 0.1 h for SN2006aj, and 0.1 ± 2.6 h for SN1987A. For SN2008D, the theoretical uncertainty associated with the use of the time of the XRF as the reference for t_0 is smaller than the resolution on t_0 from the fits. The fits in all bands give explosion times that are slightly later than the time of the XRF, indicative of limitations in the rather simple underlying physical model. For SN2006aj, the explosion date was determined from the fit to the light curve to be 1.0 h before the XRF. As mentioned earlier, this is larger than the estimated time needed for the shock to propagate to the surface of the progenitor. Resolving this discrepancy would require more detailed modeling of the light curve and/or shock propagation. The model does not take into account possible effects due to circumstellar interactions, asymmetries in the ejecta or the differences in the density profiles of the progenitors. These effects might explain the observed deviations that are difficult to explain with statistical errors alone. In any case, the discrepancy for both type Ibc SNe investigated is < 4 h, which can be considered the characteristic size of the systematic uncertainties in t_0. Hence, the fitted SN explosion time t_0 represents a successful extrapolation of the data to earlier times, and the magnitude of the extrapolation is large compared to the quoted error. This suggests that the model captures dominant physical properties of the SN during the period shortly after its explosion.
Note that the resolution on t_0 for both SNe is larger than what is expected for the high energy neutrino emission, which is a small delay of < 200 s [180]. between the collapse and the launch of the jet producing neutrinos.

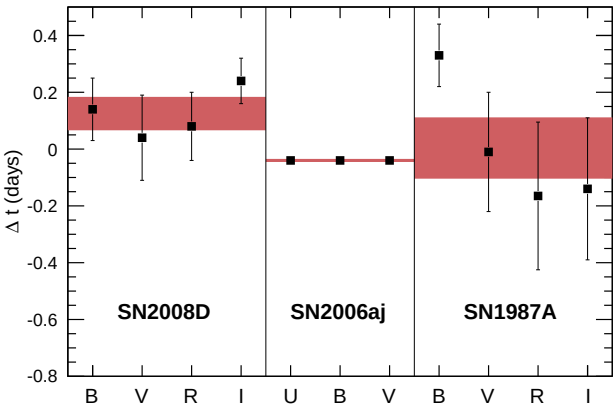

Figure 8.5: Summary of the results of the fits to the light curves of SN2008D (left), SN2006aj (center) and SN1987A (right) in each optical band that was used. The horizontal shaded regions are centered vertically on the error-weighted mean of Δt (the difference between the fitted t_0 and the time of the X-ray flash or neutrino burst) and have a width corresponding to the error on the mean. The t^2 formulation is used throughout since it provides comparable or better quality fits relative to that of Arnett.

8.5 Importance of Early Light Curve Data

Using the SN2006aj data, the importance of the early data points is demonstrated by manually removing the earliest data points, one at a time, and re-fitting the data each time. A summary of the result of this exercise is shown in Fig. 8.6. The figure makes evident the importance of the early data points, showing how the accuracy of the fitted t_0 depends strongly on these early data, although the accuracy drops most dramatically after about a day. This is consistent with the observation made for the other SNe: With a first data point at ~0.7 d

for SN2008D, the explosion date can still be determined to within about 0.2 d, while for SN1987A, with a first data point at 1.1 d after the explosion, the uncertainty is around 0.3 d. It is also informative to compare the accuracy of the t_0 from the fit with that obtained by simply using the first available point on the light curve. The dot-dash line in Fig. 8.6 shows this t_0 estimate, which is simply the difference in time between the XRF and the earliest remaining data point on the light curve. The figure thus shows that, if light curve data are acquired with about a six hours or greater delay from the explosion time, the fitting technique provides a more accurate and precise measure of the explosion time than simply using the earliest point on the light curve. The presented method thus relies explicitly on the early detection of the light curve.

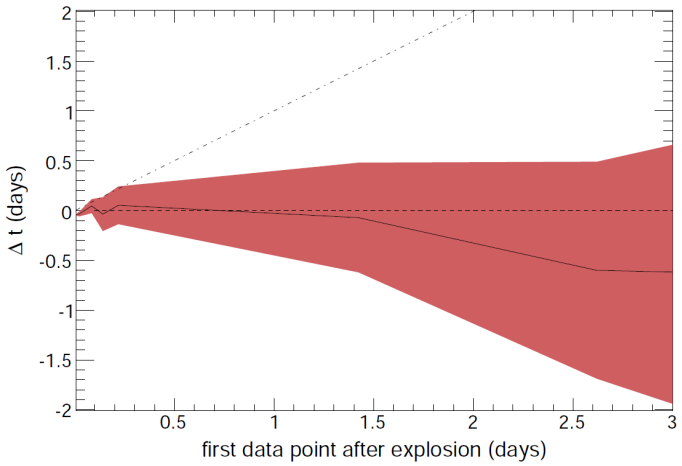

Figure 8.6: To quantify the importance of acquiring data points early in the SN light curve, the earliest V-band data points are manually removed, one at a time, and the light curve is refitted for t_0 after each removal. The solid black line shows the resulting fitted t_0 values and the vertical height of the shaded region shows their 1-σ resolutions, as a function of the time of the earliest used data point in the fit. The dot-dash line shows the value obtained for t_0 simply using the earliest available data point. Comparing this curve to the black line from the fitted t_0 values, one sees that, if there is a latency of roughly six or more hours after the putative explosion time before the first optical observation is made, the fitting technique provides a more accurate explosion time estimate than simply using the earliest point on the light curve.

Chapter 9

Significance and Limit Calculation

Roughly one year of data collected by the optical follow-up program is analyzed as described in Chap. 5 and Chap. 7. To evaluate the results of the measurement, a mathematical recipe was developed to compute the significance of the measurement and to calculate a limit restricting the parameter space of the soft jet SN model. The method was predefined before the analysis was applied to the data in order to avoid the introduction of a bias.

9.1 Significance Calculation

To calculate the significance of the measurement, its compatibility with the background expectation needs to be calculated. A test statistic, λ. is defined consisting of an IceCube term λ_ν and a ROTSE term λ_{SN}. The test statistic describes the probability, that an excess similar or stronger than that obtained from the data sample occurs under the assumption that the data sample contains no signal, i.e. only consists of background.
The probability to detect N_k ore more events with multiplicity k over a background expectation of μ_k is given by the sum over Poisson probabilities:

$$P(N_k, \mu_k) = \sum_{i=N_k}^{\infty} \frac{\mu_k^i}{i!} e^{-\mu_k}. \tag{9.1}$$

Combining all multiplicities and the two IceCube data sets (IC40 and IC59) yields the test statistic

$$\lambda_\nu = \prod_{k=2}^{\infty} P(N_k^{IC40}, \mu_k^{IC40}) \cdot P(N_k^{IC59}, \mu_k^{IC59}). \tag{9.2}$$

In addition to the IceCube information (i.e. number of doublets and multiplets of higher order) information obtained by the optical observations is included in the test statistic. The probability to observe N_{SN} or more optical SN counterparts based on the expected number μ_{SN} of accidentally observed SN in coincidence with an IceCube multiplet is given by the sum of Poisson probabilities:

$$P_{\mathrm{SN}}(N_{\mathrm{SN}}, \mu_{\mathrm{SN}}) = \sum_{i=N_{\mathrm{SN}}}^{\infty} \frac{(\mu_{\mathrm{SN}})^i}{i!} e^{-\mu_{\mathrm{SN}}}. \tag{9.3}$$

If one or more optical counterparts were observed the significance can be improved by adding neutrino timing information as well as the distance information of the object found. The probability P_t to find a time difference Δt or smaller due to a background fluctuation

assuming a uniform background is given by

$$P_t(\Delta t) = \frac{\Delta t}{100\,\mathrm{s}}, \tag{9.4}$$

where $\Delta T = 100\,\mathrm{s}$ is the multiplet time window. Hence, assuming a generic prediction of a $10\,\mathrm{s}$ wide SN neutrino pulse results in a factor of ten lower chance probability.
While ROTSE can only detect close-by SNe, more powerful telescopes can access a much larger volume and would essentially always detect a SN in their field of view. Hence, an additional factor P_d, describing the probability to observe a SN at a distance $d \leq d_{SN}$, becomes important:

$$P_d(d_{\mathrm{SN}}) = \frac{N_{\mathrm{SN,ROTSE}}(d \leq d_{\mathrm{SN}})}{N_{\mathrm{SN,ROTSE}}}, \tag{9.5}$$

where $N_{\mathrm{SN,ROTSE}}(d \leq d_{\mathrm{SN}})$ is the number of SNe observable by the ROTSE telescopes within a sphere of radius d_{SN}. $N_{\mathrm{SN,ROTSE}}$ is the total number of SN observable by ROTSE. Accidental coincidences will be distributed following the square of the distance folded with ROTSE's sensitivity as a function of distance $\epsilon_{\mathrm{ROTSE}}(d)$ as defined in Sec. 7.6. Signal events are more likely to stem from close-by SNe, since only these will lead to a neutrino flux large enough to produce a detectable multiplet in IceCube.
The additional terms P_t and P_d for each observed SN light curve are combined with P_{SN} yielding the test statistic λ_{SN}.

$$\lambda_{\mathrm{SN}} = P_{\mathrm{SN}}(N_{\mathrm{SN}}, \mu_{\mathrm{SN}}) \prod_{i=1}^{N_{\mathrm{SN}}} P_t(\Delta t_i) \cdot P_d(d_{\mathrm{SN,i}}). \tag{9.6}$$

Combining all information into one test statistic λ results in:

$$\lambda = \lambda_\nu \cdot \lambda_{\mathrm{SN}}. \tag{9.7}$$

To obtain the p-value, i.e. the probability to find a similar excess than the one found in the data sample in a background only sample, 10^6 Monte Carlo (MC) experiments are performed: The number of multiplets (for multiplicities $2 \leq k < 4$)[1] and supernova counterparts are drawn following a Poisson distribution with the mean given by the expected average background, μ_k. This neutrino multiplet background is obtained from scrambled data sets following the prescription in Sec. 5.8, while the number of accidental detected optical SNe is computed as described in Sec. 7.7.
For each MC experiment, λ is calculated by inserting the drawn numbers in Eq. 9.7. The fraction of MC experiments resulting in a smaller value of λ compared to that obtained from the data sample (i.e. fraction of outcomes of the MC experiment, which show worse agreement with the background-only hypothesis than the measurement) yields the desired p-value. The significance of the IceCube only result can be obtained in a similar way using λ_ν instead of the combined test statistic λ.

[1] The upper bound of 4 was chosen to save computing time. The contribution of higher order multiplets is insignificant.

9.2 Limit Calculation

In order to test the soft jet SN model [100] a test statistic, λ, identical to that used in the significance calculation presented above, is used. In contrast to the significance calculation, which tests the compatibility of the measurement with the background-only hypothesis, here its compatibility with the model expectation is inspected. If a set of model parameters predicts a significant larger amount of multiplets and SN counterparts than measured in the data sample, the model can be excluded.
To obtain a proper confidence region for exclusion of the model, 10^4 Monte Carlo experiments are performed for each combination of model parameters. For each MC experiment the number of signal and background multiplets (with multiplicities of $2 \leq k < 5$) as well as SN counterparts are drawn following a Poisson distribution. The Poisson mean of the background distributions, $\mu_{k,b}$ and $\mu_{\mathrm{SN,b}}$ for neutrino multiplets and SN counterparts respectively are obtained in a similar way as described in the previous section, Sec. 9.1.
The signal estimation does not account for mixed multiplets due to a single SN neutrino in coincidence with a background neutrino. While in principle, these can be identified through an optical counterpart, the rate is estimated to be at most a few percent of the pure, signal-only multiplets. Hence, this extra contribution is neglected.
The mean number of expected signal neutrino multiplets $\mu_{k,s}$ and expected SN counterparts $\mu_{\mathrm{SN,s}}$, depend on the model parameters, E_{jet}, Γ and ρ. $\mu_{k,s}$ is obtained from the neutrino signal simulation weighted with the corresponding spectrum as predicted by Ando and Beacom [100]. The neutrino spectrum varies with E_{jet} and Γ as presented in Sec. 2.6 and the average number of SN detections scales with ρ. The average number of predicted SNe counterpart detections, $\mu_{\mathrm{SN,s}}$, depends on the number of neutrino multiplets, i.e. number of telescope pointings, folded with the sensitivity of the telescope.
For each MC experiment, λ is calculated following Eq. 9.7 with $N_k = N_{k,b} + N_{k,s}$ and $N_{\mathrm{SN}} = N_{\mathrm{SN,b}} + N_{\mathrm{SN,s}}$, where $N_{k,b}$ and $N_{k,s}$ are the drawn number of background and signal multiplets with multiplicity k and $N_{\mathrm{SN,b}}$ and $N_{\mathrm{SN,s}}$ are the number of drawn background and signal SN counterparts. If one or more optical counterparts are drawn in the MC simulation, the additional terms P_t and P_d are calculated following Eq. 9.4 and Eq. 9.5. The time difference between the SN neutrinos, i.e. the length of the neutrino burst, is set to $\Delta t = 10\,\mathrm{s}$. Since the arrival time distribution is not known and theories predict the high-energy neutrinos to arrive within $10\,\mathrm{s}$, this is a conservative assumption. The SN distance is drawn following a spatially isotropic distribution folded with ROTSE's efficiency.
The systematic uncertainties listed in Sec. 10 are included by smearing the Poisson mean, i.e. the Poisson mean of the respective parameter is multiplied by a factor following a Gaussian distribution with mean one (or slightly shifted from one if the uncertainties are not symmetric with respect to zero) and a width given by the systematic uncertainties.
The fraction of MC experiments resulting in a smaller value of λ than that obtained from the data sample is the desired confidence level for the exclusion of this combination of model parameters, i.e. if a model predicts a worse agreement with the background-only hypothesis (i.e. a larger excess) in 90% of all cases it can be excluded with 90% confidence. Figure 9.1 illustrates the calculation of the confidence level for one combination of model parameters.

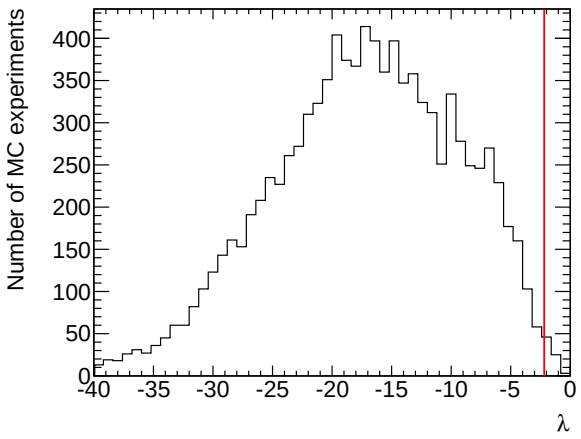

Figure 9.1: Example for confidence level calculation: 10000 Monte Carlo Experiments are performed. For each experiment $N_k = N_{k,b} + N_{k,s}$ (for multiplicities $2 \leq k < 5$) and $N^{\mathrm{SN}} = N_{\mathrm{SN,b}} + N_{\mathrm{SN,s}}$ are drawn following a Poisson distribution and the test statistic λ is calculated. The red line indicates the test statistic obtained from the data sample. The fraction of MC experiments with λ smaller than that from the data sample yields the confidence level, 99.3% in this example.

Chapter 10

Systematic Uncertainties

The result of this work, i.e. the limit on parameters of the soft jet SN model, is influenced by systematic uncertainties. Both the simulated neutrino sensitivity and the SN sensitivity are subject to systematic uncertainties. These systematic uncertainties are included in the limit calculation. In this limit calculation, Monte Carlo experiments are performed drawing the number of signal and background neutrino multiplets and optical counterparts following a Poisson distribution as described in Chap. 9.2. Systematic uncertainties are included by smearing the Poisson mean, i.e. the Poisson mean is multiplied by a factor following a Gaussian distribution with mean one (or slightly shifted from one if the uncertainties are not symmetric with respect to zero) and a width given by the systematic uncertainties.

10.1 Systematic Uncertainties on the Neutrino Sensitivity

The systematic uncertainties are dependent on the signal neutrino energy spectrum. The SN neutrino spectrum varies with the model parameters. Therefore, the systematic uncertainties are obtained for various model parameter combinations in the range $2 \leq \Gamma \leq 10$ and $3.1 \times 10^{49}\,\mathrm{erg} \leq E_{\mathrm{jet}} \leq 3 \times 10^{53}\,\mathrm{erg}$.
The main sources of systematic uncertainties are the DOM efficiency and the photon propagation in ice. Dedicated simulations varying the absorption and scattering coefficients as well as the DOM efficiency within their systematic uncertainties (~10% [125, 181]) were used to study the influence on the predicted event rate. It was found that the largest effect on the event rate (up to 13%) occurred when decreasing or increasing absorption and scattering coefficient at the same time. Varying the DOM efficiency resulted in a variation of the event rate of up to 18%.
The neutrino cross section used in the neutrino simulation, σ_{CTEQ}, is based on CTEQ5 [182] results, which have been superseded by a more accurate parameter set based on more recent measurements [183, 184]. The latest cross section calculation by Cooper-Sakar and Sakar [112], σ_{CSS}, differ from the cross sections used in the IceCube neutrino simulation as illustrated in Fig. 10.1, which shows the discrepancy in the cross section for charged current neutrino interactions. To first order, the rate of detected neutrinos depends linearly on the cross section. Folding the expected SN neutrino spectrum with an energy dependent correction factor given by $\sigma_{\mathrm{CSS}}/\sigma_{\mathrm{CTEQ}}$ allows to calculate the effect on the neutrino event rate, which is up to 6%.
Finally, the uncertainty in the muon energy loss is 1%, resulting in a 1% influence on the event rate [185].
The systematic uncertainties mentioned above are combined by a quadratic sum. Table 10.1 summarizes the systematic uncertainties considered in this analysis and their influence on

the event rate (for those model parameters, where the effect is largest), while Fig. 10.2 shows the quadratic sum of the systematic uncertainties for various model parameters. The Poisson mean used to draw the number of detected SN neutrino multiplets in MC experiments in the limit calculation is smeared by multiplying it with a factor following a Gaussian distribution with mean one and a width given by the quadratic sum of the systematic uncertainies. This factor is drawn in each MC experiment.
The background expectation is obtained from scrambled data sets and is thus not subject to any systematic uncertainties.

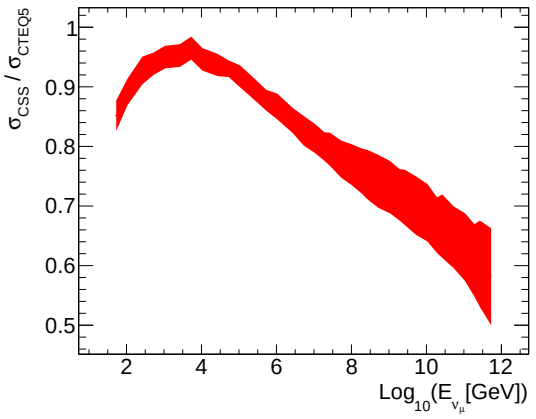

Figure 10.1: Ratio of neutrino cross sections obtained from CTEQ5 results and calculated based on more recent measurements by Cooper-Sakar and Sakar [112] as a function of energy. The uncertainty band includes statistic and systematic errors [112].

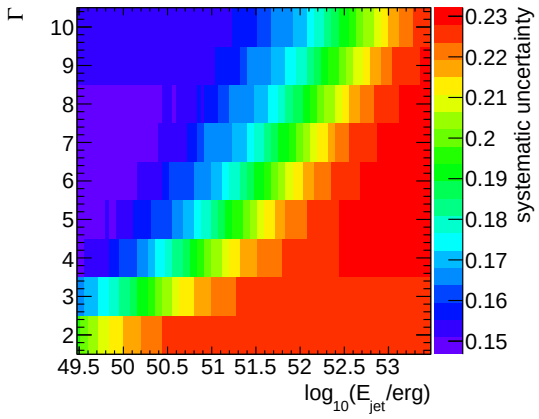

Figure 10.2: Systematic uncertainty (relative to the predicted SN neutrino event rate) depending on the model parameters Γ and E_{jet}.

Table 10.1: Systematic Uncertainties on the Neutrino Sensitivity

Source of uncertainty	Uncertainty	Influence on event rate
DOM Efficiency	$\pm 10\%$	$\pm 18\%$
Photon propagation	$\pm 10\%$	$\pm 13\%$
Neutrino cross section	see Fig. 10.1	-6%
Muon energy loss	$\pm 1\%$	$\pm 1\%$

10.2 Systematic Uncertainties on the SN Sensitivity

The number of expected observed SNe depends on the telescope's sensitivity. The estimate described in Sec. 7.6 yields the efficiency as a function of the apparent SN peak magnitude. The photometric zero-points as determined from USNO A2.0 R-band magnitudes have typical systematic uncertainties of up to 0.3 mag ([186] and references therein). Shifting the efficiency curve by ± 0.3 mag results in a variation of the expected number of SNe measured

by ROTSE of $[-17.6\%, +26.6\%]$.
The expected number of accidentally found SNe depends on the overall core-collapse SN rate, which is assumed to be 1 SN per year within a sphere of radius $10\,\mathrm{Mpc}$ (continuum limit from [187]). The true SN rate might be higher since nearby supernovae surveys tend to not target small galaxies [188]. A systematic error of 30% is assumed due to inhomogeneity of the local universe and 30% on the core-collapse supernova rate.
The visual scanning of the final candidates was carried out by three individuals, who obtained similar results. All simulated SNe that passed the computer selection were identified in the scanning by all three individuals, i.e. the efficiency was 100%. Also the rate of false positives is expected to be small, because potential SN candidates would be inspected in detail (e.g. their light curve and the host galaxy, see also Sec. 11.2.1). Therefore, the systematic uncertainty introduced by the scanning process is neglected. Note that in the future, for candidates identified in real time, a spectrum can be obtained to ensure an unambiguous identification of the SN.
Table 10.2 summarizes the systematic uncertainties on the SN sensitivity. The number of signal SN counterparts is influenced by the magnitude measurement, but not by the CCSN rate. The rate of CCSN with jets is a parameter in the limit calculation, i.e. the limit is quoted for a certain rate of CCSNe with jets. The Poisson mean used to draw the number of detected optical SN counterparts in MC experiments in the limit calculation is smeared by multiplying it with a factor following a Gaussian distribution with mean 1.045 and a width 0.221. The mean is shifted from zero since the systematic uncertainties due to the magnitude measurement are not symmetric with respect to zero.
The background expectation is also subject to systematic errors introduced by the magnitude measurement and in addition to the uncertainty of the CCSN rate as well as the inhomogeneity of the local universe. The Poisson mean to draw the number of accidentially detected SNe, i.e. the background expectation, is thus multiplied by a factor following a Gaussian with mean 1.021 and a width given by the quadratic sum of the three mentioned uncertainties, 0.48.

Table 10.2: Systematic Uncertainties on the SN Sensitivity

Source of uncertainty	**Uncertainty**	**Influence on SN rate**
Magnitude measurement	$0.3\mathrm{mag}$	$-17.6\%, +26.6\%$
CCSN rate	$\pm 30\%$	$\pm 30\%$
Inhomogeneity of the local universe	$\pm 30\%$	$\pm 30\%$
Quadratic sum		$-45.9, +50.1\%$

Chapter 11

Results

In this chapter, the results from the analysis of data taken by the optical follow-up program in the period of December 16, 2008 to December 31, 2009 are presented. IceCube was running initially in the 40-string configuration (December 16, 2008 to May 20, 2009), IC40, and later in the 59-string configuration (May 20, 2009 to Dec 31, 2009), IC59[1]. Table 11.1 summarizes the results of the neutrino multiplet and the optical counterpart search. It shows the number of detected and expected doublets and triplets for the IC40 and the IC59 data sets as well as the number of detected and expected optical SN counterparts. The results are discussed in detail below.
Appendix C provides a detailed table containing all alert information.

Table 11.1: Measured and Expected Multiplets

	SN	Doublets		Triplets	
		IC40	IC59	IC40	IC59
measured	0	15	19	0	0
expected	0.074	8.55	15.66	0.0028	0.0040

11.1 IceCube Multiplets

A total of 34 doublets (15 in IC40 and 19 in IC59) are detected while no triplet or multiplet of higher order was observed. The IceCube expectation based on a background only hypothesis was obtained from scrambled data sets (see Sec. 5.8). The number of doublets shows a small upward fluctuation. The significance of the excess is calculated following the description in Sec. 9.1 (see Fig. 11.1 for illustration). The method was predefined before the analysis was applied to the data in order to avoid the introduction of a bias. The obtained p-value is 0.0348, i.e. a similar or larger excess was found in 3.48% of all scrambled data sets, corresponding to 2.1σ and is thus not statistically significant.

[1]Note that the IceCube detector was running in the 40-string configuration already before Dec. 2008 and took data with the 59-string configuration also after Dec. 2009. The 2010 data set is currently analyzed.

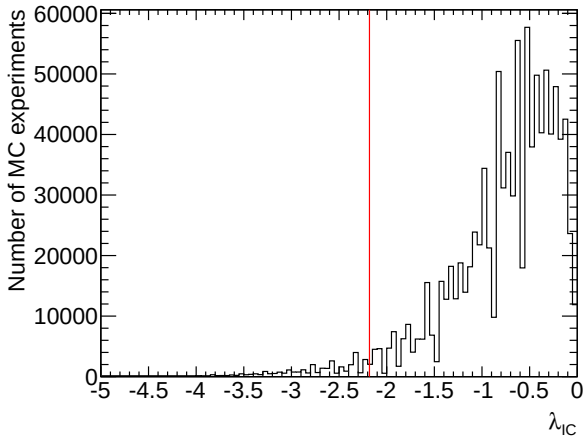

Figure 11.1: Significance calculation: 10^6 Monte Carlo experiments are performed. For each experiment N_k (for multiplicities 2 and 3) are drawn following a Poisson distribution according to the background only hypothesis and the test statistic λ_{IC} is calculated. The red line indicates the test statistic obtained from the data sample. The fraction of MC experiments with λ_{IC} smaller than the measured value yields the p-value, which is 0.0348 and corresponds to 2.1σ.

To check if the measured doublets are consistent with background the following parameter distributions are inspected and compared to the expected background distributions:

- Arrival time distribution of doublets (Fig. 11.2).
- θ and ϕ distribution, i.e. direction in detector coordinates (Fig. 11.3 and Fig. 11.4).
- ΔT and $\Delta\Psi$ distribution, i.e. time and angular difference between the two events comprising a doublet (Fig. 11.5 and Fig. 11.6).

The statistical errors for the measurement doublets are large and a meaningful comparison is limited by the lack of statistics. No obvious deviation from the expectation is found.

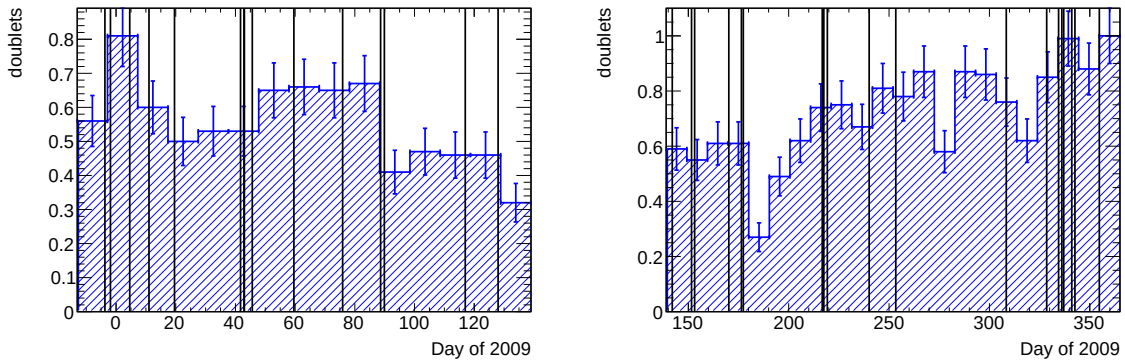

(a) IC40 (b) IC59

Figure 11.2: Arrival time distribution of doublets obtained from scrambling (blue) and all measured doublets (black).

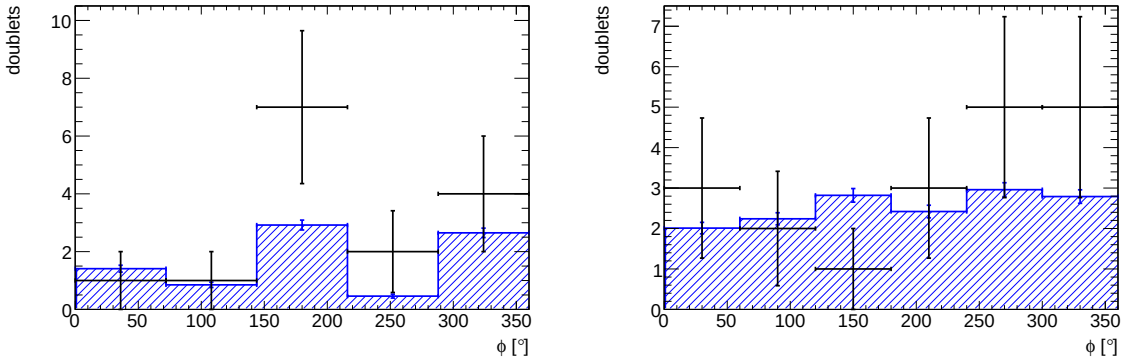

(a) IC40 (b) IC59

Figure 11.3: Distribution of the azimuth angle, ϕ, of all measured doublets (black) compared to the expected distribution obtained from scrambling (blue).

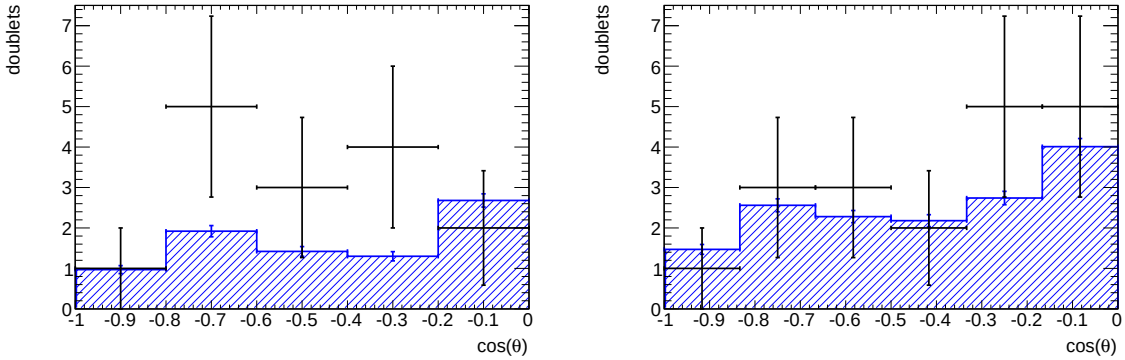

(a) IC40 (b) IC59

Figure 11.4: Distribution of the zenith angle, θ, of all measured doublets (black) compared to the expected distribution obtained from scrambling (blue).

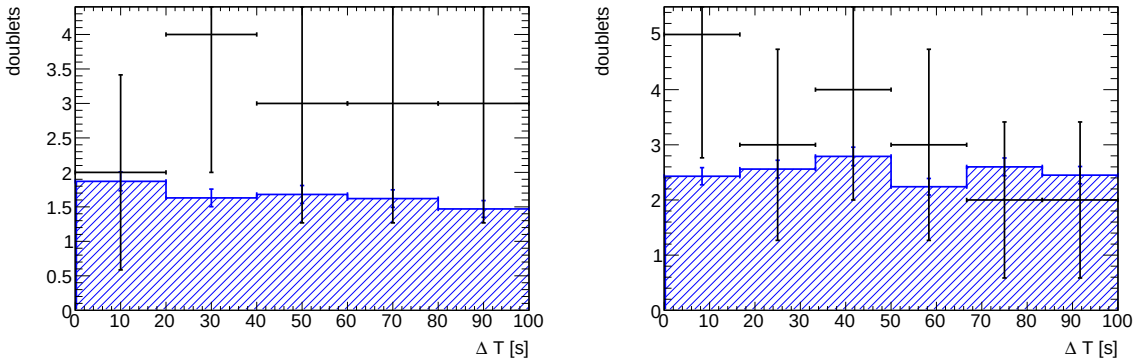

(a) IC40 (b) IC59

Figure 11.5: Distribution of the time difference, ΔT, between the two neutrino events for each measured doublet (black) compared to the expected distribution obtained from scrambling (blue).

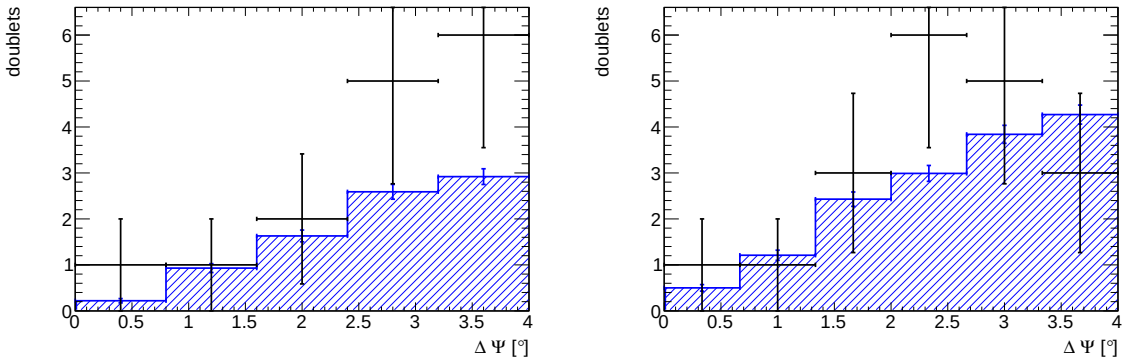

(a) IC40 (b) IC59

Figure 11.6: Distribution of the angular difference, $\Delta\Psi$, between the two neutrino events for each measured doublet (black) compared to the expected distribution obtained from scrambling (blue).

11.2 Optical Counterpart

In total 31 alerts were forwarded to the ROTSE telescopes. Five of these could not be observed because they were too close to the sun. For two alerts no good imaging data could be collected. Fields that contained more than 85000 USNO catalog stars or where closer than 5° to the Galactic plane, where discarded. Those fields are crowded with stars and the single point spread functions start overlapping causing the convolution algorithm and hence the subtraction to fail. Furthermore, the extinction caused by dust and gas in the Galactic plane increases for decreasing distance to the Galactic plane (see Fig. 11.7). Seven alerts were discarded because the corresponding fields were too close to the Galactic plane or too crowded. Thus, 17 good optical datasets remain for the analysis. Table C.1 in appendix C summarizes the triggers sent to ROTSE.
The data are processed as described in Chap. 7. No optical SN counterpart was found. The most interesting candidate found in the optical data is identified as a mis-subtraction and is exemplarily discussed in Sec. 11.2.1.
The expected background of accidentally observed SNe is calculated according to equation 7.13. The null result is consistent with the small expectation value of 0.074 accidentally discovered SNe.

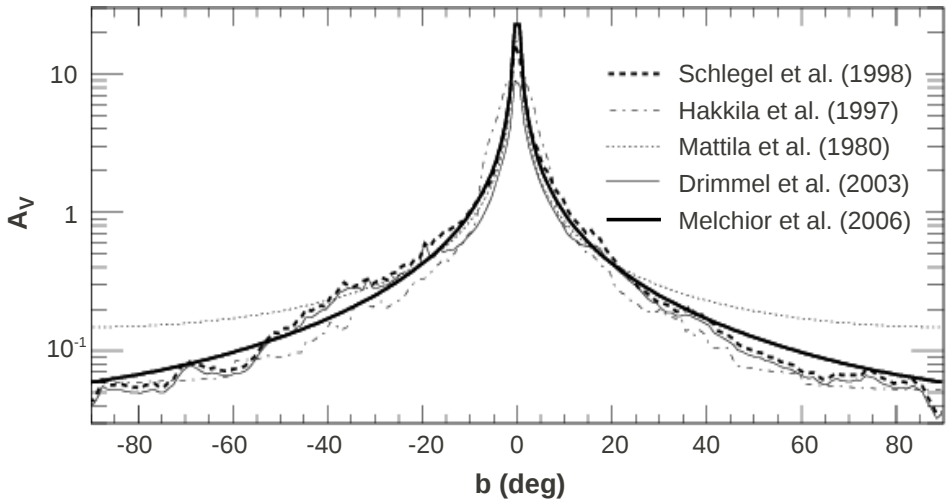

Figure 11.7: Extinction as a function of Galactic latitude according to different models (modified from [189]). Close to the Galactic center the extinction is highest.

11.2.1 Most interesting SN candidate

Several candidates with only two or three detections were found on top of large galaxies. Their location on top of a galaxy makes them potentially interesting supernova candidates. On the other hand the bright center of a galaxy can complicate the image subtraction. All candidates except one disappeared when a new deeper reference image was used and hence were discarded as bad subtractions. However, one candidate still occurred after updating the reference image. This candidate was found at the position of the galaxy CGCG 424-006 (see Fig. 11.8 for the SDSS image), which has a distance of 119.2 ± 8.3 Mpc. The galaxy is classified as a spiral galaxy containing a weak nuclear bar [190] and can not be resolved in the ROTSE images.

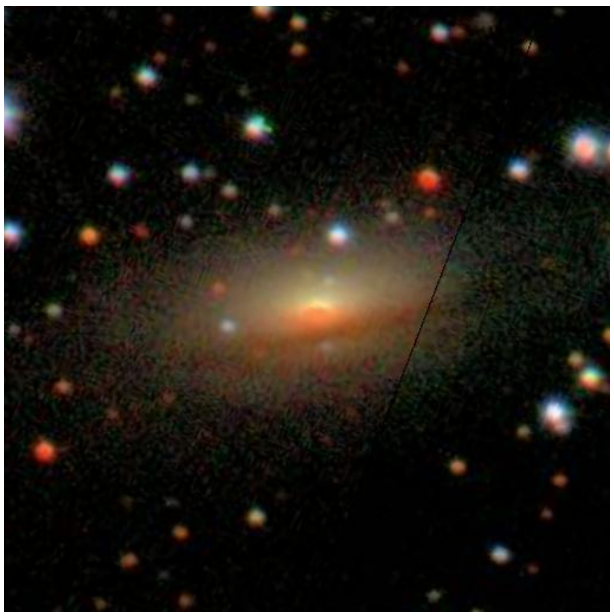

Figure 11.8: SDSS image of the galaxy CGCG 424-006.

Inspecting the light curve

The obtained light curve shown in Fig. 11.10 is inspected in order to check its consistency with a SN light curve. Bad images with an average $\mathrm{FWHM} > 5$ were excluded from the light curve plot. A triangle indicates the limiting magnitude for each image, while a red square indicates, that the candidate was detected in this night and shows the magnitude of the detection. If the candidate is a SN, its light curve is expected to follow a continuous slowly rising curve starting with the neutrino detection, which is indicated by an orange line in Fig. 11.10.
Obviously the light curve does not follow the expected slowly rising behavior. However, a plateau SN (type IIP) can be considered in order to explain the fast rise and flat plateau. Therefore, the observed plateau is fitted with a constant. The fit is drawn as a blue line with uncertainties marked as shaded red region.
The uncertainties on the magnitude were obtained by studying the variation of the detected magnitude of stars from the USNO catalog (see Fig. 11.11) in different nights. If a star with constant magnitude is observed at different nights the detected magnitude might differ from night to night depending on weather, atmosphere, calibration etc. The standard deviation of the magnitude measurement for each star, which was detected in all nights of this data set, is one entry in the histogram shown in Fig. 11.11. Bright stars show less variations from night to night compared to dim stars. Mean and median for each magnitude bin are displayed as black rectangles and circles respectively. A polynomial of order 7 is fitted to the histogram and drawn as a black line. The error bars displayed in Fig. 11.10 are calculated using the fitted function.
One expects to find red squares indicating a detection for every night lying within the error band shown in Fig. 11.10. However, if the limiting magnitude is smaller than the expected magnitude of the candidate in this night, the object would be too dim to be detected (e.g. data point of 090607). Another possible explanation for a missing detection is a bad subtraction of the image (e.g. data point of 090616), which can be discovered by a visual inspection as illustrated in Fig. 11.9.
Green triangles show the limiting magnitude of each image with a found detection. Lim-

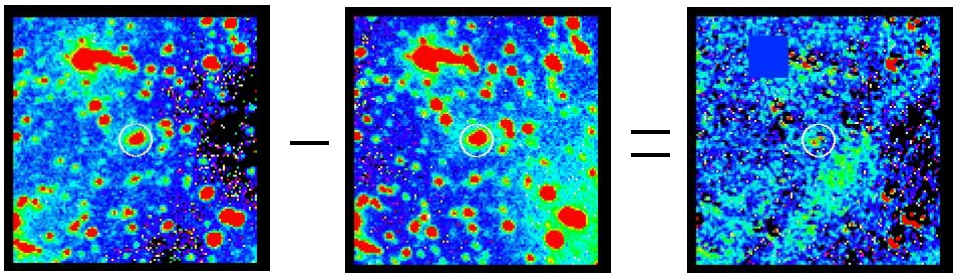

Figure 11.9: Bad subtraction of night 090616. Left: new image, center: reference image, right: subtracted image. Dipole pattern is present for all subtracted objects.

iting magnitudes of images without detection of the object are marked with blue triangles. The non detections can be explained by mis-subtraction after visual inspection of the subtractions in all cases but two. Those two cases are marked with red boxes. These two observations occur with limiting magnitudes significantly dimmer than the expected plateau. One could suggest that the brightness of the object varies on the time scale of days to explain the detection in some nights and the non detection in other nights. However, variations on the time-scale of days have not been observed in SN light curves and have no physical foundation. Hence, the shape of the light curve does not look consistent with a plateau supernova or any other SN type.
A second argument indicating this candidate is likely not a SN is the following: The observed apparent R-band plateau magnitude obtained by the fit is 16.4 mag. Taking into account the galaxy's distance of 119.2 Mpc the resulting absolute magnitude would be -19, which seems unreasonable bright for a plateau SN. The absolute I-band plateau magnitudes of plateau SNe have been observed to follow a Gaussian distribution with mean -17.75 mag and width 1 mag [191]. According to the light curve templates shown in Fig. 7.7, the expected R-band magnitude would be even dimmer than the I-band.
For this two reasons, this candidate is rejected as a SN candidate.

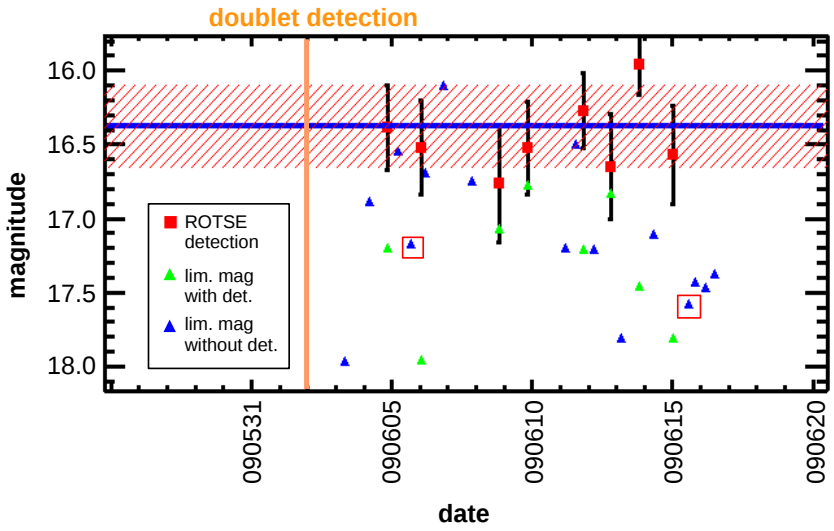

Figure 11.10: Light curve of most interesting candidate: Red squares indicate detections of the object by the processing pipeline. Green triangles show the limiting magnitude of each image with a found detection. Limiting magnitudes of images without detections of the object are marked with blue triangles. The plateau is fitted with a constant (blue, uncertainties in red). See text for details.

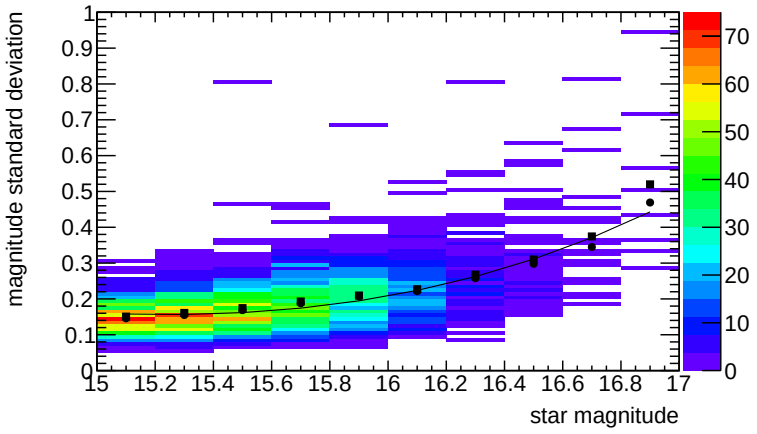

Figure 11.11: Estimating the magnitude error: Each entry in the histogram represents the standard deviation in the magnitude measurement between different nights of individual stars from the USNO catalog. Mean and median for each magnitude bin are displayed as rectangles and circles respectively. A polynomial of order 7 is fitted to the data and drawn as a black line.

11.3 Combined Results - Limit Calculation

Both the IceCube results and the result of the optical data analysis are combined to obtain a limit on the SN model parameters. Those model parameters are the Lorentz boost factor of the jet Γ, the jet energy $E_{\rm jet}$ and the rate of CCSN producing relativistic jets, ρ. The limit is calculated following the description in Sec. 9.2 for the jet Lorentz boost factors $\Gamma = 6, 8, 10$, for jet energies in the range $3 \times 10^{49}\,\mathrm{erg} \leq E_{\rm jet} \leq 3 \times 10^{53}\,\mathrm{erg}$ and CCSN rates in the range of $7.9 \times 10^{-4}\,\mathrm{Mpc^{-3}y^{-1}} \leq \rho \leq 1.3 \times 10^{-6}\,\mathrm{Mpc^{-3}y^{-1}}$. The algorithm was formulated prior to the start of the program. The systematic errors discussed in Sec. 10 are included in the limit calculation.
The 90% confidence regions for each Γ-value are displayed in the $E_{\rm jet}$-ρ-plane in Fig. 11.12. The basic shape of the constraints that can be obtained in the $E_{\rm jet}$-ρ plane can be understood from the following considerations: If the flux of neutrinos is a factor $\epsilon_{\rm jet}$ larger, one will be able to detect neutrino multiplets from a $\sqrt{\epsilon_{\rm jet}}$ more distant object. Correspondingly, the rate of detections will increase as the volume $\propto \epsilon_{\rm jet}^{3/2}$. Furthermore, the expected number of detections scales linearly with the rate of SNe ρ. Therefore, the total number of SNe detections as a function of SN rate and jet kinetic energy scales as $\rho\epsilon_{\rm jet}^{3/2}$.
The break at large jet energies is due to the cutoff in the neutrino spectrum caused by a cutoff in the proton spectrum when the proton energy reaches the photo-pion production threshold (see also Fig. 2.18).
The most stringent limit can be set for high Γ-factors, while for small Γ the constraints are weak. The Γ dependence is less obvious. The normalization of the SN neutrino flux depends on Γ^2. On the other hand a narrow jet pointing reduces the probability of the jet pointing toward Earth by $1/\Gamma^2$ resulting from the assumed collimation of the jet with an opening angle of $\theta = 1/\Gamma$. Furthermore, the radiative and hadronic cooling breaks of the neutrino spectrum scale with Γ^5 and Γ respectively. Large rates of SNe with jets and large jet energies

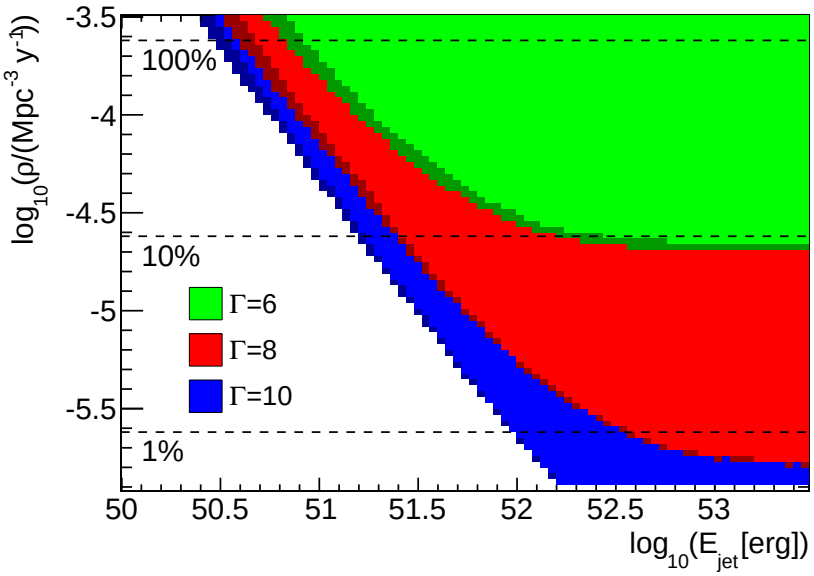

Figure 11.12: Limit (90% confidence level) to choked jet SN model for different Lorentz boost factors. Blue: $\Gamma = 10$. Red: $\Gamma = 8$. Green: $\Gamma = 6$. Horizontal dashed lines indicate a fraction of SNe with jets of 100%, 10% or 1%. Darker colors indicate the improvement obtained by including the optical information.

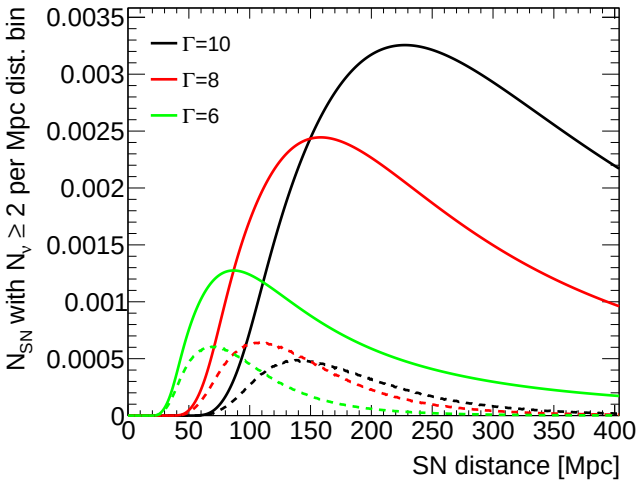

Figure 11.13: Number of SN per 1 Mpc distance bin producing at least two detectable neutrinos in IceCube (solid lines) and have an optical counterpart detected by ROTSE (dashed line) as a function of the SN distance for different Lorentz factors Γ assuming $E_{\rm jet} = 3 \times 10^{51}$ erg and 1% of all CCSN producing a jet. At larger distances the neutrino flux becomes too small to produce two detectable neutrinos in IceCube. ROTSE cannot detect the optical counterpart of distant and thus dim SNe.

can be excluded, since those lead to high neutrino flux predictions. No constraints can be made for small rates due to the limited volume accessible to IceCube and ROTSE as illustrated in Fig. 11.13. Smaller rates can be excluded with growing jet energies limited, however, at large jet energies due to the cutoff in the neutrino spectrum.
At 90% confidence level, a sub-population of SNe with typical values of Γ and $E_{\rm jet}$ of 10 and 3×10^{51} erg, respectively, does not exceed 4.2%. Including the optical information into the limit calculation improved the limit and allows to test $5 - 25\%$ smaller CCSN rates. The largest improvement is obtained for small jet energies and large CCSN rates.
This is the first limit on CCSN jets using neutrino information. Already after one year of data taking with the optical follow-up program a large fraction of the model parameter space can be excluded. A much stronger limit will be obtained with the, now completed, IceCube detector over its anticipated lifetime of at least 10 years (see Chap. 12).

Chapter 12

Summary and Outlook

This first analysis, using the four ROTSE telescopes, proves the feasibility of the program for follow-up observations triggered by neutrino multiplets detected by IceCube. The technical challenge of analyzing neutrino data in real time at the remote location of the South Pole and triggering optical telescopes has been solved. First meaningful limits to the SN slow-jet hypothesis could be derived already after the first year of operation. Especially in cases of high Lorentz boost factors of $\Gamma = 10$ stringent limits to the soft jet SN model are obtained: a sub-population of SNe with typical values of $\Gamma = 10$ and $E_{\rm jet} = 3 \times 10^{51}$ erg does not exceed 4.2% (at 90% confidence level).
Soderberg et al. [192] obtain an estimate on the fraction of SNe harboring a central engine from a radio survey of type Ibc SNe. They conclude that the rate is about 1%, consistent with the inferred rate of nearby GRBs. The approach presented here is completely independent and for the first time directly tests hadronic acceleration in core-collapse supernovae, while the radio counterpart indicates leptonic acceleration. While radio programs are typically limited in observation time, IceCube continuously monitors half of the sky. Hence, this limit is expected to improve faster than the radio limit. However, the radio limit might profit from future wide field radio observatories such as Lofar [193] and SKA [194].
Meanwhile, the instrumented volume of IceCube has increased to a cubic kilometer yielding an increased sensitivity to high-energy neutrinos. Almost twenty more month of data have been recorded already and the livetime is growing continuously. Figure 12.1 shows the number of predicted SN, which create a signal of two or more detectable neutrinos in IceCube. It compares the number expected for this work (Fig. 12.1(a)) with 10 years of operations with the completed IceCube detector consisting of 86 strings (Fig. 12.1(b)). The number of SNe grows linearly with the accumulated livetime and increases with $x^{3/2}$, if the number of detected neutrinos increases with x. The number of neutrinos per SN increases by a factor of ~1.8 due to the larger detector volume and improved event selection and the livetime by a factor of 10, thus the number of expected SN detections increases by $(1.8)^{3/2} \cdot 10 = 24$. Hence, a detection of high-energy SN neutrinos as predicted by the slow jet model within the operation time of IceCube (at least 10 years with the full IC86 detector) becomes much more likely. If IceCube does not succeed in detecting the predicted SN neutrino flux in the future, a large fraction of the model parameter space can be excluded. An estimated limit after 10 years of observation with IC86 assuming that the number of detected multiplets is equal to the background expectation is shown in Fig. 12.2. Note that the limit improved by more than a factor of ~24 compared to the result of this analysis (see Fig. 11.12). This is due to the fact that an upward fluctuation in the number of doublets was observed in IC40 and IC59 while the number of measured doublets was set equal to the number of expected doublets to compute the future limit. In the future the limit could be improved further by performing the optical observations of the IceCube triggers with a more powerful telescopes. Figure 12.2

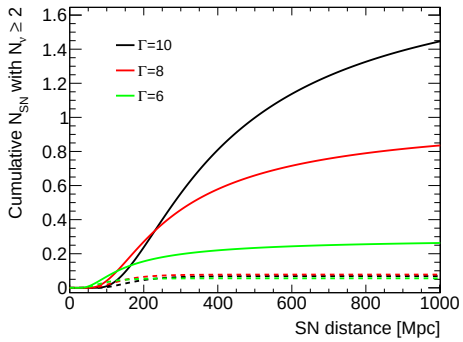

(a) This work (~130 d with IC40 and ~200 d with IC59) in combination with ROTSE.

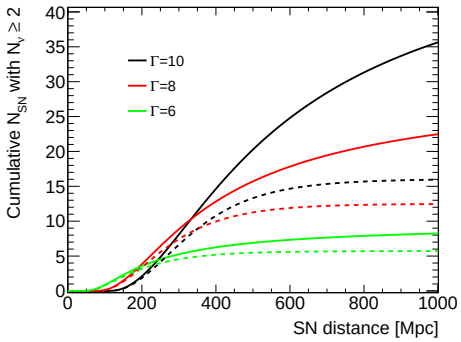

(b) 10 years operation with IC86 combined with a more powerful telescope (assuming it is capable of detecting SNe with a peak magnitude of 20.5 mag).

Figure 12.1: Expected number of SN with two or more neutrinos detected by IceCube assuming a jet energy of $E_{\rm jet} = 3 \times 10^{51}$ erg and that 1% of all CCSN produce a jet.

(darker colors) shows the expected limit assuming a telescope, which is capable of detecting SNe with an apparent peak magnitude of 20.5 mag. Furthermore a more powerful optical instrument allows the identification of more distant sources (see Fig. 12.1(b)) Due to the successful operation of the optical follow-up program with ROTSE, the program was extended in August 2010 to the Palomar Transient Factory (PTF) [195, 196], which offers a fast processing pipeline including a spectroscopic follow-up of interesting SN candidates. It has a limiting magnitude of 21.2 mag [195] in the R-band and will thus provide deeper images compared to ROTSE.

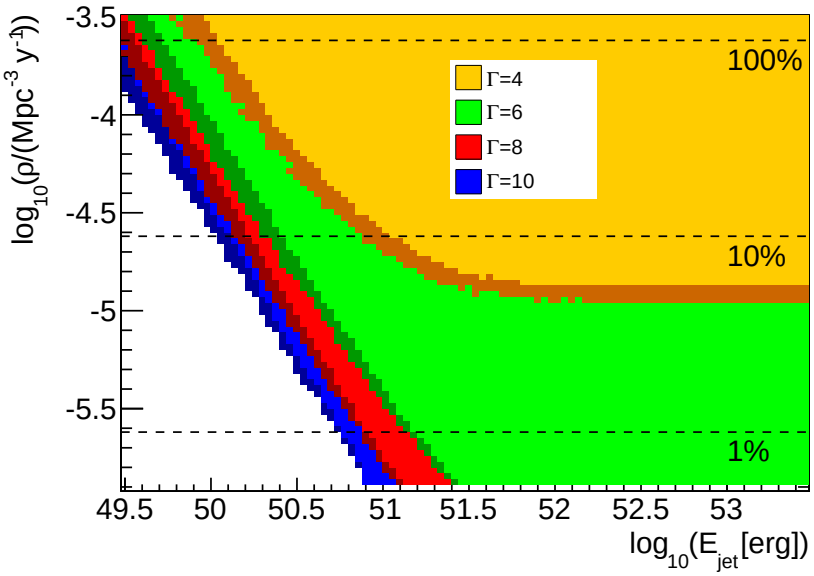

Figure 12.2: Estimated limit for 10 year of operation with the full IceCube detector combined with a more powerful telescope (darker colors), which is capable of detecting SNe with an apparent peak magnitude of 20.5 mag. It is assumed that the number of detected multiplets and SN counterparts are equal to the background expectation.

Furthermore, the delay of processing neutrino data at the South Pole has been reduced significantly from several hours to a few minutes. This results in the possibility of a very fast follow-up and allows the detection of GRB afterglows, which fade rapidly below the telescope's detection threshold. In addition, GRB neutrinos follow a harder energy spectrum compared to the predicted SN neutrinos. Another interesting possibility for the detection of high-energy GRB neutrinos therefore is a single ultra-high energy event trigger. This trigger is currently under development [197] and is expected to increase the detection probability for GRB neutrinos.
In addition, an X-ray follow-up [198] of the most significant multiplets performed by the Swift satellite [199] has been set up and started operations in February 2011. The X-ray follow-up increases the sensitivity especially for GRBs. An X-ray afterglow can be detected for ~95% [63] of all bursts, while an optical afterglow can only be detected for ~60% [72] of all bursts. The X-ray follow up is sensitive to typical GRBs, but also to SN shock breakouts, slightly off-axis GRBs [200] and gamma-dark GRBs [201], which will not emit any gamma-rays but might still have a neutrino and an optical signal. While no firm estimate exists, the number of these dark bursts might be ten times larger than gamma-bright bursts.
The optical follow-up program delivered first results and opens a wide variety of possibilities, and - with the data it will acquire in the future - may provide more insight in the most violent events in the universe.

"Neutrino physics is largely an art
of learning a great deal by observing nothing."

Haim Harari

Bibliography

[1] W. Pauli. in "Rapports du Septième Conseil de Physique Solvay", Brussels, 1933 (Gauthier-Villars, Paris, 1934).

[2] F. Reines and C. L. Cowan, "Detection of the free neutrino," *Phys. Rev.* **92** (1953) 830–831.

[3] C. L. Cowan, F. Reines, F. B. Harrison, H. W. Kruse, and A. D. McGuire, "Detection of the free neutrino: A Confirmation," *Science* **124** (1956) 103–104.

[4] G. Danby, J. Gaillard, K. A. Goulianos, L. Lederman, N. B. Mistry, *et al.*, "Observation of High-Energy Neutrino Reactions and the Existence of Two Kinds of Neutrinos," *Phys.Rev.Lett.* **9** (1962) 36–44.

[5] **DONUT** Collaboration, K. Kodama *et al.*, "Observation of tau neutrino interactions," *Phys.Lett.* **B504** (2001) 218–224, `hep-ex/0012035`.

[6] M. Gonzalez-Garcia and Y. Nir, "Neutrino masses and mixing: Evidence and implications," *Rev.Mod.Phys.* **75** (2003) 345–402, `hep-ph/0202058`.

[7] **Particle Data Group** Collaboration, K. Nakamura *et al.*, "Review of particle physics," *J.Phys.G* **G37** (2010) 075021.

[8] R. Davis, D. S. Harmer, and K. C. Hoffman, "Search for Neutrinos from the Sun," *Phys. Rev. Lett.* **20** (May, 1968) 1205–1209.

[9] J. Bahcall, W. A. Fowler, J. Iben, I., and R. Sears, "Solar neutrino flux," *Astrophys.J.* **137** (1963) 344–346.

[10] **Super-Kamiokande** Collaboration, K. Abe *et al.*, "Solar neutrino results in Super-Kamiokande-III," *Phys.Rev.* **D83** (2011) 052010, `hep-ex/1010.0118`.

[11] R. Svoboda, "The sun in neutrino light." Louisiana State.

[12] C. Burrows, "Image of SN1987A observed by HST." HST, NASA.

[13] **KAMIOKANDE-II** Collaboration, K. Hirata *et al.*, "Observation of a Neutrino Burst from the Supernova SN 1987a," *Phys.Rev.Lett.* **58** (1987) 1490–1493.

[14] **IMB** Collaboration, J. Van Der Velde *et al.*, "Neutrinos from SN1987A in the IMB Detector," *Nucl.Instrum.Meth.* **A264** (1988) 28–31.

[15] E. Alekseev, L. Alekseeva, I. Krivosheina, and V. Volchenko, "Detection of the Neutrino Signal from SN1987A using the INR BAKSAN Underground Scintillation Telescops,".

[16] V. Hess and W. Kolhoerster, "Über Beobachtungen der durchdringenden Strahlung bei sieben Freiballonfahrten," *Physikalische Zeitschrift* (1912).

[17] R. M. Kulsrud, J. P. Ostriker, and J. E. Gunn, "Acceleration of Cosmic Rays in Supernova Remnants," *Phys. Rev. Lett.* **28** (Mar, 1972) 636–639.

[18] A. Hillas, "The Origin of Ultrahigh-Energy Cosmic Rays," *Ann.Rev.Astron.Astrophys.* **22** (1984) 425–444.

[19] **The Pierre Auger** Collaboration, M. Unger, "Study of the Cosmic Ray Composition above 0.4 EeV using the Longitudinal Profiles of Showers observed at the Pierre Auger Observatory,".

[20] K. Greisen, "End to the cosmic ray spectrum?," *Phys.Rev.Lett.* **16** (1966) 748–750.

[21] G. Zatsepin and V. Kuzmin, "Upper limit of the spectrum of cosmic rays," *JETP Lett.* **4** (1966) 78–80.

[22] L. A. Anchordoqui and T. Montaruli, "In Search for Extraterrestrial High Energy Neutrinos," *Ann.Rev.Nucl.Part.Sci.* **60** (2010) 129–162, astro-ph/0912.1035.

[23] T. Chiarusi and M. Spurio, "High-Energy Astrophysics with Neutrino Telescopes," *Eur.Phys.J.* **C65** (2010) 649–701, astro-ph/0906.2634.

[24] J. K. Becker, "High-energy neutrinos in the context of multimessenger physics," *Phys.Rept.* **458** (2008) 173–246, astro-ph/0710.1557.

[25] P. Lipari, "Perspectives of High Energy Neutrino Astronomy," *Nucl.Instrum.Meth.* **A567** (2006) 405–417, astro-ph/0605535.

[26] E. Waxman, "Cosmological gamma-ray bursts and the highest energy cosmic rays," *Phys.Rev.Lett.* **75** (1995) 386–389, astro-ph/9505082.

[27] A. MacFadyen and S. Woosley, "Collapsars: Gamma-ray bursts and explosions in 'failed supernovae'," *Astrophys.J.* **524** (1999) 262, astro-ph/9810274.

[28] B. Paczynski, "Are gamma-ray bursts in star forming regions?," *Astrophys.J.* **494** (1998) L45, astro-ph/9710086.

[29] S. E. Woosley, "Gamma-ray bursts from stellar mass accretion disks around black holes," *Astrophys.J.* **405** (1993) 273.

[30] **IceCube and IPN** Collaboration, A. Achterberg *et al.*, "The Search for Muon Neutrinos from Northern Hemisphere Gamma-Ray Bursts with AMANDA," *Astrophys.J.* **674** (2008) 357–370, astro-ph/0705.1186.

[31] **IceCube** Collaboration, R. Abbasi *et al.*, "Limits on Neutrino Emission from Gamma-Ray Bursts with the 40 String IceCube Detector," *Phys.Rev.Lett.* **106** (2011) 141101, astro-ph/1101.1448.

[32] **IceCube** Collaboration, R. Abbasi *et al.*, "Constraints on high-energy neutrino emission from SN 2008D," *Astron.Astrophys.* **527** (2011) A28, astro-ph/1101.3942.

[33] M. Kowalski and A. Mohr, "Detecting neutrino-transients with optical follow-up observations," *Astropart.Phys.* **27** (2007) 533–538, astro-ph/0701618.

[34] D. A. Green and F. R. Stephenson, "The Historical Supernovae," astro-ph/0301603.

[35] S. Woosley and T. Janka, "The physics of core-collapse supernovae," *Nature Physics* (2006) astro-ph/0601261.

[36] J. Warren, J. Hughes, *et al.*, "Image of SNR Tycho observed by Chandra." NASA, CXC.

[37] J. Hester, A. Loll, *et al.*, "Image of Crab Nebula observed by HST." NASA, ESA.

[38] S. Reynoolds *et al.*, "Image of Kepler's SNR observed by Chandra." NASA, CXC, NCSU.

[39] P. Nugent, "Peter Nugent's Spectral Templates." http://supernova.lbl.gov/ nugent/nugent_templates.html.

[40] J. B. Doggett and D. Branch, "A comparative study of supernova light curves," *Astron.J.* **90** (1985) 2303–2311.

[41] Wikipedia, "Binding energy curve." http://en.wikipedia.org/wiki/File:Binding_energy_curve_-_common_isotopes.svg.

[42] H.-T. Janka, K. Langanke, A. Marek, G. Martinez-Pinedo, and B. Mueller, "Theory of Core-Collapse Supernovae," *Phys.Rept.* **442** (2007) 38–74, astro-ph/0612072.

[43] S. Campana *et al.*, "The shock break-out of GRB 060218/SN 2006aj," *Nature* **442** (2006) 1008–1010, astro-ph/0603279.

[44] R. McCray, "Supernova 1987a revisited," *Ann. Rev. Astron. Astrophys.* **31** (1993) 175–216.

[45] P. A. Pinto and R. G. Eastman, "The Physics of the type Ia supernova light curves. 1. Analytic results and time dependence," *Astrophys. J.* **530** (2000) 744–756.

[46] B. Mueller, H.-T. Janka, and H. Dimmelmeier, "A new multi-dimensional general relativistic neutrino hydrodynamics code for core-collapse supernovae. I. Method and code tests in spherical symmetry," *Astrophys.J.Suppl.* **189** (2010) 104–133, astro-ph/1001.4841.

[47] S. Horiuchi, J. F. Beacom, C. S. Kochanek, J. L. Prieto, K. Stanek, *et al.*, "The Cosmic Core-collapse Supernova Rate does not match the Massive-Star Formation Rate," astro-ph/1102.1977.

[48] S. Ando, J. F. Beacom, and H. Yuksel, "Detection of neutrinos from supernovae in nearby galaxies," *Phys.Rev.Lett.* **95** (2005) 171101, astro-ph/0503321.

[49] **The GALEX-VVDS** Collaboration, D. Schiminovich *et al.*, "The GALEX-VVDS Measurement of the Evolution of the Far- Ultraviolet Luminosity Density and the Cosmic Star Formation Rate," *Astrophys. J.* **619** (2005) L 47, astro-ph/0411424.

[50] R. W. Klebesadel, I. B. Strong, and R. A. Olsen, "Observation of Gamma-Ray-Bursts of Cosmic Origin," *Astrophys. J.* **182** (1973) L85–L88.

[51] B. Zhang and P. Meszaros, "Gamma-Ray Bursts: Progress, Problems and Prospects," *Int. J. Mod. Phys.* **A19** (2004) 2385–2472, astro-ph/0311321.

[52] M. Schmidt, "Luminosity function of gamma-ray bursts derived without benefit of redshifts," *Astrophys. J.* **552** (2001) 36, astro-ph/0101163.

[53] R. Salvaterra *et al.*, "GRB 090423 reveals an exploding star at the epoch of re-ionization," astro-ph/0906.1578.

[54] B. Paczynski, "Gamma-ray bursters at cosmological distances," *Astrophys. J.* **308** (1986) L43–L46.

[55] M. Vietri, "On the acceleration of ultrahigh-energy cosmic rays in gamma-ray bursts," *Astrophys.J.* **453** (1995) 883–889, astro-ph/9506081.

[56] B. Paczynski and G. Xu, "Neutrino bursts from gamma-ray bursts," *Astrophys.J.* **427** (1994) 708–713.

[57] E. Waxman and J. N. Bahcall, "High-energy neutrinos from cosmological gamma-ray burst fireballs," *Phys.Rev.Lett.* **78** (1997) 2292–2295, astro-ph/9701231.

[58] J. N. Bahcall and P. Meszaros, "5-GeV to 10-GeV neutrinos from gamma-ray burst fireballs," *Phys.Rev.Lett.* **85** (2000) 1362–1365, hep-ph/0004019.

[59] P. Meszaros and E. Waxman, "TeV neutrinos from successful and choked gamma-ray bursts," *Phys.Rev.Lett.* **87** (2001) 171102, astro-ph/0103275.

[60] C. S. Kochanek and T. Piran, "Gravitational waves and gamma-ray bursts," *Astrophys.J.* **417** (1993) L17–L20, astro-ph/9305015.

[61] S. Kobayashi and P. Meszaros, "Gravitational radiation from gamma-ray burst progenitors," *Astrophys.J.* **589** (2003) 861–870, astro-ph/0210211.

[62] C. Kouveliotou, C. A. Meegan, G. J. Fishman, N. P. Bhyat, M. S. Briggs, *et al.*, "Identification of two classes of gamma-ray bursts," *Astrophys.J.* **413** (1993) L101–104.

[63] N. Gehrels, E. Ramirez-Ruiz, and D. B. Fox, "Gamma-Ray Bursts in the Swift Era," *Ann.Rev.Astron.Astrophys.* **47** (2009) 567–617, astro-ph/0909.1531.

[64] W. S. Paciesas *et al.*, "The Fourth BATSE Gamma-Ray Burst Catalog (Revised)," *Astrophys. J. Suppl.* **122** (1999) 465–495, astro-ph/9903205.

[65] G. Fishman and C. Meegan, "Gamma-ray bursts," *Ann.Rev.Astron.Astrophys.* **33** (1995) 415–458.

[66] D. Band *et al.*, "BATSE observations of gamma-ray burst spectra. 1. Spectral diversity," *Astrophys. J.* **413** (1993) 281–292.

[67] J. K. Becker, M. Stamatikos, F. Halzen, and W. Rhode, "Coincident GRB neutrino flux predictions: Implications for experimental UHE neutrino physics," *Astropart. Phys.* **25** (2006) 118–128, astro-ph/0511785.

[68] D. Guetta, D. Hooper, J. Alvarez-Muniz, F. Halzen, and E. Reuveni, "Neutrinos from individual gamma-ray bursts in the BATSE catalog," *Astropart. Phys.* **20** (2004) 429–455, astro-ph/0302524.

[69] B. Zhang, "Gamma-Ray Bursts in the Swift Era," *Chin.J.Astron.Astrophys.* **7** (2007) 1–50, astro-ph/0701520.

[70] E. Cota, F. Frontera, J. Heise, M. Feroci, J. in 't Zand, *et al.*, "Discovery of an X-ray afterglow associated with the gamma-ray burst of 28 February 1997," *Nature* **387** (1997) 783–785.

[71] C. Akerlof, R. Balsano, S. Barthelmy, J. Bloch, P. Butterworth, *et al.*, "Observation of contemporaneous optical radiation from a gamma-ray burst," *Nature* **398** (1999) 400–402, astro-ph/9903271.

[72] P. W. A. Roming *et al.*, "The First Swift Ultra-Violet/Optical Telescope GRB Afterglow Catalog," *Astrophys. J.* **690** (2009) 163–188, astro-ph/0809.4193.

[73] D. Kann, S. Klose, B. Zhang, A. Wilson, N. Butler, *et al.*, "The Afterglows of Swift-era Gamma-Ray Bursts II.: Type I GRB versus Type II GRB Optical Afterglows," astro-ph/0804.1959.

[74] S. Kulkarni, D. Frail, M. Wieringa, R. Ekers, E. Sadler, *et al.*, "Radio emission from the unusual supernova 1998bw and its association with the gamma-ray burst of 25 April 1998," *Nature* **395** (1998) 663–669.

[75] S. E. Woosley and J. S. Bloom, "The Supernova – Gamma-Ray Burst Connection," *Ann. Rev. Astron. Astrophys.* **44** (2006) 507–556, astro-ph/0609142.

[76] T. Piran, "Gamma-Ray Bursts and the Fireball Model," *Phys. Rept.* **314** (1999) 575–667, astro-ph/9810256.

[77] P. Meszaros and M. J. Rees, "High-entropy fireballs and jets in gamma-ray burst sources," *Mon. Not. Roy. Astron. Soc.* **257** (1992) 29–31.

[78] W. K. H. Schmidt, "Distance limit for a class of model gamma-ray burst sources," *Nature* **271** (1978) 525–527.

[79] E. E. Fenimore, R. I. Epstein, and C. Ho, "The escape of 100 MeV photons from cosmological gamma-ray bursts," *Astronomy and Astrophysics Supplement Series* **97** (1993) 59–62.

[80] P. Meszaros and M. Rees, "Delayed GeV emission from cosmological gamma-ray bursts: Impact of a relativistic wind on external matter," *Mon.Not.Roy.Astron.Soc.* **269** (1994) L41, astro-ph/9404056.

[81] R. Narayan, B. Paczynski, and T. Piran, "Gamma-ray bursts as the death throes of massive binary stars," *Astrophys.J.* **395** (1992) L83–L86, astro-ph/9204001.

[82] R. Sari and T. Piran, "Variability in GRBs: A Clue," *Astrophys.J.* **485** (1997) 270, astro-ph/9701002.

[83] E. Woods and A. Loeb, "Empirical constraints on source properties and host galaxies of cosmological gamma-ray bursts," *Astrophys.J.* **453** (1995) 583, astro-ph/9503070.

[84] E. Waxman, "Gamma-ray bursts: The Underlying model," *Lect.Notes Phys.* **598** (2003) 393, astro-ph/0303517.

[85] T. Piran, "Gamma-Ray Bursts - When Theory Meets Observations," astro-ph/0104134.

[86] T. Piran, "Gamma-Ray Bursts - a Primer For Relativists," gr-qc/0205045. Talk given at 16th International Conference On General Relativity And Gravitation, 15-21 Jul 2001, Durban, South Africa.

[87] T. Prian, "Demotion Looms for Gamma-Ray Bursts," *Science* **295** (2002) 986–987.

[88] D. Eichler, M. Livio, T. Piran, and D. N. Schramm, "Nucleosynthesis, Neutrino Bursts and Gamma-Rays from Coalescing Neutron Stars," *Nature* **340** (1989) 126–128.

[89] T. Galama, P. M. Vreeswijk, J. van Paradijs, C. Kouveliotou, T. Augusteijn, *et al.*, "Discovery of the peculiar supernova 1998bw in the error box of GRB 980425," *Nature* **395** (1998) 670, astro-ph/9806175.

[90] D. Malesani, G. Tagliaferri, G. Chincarini, S. Covino, M. Della Valle, *et al.*, "SN 2003lw and GRB 031203: A bright supernova for a faint gamma-ray burst," *Astrophys.J.* **609** (2004) L5, astro-ph/0405449.

[91] J. Hjorth, J. Sollerman, P. Moller, J. P. Fynbo, S. E. Woosley, *et al.*, "A Very energetic supernova associated with the gamma-ray burst of 29 March 2003," *Nature* **423** (2003) 847–850, astro-ph/0306347.

[92] E. Pian, P. Mazzali, N. Masetti, P. Ferrero, S. Klose, *et al.*, "An optical supernova associated with the X-ray flash XRF 060218," *Nature* **442** (2006) 1011–1013, astro-ph/0603530.

[93] A. Soderberg, E. Berger, K. Page, P. Schady, J. Parrent, *et al.*, "An Extremely Luminous X-ray Outburst Marking the Birth of a Normal Supernova," *Nature* **453** (2008) 469–474, astro-ph/0802.1712.

[94] R. Starling, K. Wiersema, A. Levan, T. Sakamoto, D. Bersier, *et al.*, "Discovery of the nearby long, soft GRB 100316D with an associated supernova," *Mon.Not.Roy.Astron.Soc.* **411** (2011) 2792–2803, astro-ph/1004.2919.

[95] J. S. Bloom *et al.*, "The unusual afterglow of GRB 980326: evidence for the gamma-ray burst/supernova connection," *Nature* **401** (1999) 453, astro-ph/9905301.

[96] D. E. Reichart, "GRB 970228 Revisited: Evidence for a Supernova in the Light Curve and Late Spectral Energy Distribution of the Afterglow," *Astrophys. J.* **521** (1999) L111–L115, astro-ph/9906079.

[97] A. Hakobyan, A. Petrosian, G. Mamon, B. McLean, D. Kunth, *et al.*, "Five supernova survey galaxies in the southern hemisphere. II. The supernova rates," astro-ph/1104.0300.

[98] A. Gal-Yam, E. O. Ofek, D. Poznanski, A. Levinson, E. Waxman, *et al.*, "A complete survey of the transient radio sky and implications for gamma-ray bursts, supernovae, and other relativistic explosions," *Astrophys.J.* **639** (2006) 331–339, astro-ph/0508629.

[99] S. Razzaque, P. Meszaros, and E. Waxman, "High energy neutrinos from a slow jet model of core collapse supernovae," *Mod.Phys.Lett.* **A20** (2005) 2351–2368, astro-ph/0509729.

[100] S. Ando and J. F. Beacom, "Revealing the supernova-gamma-ray burst connection with TeV neutrinos," *Phys. Rev. Lett.* **95** (2005) 061103, astro-ph/0502521.

[101] T. K. Gaisser, "Cosmic rays and particle physics,".

[102] E. Fermi, "On the Origin of the Cosmic Radiation," *Phys. Rev.* **75** (1949) 1169–1174.

[103] A. R. Bell, "The acceleration of cosmic rays in shock fronts. II," *Mon. Not. Roy. Astron. Soc.* **182** (1978) 443–455.

[104] **AMANDA** Collaboration, J. Ahrens *et al.*, "Muon Track Reconstruction and Data Selection Techniques in AMANDA," *Nucl. Instrum. Meth.* **A524** (2004) 169–194, astro-ph/0407044.

[105] A. Roberts, "The Birth of high-energy neutrino astronomy: A Personal history of the DUMAND project," *Rev.Mod.Phys.* **64** (1992) 259–312.

[106] A. Avrorin, V. Aynutdinov, V. Balkanov, I. Belolaptikov, D. Bogorodsky, *et al.*, "The Baikal neutrino telescope: Results and plans," *Nucl.Instrum.Meth.* **A630** (2011) 115–118.

[107] G. Aggouras, E. Markopoulos, K. Papageorgiou, T. Staveris, V. Tsagli, *et al.*, "Operation and performance of the NESTOR test detector," *Nucl.Instrum.Meth.* **A552** (2005) 420–439.

[108] **ANTARES** Collaboration, J. Aguilar *et al.*, "First results of the Instrumentation Line for the deep-sea ANTARES neutrino telescope," *Astropart.Phys.* **26** (2006) 314–324, astro-ph/0606229.

[109] **KM3NeT** Collaboration, U. Katz, "The KM3NeT project," *Nucl.Instrum.Meth.* **A626-627** (2011) S57–S63.

[110] E. Andres, P. Askebjer, X. Bai, G. Barouch, S. Barwick, *et al.*, "Observation of high-energy neutrinos using Cherenkov detectors embedded deep in Antarctic ice," *Nature* **410** (2001) 441–443.

[111] R. Gandhi, C. Quigg, M. H. Reno, and I. Sarcevic, "Neutrino interactions at ultrahigh energies," *Phys. Rev. D* **58** (Sep, 1998) 093009.

[112] A. Cooper-Sarkar and S. Sarkar, "Predictions for high energy neutrino cross-sections from the ZEUS global PDF fits," *JHEP* **01** (2008) 075, hep-ph/0710.5303.

[113] A. Gazizov and M. P. Kowalski, "ANIS: High energy neutrino generator for neutrino telescopes," *Comput.Phys.Commun.* **172** (2005) 203–213, astro-ph/0406439.

[114] **CTEQ** Collaboration, H. Lai *et al.*, "Global QCD analysis of parton structure of the nucleon: CTEQ5 parton distributions," *Eur.Phys.J.* **C12** (2000) 375–392, hep-ph/9903282.

[115] K. Zuber, *Neutrino Physics*. IOP Publishing, 2004.

[116] H. Athar, M. Jezabek, and O. Yasuda, "Effects of neutrino mixing on high-energy cosmic neutrino flux," *Phys. Rev.* **D62** (2000) 103007, hep-ph/0005104.

[117] L. Wolfenstein, "Neutrino oscillations in matter," *Phys. Rev. D* **17** (May, 1978) 2369–2374.

[118] J. G. Learned and K. Mannheim, "High-energy neutrino astrophysics," *Ann. Rev. Nucl. Part. Sci.* **50** (2000) 679–749.

[119] S. I. Dutta, M. H. Reno, I. Sarcevic, and D. Seckel, "Propagation of muons and taus at high energies," *Phys. Rev.* **D63** (2001) 094020, hep-ph/0012350.

[120] P. Cerenkov, "Visible radiation produced by electrons moving in a medium with velocities exceeding that of light," *Phys.Rev.* **52** (1937) 378–379.

[121] C. A. Mead, "Quantum Theory of the Refractive Index," *Phys. Rev.* **110** (Apr, 1958) 359–369.

[122] F. Halzen and S. R. Klein, "IceCube: An Instrument for Neutrino Astronomy," *Rev.Sci.Instrum.* **81** (2010) 081101, astro-ph/1007.1247.

[123] **IceCube** Collaboration, O. Schulz, "The IceCube DeepCore," *AIP Conf.Proc.* **1085** (2009) 783–786.

[124] **IceCube** Collaboration, T. Stanev, "Status, performance, and first results of the IceTop array," *Nucl.Phys.Proc.Suppl.* **196** (2009) 159–164, astro-ph/0903.0576.

[125] M. Ackermann *et al.*, "Optical properties of deep glacial ice at the South Pole," *J. Geophys. Res.* **111** (2006) D13203.

[126] N. E. Bramall *et al.*, "A deep high-resolution optical log of dust, ash, and stratigraphy in South Pole glacial ice," *Geophys. Res. Lett.* **32** (2005) L21815.

[127] **IceCube** Collaboration, K. Hanson and O. Tarasova, "Design and production of the IceCube digital optical module," *Nucl.Instrum.Meth.* **A567** (2006) 214–217.

[128] J. Kelly and J. Braun, "DOM-Cal Users' Guide." http://icecube.wisc.edu/~krasberg/doc/domcal_user_guide.ps, 2005.

[129] C. Mackenzie, "Introduduction to to the Data Movement and Archival System for IceCube." https://docushare.icecube.wisc.edu/dsweb/Get/Document-7215/Data_Movement_Intro.pdf.

[130] D. "Pandel, ""Bestimmung von Wasser- und Detektorparametern und Rekonstruktion von Myonen bis 100 TeV mit dem Baikal-Neutrinoteleskop NT-72"," Diploma thesis, "Humboldt-Universitaet zu Berlin", 1996.

[131] T. Neunhoffer, "Estimating the angular resolution of tracks in neutrino telescopes based on a likelihood analysis," *Astropart.Phys.* **25** (2006) 220–225, astro-ph/0403367.

[132] A. Mohr, "Development of a Neutrinos Burst Filter for IceCube," Diploma thesis, Humboldt Universität zu Berlin, 2008.

[133] T. K. Gaisser and M. Honda, "Flux of atmospheric neutrinos," *Ann. Rev. Nucl. Part. Sci.* **52** (2002) 153–199, hep-ph/0203272.

[134] **IceCube** Collaboration, R. Abbasi *et al.*, "Measurement of the atmospheric neutrino energy spectrum from 100 GeV to 400 TeV with IceCube," *Phys.Rev.* **D83** (2011) 012001, astro-ph/1010.3980.

[135] M. Honda, T. Kajita, K. Kasahara, S. Midorikawa, and T. Sanuki, "Calculation of atmospheric neutrino flux using the interaction model calibrated with atmospheric muon data," *Phys.Rev.* **D75** (2007) 043006, astro-ph/0611418.

[136] R. Enberg, M. H. Reno, and I. Sarcevic, "Prompt neutrino fluxes from atmospheric charm," *Phys.Rev.* **D78** (2008) 043005, hep-ph/0806.0418.

[137] G. Fiorentini, V. A. Naumov, and F. L. Villante, "Atmospheric neutrino flux supported by recent muon experiments," *Phys.Lett.* **B510** (2001) 173–188, hep-ph/0103322.

[138] A. Martin, M. Ryskin, and A. Stasto, "Prompt neutrinos from atmospheric $c\bar{c}$ and $b\bar{b}$ production and the gluon at very small x," *Acta Phys.Polon.* **B34** (2003) 3273–3304, hep-ph/0302140.

[139] D. Chirkin and W. Rhode, "Muon Monte Carlo: A New high precision tool for muon propagation through matter,". Contributed to 27th International Cosmic Ray Conference (ICRC 2001), Hamburg, Germany, 7-15 Aug 2001.

[140] J. Lundberg, P. Miocinovic, T. Burgess, J. Adams, S. Hundertmark, *et al.*, "Light tracking for glaciers and oceans: Scattering and absorption in heterogeneous media with Photonics," *Nucl.Instrum.Meth.* **A581** (2007) 619–631, astro-ph/0702108.

[141] J. Knapp and D. Heck, "Extensive air shower simulations with the CORSIKA code," *Nachr.Forsch.zentr.Karlsruhe* **30** (1998) 27–37.

[142] **IceCube** Collaboration, P. Berghaus, "Direct Measurement of the Atmospheric Muon Energy Spectrum with IceCube," *ICRC Proc.* (2009) astro-ph/0909.0679.

[143] **IceCube** Collaboration, R. Abbasi *et al.*, "Time-Integrated Searches for Point-like Sources of Neutrinos with the 40-String IceCube Detector," *Astrophys. J.* **732** (2011) 18, astro-ph/1012.2137.

[144] **IceCube** Collaboration, R. Abbasi *et al.*, "Search for Dark Matter from the Galactic Halo with the IceCube Neutrino Observatory," astro-ph/1101.3349.

[145] **IceCube** Collaboration, C. Rott, "Good run list." Internal web pages: IC40: http://www.icecube.wisc.edu/~carott/good_run_list_IC40/goodrunlist-IC40.html, IC59: http://www.icecube.wisc.edu/~carott/good_run_list_IC59/goodrunlist-IC59.html.

[146] **AMANDA Collaboration** Collaboration, A. Bouchta, "Seasonal variation of the muon flux seen by AMANDA," in *Proceedings of 8th International Workshop On Neutrino Telescopes*. 1999.

[147] C. W. Akerlof *et al.*, "The ROTSE-III Robotic Telescope System," *Publ. Astron. Soc. Pac.* **115** (2003) 132–140, astro-ph/0210238.

[148] G. Bernstein, "Modern Astronomical Observations." http://www.physics.upenn.edu/~garyb/501notes.ps.gz. Astronomy Lecture.

[149] D. C. Wells, E. W. Greisen, and R. H. Harten, "FITS - a Flexible Image Transport System," *Astron.Astrophys.* **44** (June, 1981) 363.

[150] E. Rykoff and D. Smith, "Components and Opertaion of the ROTSE-III Telescope System." http://www.rotse.net/equipment/docs/rotsedocs.pdf. ROTSE manual.

[151] E. Bertin and S. Arnouts, "SExtractor: Software for source extraction.," *Astron. and Astroph. Suppl.* **117** (June, 1996) 393–404.

[152] D. Monet *et al.*, "USNO-A2.0, A Catalog of Astrometric Standards." http://tdc-www.harvard.edu/catalogs/ua2.html.

[153] F. Yuan and C. W. Akerlof, "Astronomical Image Subtraction by Cross-Convolution," *Astrophys. J.* **677** (2008) 808–812, astro-ph/0801.0336.

[154] C. Alard and R. H. Lupton, "A method for optimal image subtraction," *Astrophys. J.* **503** (1998) 325, astro-ph/9712287.

[155] C. A. Gossl and A. Riffeser, "Image reduction pipeline for the detection of variable sources in highly crowded fields," *Astron. Astrophys.* **381** (2002) 1095–1109, astro-ph/0110704.

[156] M. F. Skrutskie *et al.*, "The Two Micron All Sky Survey (2MASS)," *Astron. J.* **131** (2006) 1163–1183.

[157] R. Cutri *et al.*, "Explanatory Supplement to the 2MASS All Sky Data Release and Extended Mission Products." http://www.ipac.caltech.edu/2mass/releases/allsky/doc/explsup.html.

[158] B. Reed, "New estimates of the solar-neighborhood massive-stars birthrate and the Galactic supernova rate," *Astron.J.* **130** (2005) 1652–1657, astro-ph/0506708.

[159] P. Speckmayer, A. Hocker, J. Stelzer, and H. Voss, "The toolkit for multivariate data analysis, TMVA 4," *J.Phys.Conf.Ser.* **219** (2010) 032057.

[160] I. Antcheva, M. Ballintijn, B. Bellenot, M. Biskup, R. Brun, *et al.*, "ROOT: A C++ framework for petabyte data storage, statistical analysis and visualization," *Comput.Phys.Commun.* **182** (2011) 1384–1385.

[161] M. Hamuy *et al.*, "Optical and Infrared Spectroscopy of SN 1999ee and SN 1999ex," *Astron. J.* **124** (2002) 417–429, astro-ph/0203491.

[162] M. Hamuy *et al.*, "Evidence for Core Collapse in the Type Ib/c SN 1999ex," astro-ph/0212368.

[163] **SDSS** Collaboration, D. P. Schneider *et al.*, "The Sloan Digital Sky Survey Quasar Catalog V. Seventh Data Release," *Astron.J.* **139** (2010) 2360–2373, astro-ph/1004.1167.

[164] **The NED Team** Collaboration, J. M. Mazzarella, B. F. Madore, and G. Helou, "Capabilities of the NASA/IPAC Extragalactic Database (NED) in the Era of a Global Virtual Observatory," astro-ph/0111200.

[165] A. Hoecker, P. Speckmayer, J. Stelzer, J. Therhaag, E. von Toerne, H. Voss, M. Backes, T. Carli, O. Cohen, A. Christov, D. Dannheim, K. Danielowski, S. Henrot-Versille, M. Jachowski, K. Kraszewski, A. K. Jr., M. Kruk, Y. Mahalalel, R. Ospanov, X. Prudent, A. Robert, D. Schouten, F. Tegenfeldt, A. Voigt, K. Voss, M. Wolter, and A. Zemla, "TMVA - Toolkit for Multivariate Data Analysis," physics/0703039.

[166] M. Wenger, F. Ochsenbein, D. Egret, P. Dubois, F. Bonnarel, S. Borde, F. Genova, G. Jasniewicz, S. Laloë, S. Lesteven, and R. Monier, "The SIMBAD astronomical database. The CDS reference database for astronomical objects," *Astron.Astrophys.* **143** (2000) 9–22, astro-ph/0002110.

[167] D. Richardson, D. Branch, and E. Baron, "Absolute-Magnitude Distributions and Light Curves of Stripped-Envelope Supernovae," *Astron. J.* **131** (2006) 2233–2244, astro-ph/0601136.

[168] D. Cowen, A. Franckowiak, and M. Kowalski, "Estimating the Explosion Time of Core-Collapse Supernovae from Their Optical Light Curves," *Astropart.Phys.* **33** (2010) 19–23, astro-ph/0901.4877.

[169] M. Modjaz *et al.*, "From Shock Breakout to Peak and Beyond: Extensive Panchromatic Observations of the Aspherical Type Ib Supernova 2008D associated with Swift X-ray Transient 080109," *Astrophys. J.* **702** (2009) 226–248, astro-ph/0805.2201.

[170] E. Waxman, P. Meszaros, and S. Campana, "GRB060218: A Relativistic Supernova Shock Breakout," *Astrophys.J.* **667** (2007) 351–357, astro-ph/0702450.

[171] L. Ensman and A. Burrows, "Shock breakout in SN1987A," *Astrophys.J.* **393** (1992) 742.

[172] C. D. Matzner and C. F. McKee, "Efficiencies of low-mass star and star cluster formation," *Astrophys. J.* **510** (2000) 379, astro-ph/0007383.

[173] R. A. Chevalier and C. Fransson, "Shock Breakout Emission from a Type Ib/c Supernova: XRF 080109/SN 2008D," *Astrophys. J.* **683** (2008) 135, astro-ph/0806.0371.

[174] P. A. Mazzali *et al.*, "The Metamorphosis of Supernova SN 2008D/XRF 080109: A Link Between Supernovae and GRBs/Hypernovae," *Science* **321** (2008) 1185–1188.

[175] M. Hamuy, N. B. Suntzeff, R. Gonzalez, and G. Martin, "SN 1987A in the LMC - UBVRI photometry at Cerro Tololo," *Astron. J.* **95** (Jan., 1988) 63–83.

[176] W. Arnett, "Type I supernovae. I - Analytic solutions for the early part of the light curve," *Astrophys. J.* **253** (1982) 785.

[177] G. Goldhaber *et al.*, "A Universal B-band Lightcurve for Type IA Supernovae and Direct Evidence for the Expansion of the Universe," *Bulletin of the American Astronomical Society* **30** (Dec, 1998) 1325.

[178] A. Riess *et al.*, "The rise time of nearby type Ia supernova," *Astron. J.* **118** (1999) 2675.

[179] A. Conley *et al.*, "The Rise Time of Type Ia Supernovae from the Supernova Legacy Survey," *Astron. J.* **132** (2006) 1707–1713, astro-ph/0607363.

[180] C. L. Fryer and P. Mészáros, "Neutrino driven explosions in GRBs and hypernovae," *Astrophys. J.* **588** (2003) L25–L28, astro-ph/0303334.

[181] **The IceCube** Collaboration, R. Abbasi *et al.*, "Calibration and Characterization of the IceCube Photomultiplier Tube," *Nucl. Instrum. Meth.* **A618** (2010) 139–152, astro-ph/1002.2442.

[182] S. Kuhlmann, "CTEQ5 parton distributions and ongoing studies," *Nucl. Phys. Proc. Suppl.* **79** (1999) 108–110.

[183] A. D. Martin, R. G. Roberts, W. J. Stirling, and R. S. Thorne, "MRST2001: Partons and alpha(s) from precise deep inelastic scattering and Tevatron jet data," *Eur. Phys. J.* **C23** (2002) 73–87, hep-ph/0110215.

[184] J. Pumplin *et al.*, "New generation of parton distributions with uncertainties from global QCD analysis," *JHEP* **07** (2002) 012, hep-ph/0201195.

[185] **IceCube** Collaboration, A. Achterberg *et al.*, "Five years of searches for point sources of astrophysical neutrinos with the AMANDA-II neutrino telescope," *Phys. Rev.* **D75** (2007) 102001, astro-ph/0611063.

[186] E. S. Rykoff *et al.*, "A Search for Untriggered GRB Afterglows with ROTSE-III," *Astrophys. J.* **631** (2005) 1032–1038, astro-ph/0506442.

[187] S. Ando, J. F. Beacom, and H. Yuksel, "Detection of neutrinos from supernovae in nearby galaxies," *Phys.Rev.Lett.* **95** (2005) 171101, astro-ph/0503321.

[188] M. D. Kistler, H. Yuksel, S. Ando, J. F. Beacom, and Y. Suzuki, "Core-Collapse Astrophysics with a Five-Megaton Neutrino Detector," astro-ph/0810.1959.

[189] A. L. Melchior, F. Combes, and A. Gould, "The surface brightness of the Galaxy at the Solar Neighbourhood," astro-ph/0610884.

[190] C. M. Springob, M. P. Haynes, R. Giovanelli, and B. R. Kent, "A Digital archive of HI 21 cm line spectra of optically-targeted galaxies," *Astrophys.J.Suppl.* (2005) astro-ph/0505025.

[191] P. Nugent, M. Sullivan, R. Ellis, A. Gal-Yam, D. C. Leonard, *et al.*, "Towards a Cosmological Hubble Diagram for Type II-P Supernovae," *Astrophys.J.* **645** (2006) 841–850, astro-ph/0603535.

[192] A. Soderberg *et al.*, "A relativistic type Ibc supernova without a detected γ-ray burst," *Nature* **463** (2010) 513–515.

[193] G. Heald, M. R. Bell, A. Horneffer, A. R. Offringa, R. Pizzo, *et al.*, "LOFAR: Recent imaging results and future prospects," astro-ph/1106.3195.

[194] P. Dewdney, P. Hall, Schilizzi, R.T., T. Joseph, and L. Lazio, "The SquareKilometre Array," in *Proceedings of the IEEE*, vol. 97, pp. 1482–1503. August, 2009.

[195] N. Law, S. Kulkarni, R. Dekany, E. Ofek, R. Quimby, *et al.*, "The Palomar Transient Factory: System Overview, Performance and First Results," astro-ph/0906.5350.

[196] A. Rau, S. R. Kulkarni, N. M. Law, J. S. Bloom, D. Ciardi, *et al.*, "Exploring the Optical Transient Sky with the Palomar Transient Factory," *Publ.Astron.Soc.Pac.* **121** (2009) 1334–1351, astro-ph/0906.5355.

[197] A. Stasik, S. Boeser, A. Franckowiak, A. Homeier, and M. Kowalski, "Study of a high energy single neutrino online filter for downgoing neutrinos." IceCube Internal Report, 2011.

[198] **IceCube and SWIFT** Collaboration, A. Homeier, "SWIFT Follow-Up of IceCube neutrino multiplets," in *32th ICRC*. 2011. to be published.

[199] **Swift Science** Collaboration, N. Gehrels *et al.*, "The Swift Gamma-Ray Burst Mission," *AIP Conf.Proc.* **727** (2004) 637–641, astro-ph/0405233.

[200] R. Yamazaki, K. Toma, K. Ioka, and T. Nakamura, "Tail emission of prompt gamma-ray burst jets," *Mon.Not.Roy.Astron.Soc.* **369** (2006) 311–316, astro-ph/0509159.

[201] P. Meszaros, "Gamma-Ray Bursts," *Rept.Prog.Phys.* **69** (2006) 2259–2322, astro-ph/0605208.

[202] F. Hastie, Tibshirani, *The Elements of Statistical Learning*. Springer-Verlag, 2011.

Appendix A

IceCube Reconstruction Parameter Plots

This chapter contains plots comparing background and signal distributions of the used selection parameters at different cut levels. Two different signal distributions are shown, one following a soft spectrum weighted with E^{-3} and another one follwing a hard spectrum weighted with E^{-2}. The signal distributions are scaled to the maximum of the data distribution. The comparison of those distributions shows the separation power between signal and background events for the different selection variables.
Furthermore, data and Monte Carlo (MC) distributions are compared at Level 2 and at neutrino level. Studying the distributions of the different MC components (single and coincident atmospheric muons) can be useful to better understand and thus to reject the background. A good agreement at neutrino level is required in order to trust the signal simulation, because the same neutrino signal data set is used to describe the atmospheric neutrino background (weighted with the atmospheric neutrino spectrum) and the SN neutrino signal (weighted with the soft jet SN neutrino model).

A.1 Level 1 Filter

A.1.1 Level 1 - Background and Signal Distributions

The following figures show the distributions after applying the Level 1 filter cuts.

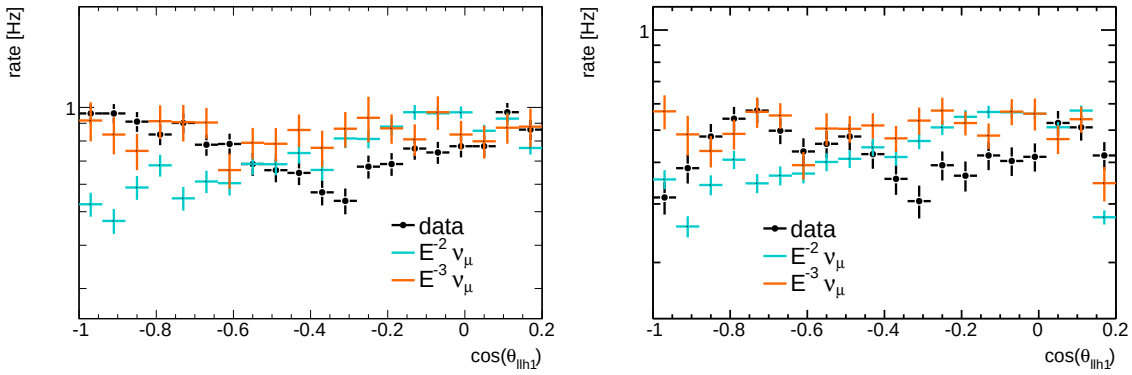

(a) IC40 (b) IC59

Figure A.1: Zenith angle distribution as obtained from the single iteration likelihood fit *llh1*. The zenith angle distribution of the two iteration likelihood fit *llh2* (first iteration seeded with linefit and second iteration seeded with the inverted linefit), which was only available in IC40, shows a similar behavior.

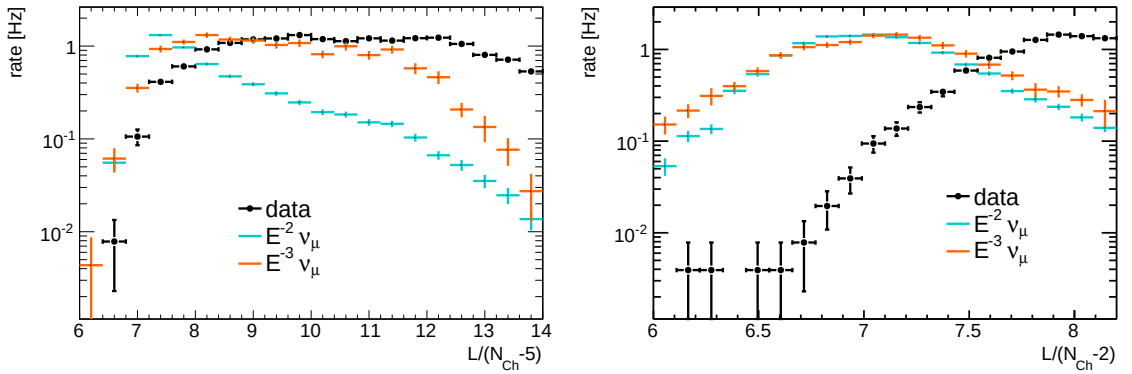

(a) IC40 (b) IC59

Figure A.2: $\mathcal{L}/(\mathrm{N_{Ch}}-5)$ distribution obtained from *llh2* for IC40 (left) and $\mathcal{L}/(\mathrm{N_{Ch}}-2)$ obtained from *llh1* for IC59 (right). Signal events tend to have small values, while the background dominated by misreconstructed muons takes large values. $\mathcal{L}/(\mathrm{N_{Ch}}-2)$ reduces the energy dependence compared to $\mathcal{L}/(\mathrm{N_{Ch}}-5)$ causing the two signal distributions, which are weighted with different energy spectra, to show a similar behavior.

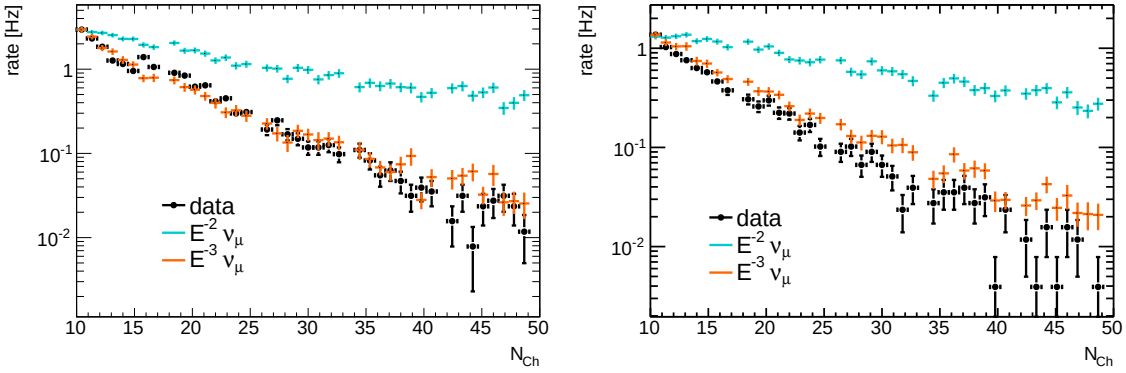

(a) IC40 (b) IC59

Figure A.3: N_{Ch} distribution obtained from *llh2* for IC40 (left) and *llh1* for IC59 (right). Signal events generated according to a hard energy spectrum generally produce more light and hence cause more sensors to be hit.

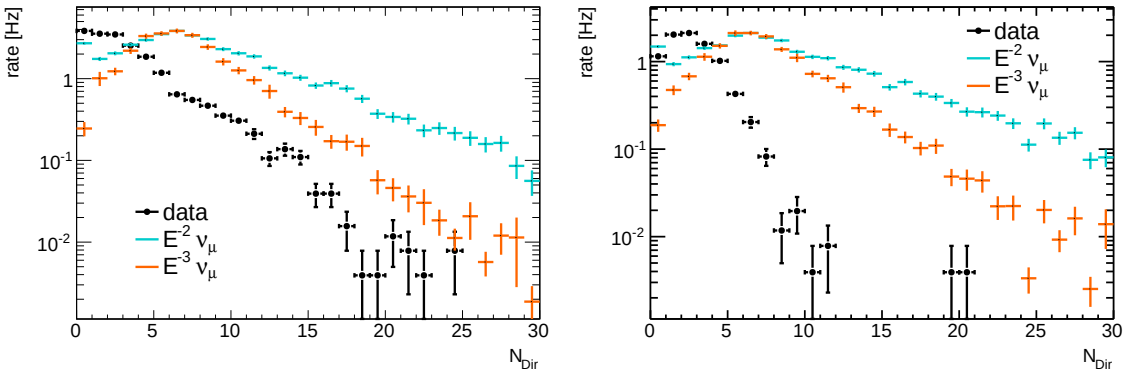

(a) IC40 (b) IC59

Figure A.4: N_{DirC} distribution obtained from *llh2* for IC40 (left) and *llh1* for IC59 (right). Signal events have more direct hits, indicating a better reconstruction quality compared to background events, which are mainly misreconstructed atmospheric muons. The separation works better for IC59 indicating improved reconstruction quality with the larger detector.

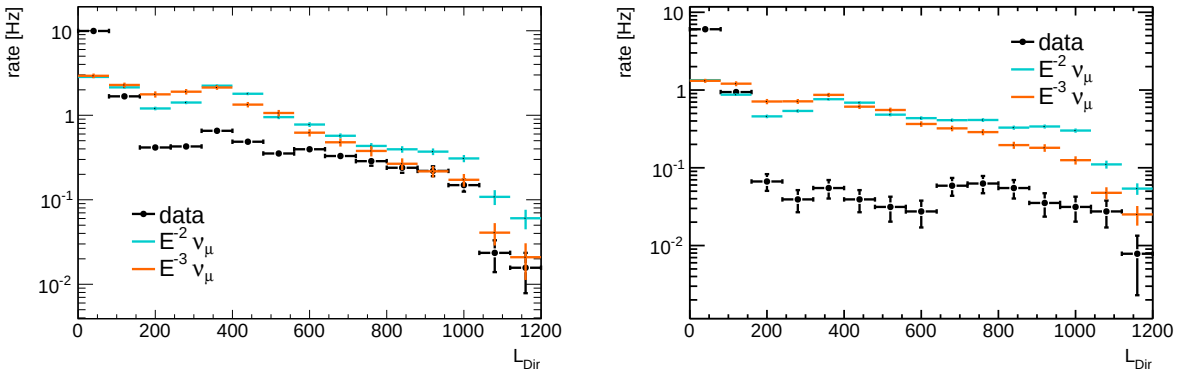

(a) IC40 (b) IC59

Figure A.5: L_{DirC} distribution obtained from *llh2* for IC40 (left) and *llh1* for IC59 (right). Signal events have more direct hits which are distributed along the reconstructed track thus causing larger L_{DirC}, indicating a better reconstruction quality compared to background events, which are mainly misreconstructed atmospheric muons.

A.2 Level 2

A.2.1 Level 2 - Background and Signal Distributions

The same variable distributions as shown in the previous section are displayed here after application of the Level 2 cuts.

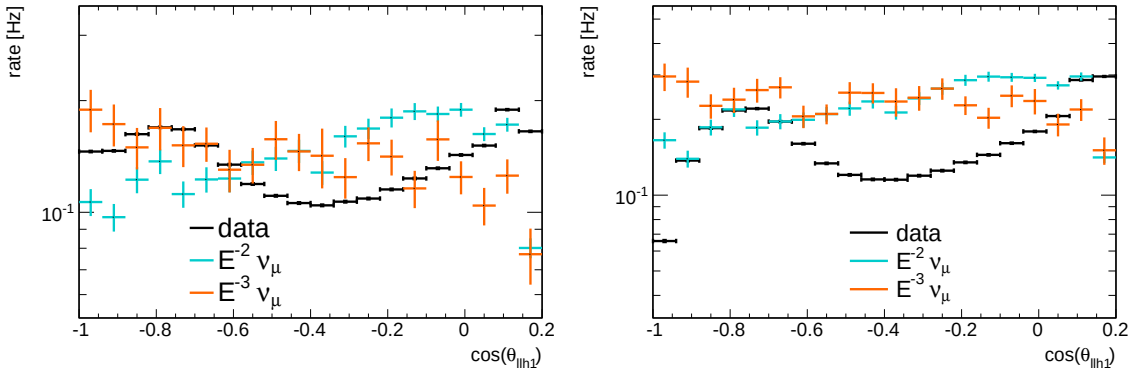

(a) IC40 (b) IC59

Figure A.6: Zenith angle distribution as obtained from single iteration likelihood fit *llh1*. The zenith angle distribution of the ten iteration likelihood fit, the paraboloid fit and the two iteration likelihood fit *llh2* (first iteration seeded with linefit and second iteration seeded with the inverted linefit), which was only available in IC40, show a similar behavior.

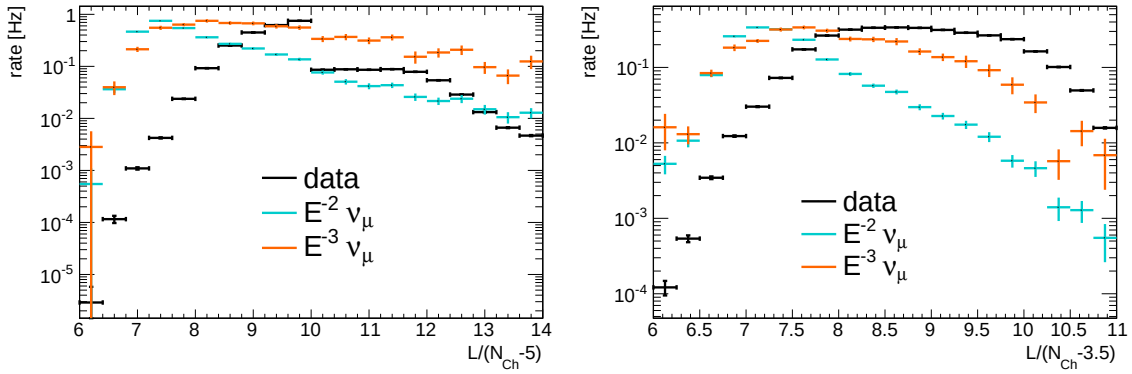

(a) IC40 (b) IC59

Figure A.7: $\mathcal{L}/(\mathrm{N_{Ch}} - 5)$ distribution obtained from *llh2* for IC40 (left) and $\mathcal{L}/(\mathrm{N_{Ch}} - 3.5)$ obtained from *llh1* for IC59 (right). Signal events tend to have small values, while the background dominated by misreconstructed muons takes large values. The IC40 distribution shows a small step due to the applied cut $\mathcal{L}/(\mathrm{N_{Ch}} - 5) \leq 10$ combined by an or-condition with an $\mathrm{N_{DirC}} \geq 5$ cut.

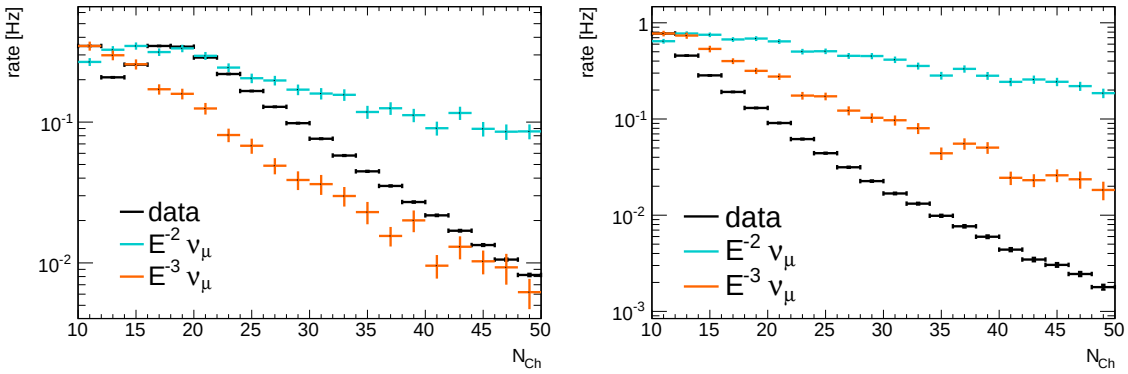

(a) IC40 (b) IC59

Figure A.8: N_{Ch} distribution obtained from *llh2* for IC40 (left) and *llh1* for IC59 (right). Signal events generated according to a hard energy spectrum generally produce more light and hence cause more sensors to be hit.

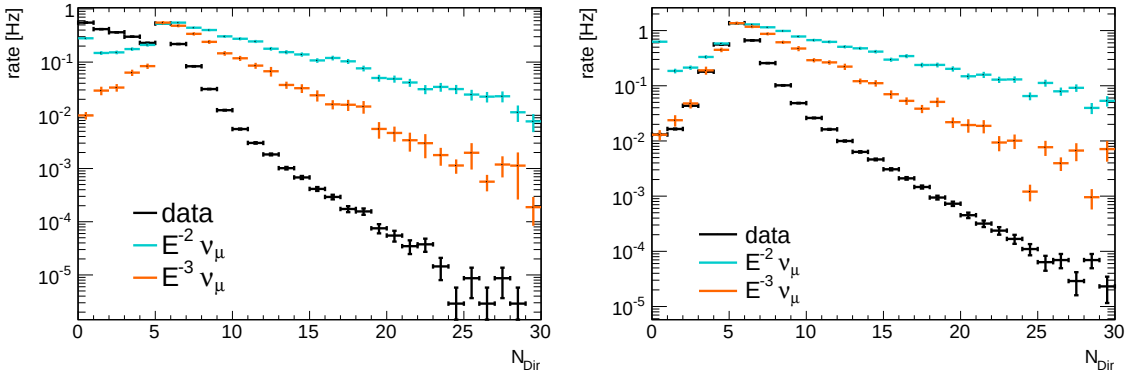

(a) IC40 (b) IC59

Figure A.9: N_{DirC} distribution obtained from *llh2* for IC40 (left) and *llh1* for IC59 (right). Signal events have more direct hits, indicating a better reconstruction quality compared to background events, which are mainly misreconstructed atmospheric muons.

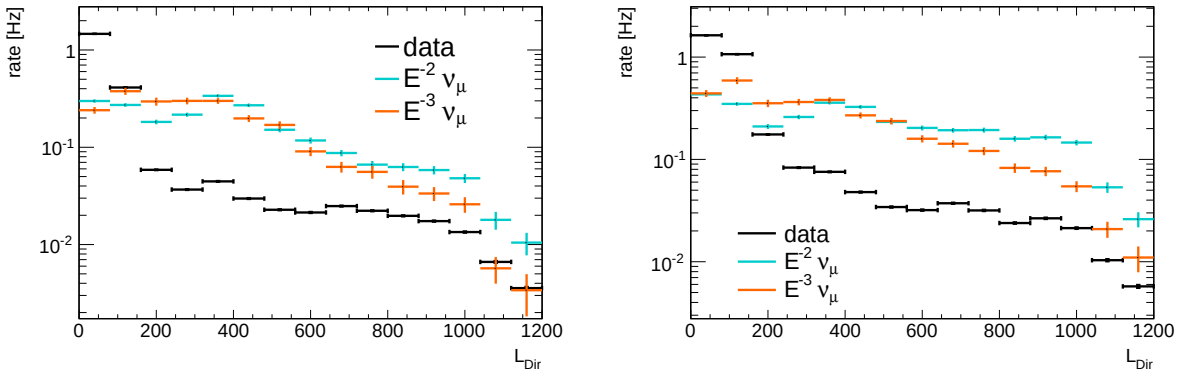

(a) IC40 (b) IC59

Figure A.10: L_{DirC} distribution obtained from *llh2* for IC40 (left) and *llh1* for IC59 (right). Signal events have more direct hits which are distributed along the reconstructed track thus causing larger L_{DirC}, indicating a better reconstruction quality compared to background events, which are mainly misreconstructed atmospheric muons.

A.2.2 Level 2 - Data Monte Carlo Comparison

Data and background, consisting of single and coincident atmospheric muons generated with the air shower simulation program CORISKA, show reasonable agreement. The following plots are useful to estimate the contribution of the single and coincident muon component to the total background. In total 32.5% (74.1%) of the Level 2 data stream consist of single muons and 67.5% (25.9%) of coincident muons for IC40 (IC59).

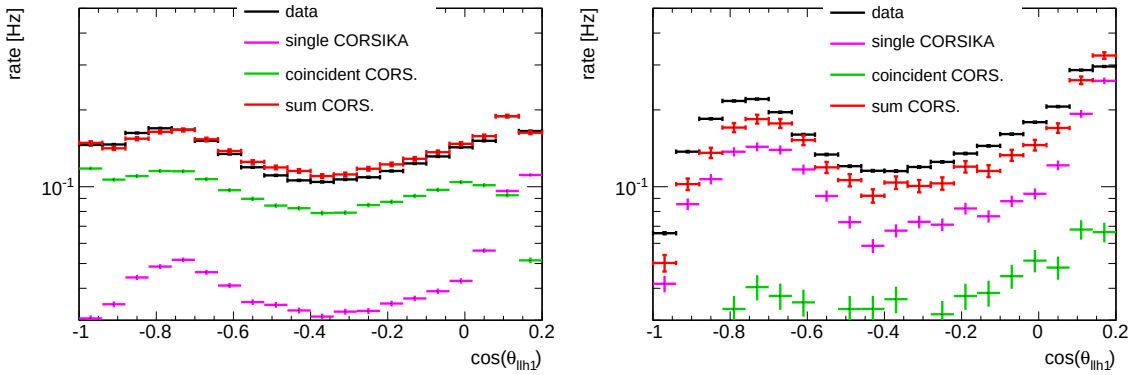

(a) IC40 (b) IC59

Figure A.11: Zenith angle distribution as obtained from single iteration likelihood fit *llh1*. The zenith angle distribution of the ten iteration likelihood fit, the paraboloid fit and the two iteration likelihood fit *llh2* (first iteration seeded with linefit and second iteration seeded with the inverted linefit), which was only available in IC40, show a similar behavior.

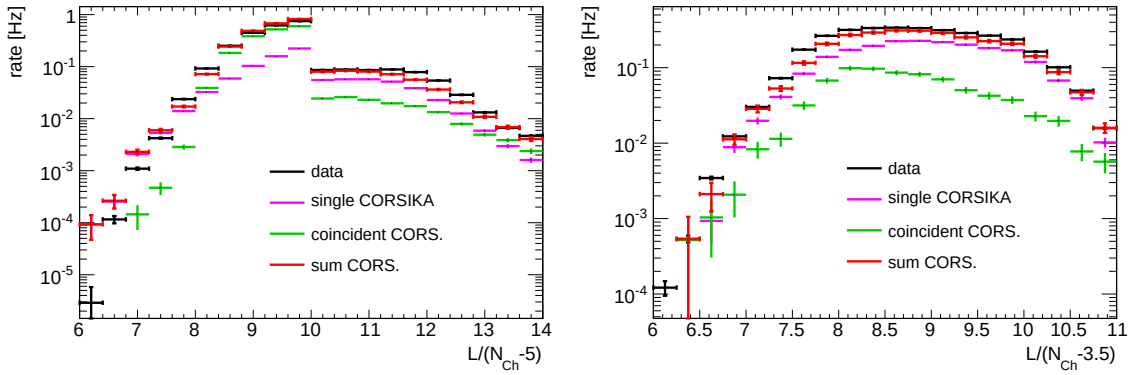

(a) IC40 (b) IC59

Figure A.12: $\mathcal{L}/(\mathrm{N_{Ch}}-5)$ distribution obtained from *llh2* for IC40 (left) and $\mathcal{L}/(\mathrm{N_{Ch}}-3.5)$ obtained from *llh1* for IC59 (right).

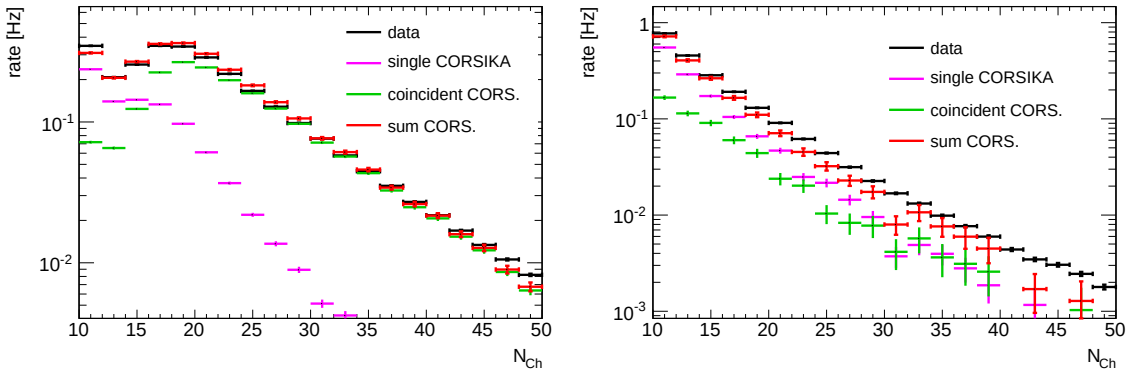

(a) IC40 (b) IC59

Figure A.13: N_{Ch} distribution obtained from *llh2* for IC40 (left) and *llh1* for IC59 (right).

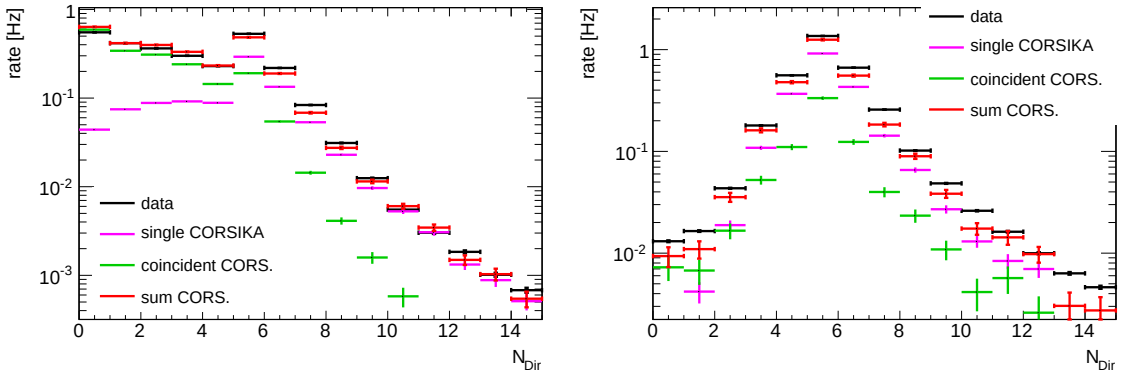

(a) IC40 (b) IC59

Figure A.14: N_{DirC} distribution obtained from *llh2* for IC40 (left) and *llh1* for IC59 (right).

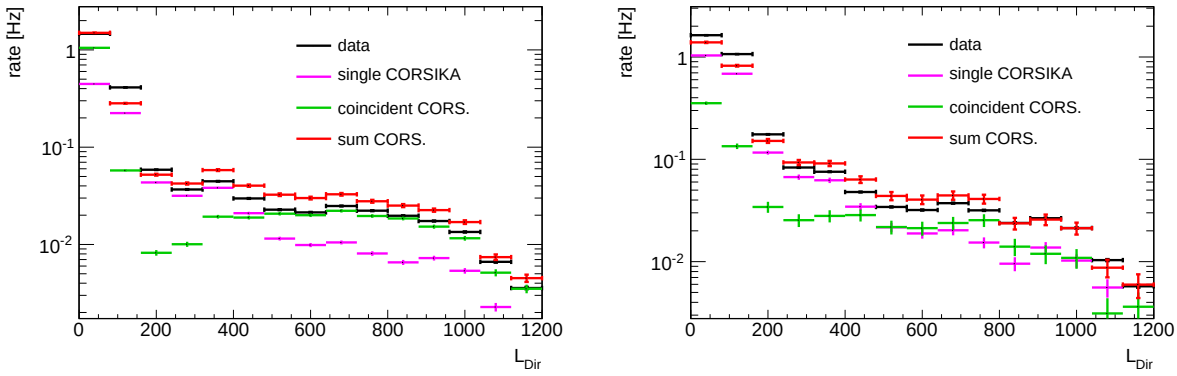

(a) IC40 (b) IC59

Figure A.15: L_{DirC} distribution obtained from *llh2* for IC40 (left) and *llh1* for IC59 (right).

A.3 Level 3

A.3.1 Level 3 - Background and Signal Distributions

The same variable distributions as shown in the previous sections are displayed here after the application of the Level 3 cuts. In addition to the two signal distributions weighted with E^{-2} and E^{-3}, the distributions for atmospheric neutrinos are shown. A clean neutrino sample would match the atmospheric neutrino sample. However, the Level 3 sample is still contaminated with atmospheric muons (63% contamination in IC40 and 30% in IC59).

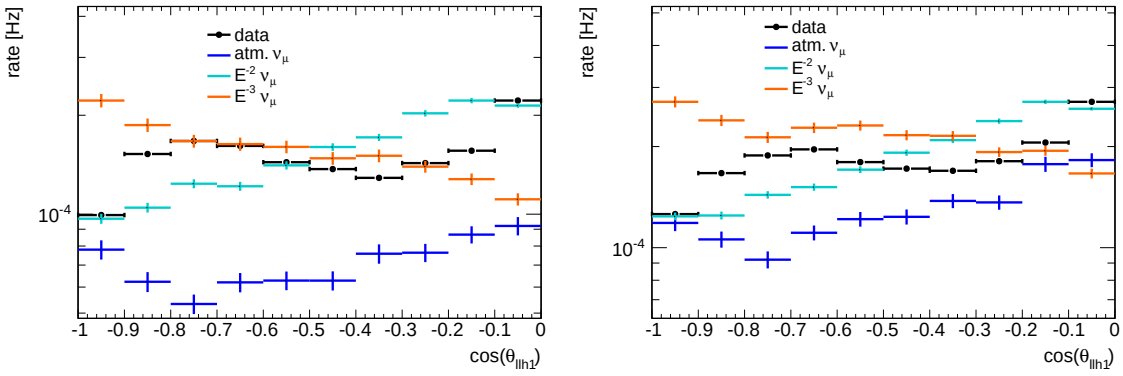

(a) IC40 (b) IC59

Figure A.16: Zenith angle distribution as obtained from single iteration likelihood fit *llh1*. The zenith angle distribution of the ten iteration likelihood fit, the paraboloid fit and the two iteration likelihood fit *llh2* (first iteration seeded with linefit and second iteration seeded with the inverted linefit), which was only available in IC40, show a similar behavior.

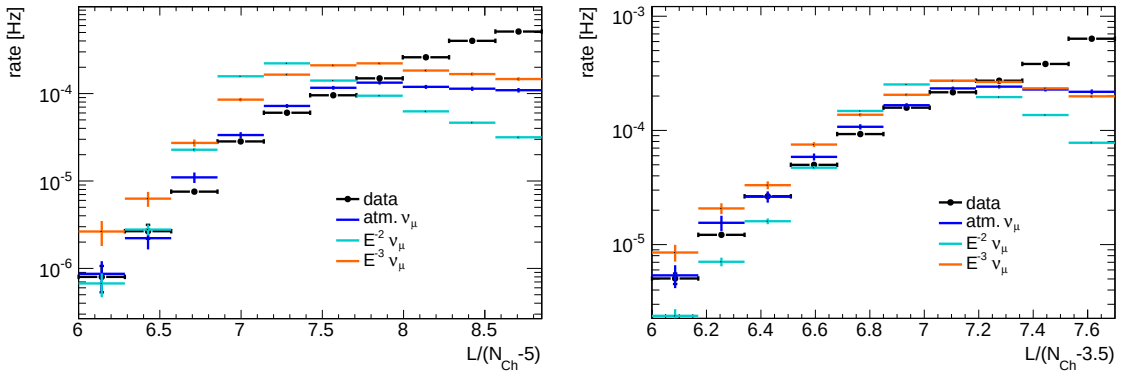

(a) IC40 (b) IC59

Figure A.17: $\mathcal{L}/(\mathrm{N_{Ch}} - 5)$ distribution obtained from *llh2* for IC40 (left) and $\mathcal{L}/(\mathrm{N_{Ch}} - 3.5)$ obtained from *llh1* for IC59 (right). Good agreement of data and atmospheric neutrino background is obtained for small values, while a contamination of atmospheric muons is visible at large values.

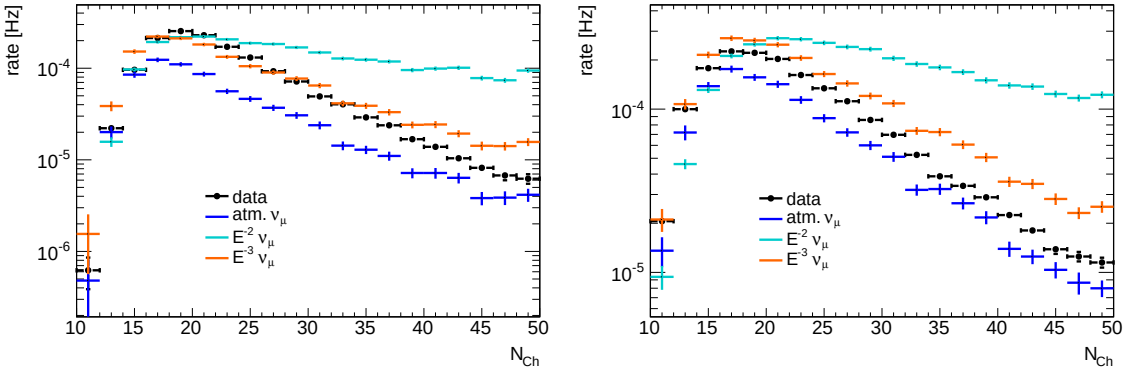

(a) IC40 (b) IC59

Figure A.18: N_{Ch} distribution obtained from *llh2* for IC40 (left) and *llh1* for IC59 (right). Signal events generated according to a hard energy spectrum generally produce more light and hence cause more sensors to be hit.

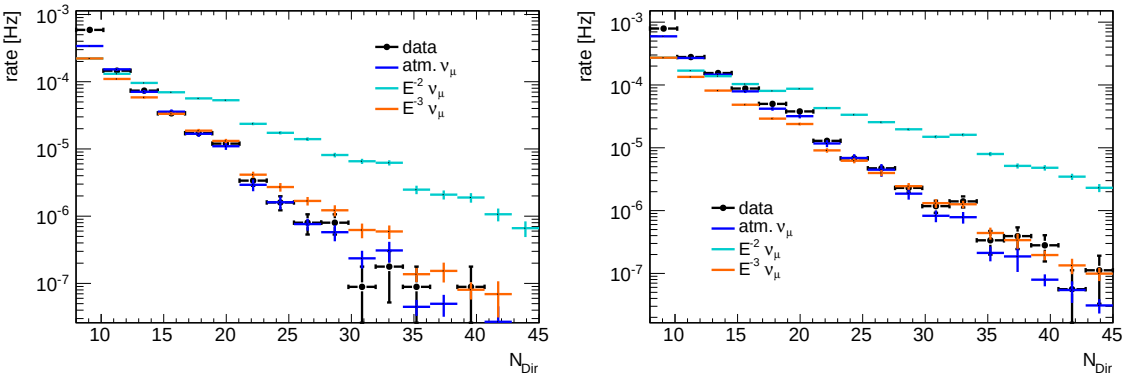

(a) IC40 (b) IC59

Figure A.19: N_{DirC} distribution obtained from *llh2* for IC40 (left) and *llh1* for IC59 (right). Especially hard spectra cause more direct hits. Data and atmospheric neutrino background agree well for values larger than ~15, while a remaining contamination of atmospheric muons is visible in the first bins.

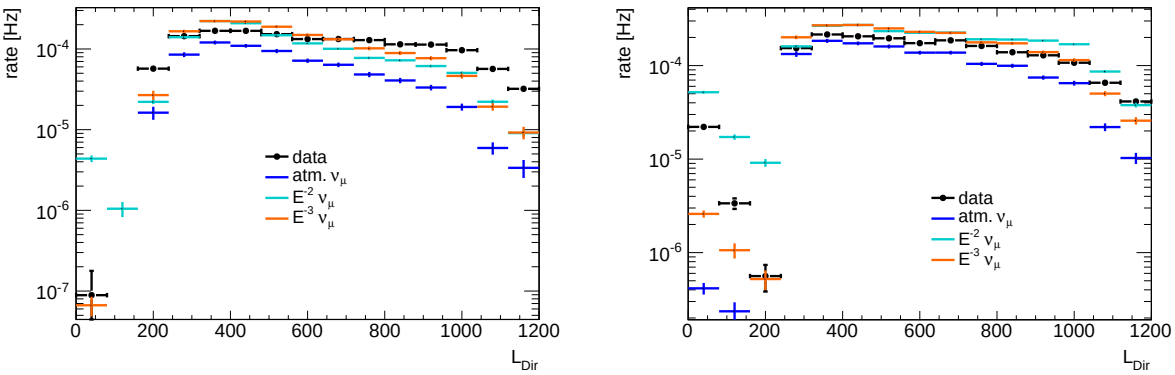

(a) IC40 (b) IC59

Figure A.20: L_{DirC} distribution obtained from *llh2* for IC40 (left) and *llh1* for IC59 (right).

A.4 Neutrino Level

To reach the neutrino level, i.e. remove the remaining background of atmospheric muons at Level 3, two cuts are tightened while retaining the Level 3 cut logic. First, the direct hit cut is set to $N_{Dir} \geq 12$ (instead of $N_{Dir} \geq 7$) and second the likelihood criteria are set to $\mathcal{L}/(N_{Ch}-5) \leq 7.7$ (instead of $\mathcal{L}/(N_{Ch}-5) \leq 8.85$) for IC40 and $\mathcal{L}/(N_{Ch}-3.5) \leq 7.0$ (instead of $\mathcal{L}/(N_{Ch}-3.5) \leq 7.7$). The comparison of data and Monte Carlo at neutrino level is important to check the reliability of the neutrino signal simulation. The following plots compare data with simulated atmospheric neutrino events for the variables used in the event selection. Furthermore, the ratio of data and Monte Carlo is shown, which scatters around one in case of good agreement between data and simulation. Data and Monte Carlo show a reasonable good agreement for the used selection parameters. However, the agreement was worse in IC40. The understanding of the detector and hence the simulation has improved for IC59.

A.4.1 Neutrino Level - Data Monte Carlo Comparison

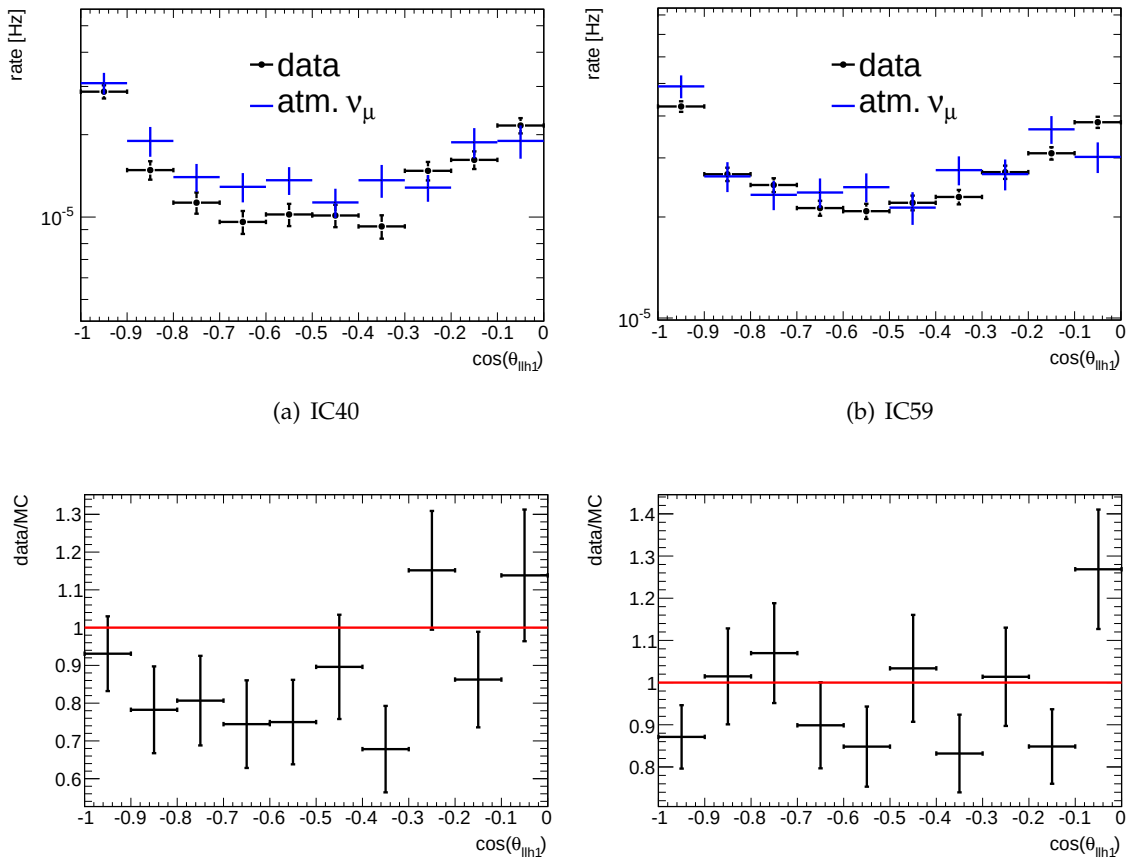

(a) IC40

(b) IC59

(c) IC40: Data MC Ratio

(d) IC59: Data MC Ratio

Figure A.21: Zenith angle distribution as obtained from single iteration likelihood fit *llh1*. The data MC agreement has improved from IC40 to IC59.

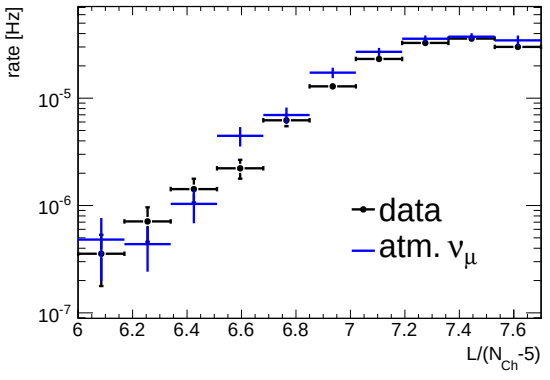

(a) IC40

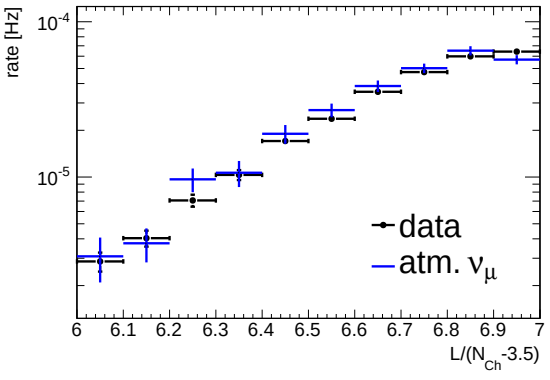

(b) IC59

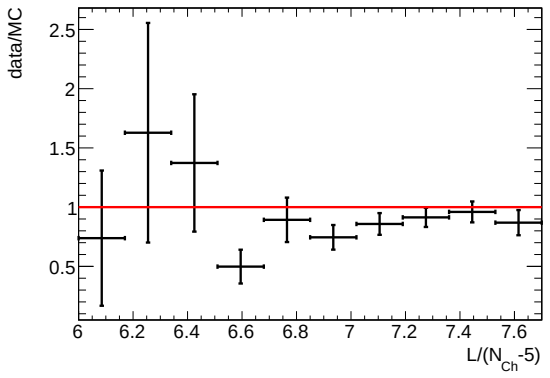

(c) IC40: Data MC Ratio

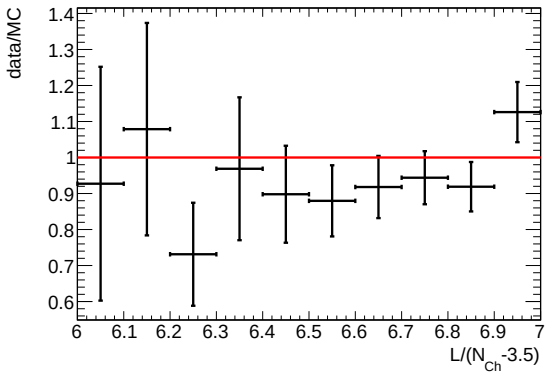

(d) IC59: Data MC Ratio

Figure A.22: $\mathcal{L}/(\mathrm{N_{Ch}} - 5)$ distribution obtained from *llh2* for IC40 (left) and $\mathcal{L}/(\mathrm{N_{Ch}} - 3.5)$ obtained from *llh1* for IC59 (right).

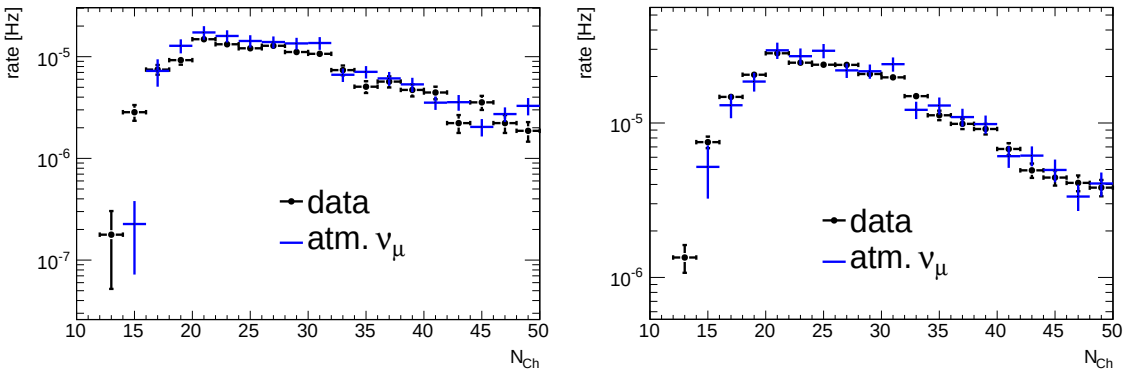

(a) IC40

(b) IC59

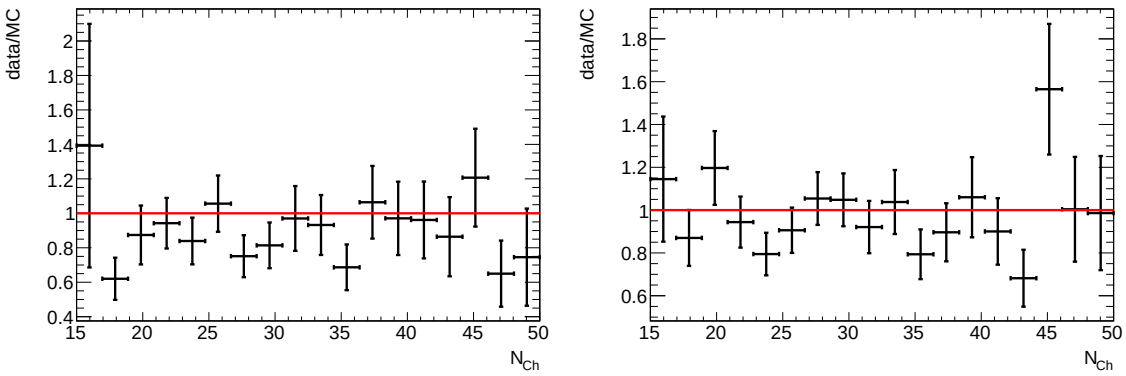

(c) IC40: Data MC Ratio

(d) IC59: Data MC Ratio

Figure A.23: N_{Ch} distribution obtained from *llh2* for IC40 (left) and *llh1* for IC59 (right).

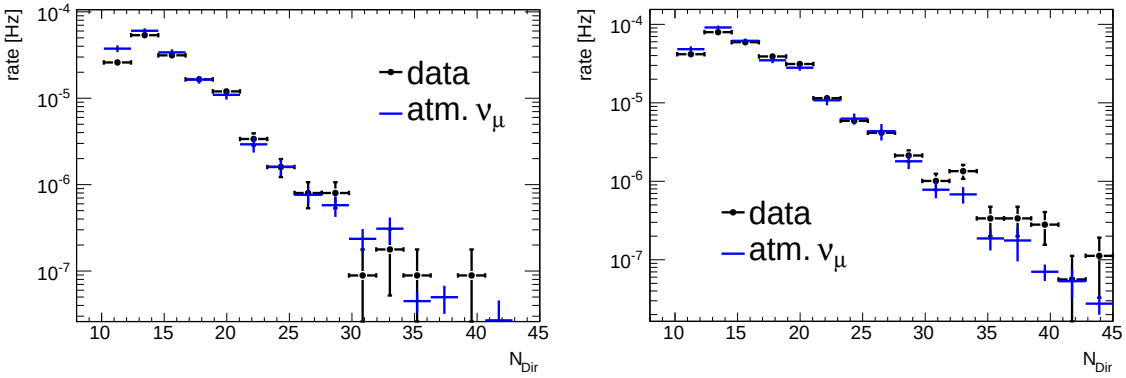

(a) IC40

(b) IC59

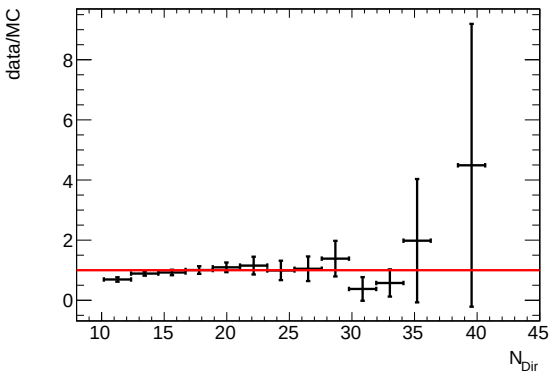

(c) IC40: Data MC Ratio

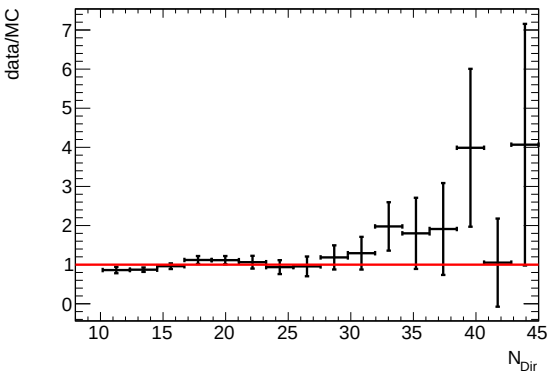

(d) IC59: Data MC Ratio

Figure A.24: N_{DirC} distribution obtained from *llh2* for IC40 (left) and *llh1* for IC59 (right).

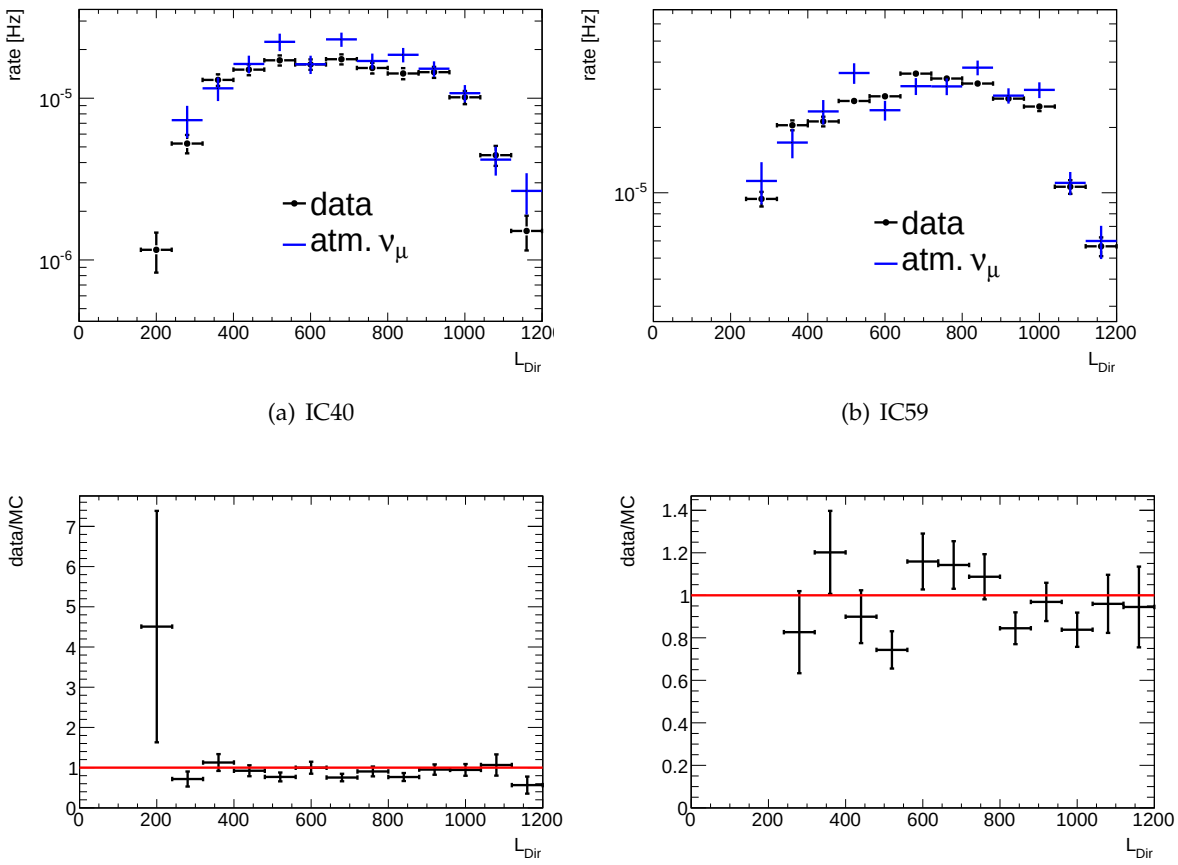

(a) IC40

(b) IC59

(c) IC40: Data MC Ratio

(d) IC59: Data MC Ratio

Figure A.25: L_{DirC} distribution obtained from *llh2* for IC40 (left) and *llh1* for IC59 (right).

Appendix B

Multivariate Analysis (MVA)

Different from traditional analyses, which usually use a few cuts on variables having some discrimination power to select interesting signal events from a possibly large background, multivariate analysis techniques involve the observation and analysis of more than one variable at a time and can possibly lead to better selection efficiencies. Aim of a selection procedure is to find the region in the multidimensional space of variables where the background suppression is minimal and the signal rejection is minimal. The application of simple cuts defines this region as one hypercube in the phase space. Multivariate methods can describe more complicated signal regions by using many variables simultaneously. The parameters of a multivariate method need to be determined from simulated data. The dataset is split into two statistically independent datasets: the training and the test dataset. The training dataset is used to determine the parameters yielding the best separation of background and signal. Then the efficiency of the selection is determined on the test dataset. Application of the selection to the independent test dataset allows to inspect over-training effects. Over-training is the result of instabilities of the algorithm with respect to statistical fluctuations in the training sample from which the parameters are derived. In cases of over-training the selection provides good results on the training data set, but bad results on the test data set. The ROOT TMVA package applies training and testing to a given dataset. TMVA provides a multitude of classifier algorithms. In this work several algorithms have been tested (see section 7.5.2) and found that the boosted decision trees (BDTs) performed best for our application. A detailed description of all implemented algorithms can be found in the TMVA user's guide [165]. Here, only a brief overview of the boosted decision trees including different boosting algorithms is given.

B.1 Boosted Decision Trees

A decision tree is a classifier, which is structured in form of a binary tree. Each step represents a yes/no decision (binary split) applied to the data. In each step the variable that gives the best separation between signal and background when being cut on is used to define the yes/no decision. Decision points are called nodes and the first node is referred to as root node. At each decision point the training data set is split in two disjunct distributions. The same algorithm is applied to both subsets in order to determine the next splitting criteria. The same variable may be used at several nodes, while others might not be used at all. The yes/no decisions are repeated until a minimum number of events, specified in the configuration, is reached. The ending nodes are referred to as leaves. The forking decision pattern consisting of several nodes builds a tree. The path down the tree to each leaf node represents an individual cut sequence that selects signal or background depending on the type of the

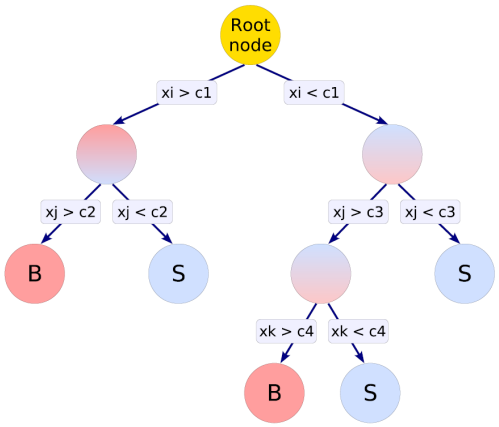

Figure B.1: Decision tree: Starting from the root node, a sequence of yes/no decisions (binary splits) is applied to the data using the variable that at this node gives the best separation between signal and background when being cut on (image adopted from [165]).

leaf node.

The phase space is split this way into many regions (hypercubes) that are eventually classified as signal or background, depending on the majority of training events that end up in the final leaf node. Figure B.1 illustrates a binary decision structure.

Compared to rectangular cuts, which select only one-hypercube, decision trees usually show better separation power. A downside of classification trees is the possible occurrence of over-training, i.e. adaption to very particular features (outliers, statistical fluctuations) of the training sample which leads to overperformance for the training sample and lower performance on the independent test data set. This problem can be overcome by *boosting* the tree as described in the next section.

B.1.1 Boosting and Bagging

The idea of boosting is to combine several weak classifiers to one strong classifier by reweighting (boosting) versions of the training sample and taking a majority vote for the final classifier. Boosting enhances the classification performance and stabilizes the response of the decision tree with respect to statistical fluctuations in the training sample.

Adaptive Boosting

In the adaptive boosting procedure M trees are derived from the same training sample, each tree is represented by a classifier $G_i(\vec{x})$, where $\vec{x}$ is a vector of cut variables. The classifier can identify the event either as signal $G(\vec{x}) = 1$ or as background $G(\vec{x}) = -1$. The first decision tree is trained using the original event weights. The subsequent tree is trained on a reweighted (boosted) event sample, where events that were misclassified during the previous training are given a higher event weight. Previously misclassified events have their weight increased by a factor $\exp(\alpha)$ with the boosting weight

$$\alpha = \frac{1-\epsilon}{\epsilon}, \tag{B.1}$$

where ϵ is the misclassification rate of the previous tree. To ensure a constant sum of weights, the weights of the entire sample are renormalized. By this way a *forest* of decision trees is

defined. Each event is processed by all trees in the forest and the final output is an average of results of each tree:

$$G(\vec{x}) = \text{sign}\left(\sum_{\text{m=1}}^{\text{M}} \alpha_{\text{m}} \text{G}_{\text{m}}(\tilde{\text{x}})\right) \tag{B.2}$$

The coefficients α_m are the boosting weights. The adaptive boosting method is illustrated in figure B.2.
On the one hand the adaptive boosting algorithm yields good performance in classification problems, but on the other hand it is sensitive to outliers and noisy data.

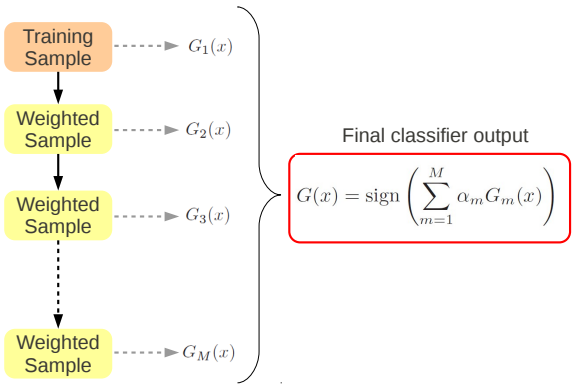

Figure B.2: Adaptive boosting: M trees are derived from the same training sample, each tree is represented by a classifier $G_i(\vec{x})$, a function of the cut variables $\vec{x}$. The first decision tree is trained using the original event weights, while subsequent trees are trained on a reweighted (boosted) event sample, where events that were misclassified during the previous training are given a higher event weight. The final output is an average of the results of all trees (illustration adopted from [202]).

Gradient Boosting

Boosting can be generalized as the minimization of a specific loss function. Mathematically each event can be described as a set of input variables $\vec{x} = x_1, x_2, ..., x_n$ and the corresponding classifier output y. The training sample consists of N events $y_i, \vec{x}_i{}_1^N$ with known $y, \vec{x}$-values. Solving the classification problem means to find a close approach to the function $F(\vec{x})$ that maps $\vec{x}$ to y, for each event i characterized by the variables $\vec{x}_i$. $F(\vec{x}_i)$ allows the identification of the event as signal or background. $F(\vec{x})$ can be estimated as a forest of trees $f(\vec{x}, \vec{a})$, i.e. a linear expansion of several weak classifiers:

$$F(\vec{x}) = \sum_{i=1}^{M} \alpha_i f_i(\vec{x}), \tag{B.3}$$

where M is the number of trees. The deviation of $F(\vec{x})$ to the true value y can be measured by the loss function $L(y, F(\vec{x}))$. The weights α are adjusted by minimizing the average of the loss function $\sum_i L_i(y, F(\vec{x}_i))$ in a steepest-descent approach. The whole boosting procedure is determined by the definition of the loss function. It can be shown that the adaptive boost algorithm uses the loss function:

$$L(y, F(\vec{x})) = \exp(-2yF(\vec{x})). \tag{B.4}$$

The sensitivity to outliers shown by the adaptive boosting method can be reduced by replacing the loss function. The gradient boost procedure implemented in TMVA uses a binomial log-likelihood function:

$$L(y, F(\vec{x})) = \log(1 + \exp(-yF(\vec{x}))). \tag{B.5}$$

Bagging

As opposed to boosting, bagging does not combine weak classifiers to one strong one, but it smears out statistical fluctuations and stabilizes the classifier output. The principle idea of bagging is to regard the training sample as a representation of the probability density function (PDF). A new training data set can be obtained by randomly picking events from the parent data set PDF. It is allowed to pick one event several times in order not to change the parent PDF. Several classifiers are trained with resampled training data sets and are combined to an average classifier, which is more stable to statistical fluctuations compared to a single training data set.

Appendix C

List of Alerts

The following table contains detailed information for every neutrino multiplet found in this analysis from December 16, 2008 to December 31, 2009. All found multiplets consist of two events, i.e. are doublets. Each doublet has an IceCube ID assigned. The first IceCube ID was 9. Earlier doublets were collected in a test phase and are not included in this analysis. The IceCube ID is reset to zero at the beginning of a new year.
Each doublet detection triggers an optical observation, which gets a ROTSE ID assigned. To distinguish triggers received by different instruments (e.g. HETE, Swift, IceCube), the IceCube triggers start at 2000. The first trigger used in this analysis is 2005, while earlier triggers were send during a test phase. In some cases the observation was not successful as indicated by comments in the table. In case of a successful observation, the number of nights, in which an image was recorded, are shown in the table for the 4 different telescopes: 3a (Australia), 3b (Texas), 3c (Namibia) and 3d (Turkey).
Furthermore, the table contains the date of the alert, defined as the arrival time of the first event of the recorded multiplet, and the alert direction given by right ascension (ra) and declination (dec) in degrees. The galactic latitude has been calculated from the equatorial coordinates ra and dec. In addition the table contains the number of USNO A2.0 catalog stars in the corresponding $1.85^\circ \times 1.85^\circ$ field, if it overlaps with the area covered by the catalog. Finally, the table shows the date of the reference image used in the image subtraction and the number of candidates left for visual scanning.

Table C.1: Alert Summary

IceCube ID	ROTSE ID	date	right ascension	declination	galactic latitude	USNO stars	reference image	cand. for vis. scan.	nights of observation 3a	3b	3c	3d
9	2005	2008-12-18T01:25:13	111.352	-3.361	6.0	dec<0						
10	2006	2008-12-28T02:58:24	291.424	-3.389	-9.2	dec<0						
11	2007	2008-12-28T06:22:17	275.337	66.358	27.7	18606	30/08/2009	82	0	14	0	7
12	2008	2008-12-30T02:49:40	58.459	47.691	-4.8	50742	too close to gal. plane					
13	2009	2008-12-31T18:14:22	209.366	-2.381	56.5	dec<0						
14	2010	2008-12-31T21:40:36	211.611	-3.684	54.3	dec<0						
0	2011	2009-01-04T03:00:54	73.818	-2.183	-26.7	dec<0						
1	2012	2009-01-04T13:26:06	155.123	-4.201	42.0	dec<0						
2	2013	2009-01-06T13:51:08	223.070	18.904	61.1	not sent to ROTSE						
3	2014	2009-01-13T00:40:20	7.442	41.094	-21.6	not sent to ROTSE						
4	2015	2009-01-15T10:09:25	69.164	-1.496	-30.4	dec<0						
5	2016	2009-01-16T09:51:21	249.921	-3.174	27.3	dec<0						
6	2017	2009-01-17T03:16:52	178.320	53.044	61.8	7848	20/12/2009	12	0	9	0	4
7	2018	not real alert										
8	2019	2009-02-01T05:41:34	59.706	-0.705	-37.9	dec<0						
9	2020	2009-02-07T00:37:44	152.059	-4.198	39.7	dec<0						
10	2021	2009-02-12T16:51:26	255.105	35.857	37.2	21073	30/08/2009	11	0	8	0	1
11	2022	2009-02-12T18:50:25	340.725	-1.246	-49.8	dec<0						
12	2023	2009-02-13T20:24:34	223.140	1.418	51.3	12884	19/02/2009	55	6	12	0	0
13	2024	2009-02-13T23:49:38	58.611	40.983	-9.8	not sent to ROTSE						
14	2025	2009-02-16T15:25:48	108.862	13.432	11.2	52319	20/12/2009	114	8	8	2	5
83	2026	2009-02-25T10:34:35	275.103	83.391	27.8	flasher						
81732	2088	2009-03-02T13:58:14	158.020	34.498	59.2	8370	20/12/2009	4	7	5	0	2
81733	2089	2009-03-09T04:46:23	270.595	-3.664	9.2	dec<0						
81734	2090	2009-03-15T17:25:05	265.100	-4.816	13.4	dec<0						
81735	2091	2009-03-18T21:57:13	252.927	0.036	26.5	24647	26/03/2009	455	9	9	11	0
81736	2092	2009-03-23T12:09:57	26.118	-3.875	-63.5	dec<0						
81737	2093	2009-03-31T15:17:08	19.744	18.293	-44.1	too close to the sun						

Table C.2: Alert Summary

IceCube ID	ROTSE ID	date	right ascension	declination	galactic latitude	USNO stars	reference image	nights of observation 3a	3b	3c	3d
81738	2094	2009-04-01T21:25:56	77.210	36.907	-2.1	53583	23/12/2009	too close to gal. plane			
81739	2095	2009-04-09T19:52:08	156.287	-1.950	44.3	dec<0					
81740	2096	2009-04-28T15:56:40	324.033	-3.325	-37.7	dec<0					
81741	2097	2009-04-29T00:02:10	120.454	50.527	31.4	16477	20/12/2009	0	9	0	6
81742	2098	2009-05-02T21:17:32	71.694	-3.861	-29.4	dec<0					
81743	2099	2009-05-10T00:07:04	39.843	36.526	-21.5	too close to the sun					
81744	2100	2009-05-24T00:02:00	51.626	30.221	-21.7	dec<0					
81745	2101	2009-06-02T14:30:45	307.149	14.887	-13.6	75407	22/11/2010	6	12	0	11
81746	2102	2009-06-04T03:28:01	275.589	10.527	11.3	90968	too crowded				
81747	2103	2009-06-21T04:13:12	112.663	21.708	18.0	too close to the sun					
81748	2104	2009-06-27T10:46:47	44.165	28.191	-27.1	17159	10/07/2009	0	2	3	0
81749	2105	2009-06-28T09:29:17	288.662	36.246	11.4	91955	too crowded				
81750	2106	2009-06-30T03:16:40	120.605	20.719	24.5	too close to the sun					
81751	2107	2009-08-06T17:18:00	346.773	6.213	-48.2	10706	13/08/2009	11	4	11	0
81752	2108	2009-08-07T12:05:46	201.717	43.289	72.3	7638	20/08/2009	0	5	0	1
81753	2109	2009-08-09T06:14:51	315.784	1.727	-27.9	27235	14/08/2009	11	8	12	1
81754	2110	transmission failed, send again as 2111									
	2111	2009-08-30T02:19:33	2.718	0.309	-60.9	too close to the sun					
81755	2112	2009-09-12T08:29:13	154.842	44.994	54.9	no good data					
81759	2113	2009-11-03T01:26:12	148.221	19.487	48.5	standard candle					
91300	2114	2009-11-06T09:39:48	91.155	59.547	17.6	no good data					
91301	2115	2009-11-26T12:49:20	353.845	17.520	-41.7	13049	12/12/2009	1	11	8	1
91302	2116	2009-12-02T11:02:06	73.740	36.287	-4.7	37028	too close to gal. plane				
91303	2117	2009-12-04T01:53:41	227.093	3.212	49.5	13028	11/12/2009	0	12	0	0
91304	2118	2009-12-05T00:31:13	281.635	14.679	7.7	94320	too crowded				
91305	2119	2009-12-09T00:45:12	172.979	7.189	62.6	7568	17/12/2009	1	6	12	0
91306	2120	2009-12-10T14:25:15	102.948	4.412	2.1	81765	too close to gal. plane				
91307	2121	2009-12-22T18:09:21	23.417	53.141	-9.2	65850	05/01/2010	0	13	0	0

Danksagung

An dieser Stelle möchte ich mich bei all jenen bedanken, die mich in den letzten vier Jahren unterstützt und zum Gelingen dieser Arbeit beigetragen haben.
An erster Stelle gilt mein Dank Prof. Dr. Marek Kowalski, der diese Arbeit überhaupt erst möglich gemacht hat, für die hervorragende Betreuung. Ich hätte mir kein spannenderes PhD Projekt vorstellen können. Danke, dass du mich mit deiner Begeisterung angesteckt hast und mich auch in schwierigen Zeiten immer motiviert hast.
Desweiteren wäre diese Arbeit nicht zu Stande gekommen ohne die Unterstützung der ROTSE Kollaboration, die uns großzügig Beobachtungszeit und Zugang zu ihren Teleskopen gewährt haben. Mein besonderer Dank gilt Prof. Dr. Carl Akerlof und Dr. Fang Yuan die sich liebevoll um mich gekümmert haben während meines Aufenthaltes in Ann Arbor und Dr. Weikang Zheng, der eine große Hilfe war bei der Implemention von Änderungen im Beobachtungsprogramm.
Besonderer Dank gilt meinen Arbeitskollegen, die in den letzten 4 Jahre für ein harmonisches und fruchtbares Arbeitsklima verantwortlich waren. Ich danke der HU IceCube Crew, Sebastian Panknin und Anna Mohr (die kleine Anna), für die schöne Zeit im Adlershofer Büro und geduldige Hilfe bei zahlreichen Computing Problemen. Danke an Prof. Dr. Doug Cowen für hilfreiche Diskussionen, für die Möglichkeit in einem 3-wöchigen Aufenthalt in PennState alles üeber Detektorstabilität zu lernen und die Chance 4 Wochen am Südpol zu verbringen. Danke an die DESY Kollegen, besonders Robert Franke für seine Hilfe bei technischen Problemen. Nach meinem Umzug nach Bonn verdanke ich ein mindestens genauso familiäres Arbeitsumfeld meinen IceCube Kollegen Dr. Sebastian Böser, Andreas Homeier, Markus Voge, Nora Strotjohann, Tobias Degner und Martin Stüer, sowie der SNFactory Gruppe Dr. Clement Buton (hot like fire!!!), Dr. Kerstin Paech, Dr. Matthias Kerschaggl, Ulrich Feindt and Amir Moqanaki. Besonderer Dank gilt Kerstin für eine gute Zeit im PI Büro und Andreas und Markus für die gemeinsame Zeit und die vielen Kekse in der IceCube Villa.
Sehr dankbar bin ich all denen, die einen Teil dieser Arbeit gelesen haben und mir behilflich waren diesen Text mehr oder weniger von inhaltlichen Unklarheiten und Rechtschreibfehlern zu befreien. Danke, Daniel, Sebastian, Kerstin, Peter, Torsten, Andi, Andreas, Markus, Clement und Marek.
Danke, Mareike und Verena, für nette Mittagessen in der Mensa! Danke Ruth für die tolle WG-Zeit! Danke Daniel für den gemeinsamen “Kampf” durchs Studium.
Ganz besonderer Dank geht an die Firma high-tech consulting, d.h. Dr. Torsten Schmidt, für stetiges an-den-Ohren-Ziehen und Nachhilfe im Programmieren. Ohne Torsten würde heute vermutlich kein optical follow-up code am Südpol laufen. Danke für die schöne Zeit in Berlin – ich bin froh dich als Freund zu haben.
Schließlich bin ich meiner Familie und meinen Freunden zu großem Dank verpflichtet für Ihre langjährige moralische Unterstützung. Besonderer Dank gilt meinen Eltern, Ulla und Jürgen sowie meinen Freunden Torsten, Jenny, Daniel, Ruth und Henrik.
Danke Andi - du bist meine Süßwarenabteilung im Supermarkt.